University College London - UCL

Centre for Doctoral Training in Data Intensive Science Department of Physics & Astronomy

A multi-wavelength observational study of white dwarfs with anomalous atmospheric signatures

PhD Thesis

Submitted by: **Nikolay Walters**

Supervisor: **Prof. J. Farihi**

Declaration

I, Nikolay Walters, confirm that the work presented in this thesis is my own. Where information has been derived from other sources, I confirm that this has been indicated in the thesis.

Abstract

This thesis explores extrinsic interaction signatures in cool white dwarfs through multicomponent optical and infrared spectra coupled with photometry. The first part of the thesis investigates the mechanism behind Balmer emission lines in isolated white dwarfs, focusing on the unipolar inductor model. The model involves a magnetic interaction between a star and a closely orbiting planet whose motion induces heating in the stellar photosphere. Observations suggest that the emission is intrinsic and rule out star-planet interaction as the cause. The study of the prototype and similar white dwarfs indicates the presence of chromospheres in magnetic white dwarfs, thus forming a new evolutionary class of emitting white dwarfs. The second part of the thesis investigates two possible substellar survivors orbiting white dwarf stars. Infrared and optical spectroscopy of GD 1400 reveals a 70 M_{Jup} brown dwarf, while PG 0010+281 may be orbited by a debris disc. An empirical benchmark of 50 M_{Jup} is placed on the minimal required mass for a closely orbiting companion to avoid post-main sequence annihilation via stellar evolution. The last part of the thesis examines intrinsic mass loss (wind) from low-mass companions in white dwarf binary systems through the pollution observed in the photospheres of white dwarfs. Mass loss estimates are calculated for M dwarf secondaries and limits on substellar wind accretion are placed based on four white dwarfs with L-type brown dwarf companions, with one case of a highly non-solar abundance ratio detection. The study provides a unique window into brown dwarf activity and upper layer chemical composition through white dwarf atmospheric pollution. Overall, the results described in this thesis offer insight into the properties and evolution of white dwarfs and their companions. This includes the potential presence of chromospheres as well as the survival and behavioural properties of substellar objects during post-main sequence evolution.

Impact Statement

In contemporary astrophysical research, white dwarfs, being the evolutionary endpoints of low-to-intermediate mass stars, serve as vital cosmic chronometers that encode crucial information about the history and future of galactic populations. Multi-wavelength observational studies of white dwarfs presenting anomalous atmospheric signatures can shed light on various phenomena, notably the intricacies of late-stage stellar evolution, the accretion of substellar and planetary material, and the intricately complex interplay between their inherent magnetic fields and stellar atmospheres. Such a multi-wavelength approach, encompassing the ultraviolet, optical, and infrared spectra, is imperative because these anomalies often manifest distinctly across different energy bands, revealing a wealth of data that can be otherwise concealed in single-wavelength observations. Moreover, understanding these anomalous signatures can inform models of stellar evolution, potentially revealing overlooked processes or refining existing paradigms.

Chapter 2 provides a comprehensive analysis of the enigmatic white dwarf GD 356, utilising optical photometric, spectroscopic, and spectropolarimetric observations to characterise its Balmer emission lines. Although the genesis of these lines remains enigmatic, substantial progress has been made in ascertaining their intrinsic nature and in identifying a distinct class of white dwarfs that manifest similar features. Subsequently, Chapter 3 expands on this investigation by incorporating both near and far ultraviolet spectroscopic data.

The complexities inherent to the common envelope phase of close binary evolution pose considerable challenges to theoretical modeling. Chapter 4 addresses this problem by employing an observational methodology to characterise two putative post-common envelope binaries. It proposes an empirical benchmark for a mass for a close-in companion necessary for the said companion to endure the giant phases undergone by the white dwarf progenitor.

Furthermore, the extreme atmospheric purity of certain low-temperature white dwarfs makes them perfect detectors of pollution from proximate companions. Chapter 5 explores this avenue, focusing on the detectable atmospheric features caused by stellar wind from close brown dwarf companions – a subject that remains largely uncharted in terms of wind behaviour. Through analysing the composition and abundance of such atmospheric pollutants, this chapter endeavors to estimate both the mass loss rate and chemical composition of these elusive stellar winds.

Overall, this thesis has catalysed the publication of three peer-reviewed articles and multiple successful observing proposals, including observations using the *Hubble Space Telescope*. These contributions have been disseminated through presentations at both a specialised conference and a workshop that focused explicitly on advancing the frontiers of white dwarf research.

Acknowledgements

First and foremost, I would like to express my deepest gratitude to my supervisor, Jay Farihi, whose guidance, support, and expertise have been invaluable throughout this journey. Jay, your insights and unwavering commitment have truly shaped this research, and I am forever thankful for your mentorship.

I extend my heartfelt thanks to my family for their constant encouragement. My friends and collaborators have also played an invaluable role in this research, and I am grateful for their camaraderie and feedback.

In the midst of this academic endeavor, I was fortunate to cross paths with Maple. Though our encounter was brief, the joy and positivity you brought into my life have left a lasting impact. While you may remain distanced from the intricacies of astrophysical research, the happiness and inspiration you provided have been essential to my journey. Because of this, I would like to dedicate this thesis to you. Your influence, though subtle, has been profound, reminding me that sometimes the most unexpected connections can leave the deepest imprints.

UCL Research Paper Declaration Form: referencing the doctoral candidate's own published work(s)

I

- 1. For a research manuscript that has already been published (if not yet published, please skip to section 2):
 - (a) What is the title of the manuscript? A test of the planet-star unipolar inductor for magnetic white dwarfs
 - (b) Please include a link to or doi for the work: 10.1093/mnras/stab617
 - (c) Where was the work published? Monthly Notices of the Royal Astronomical Society (MNRAS)
 - (d) Who published the work? Oxford University Press
 - (e) When was the work published? 05/03/2021
 - (f) List the manuscript's authors in the order they appear on the publication: N Walters, J Farihi, T R Marsh, S Bagnulo, J D Landstreet, J J Hermes, N Achilleos, A Wallach, M Hart, C J Manser
 - (g) Was the work peer reviewd? Yes
 - (h) Have you retained the copyright? No
 - (i) Was an earlier form of the manuscript uploaded to a preprint server (e.g. medRxiv)? If 'Yes', please give a link or doi https://arxiv.org/abs/2103.01993
 - I acknowledge permission of the publisher named under 1d to include in this thesis portions of the publication named as included in 1c.
- 2. For a research manuscript prepared for publication but that has not yet been published (if already published, please skip to section 3):
 - (a) What is the current title of the manuscript?
 - (b) Has the manuscript been uploaded to a preprint server 'e.g. medRxiv'? If 'Yes', please please give a link or doi:
 - (c) Where is the work intended to be published?
 - (d) List the manuscript's authors in the intended authorship order:
 - (e) Stage of publication:
- 3. For multi-authored work, please give a statement of contribution covering all authors (if single-author, please skip to section 4):

NW: Data reduction, data analysis, data interpretation, and writing the manuscript

JF: Data acquisition, advise on data reduction, advise on data analysis, advise on data interpretation, and advise on the manuscript

TRM: Data acquisition, advise on data reduction, advise on data analysis, advise on data interpretation, and advise on the manuscript

SB: Data acquisition, data reduction, data analysis, data interpretation, and contribution to the manuscript

JDL: Data acquisition, data reduction, data analysis, data interpretation, and contribution to the manuscript

JJH: Advise on data analysis, advise on data interpretation, and advise on the manuscript

NA: Advise on data interpretation and contribution to the manuscript

AW: Data acquisition and data reduction

MH: Data acquisition

CJM: Advise on data analysis and data interpretation

4. In which chapter(s) of your thesis can this material be found? Chapter 2

II

- 1. For a research manuscript that has already been published (if not yet published, please skip to section 2):
 - (a) What is the title of the manuscript? Two substellar survivor candidates: one found and one missing
 - (b) Please include a link to or doi for the work: 10.1093/mnras/stac3603
 - (c) Where was the work published? Monthly Notices of the Royal Astronomical Society (MNRAS)
 - (d) Who published the work? Oxford University Press
 - (e) When was the work published? 09/12/2022
 - (f) List the manuscript's authors in the order they appear on the publication: N Walters, J Farihi, T R Marsh, E Breedt, P W Cauley, T von Hippel, J J Hermes
 - (g) Was the work peer reviewd? Yes
 - (h) Have you retained the copyright? No
 - (i) Was an earlier form of the manuscript uploaded to a preprint server (e.g. medRxiv)? If 'Yes', please give a link or doi https://arxiv.org/abs/2207.07022
 - I acknowledge permission of the publisher named under 1d to include in this thesis portions of the publication named as included in 1c.
- 2. For a research manuscript prepared for publication but that has not yet been published (if already published, please skip to section 3):
 - (a) What is the current title of the manuscript?
 - (b) Has the manuscript been uploaded to a preprint server 'e.g. medRxiv'? If 'Yes', please please give a link or doi:
 - (c) Where is the work intended to be published?
 - (d) List the manuscript's authors in the intended authorship order:
 - (e) Stage of publication:

3. For multi-authored work, please give a statement of contribution covering all authors (if single-author, please skip to section 4):

NW: Data reduction, data analysis, data interpretation, and writing the manuscript

JF: Data acquisition, data reduction, data analysis, advise on data interpretation, and advise on the manuscript

TRM: Data acquisition, advise on data analysis, advise on data interpretation, and advise on the manuscript

EB: Data acquisition, advise on data reduction, and advise on data analysis

PWC: Data acquisition, data reduction, advise on data analysis, and advise on data interpretation

TvH: Data analysis and advise on data interpretation

JJH: Advise on data interpretation and advise on the manuscript

4. In which chapter(s) of your thesis can this material be found? Chapter 4

Ш

- 1. For a research manuscript that has already been published (if not yet published, please skip to section 2):
 - (a) What is the title of the manuscript? Measurement of stellar and substellar winds using white dwarf hosts
 - (b) Please include a link to or doi for the work: 10.1093/mnras/stad1885
 - (c) Where was the work published? Monthly Notices of the Royal Astronomical Society (MNRAS)
 - (d) Who published the work? Oxford University Press
 - (e) When was the work published? 23/06/2023
 - (f) List the manuscript's authors in the order they appear on the publication: N Walters, J Farihi, P Dufour, J S Pineda, R G Izzard
 - (g) Was the work peer reviewd? Yes
 - (h) Have you retained the copyright? No
 - (i) Was an earlier form of the manuscript uploaded to a preprint server (e.g. medRxiv)? If 'Yes', please give a link or doi

https://arxiv.org/abs/2306.11806

- riangleq I acknowledge permission of the publisher named under 1d to include in this thesis portions of the publication named as included in 1c.
- 2. For a research manuscript prepared for publication but that has not yet been published (if already published, please skip to section 3):
 - (a) What is the current title of the manuscript?
 - (b) Has the manuscript been uploaded to a preprint server 'e.g. medRxiv'? If 'Yes', please please give a link or doi:
 - (c) Where is the work intended to be published?
 - (d) List the manuscript's authors in the intended authorship order:

(e) Stage of publication:

3. For multi-authored work, please give a statement of contribution covering all authors (if single-author, please skip to section 4):

NW: Data reduction, data analysis, data interpretation, and writing the manuscript

JF: Advise on data reduction, advise on data analysis, advise on data interpretation, and advise on the manuscript

PD: Data analysis

JSP: Advise on data interpretation and advise on the manuscript

RGI: Advise on data interpretation

4. In which chapter(s) of your thesis can this material be found? Chapter 5

e-Signatures confirming that the information above is accurate (this form should be co-signed by the supervisor/ senior author unless this is not appropriate, e.g. if the paper was a single-author work):

Candidate: Luculo
Date: 10/12/2023

Supervisor/Senior Author signature (where appropriate):

Date: 10/12/2023

Contents

List of Figures			iv	
Li	List of Tables			vi
1	Introduction			
	1.1	The pa	st and the future	1
	1.2	-	evolution	3
		1.2.1	Main sequence to white dwarf	3
		1.2.2	White dwarf cooling sequence	5
	1.3	Binario	es	11
		1.3.1	Binary evolution	11
		1.3.2	Period-mass distribution	14
		1.3.3	Observing binary systems	17
	1.4	Magne	etism	19
2	A 40	at of the	a planet stan uninglan industry for magnetic white devoufs	25
4	2.1		e planet-star unipolar inductor for magnetic white dwarfs	25 25
	2.1		ct	23 26
	2.2		action	20
	2.3	2.3.1	vations and data	27
		2.3.1	Time-series spectroscopy	28
		2.3.2	Spectropolarimetry	33
		2.3.4	The Liverpool Telescope	33
		2.3.4	The Perkins Telescope Observatory	35
	2.4		sis and results	35
	∠.¬	2.4.1	Photometric variability	38
		2.4.2	Spectroscopic variability	39
		2.4.3	Possible emission feature evolution	42
		2.4.4	Spectropolarimetric measurements and variability	42
	2.5		sion	47
	2.3	2.5.1	Implications of the photometric and spectroscopic variability	48
		2.5.2	Interpretation of the magnetic measurements	49
		2.5.3	Challenges to unipolar inductor model	51
		2.5.4	Intrinsic chromospheric activity in white dwarfs	54
	2 (<i>-</i> 0

3	Refl	ections on GD 356	61
	3.1	DAHe predictions	. 61
	3.2	My continuation of the research	. 66
		3.2.1 <i>Gaia</i>	. 66
		3.2.2 Further GD 356 observations	. 69
		3.2.3 WHT	. 70
		3.2.4 <i>HST</i>	
	3.3	Conclusions	. 75
4	Two	substellar survivor candidates; one found and one missing	77
	4.1	Abstract	. 77
	4.2	Introduction	. 78
	4.3	Observations and data	. 79
		4.3.1 GD 1400	
		4.3.2 PG 0010+281	. 83
	4.4	Analysis and results: GD 1400	. 86
		4.4.1 Stellar parameters	. 86
		4.4.2 Optical radial velocities of GD 1400A	
		4.4.3 Infrared radial velocities of GD 1400B	. 87
		4.4.4 Orbital period determination	. 89
		4.4.5 Discussion	. 91
	4.5	Analysis and results: PG 0010+281	. 95
		4.5.1 Stellar parameters	. 95
		4.5.2 Radial velocities	. 95
		4.5.3 Companion limits	. 97
		4.5.4 Time-series photometry	. 101
		4.5.5 Infrared flux excess	. 101
	4.6	L dwarf survivors of giant encounters	. 105
	4.7	Summary and conclusions	. 105
5	Mea	surement of stellar and substellar winds using white dwarf hosts	107
	5.1	Abstract	. 107
	5.2	Introduction	. 108
	5.3	Observations and data	. 109
		5.3.1 GD 1400	. 110
		5.3.2 WD 0137–349	. 110
		5.3.3 NLTT 5306	. 110
		5.3.4 SDSS J141126.20+200911.1	
	5.4	Data analysis	. 111
		5.4.1 Fitting Balmer features	. 111
		5.4.2 Construction of white dwarf rest-frame co-added spectra	
		5.4.3 Abundance determinations and upper limits	
		5.4.4 Brown dwarf mass-loss rates	
	5.5	Results	
		5.5.1 Brown dwarf winds	
		5.5.2 Stellar winds	
	5.6	Discussion	
		5.6.1 Prior work and measurements	

6	Conclusions			130
	5.7	Conclu	asions	. 128
		5.6.4	The detection of Na in NLTT 5306	. 124
		5.6.3	Mass loss and activity across the substellar boundary	. 122
		5.6.2	New M dwarf wind estimates	. 122

List of Figures

1.1	White dwarf spectral types	6
1.2	Evolution track of a white dwarf	7
1.3	Colour-magnitude diagram of the 100 pc sample of white dwarfs	10
1.4	Orbital separation and mass of substellar objects with a white dwarf primary	16
1.5	Trailed spectra of a double-lined binary	18
1.6	Composite spectral energy distribution	20
1.7	Magnetic transitions of Balmer lines	21
1.8	Histograms of magnetic field strengths for crystallized and non-crystallized	
	white dwarfs	23
2.1	Phase-folded and trailed spectra of GD 356	30
2.2	Spectropolarimetry of GD 356	32
2.3	TESS variability in the GD 356 area	34
2.4	Lomb-Scargle periodogram of GD 356 spectra and photometry	36
2.5	O-C diagram of GD 356 and a Lomb-Scargle periodogram of the $O-C$	
	data	37
2.6	Phase-folded light curve, equivalent widths and central wavelengths of	
	emission lines of GD 356	40
2.7	Potential morphological dissimilarity in the emission of GD 356	43
2.8	Potential change in the equivalent widths of GD 356	44
2.9	Comparison of GD 356 between the recent spectropolarimetric data and	
	data from Ferrario et al. (1997a)	48
2.10	$\langle B_z \rangle$ and $\langle B \rangle$ as a function of photometric phase of GD 356	50
2.11	Lomb-Scargle periodogram of J0412	56
2.12	Colour-magnitude diagram of white dwarfs and the four DA(H)e stars	57
3.1	Colour-magnitude diagram of white dwarfs and and the new DAHe can-	
	didates	62
3.2	The cumulative distribution of the known DAHe stars as a function of	
	cubic volume and distance	63
3.3	A kernel density estimates of DAH and DAHe stars for mass and magnetic	
	field strengths	65
3.4	Examples of <i>Gaia</i> BP/RP spectra compared to typical low resolution spectra	68
3.5	Variable white dwarfs on the colour magnitude diagram	69
3.6	Ultraviolet phase-folded light curves of GD 356	72
3.7	Semi-amplitudes of GD 356 variability in different filters	73
3.8	Further subdivided semi-amplitudes of GD 356 variability in different filters	73
3.9	O-C diagram of GD 356 including the new data	74

3.10	TESS amplitudes of variability of GD 356 across different sectors
4.1	Flux density contours of GD 1400
4.2	GD 1400 infrared spectrum and the best matching synthetic spectra 88
4.3	GD 1400A and GD 1400B radial velocities
4.4	PG 0010+281 radial velocities from multiple instruments 94
4.5	Detection probabilities as a function of orbital period for a range of sub-
	stellar companion masses for PG 0010+281
4.6	Lomb-Scargle periodogram of PG 0010+281
4.7	Infrared spectra of PG 0010+281
4.8	Spectral energy distribution of PG 0010+281
5.1	Spectra of Ca II K and Na I D lines
5.2	Accretion estimates based on different chemical elements and mass-loss
	as a function of Rossby number

List of Tables

2.1	Published parameters of GD 356	28
2.2	Journal of observations of GD 356	31
2.3	Re-constructed spectral energy distribution of GD 356 convolved with the various light curve filters	38
2.4	Magnetic field measurements of GD356 using H α and H β	46
4.1	Journal of observations of GD 1400 and PG 0010+281	81
4.2	Orbital and (sub)stellar parameters of the GD 1400 binary	91
4.3	Summary of radial velocity measurements for PG 0010+281	96
5.1	Adopted stellar parameters, abundance determinations, accretion and mass-loss rates for (sub)stellar winds captured by white dwarfs	116

Chapter 1

Introduction

White dwarf stars remain pivotal in astrophysical research, offering unparalleled insights into stellar evolution, galaxy history, and fundamental physics (Fontaine et al., 2001; Althaus et al., 2010). Their intricate cooling processes (Winget et al., 2009), mass-radius relationship (Provencal et al., 1998), luminosity function (García-Berro & Oswalt, 2016), anomalous atmospheric compositions (Farihi et al., 2010b; Koester et al., 2014; Harrison et al., 2018), dynamic interactions in binary systems (Marsh, 2011), associations with dark matter candidates (Bertone & Fairbairn, 2008), related planetary systems (Farihi, 2016), and pre-white dwarf evolution (Miller Bertolami, 2016) have all been subjects of intensive study. These investigations not only deepen our understanding of white dwarfs but also shed light on broader topics such as Type Ia supernovae mechanisms (Maoz et al., 2014), cosmic age determination (Winget & Kepler, 2008), and galactic chemical evolution (Kobayashi et al., 2020). In the context of this thesis, three specific areas are of paramount interest: magnetism, common envelope efficiency, and post common envelope binaries with substellar companions. However, I will introduce some basic concepts to get a more broad understanding of these important stars.

1.1 The past and the future

Although the first observation of a white dwarf star was performed by Sir William Herschel in 1783 (Herschel, 1785; Kawaler & Dahlstrom, 2000) during an observational program of 'double stars' that acted as the first observational proof of Newtonian gravity outside the solar system, the observed white dwarf 40 Eridani B was not recognised as anything unusual. Half a century later, observations by Friedrich Bessel in 1844 resulted in a strange detection of movement in the star Sirius making him conclude that it must have an unseen companion (Bessel, 1844). This was later confirmed, when, in 1862, Alvan Graham Clark first observed the companion, Sirius B (Bond, 1862). At the time, the theory of gravitational contraction as the source of energy for the Sun and stars, proposed by Herman von Helmholtz in 1854, was widely accepted. This led some scholars to the idea that the companion of Sirius could even be a planet, reflecting light from the primary star due to a luminosity difference of 10 000 observed in the system. It was only in 1891 that John Ellard Gore conclusively demonstrated that Sirius B must be a self-luminous object (Gore, 1891). The significance of the Sirius B observations, even though the white dwarf nature of the star was not yet known, is that they provided one of the earliest

confirmations of Einstein's theory of general relativity. Clearly, white dwarfs played an important role in the understanding of gravity before they were even discovered!

The first identification of a white dwarf, as it is understood today, was made by Walter Sydney Adams in the 1910s. His detailed spectroscopic studies of Sirius B led to the first inference of the composition of a white dwarf (Adams, 1915). The first isolated white dwarf - van Maanen 2, more commonly known as van Maanen's Star was discovered by Adriaan van Maanen in 1917 (van Maanen, 1917) and recognised as a white dwarf in 1919. These discoveries prompted Ralph Fowler in 1926 to approach white dwarfs from the theoretical point of view (Fowler, 1926). By using the newly developed quantum mechanics to explain the high density and low luminosity of white dwarfs he proposed that white dwarfs are degenerate stars, with particles inside the star being packed as closely as the laws of quantum mechanics allow. White dwarf physics would not be complete without the mention of Subrahmanyan Chandrasekhar who in 1931 calculated a mass limit (now known as the Chandrasekhar limit) beyond which any object would not be able to support itself against self-gravity and collapse (Chandrasekhar, 1931). Although I have outlined the basic history of white dwarf discovery, a much more detailed overview can be found in an excellent chapter by Holberg (2009).

By the end of the twentieth century, a white dwarf catalogue had documented approximately 2000 of these celestial bodies (McCook & Sion, 1999). Fast forward to the present day, and the *Gaia*-based catalogue has increased dramatically the number of white dwarfs, boasting a comprehensive list of 359 000 high-confidence candidates, alongside an expansive reservoir of more than one million potential candidates (Gentile Fusillo et al., 2021b). This exponential growth is indicative not merely of advances in the specialised area of white dwarf research, but is rather emblematic of the broader surge in data volume within the global astrophysical community, precipitated by an array of both established and emergent surveys.

A case in point is the Dark Energy Spectroscopic Instrument (DESI; DESI Collaboration et al. 2016). In the initial year of observations alone, this survey flagged over 47 000 prospective white dwarfs spectroscopically. This represents a substantial leap forward in our quest to comprehend the physics of white dwarfs and their associated phenomena. Looking ahead, the wave of new data from observational missions and multi-object spectroscopic sky surveys is set to further illuminate our understanding of these intriguing celestial objects. The roster of these surveys includes a variety of advanced observatories, such as the James Webb Space Telescope (JWST; Gardner et al. 2006) and the Cosmological Advanced Survey Telescope for Optical and UV Research (Fantin et al., 2019), as well as ground-breaking initiatives like the Large Synoptic Survey Telescope (LSST; Ivezić et al. 2019), the Sloan Digital Sky Survey-V (SDSS-V; Kollmeier et al. 2017), the 4-metre multi-object spectroscopic telescope (de Jong et al., 2019), and the William Herschel Telescope Enhanced Area Velocity Explorer (WEAVE; Dalton et al. 2014). Moreover, ongoing data extraction from the Gaia mission is expected to continually enrich our comprehension of white dwarf physics (Gaia Collaboration et al., 2016). This confluence of data sources promises to yield an unparalleled perspective on white dwarfs and their cosmic milieu.

1.2 Stellar evolution

The majority of main-sequence stars, which are part of the vast population of stars in our galaxy, are destined to evolve into white dwarfs, depending on their mass. This transformation is a complex journey that takes place through various phases of stellar evolution. As stars progress from the main-sequence stage, they undergo changes that have considerable implications for the planets orbiting them and for close binary components. The evolution towards the white dwarf stage is marked by specific transitions and processes, and is summarised below.

1.2.1 Main sequence to white dwarf

The current understanding of stellar evolution states that stars possessing initial masses lower than approximately 8 M_{\odot} (Weidemann & Koester, 1983; Cummings et al., 2019) will ultimately complete their nucleosynthetic processes and eventually transform into white dwarfs, which are, in essence, remnants of the stellar core. A notable proportion, constituting over 97 per cent (Fontaine et al., 2001) of the stars in the Milky Way, are projected to undergo this evolutionary transition to white dwarfs. It is, however, important to acknowledge that every white dwarf was once a main-sequence star in the early stages of its stellar existence.

During the main sequence, stars remain in a state of hydrostatic equilibrium, establishing a balance between the pressure generated by nuclear fusion and the inward pull of gravity. The specifics of the main sequence phase of a star are largely determined by its initial mass, along with the integral factor of chemical composition (Kippenhahn et al., 2013). The mass of a star significantly impacts its surface gravity, temperature, and core pressure. Thus, the mass of a star directly influences its lifespan within the main sequence, with stars of greater mass consuming their fuel at a swifter pace and consequently having shorter overall lifespans.

Throughout the main sequence, the star maintains a relatively stable rate of energy production. However, this period concludes when the star has depleted the hydrogen fuel within its core. When the force of gravity becomes stronger than the pressure from fusion, the stellar core contracts. This marks the beginning of the next phase in the evolution: the red giant branch (RGB; Salaris et al. 2002). Concurrently, the outer layers of the star, responding to the heightened core temperature, expand. This sets the stage for the vigorous burning of a hydrogen shell encompassing the degenerate helium core. As these RGB stars progress in their evolution, a convective envelope situated above the core continues to deepen progressively, consequently constricting the hydrogen-burning shell which is situated at the bottom of the envelope.

The steady deepening of the convective region ensures that the lower boundary of the convective envelope encroaches upon regions chemically processed by the core. As a result, processed material, such as He, C, and N, is rapidly mixed throughout the convective envelope, in an event typically referred to as the first dredge-up (Boothroyd & Sackmann, 1999).

Eventually, upon the helium core achieving an approximate mass of $0.5~M_{\odot}$, the core undergoes ignition, leading to the helium flash (Sweigart & Gross, 1976). This event dispels the electron degeneracy in the core, marking the termination of the RGB phase and propelling the star into the horizontal branch (HB; Castellani et al. 1985). The onset of the

HB stage marks the initiation of quiescent central helium burning accompanied by shell hydrogen burning. The HB extends horizontally on the Hertzsprung-Russell diagram (HRD), as the helium core-burning stars possess approximately equal luminosities but diverging surface temperatures (Catelan, 2009; Girardi, 2016).

Once the helium within the core is consumed, the star undergoes another expansion, entering the asymptotic giant branch (AGB) phase. Here, the star comprises a carbon-oxygen core encircled by shells of helium- and hydrogen-burning layers. One of the unique characteristics of AGB stars is this dual shell burning (Höfner & Olofsson, 2018), featuring both a hydrogen and a helium shell burning exterior to an inert, degenerate core - contrasting with the single hydrogen shell burning exhibited in RGB stars. As helium from the hydrogen shell is increasingly deposited into the helium-burning shell, the star undergoes periodic thermal pulses, inducing fluctuations in its size and luminosity. Analogous to the RGB phase, the star swells and cools during the AGB phase, growing in size and luminosity, but featuring a cooler surface.

Two additional dredge-up processes transpire during this phase, one in the early AGB stage and another subsequent to a thermal pulse (Herwig, 2005). AGB stars experience substantial mass loss owing to potent stellar winds, which can strip away a significant fraction of the stellar mass while enriching the surrounding interstellar medium with elements heavier than helium (Willson, 2000; Tielens, 2005). These stellar winds, and hence the mass loss process, are further bolstered by thermal pulses (Engels, 2005). The AGB phase culminates when the outer envelope is nearly entirely stripped away by these stellar winds, revealing a hot, compact core - a nascent white dwarf. The ejected envelope is ionized by the exposed core, leading to the creation of a planetary nebula (Balick & Frank, 2002).

The planetary nebula phase is the final stage of stellar evolution before a star becomes a white dwarf. Ionizing radiation from the central star illuminates the ejected envelope, which causes it to glow (Kwitter & Henry, 2022). Despite its name, a "planetary nebula" bears no association with planets. The name was coined due to their planet-like appearance in early telescopic observations (Parker, 2022). Over time, the nebula expands and eventually dissipates into the interstellar medium, enriched with elements synthesized within the star throughout its lifespan (Dorschner & Henning, 1995; Edwards et al., 2014). As the central star cools and contracts under gravity, it eventually becomes a white dwarf, which then continues to cool.

From the observational standpoint, the newly formed white dwarfs can vary. To characterise the properties of these stars, spectroscopy, in particular, can be a powerful tool. To group white dwarfs by their spectral type a classification system by Sion et al. (1983) is commonly used. Following this system, spectral designation always starts with a 'D' to denote their degenerate nature. A spectral type DA implies the existence of hydrogen (Balmer) lines, whereas a DB indicates the manifestation of He I spectral lines. Contrarily, DO white dwarfs also exhibit helium lines in their spectra; however, distinct from DB white dwarfs, a DO spectrum will possess ionised He II lines. Moving on, DQ white dwarfs display carbon lines in their spectra. Low-temperature DQ white dwarfs ($T_{\rm eff} < 10\,000\,{\rm K}$) are hydrogen-deficient stars that dredged up carbon via convection (Blouin et al., 2023). White dwarfs displaying metal lines, exclusive of carbon, are annotated with the letter 'Z' and are linked to accretion and atmospheric pollution (Zuckerman et al., 2003). In instances where spectral lines are absent, the spectral type DC is designated. Typically, these are helium-rich white dwarfs with $T_{\rm eff} < 11\,000\,{\rm K}$ (Baglin & Vauclair, 1973),

although occasionally they can also be hydrogen-rich stars with $T_{\rm eff}$ < 5000 K (Bergeron et al., 1997). Beyond chemical classifications, suffixes may be appended to elucidate further characteristics. For example, the 'V' suffix signifies variability, more precisely, in relation to pulsating white dwarfs. The 'H' suffix is reserved for instances where spectroscopic lines are visibly split by a magnetic field.¹ If a magnetic field's presence is deduced via spectropolarimetry, a 'P' suffix is employed. Finally, an 'e' suffix designates the presence of emission lines. A selection of white dwarf spectra are shown in Figure 1.1. The next subsection then describes the white dwarf cooling process in detail.

1.2.2 White dwarf cooling sequence

White dwarf cooling behaviour is influenced by several factors, with the core composition being the most significant. These stars can be classified into three groups based on their core composition, which is largely determined by the progenitor mass from which they originated. The majority of them harbour cores of carbon and oxygen, but those with lower initial masses, less than approximately $0.4\,M_\odot$, will primarily consist of helium. Conversely, their more massive counterparts, exceeding around $1.05\,M_\odot$, possess cores composed mainly of oxygen and neon (Garcia-Berro & Iben, 1994). Core composition plays an important role in the cooling process because it has a direct effect on the specific heat capacity. For instance, oxygen-core white dwarfs are expected to cool faster than carbon-core white dwarfs (Mestel, 1952). Similarly, atmospheric composition, usually hydrogen or helium-dominated, affects the opacity experienced by photons as they radiate away (Fontaine et al., 2001). About 80 per cent of white dwarfs have a thin hydrogen layer with a slightly thicker helium envelope underneath (Isern et al., 2022).

White dwarfs embark on their cooling journey at temperatures typically exceeding $100\,000\,\mathrm{K}$, and exhibit substantial luminosity (Hügelmeyer et al., 2005). However, with nuclear fusion effectively no longer active, their energy source is finite, and they are destined to cool over time. It should be noted, however, that residual nuclear reactions are not totally extinguished (Iben & MacDonald, 1985, 1986), and there is a contribution from the CNO cycle and proton-proton chains for up to 2 Gyr in the outer shell (Iben & Tutukov, 1984b). Although their total energy contribution is negligible in terms of age delay, the luminosity increase is significant (Iben & Tutukov, 1984b; Renedo et al., 2010). Nonetheless, the initial cooling stage is relatively swift, mainly due to the high temperature and luminosity of the star, which facilitate rapid energy loss (Althaus et al., 2011). In fact, a $0.6\,M_\odot$ white dwarf experiences a drop in the effective temperature from $100\,000\,\mathrm{K}$ to $50\,000\,\mathrm{K}$ in approximately 2 Myr (Bédard et al., 2020).

This process, however, is not simplistic, and the rate of cooling undergoes several changes throughout the life of a white dwarf. At the beginning, a short-lived phase of proton-proton and helium-burning dominates the luminosity contribution. Then, from $\approx 0.4\,\mathrm{Myr}$ (Renedo et al., 2010), neutrino emission has the largest contribution to the energy loss, as these particles escape the star with little interaction (Winget et al., 2004; Kantor & Gusakov, 2007; Althaus et al., 2010). The efficiency of neutrino cooling diminishes as the white dwarf cools and its interior becomes increasingly degenerate (Renedo et al., 2010). After approximately 10 Myr, neutrino cooling becomes irrelevant (Althaus et al., 2010).

¹Frequently, suffix 'H' is used to indicate the magnetic nature of a white dwarf, regardless of the detection method used.

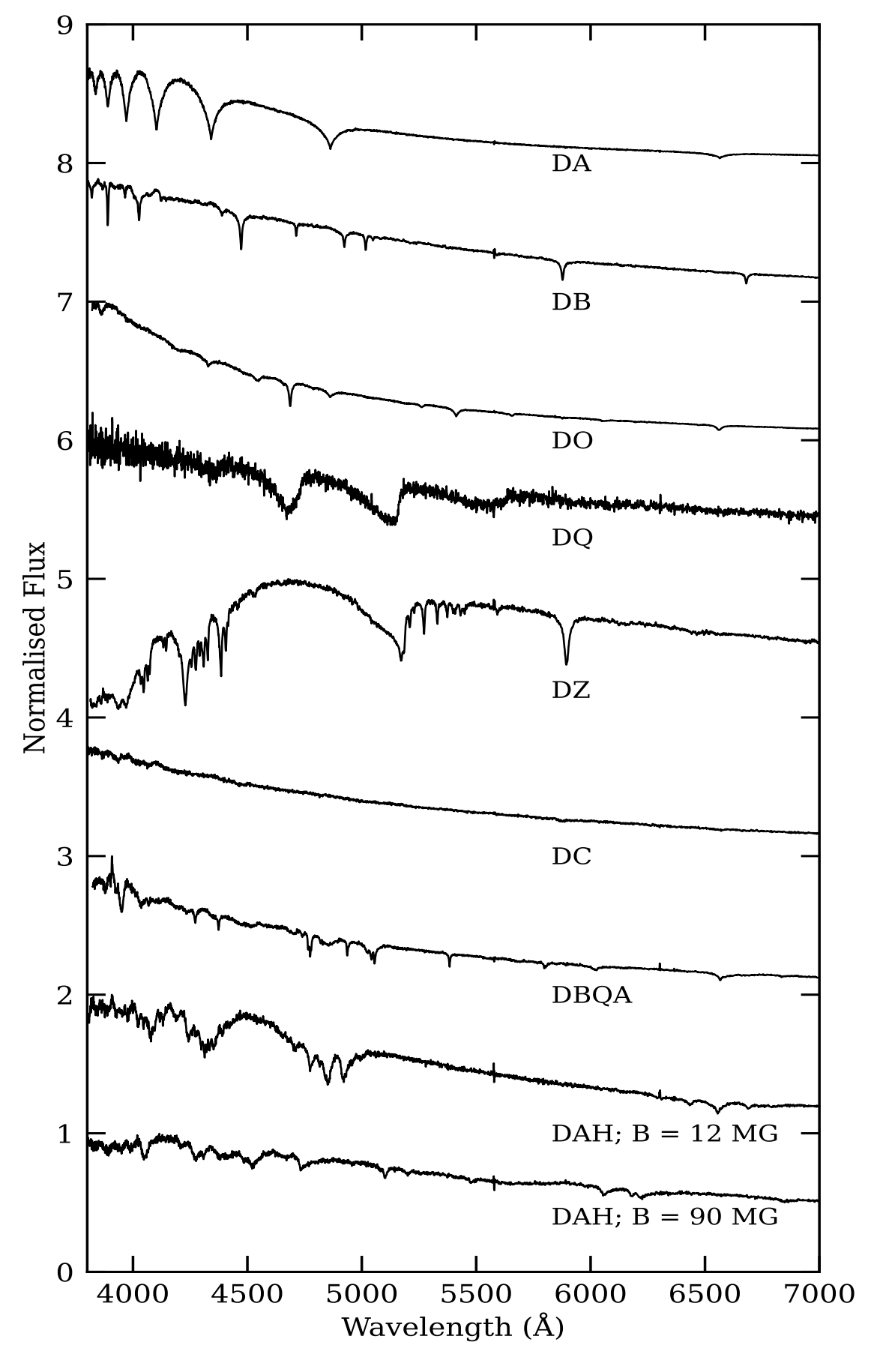


Figure 1.1: White dwarf spectral types from Sloan Digital Sky Survey. Fluxes are normalised and offset.

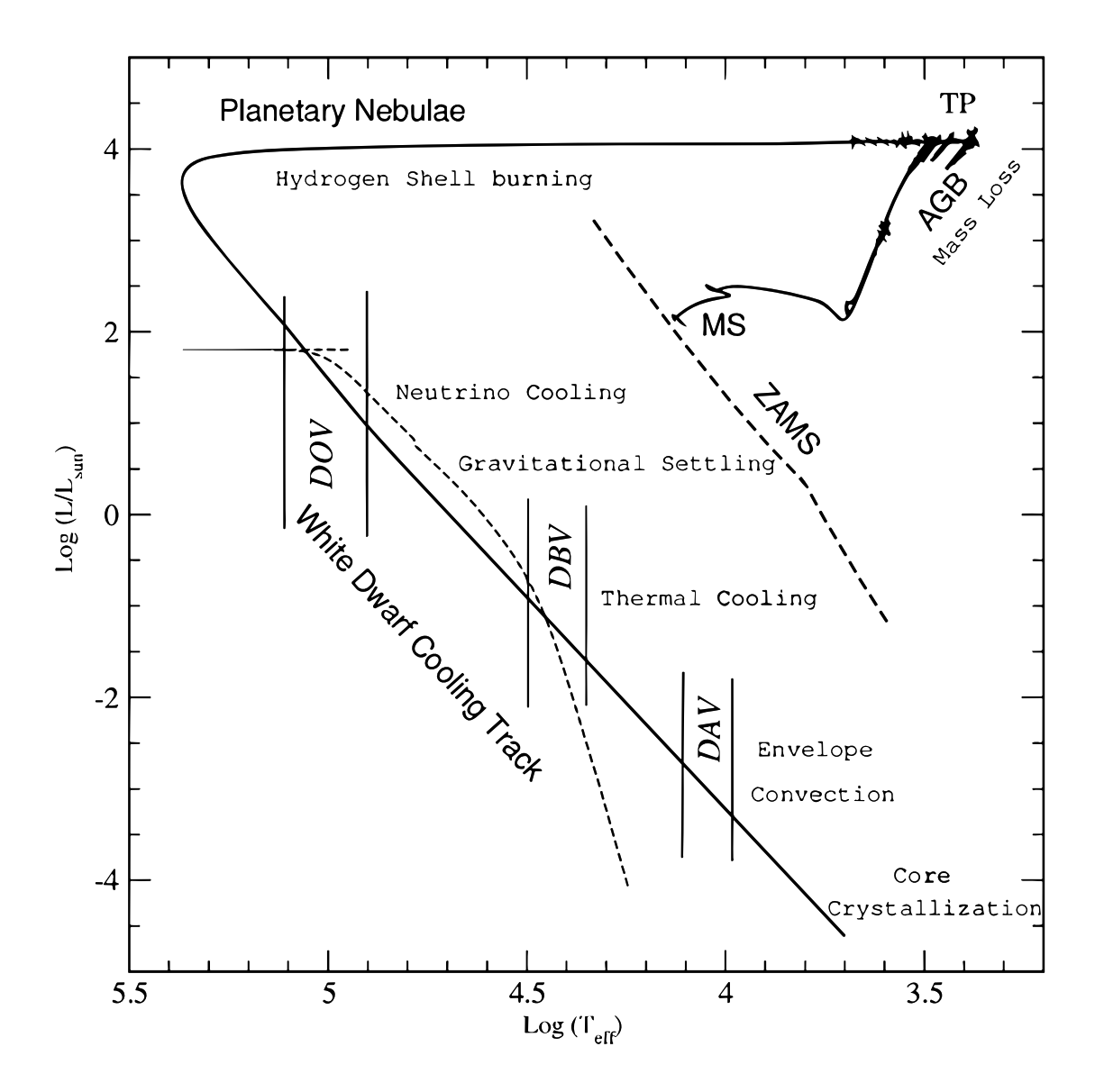


Figure 1.2: Evolution track of a $0.66\,M_\odot$ white dwarf $(3.5\,M_\odot$ zero age mass sequence mass) on the Hertzsprung-Russell diagram reproduced from Althaus et al. (2010). Different evolutionary stages, dominant cooling mechanisms and pulsating instability strips are indicated. The dashed line in the left part of the figure represents neutrino luminosity.

As the white dwarf cools further, electron degeneracy increases and the specific heat of strongly degenerate electrons approaches zero. This fact plays an important role at high luminosities, especially for low-mass white dwarfs (Althaus et al., 2010). As expected, the core composition can influence the density and electron degeneracy pressure, further impacting the cooling behaviour (García-Berro & Oswalt, 2016).

Below $T_{\rm eff} \approx 75\,000\,\rm K$ gravitational settling starts to operate leading to chemical differentiation in the white dwarf (Bédard et al., 2022). Heavier elements sink towards the centre due to the strong gravity, while lighter elements rise to the surface. Although this type of diffusion most certainly takes place in hotter white dwarfs, the overall effect is counteracted by a weak radiative stellar wind and radiative levitation (Chayer et al., 1995; Quirion et al., 2012). This gravitational settling affects the opacity of the outer layers and the cooling rate (Mochkovitch, 1983; Garcia-Berro et al., 1988).

Subsequently, at temperatures below 25 000 K, photon emission from the surface becomes the primary driver of cooling, a phase often referred to as photon cooling or thermal cooling (Hansen et al., 2015; Drewes et al., 2022). During this stage, the cooling process is regulated by the thermal conduction in the degenerate electron gas, convective heat transport in the outer layers, and radiative energy transfer at the surface.

When the temperature drops to around 10000 K, the outer hydrogen envelope of a typical white dwarf turns convective (Koester & Schoenberner, 1986; Hansen, 2004). Prior to that, the inner part of the white dwarf remains relatively well insulated by the nondegenerate envelope (Lamb & van Horn, 1975). The deeper layers of the envelope, which are rich in helium, are brought up to the surface if the hydrogen envelope is thin enough (Bergeron et al., 1997; Hansen, 2004). At that moment the envelope becomes more transparent, resulting in the release of excess energy. This initially reduces the cooling rate, but once the excess energy has been dissipated the convection process actually increases the cooling rate (Fontaine et al., 2001). This is because convection is much more efficient than radiation at transporting energy (Althaus et al., 2010).

Once the core temperature decreases to a point where the ion thermal energy is comparable to the Coulomb interaction energy between ions, the white dwarf core begins to crystallize (Tremblay et al., 2019). The crystallization stage takes place over a few Gyr (Renedo et al., 2010). The release of latent heat during crystallization further slows the cooling (Hansen, 1999, 2004). In addition to latent heat, core solidification also introduces gravitational sedimentation as a source of energy (Mochkovitch, 1983; Isern et al., 1997, 2000, 2022). It should be noted that in massive white dwarfs convective coupling occurs during the late crystallization stage, while intermediate-mass white dwarfs experience convective coupling and crystallization simultaneously (Althaus et al., 2010; Renedo et al., 2010).

Half a century ago, it was established that the crystallization phase transition in the core of white dwarfs would decelerate their cooling process, thereby leading to a statistically observable pile-up on the cooling sequence at particular temperatures and masses (van Horn, 1968). The initial evidence of this phenomenon was discovered within the cooling sequence of the globular star cluster NGC 6397 and was attributed to the latent heat release from crystallization (Winget et al., 2009; Campos et al., 2016). More recently, detailed data from *Gaia* uncovered definitive evidence of premature crystallization among white dwarfs, particularly those with masses exceeding the average in the Milky Way's disk (Cheng et al., 2019; Tremblay et al., 2019).

As the temperature of the crystallized core keeps decreasing, it eventually drops below

the Debye temperature and the heat capacity of the white dwarf reduces further (D'Antona & Mazzitelli, 1989; Renedo et al., 2010). This phase, often referred to as the Debye cooling phase, marks the transition from a fluid to a solid state (Chabrier et al., 1992; Chabrier, 1993).

After cooling for approximately 10 Gyr, a typical white dwarf would reach an effective temperature below 4000 K (García-Berro & Oswalt, 2016). At this temperature, a white dwarf would start to lose its iconic spectral energy distribution that can be approximated by a black body as H₂ molecules become abundant in the atmosphere (Saumon & Jacobson, 1999). Observationally, these white dwarfs are exceedingly difficult to detect; however, for the sake of completeness, it is worthwhile to continue examining their evolution. Eventually, white dwarfs would cool to sub-Kelvin temperatures, reaching equilibrium with the cosmic background radiation. This final evolutionary stage is commonly referred to as the black dwarf stage (not to be confused with old brown dwarfs with $M < 0.08 \,\mathrm{M}_{\odot}$; Kumar 1994). Due to pycnonuclear fusion, the black dwarf would undergo progressive stages of burning, theoretically forming an Fe⁵⁶ core. Black dwarfs with masses exceeding $1.16\,\mathrm{M}_\odot$ are expected to explode in supernova due to this process. This exciting phase of evolution could happen as soon as 10^{1100} yr, although some physical effects, such as proton decay, could have a negative effect on the formation of a black dwarf supernova (Caplan, 2020). As a final summary, Figure 1.2 shows an evolutionary track of a $0.66 \, \mathrm{M}_{\odot}$ white dwarf on HRD starting from the main sequence with the evolutionary stages that take place labelled.

Even though the theoretical cooling sequence is highly informative, further insight can be gained from the empirical positions of white dwarfs on HRD as they traverse their cooling trajectory. Figure 1.3, shows the 100 pc sample of white dwarfs from the *Gaia* catalogue (Gentile Fusillo et al., 2019) on a colour-magnitude diagram, revealing three visually-distinguishable structures within the cooling tracks: namely, the A, B, and Q branches.

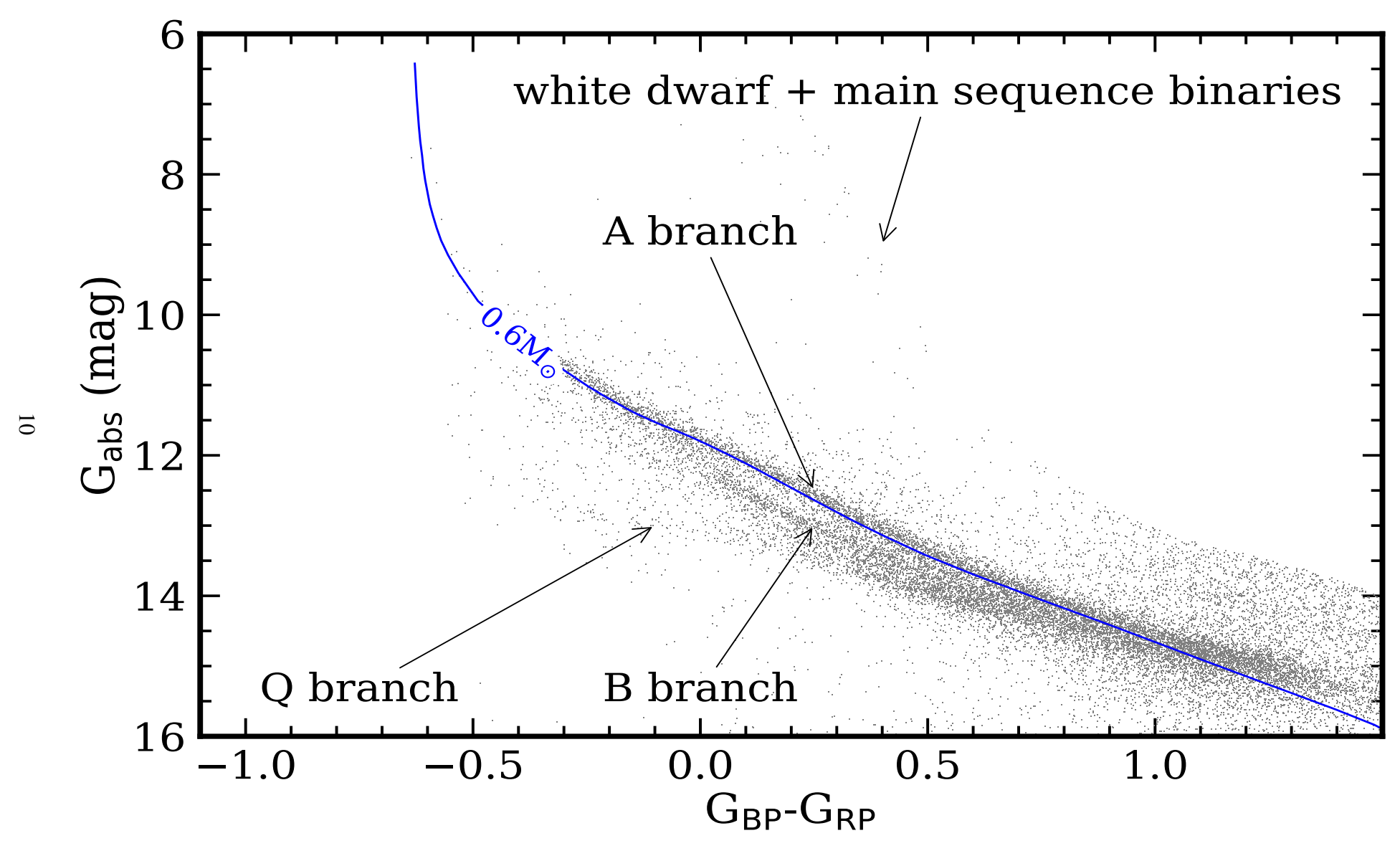


Figure 1.3: *Gaia* colour-magnitude diagram of the 100 pc sample of white dwarfs from Gentile Fusillo et al. (2019). The cooling track for the canonical $0.6 \, M_{\odot}$ pure-hydrogen atmosphere is shown (Bédard et al., 2020). The figure demonstrates the position of the three cooling branches and a region populated with white dwarf + main sequence unresolved binaries (Rebassa-Mansergas et al., 2021).

The A branch is the most comprehensively understood. It is evident from the shown theoretical cooling track that this branch represents the cooling sequence of a typical $0.6\,\mathrm{M}_{\odot}$ hydrogen-atmosphere DA white dwarf (Bergeron et al., 2019). Conversely, the B branch predominantly encompasses non-DA white dwarfs with $T_{\rm eff} < 10\,000\,{\rm K}$, including DB, DC, DZ, and DQ spectral types (Gaia Collaboration et al., 2018b). Notably, there is a minor contamination from the less numerous and more massive, DA white dwarfs with $M \approx 0.8 \,\mathrm{M}_{\odot}$. The non-consecutively titled Q branch derives its name from the high concentration of DQ white dwarfs in the region. Contrary to the prior branches, it does not exhibit a diagonal orientation on the colour-magnitude diagram, implying a distinct nature. Instead of tracking a conventional cooling path, the Q branch epitomises a cluster of white dwarfs experiencing a cooling delay within this region. Cheng et al. (2019) postulated that this delay might arise from the release of gravitational energy mediated by Ne²² settling. This hypothesis was further refined by Blouin et al. (2021), who introduced the notion of Ne²² distillation, resulting in the enrichment of Ne²² within a crystallizing core. Nonetheless, the requisite quantity of Ne²² surpasses the expected levels from isolated evolution, prompting several researchers to suggest a stellar merger as a plausible way to form the hypothesised concentrations (Shen et al., 2023).

Lastly, in Figure 1.3, the final annotated feature represents the sizeable region of unresolved binaries consisting of white dwarfs and main sequence stars. Being unresolved implies that the viewed separations between these objects are so small that they appear as a singular entity to the detector. Consequently, the measured photometry comprises contributions from both objects in the binary. Binary systems will be discussed in more detail in the following chapter.

Due to the various factors at play during the cooling process, white dwarf stars provide an invaluable platform for testing the principles of physics under conditions of high gravity and high density. Therefore, not only does the study of white dwarf cooling sequences shed light on the intricate processes within these stellar remnants, but it also offers critical insights into the fundamental workings of the universe (Raffelt, 1996; Córsico et al., 2001; García-Berro & Oswalt, 2016).

1.3 Binaries

In this section, I will conduct a brief exploration of binary systems where the primary star is either currently a white dwarf or on a trajectory to become one. This examination will emphasise the impact that such a companion exerts on the secondary star within these systems.

1.3.1 Binary evolution

During its evolution, a white dwarf progenitor, depending on its mass, could undergo up to two evolutionary phases that increase the stellar radius by a few hundred times (Schröder & Smith, 2008). Naturally, the expansion of the stellar radius might impact a nearby companion changing the nature of the binary. The Roche lobe geometry could be used to identify three types of binary stars: detached, semi-detached, and contact binaries (Kopal, 1955). Whether the outer shell of none, one, or both stars lies within their respective Roche lobes determines the type. About 30-50 per cent of binaries are sufficiently compact to

exchange mass at some point in their evolution (Duquennoy & Mayor, 1991; Kobulnicky & Fryer, 2007). For $M \ge 15 \,\mathrm{M}_{\odot}$ main-sequence stars in multiple systems, this percentage is even higher at 70 per cent (Sana et al., 2012; Kiminki & Kobulnicky, 2012; Kobulnicky et al., 2012, 2014). Below, I will briefly outline each of the three types of binary stars.

In the case of detached binaries, the Roche lobes are not filled by either of the stars. However, the stars can still influence each other via tidal interactions and stellar winds (Hurley et al., 2002). In extremely wide binaries with semi major axis exceeding 5000 au, a fast mass-loss event in comparison to the orbital timescale, such as stellar wind during the evolved stages of the stellar evolution, can dissolve the binary altogether (Toonen et al., 2017). This kind of orbital separation is characteristic of systems where the duration of the AGB phase is on a similar timescale to the orbital period (Veras et al., 2011). AGB phases are known for their extreme mass-loss via stellar wind, reaching rates up to $10^{-4} \,\mathrm{M}_{\odot} \,\mathrm{yr}^{-1}$ (Höfner & Olofsson, 2018). Binaries with orbital separation $a \geq 12$ au are expected to be non-interacting (Moe & Di Stefano, 2017).

In a semidetached binary, mass is transferred from the envelope of the Roche-lobe filling star to its companion, potentially significantly affecting the evolution of both stars (Pringle & Wade, 1985). The system could experience a phase of common envelope evolution if the mass transfer becomes unstable (Paczynski, 1976), meaning the accreting star cannot accrete all of the material. In a hypothetical close binary with an orbital period of less than ten years, a main sequence star evolving into an RGB would undergo a stage of common envelope evolution. The common envelope stage is extremely short compared to typical timescales associated with stellar evolutionary processes, lasting around 400-4000 years (Hjellming & Taam, 1991). The less massive star orbiting within the common envelope would experience a drag force from the envelope, causing it to spiral inward towards the primary star. This releases gravitational potential energy that heats the envelope. If enough energy is transferred, the envelope could be ejected, leaving behind a post-common envelope binary consisting of the core of the giant in the form of a white dwarf and the less massive secondary (Paczynski, 1976; Webbink, 2008; Ivanova et al., 2013).

A more common way for at least one star to fill its Roche lobe is via the angular momentum loss of the binary system. This can be achieved either via gravitational radiation (Faulkner, 1971) or magnetic braking (Verbunt & Zwaan, 1981). The first process is relatively well understood through general relativity and works by gravitational wave generation that carries away both energy and angular momentum. Magnetic braking relies on the magnetic coupling of stellar rotation and wind, and in general is far less well-understood.

The last type of binary stars are the contact binaries. The study of these binaries, which are hypothesized to conclude their evolution as mergers (Robertson & Eggleton, 1977), is crucial, as approximately 10-30 per cent of isolated white dwarfs are posited to be merger products (Toonen et al., 2017). Contact binaries experience Roche lobe overflow by both components, resulting in gravitational distortion to the extent that they share a common photosphere (de Marco & Izzard, 2017). In some cases, such systems could form a circumbinary disk. If such a binary eventually merges, a substantial proportion of the orbital binding energy is liberated during the process, resulting in an intense burst of radiation known as an outburst. Merger products can have complex compositions, but objects with similar compactness tend to mix completely upon coalescence (Hurley et al., 2002).

Beyond this simple division into detached, semi-detached, and contact binaries, Mohamed & Podsiadlowski (2007, 2011) have conceptualised an alternate accretion process termed as wind Roche-Lobe overflow. In this context, the donor star, which could be a mass-shedding AGB star, releases a wind with a velocity closely matching the escape velocity at the Roche surface. Even if the donor does not fill its Roche lobe, its wind could follow a natural path through the L1 inner Lagrangian point, effectively feeding the accretor. By definition, these binaries would be called detached, even though a mass transfer is taking place.

The general binary interactions have been described. However, within the scope of this work, two more specific types of systems require emphasis: binary systems with a magnetic white dwarf and those with a white dwarf + brown dwarf in a post commonenvelope configuration. In the former, there is potential for magnetic field interactions, while in the latter, the brown dwarf has interacted with the common envelope.

Starting with the magnetic white dwarfs, their fields can significantly modify the pattern of mass transfer between the stars, particularly in cases where the accretion occurs onto an evolved star like a white dwarf or a neutron star. A prototypical illustration of this phenomenon is exhibited by polars or AM Her systems (Cropper, 1990). In these short orbital period systems, a highly magnetic white dwarf (> 10 MG; Schmidt et al. 1996; Duffy et al. 2022) is in the process of accreting mass from a main-sequence companion. In lower field magnetic cataclysmic variables, the magnetic field channels the accretion stream from the inner portions of the disc directly onto the poles of the white dwarf (Wu, 2000; Hellier, 2001), or in some extreme cases of polars, directly onto the white dwarf without forming an accretion disk (Cropper, 1990; Ferrario et al., 2015b). In polars, the interaction between the magnetic field of the white dwarf and the secondary star leads to a state where both stars rotate in synchronization (Cropper, 1990).

Next is the topic of binary systems with substellar secondaries, specifically brown dwarfs. Brown dwarfs are defined as substellar objects with masses below $75\,\mathrm{M_{Jup}}$. Under the assumption of solar metallicity, they are unable to stably fuse the abundant H^1 isotope (Burrows et al., 1997). Brown dwarfs are hard to detect due to their low intrinsic brightness, which is easily overshadowed by the white dwarf in the optical (Kirkpatrick et al., 1993). Because of this, the first detection of a post common envelope binary with a brown dwarf in a close orbit was relatively recent (Maxted et al., 2006). Post common envelope binaries with a substellar component provide important insights into the common envelope evolution, in particular the expected survivability for the less massive companion.

White dwarf progenitors are known to host substellar and exoplanetary objects. After the giant branch phase, if these objects survive or are brought into a closer orbit, they could be influenced by the white dwarf's tidal forces (Veras & Fuller, 2019; Veras et al., 2019). This can result in observable debris disks (Gänsicke et al., 2006; Kilic & Redfield, 2007; Farihi, 2016; Wilson et al., 2019) or gas disks (Melis et al., 2012; Manser et al., 2016, 2020; Melis et al., 2020). Consequently, rocky bodies accreted onto a white dwarf might produce atmospheric pollution or other observable signals (Vanderburg et al., 2015; Gänsicke et al., 2019; Manser et al., 2019; Vanderbosch et al., 2020). In fact, approximately 25 to 50 per cent of white dwarfs exhibit signs of pollution (Zuckerman et al., 2003; Barstow et al., 2014; Koester et al., 2014; Wilson et al., 2019). Specifically, the spectroscopic class of metal-polluted white dwarfs can best be explained by interactions with asteroids, suggesting that 20 to 30 per cent of white dwarfs have preserved parts of their exoplanetary systems (de Marco & Izzard, 2017).

This is particularly significant in light of the recent discovery of the first transiting planet around a white dwarf in a close orbit (Vanderburg et al., 2020). The object was estimated to be less massive than $11.7 \, M_{\rm Jup}$ in a $1.4 \, {\rm d}$ orbit. Although it seems improbable that the planet could have survived in its current orbit (Villaver & Livio, 2007; Mustill & Villaver, 2012; Villaver et al., 2014), theories have been proposed suggesting potential survival through the common envelope stage (Lagos et al., 2021a; Chamandy et al., 2021; Merlov et al., 2021). Given the presence of such a relatively small object in a close orbit, but the apparent absence of less massive brown dwarfs around white dwarfs, as well as challenges associated with modeling the common envelope and estimating the process efficiency, it remains unclear which objects can survive the process and at what separation they can do so. This question can be approached observationally.

1.3.2 Period-mass distribution

As mentioned in the previous section, the orbital period of a binary system can evolve with time due to mass loss or mass transfer, as well as via gravitational waves or interactions with the external environment, while tidal interactions tend to synchronize the orbit (Hut & Tremaine, 1985; Weinberg et al., 1987; Farmer & Phinney, 2003; Jiang & Tremaine, 2010). A substantial fraction of contact binaries have a third, hierarchical component that can influence the binary evolution (Duquennoy & Mayor, 1991; D'Angelo et al., 2006; Pribulla & Rucinski, 2006). Interactions with a third body via Kozai cycles with tidal friction can affect the orbital period of the system (Fabrycky & Tremaine, 2007), as is evident from different period distributions between isolated binaries and inner binaries in triple systems (Tokovinin et al., 2006).

The initial mass function is dominated by low-mass main-sequence stars. This is also the case for the mass function for companions to white dwarfs and to their progenitors (Farihi et al., 2005b; de Rosa et al., 2014). Looking at this through the lens of formation and evolution, one can infer that there will likely be a significant number of white dwarfs that have M dwarf companions, a supposition confirmed by observations (Rebassa-Mansergas et al., 2007; Hollands et al., 2018).

A number of distributions of binary orbital parameters for white dwarfs are available in the literature (e.g., Zorotovic et al. 2010; Nebot Gómez-Morán et al. 2011; Zorotovic et al. 2011; Rebassa-Mansergas et al. 2012; Parsons et al. 2013). These studies provide a clear picture of how white dwarf binary evolution would progress. Both theoretical understanding and empirical data indicate that about two-thirds will end up in wide binaries. In these, the original semimajor axis has increased following post-main sequence mass loss. Conversely, roughly one-third will occupy short orbital periods, an outcome of the common envelope phase that shrinks the orbital separation. Indeed, a bimodal distribution of orbital periods is observed, consisting of short period post common envelope binaries and non-interacting wide binaries (Farihi et al., 2005b, 2010a; Nebot Gómez-Morán et al., 2011; Ablimit et al., 2016; Ashley et al., 2019). For white dwarf-main sequence systems that underwent a common envelope stage, a period distribution covers 2 h to 4 d periods with a mean value of 8 h (Nebot Gómez-Morán et al., 2011). However, the number of such systems with an orbital period exceeding 2.5 d is believed to be quite small (Lagos et al., 2022). At orbital periods above 100 d, white dwarf-main sequence binaries could have undergone a stable non-conservative mass transfer (Lagos et al., 2022). The white dwarf's mass, the companion's mass, and the orbital period observed distributions

have been studied and compared to simulations by Toonen & Nelemans (2013). In a double degenerate case, the expected behaviour has been studied by Korol et al. (2022). These systems have a potential to undergo two episodes of common envelope evolution, forming a gap in the separation distribution at around 1 au.

A notable pattern is that post common envelope binary systems tend to have higher white dwarf masses compared to their isolated counterparts (Liebert et al., 2005b; Holberg et al., 2008; Zorotovic et al., 2011; Rebassa-Mansergas et al., 2012; Andrews et al., 2014). However, the majority of white dwarfs with $M < 0.5 \,\mathrm{M}_\odot$ originate in close binaries (Rebassa-Mansergas et al., 2011). Systems where a companion within a common envelope facilitates a more rapid unbinding of the envelope are anticipated to produce lower mass white dwarfs compared to the isolated RGB or AGB evolutionary pathways (Marsh et al., 1995; Nelemans & Tauris, 1998; Maxted et al., 2006). Moreover, the process of common envelope ejection can significantly alter the binary system's characteristics, including reduced orbital separation or even a merger (Marsh et al., 1995; Korol et al., 2022).

Another important question in this work's context is the efficiency of the common envelope, i.e. how effective the orbital energy transfer is to the envelope. Although the common envelope evolution phase is brief, it plays a crucial role in binary evolution. However, it remains challenging to model comprehensively due to the vast range in time and length scales involved (Taam & Sandquist, 2000; Taam & Ricker, 2010; Ivanova et al., 2013). A prevalent approach employs the energy formalism described as $E_{\rm bin} = \alpha_{\rm CE} \Delta E_{\rm orb}$, developed by Webbink (1984). In this equation, $E_{\rm bin}$ represents the envelope's binding energy, $\Delta E_{\rm orb}$ denotes the change in orbital energy due to the common envelope, and $\alpha_{\rm CE}$ is the efficiency parameter. This parameter indicates how effectively certain energy sources can unbind the envelope. The formalism can be expanded to include recombination energy (Iben & Livio, 1993; Han et al., 1995; Webbink, 2008) and the influence of angular momentum (Nelemans et al., 2000; van der Sluys et al., 2006).

Related to the post common envelope systems, a useful thing to note is the absence of low mass substellar companions to white dwarfs at short orbital distances. However, due to the small number of known white dwarf-brown dwarf systems and a low predicted occurrence rate for a white dwarf to host a brown dwarf of 0.1-0.5 per cent, the pattern is uncertain (Farihi et al., 2005b; Steele et al., 2011; Rebassa-Mansergas et al., 2019)². The critical mass that is needed for a companion to survive the common envelope is also uncertain but is usually quoted to be above $0.02\,M_\odot$ (> $20\,M_{Jup}$; Livio & Soker 1983; Nelemans & Tauris 1998; Siess & Livio 1999). Similarly, Nordhaus et al. (2010) considered a $1\,M_{Jup}$ companion but concluded that no such companion can survive in a $0.1-380\,d$ orbit around a $1\,M_\odot$ primary. A distribution of known substellar post common envelope binary systems is shown in Figure 1.4.

²For sun-like stars, the fraction of brown dwarf companions is also quite small at ≈ 1 per cent (Nielsen et al., 2019; Feng et al., 2022). This percentage drops even lower at $0 \le P \le 100 \,\mathrm{d}$ and $35 \le M \le 55 \,\mathrm{M_{Jup}}$, thus forming the so-called 'brown dwarf' desert and potentially implying a distinct formation mechanism (Ma & Ge, 2014; Wilson et al., 2016; Stevenson et al., 2023).

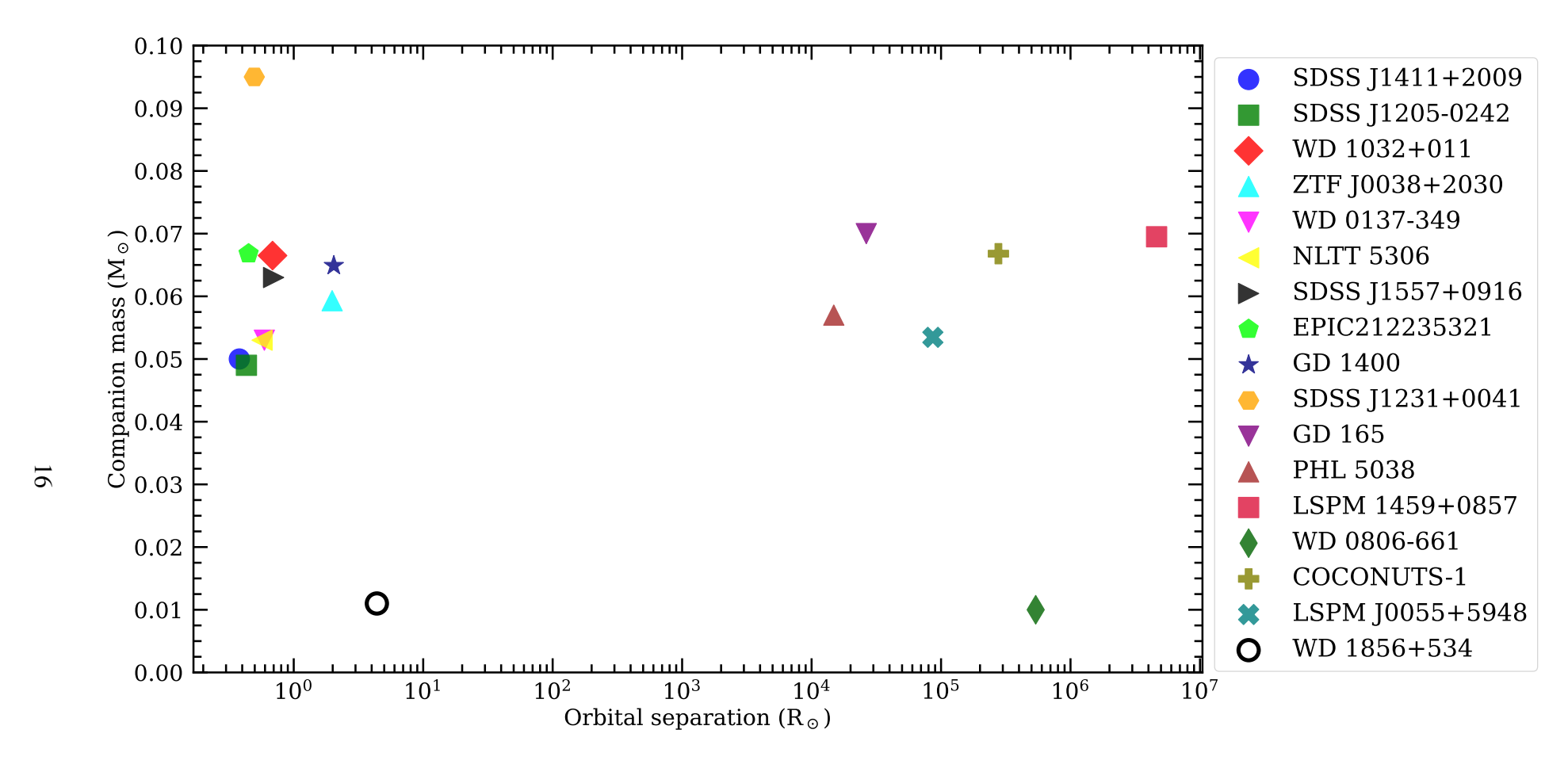


Figure 1.4: Orbital separation and mass of substellar objects with a white dwarf primary. Post common envelope white dwarf + brown dwarf binaries form a cluster on the left. The black circle is the only known white dwarf with a transiting planetary companion. The figure demonstrates an apparent lack of less massive companions at short orbital separations. *References:* Kirkpatrick et al. (1999b); Burleigh et al. (2006a); Maxted et al. (2006); Steele et al. (2009); Day-Jones et al. (2011); Rodriguez et al. (2011); Beuermann et al. (2013); Steele et al. (2013); Littlefair et al. (2014); Farihi et al. (2017); Longstaff et al. (2017); Parsons et al. (2017b); Casewell et al. (2018a, 2020a); Meisner et al. (2020); Zhang et al. (2020); van Roestel et al. (2021); Walters et al. (2022).

In contrast to post common envelope binaries, widely separated systems are unlikely to have been affected by the evolution of the white dwarf progenitor and its evolution is expected to have not been truncated during the common envelope phase (Meisner et al., 2020). Important work has been done on understanding the parameter distributions of widely separated substellar and low-luminosity companions. For example, the distribution of resolved white dwarf-brown dwarf systems shows a non-uniform distribution of companion masses with a pronounced lack of companions lighter than 45 M_{Jup} even at wide separations (French et al., 2023). Naturally, an observational bias is playing a role, but underlying binary physical processes must also contribute. For less massive companions, such as a planetary-sized counterpart, an initial orbital separation from the main sequence progenitor exceeding 5 au is considered enough for the white dwarf to retain the companion (Burleigh et al., 2002). The distribution of stellar but low-luminosity companions to white dwarfs at separations exceeding a few au have been studied in (Farihi et al., 2005b, 2006, 2010a).

1.3.3 Observing binary systems

In the realm of astrophysics, a diverse array of methodologies exists to facilitate the observation and characterization of binary systems. Predominantly, researchers employ techniques such as radial velocity measurements, the analysis of eclipsing systems, and astrometric methods. While less prevalent, other techniques encompass observations of X-ray emission, direct imaging, gravitational lensing, and pulsar timing. In the context of this research, I will outline several important methodologies.

Starting with the radial velocity technique, it necessitates spectroscopic observations of a binary system over an extended period (close to or longer than its orbital period). This method hinges on the precise fitting of observed spectroscopic lines and the subsequent measurement of any alterations in line velocity attributable to the Doppler effect over time. In instances of a double-lined binary, as shown in Figure 1.5, spectral lines from both bodies can be concurrently fitted. This concurrent fitting offers a more comprehensive understanding of the binary system. It is noteworthy that, due to observational biases, such systems are typically characterised by equal brightness and mass. However, even when spectral lines from merely one star in the binary are discernible and can be fitted, it still provides valuable insights into the configuration of the system.

Radial velocity measurements, while observationally demanding, necessitate multiple high-resolution spectra. In specific scenarios, radial velocity analyses can be augmented by photometric observations. It is imperative to note that photometric variability can arise from factors other than the presence of a companion. However, on occasion, the photometric period might correspond to the orbital period of the binary system. Given that time-series photometric data is more obtainable than time-resolved spectroscopy, the integration of the photometric period could refine the radial velocity solution, potentially reducing the requisite amount of spectroscopic data. Furthermore, this data could inform the strategy for spectra acquisition, contingent upon the premise that the photometric variability is attributed to a companion's presence. Several factors could account for such variability. Within the purview of this study, ellipsoidal variability resulting from gravitational distortion and the reflection effect due to an irradiated companion are especially important.

Subsequently, another method to discern and characterise the components of an unre-

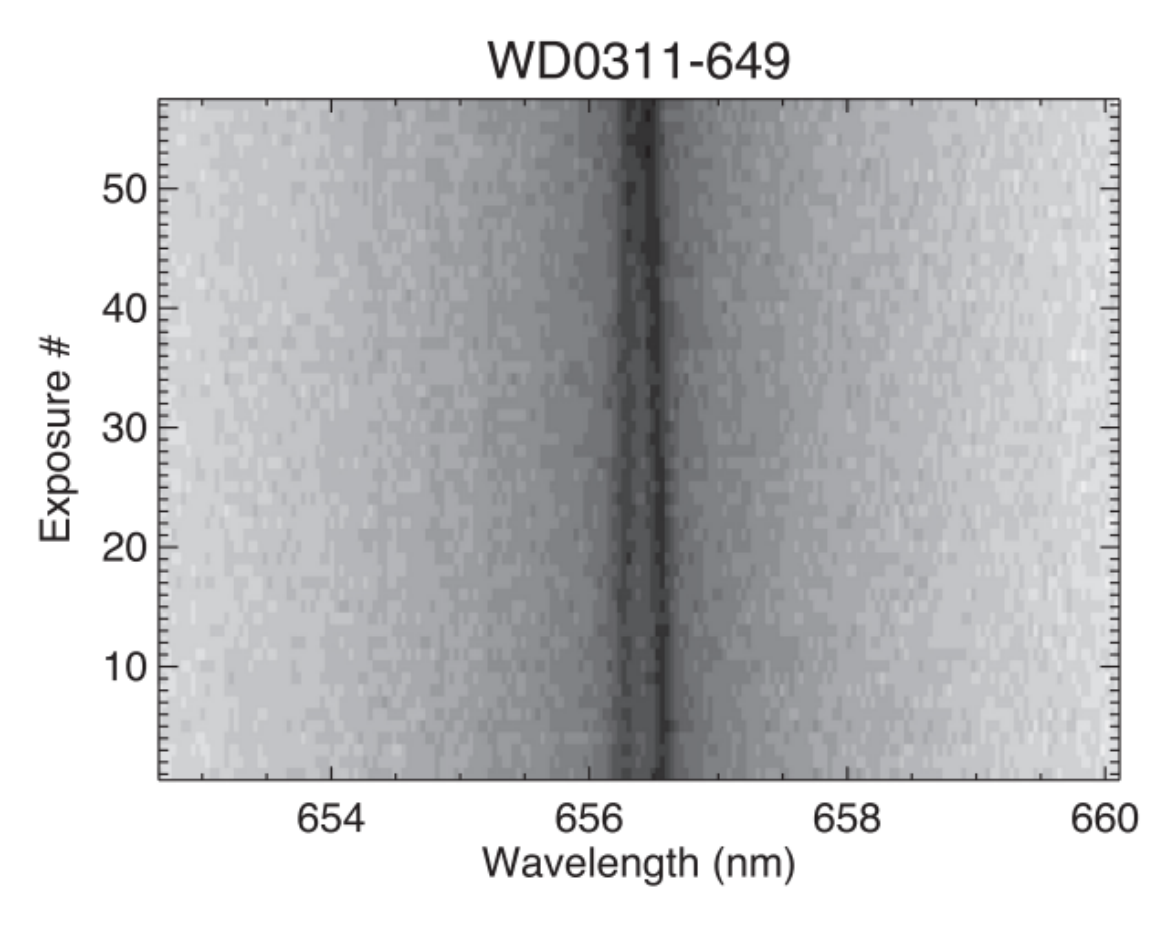


Figure 1.5: A trailed spectrum of a double-lined binary system, comprising two white dwarfs from Kilic et al. (2020). The figure emphasises two H α cores, each exhibiting subtle wavelength variations. By fitting these cores, one can determine precise wavelengths over time, which can subsequently be transformed into radial velocities. These radial velocities can then be modeled to construct a comprehensive radial velocity solution, facilitating the characterisation of the physical properties of the system.

solved binary involves fitting the system's composite spectral energy distribution. Diagram of these composite fits are presented in Figure 1.6. This methodology demands synthetic models, photometric observations, and an astrometric solution. It is crucial to emphasise that this approach is not confined to white dwarf and main sequence binaries. It exhibits efficacy across multiple types of systems, including double degenerates, systems with a substellar companion, and white dwarfs accompanied by dusty disks (e.g., Hernández Santisteban et al. 2016; Farihi et al. 2017; Parsons et al. 2020). The fitting of the spectral energy distribution emerges as a formidable technique, especially considering the comparative simplicity in procuring multi-band photometry relative to broadband spectra, coupled with the availability of published theoretical spectra.

This concludes the section on binary stars. There is just one more concept that needs to be introduced that plays an important role in both binary systems and isolated white dwarfs: magnetism.

1.4 Magnetism

The role of magnetism in white dwarfs is significant due to a large fraction of magnetic stars. Studies focusing on a volume-limited population reveal that around 20 per cent of white dwarfs are magnetic (Kawka et al., 2007; Giammichele et al., 2012; Landstreet & Bagnulo, 2019; Bagnulo & Landstreet, 2020), with detectable magnetic field ranging from 1 kG to 1000 MG. A great historical overview on the discovery of magnetism in white dwarfs is given in Landstreet (2020). That said, the essence of the history begins in 1908, when Hale made a revolutionary discovery of magnetism in sunspots by examining the Zeeman splitting of Fraunhofer lines (Hale, 1908). This marked the beginning of the concept of magnetic fields in the atmospheres of stars. Nearly four decades later, in 1947, Horace Babcock achieved the first detection of magnetism in an Ap star, which was also the first discovery of magnetism beyond our solar system (Babcock, 1947). In the same year, Blackett theorized that certain white dwarfs might have powerful magnetic fields (Blackett, 1947), although the first empirical validation of this idea would not materialise until more than twenty years later by Kemp and his colleagues (Kemp et al., 1970).

In contrast to main sequence stars, the convection zones of white dwarfs are relatively shallow and do not achieve the densities required to create observable magnetic dynamo effects (Fontaine et al., 1973). Moreover, convection becomes fully inhibited at field strengths above 50 kG (Tremblay et al., 2015b). Therefore, unlike the magnetic field in the Sun, the existence of fields in white dwarfs cannot be explained by a dynamo process driven by an outer convection zone. Different mechanisms have been proposed to account for magnetic field formation in white dwarfs, and it is possible that multiple mechanisms may be responsible for the field formation (Bagnulo & Landstreet, 2022). The origin of magnetism in white dwarfs remains debated and is an active area of research (Ferrario et al., 2015b,a, 2020b).

The underlying field strength distribution of magnetic white dwarfs is thought to be relatively uniform, the field geometry frequently dipole-like, and the fields do not appear to evolve on timescales observable by human standards (Wendell et al., 1987; Bagnulo & Landstreet, 2021). However, because the majority of known magnetic white dwarfs were discovered spectroscopically through several large medium or low resolution surveys,

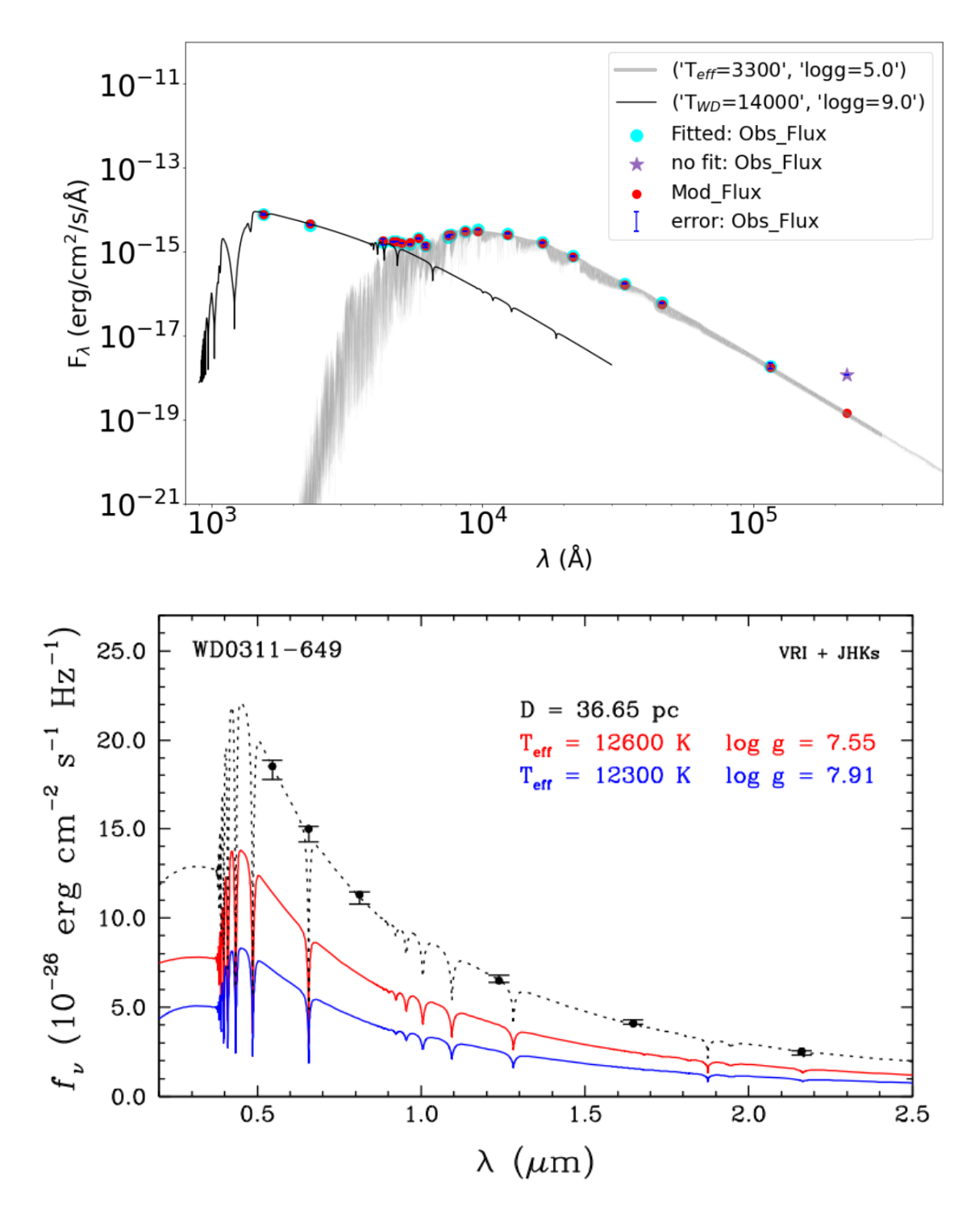


Figure 1.6: Two examples of composite spectral energy distributions. *Upper panel:* An example of a white dwarf (black) and main sequence (grey) fit, reproduced from Nayak et al. (2022). The cyan points represent the observed photometric flux, while the red points indicate the theoretical flux derived from a combination of the white dwarf and main sequence models. The synthetic models are calibrated via astrometry. *Lower panel:* Two white dwarfs at similar temperatures from Kilic et al. (2020) and the resulting spectral energy distribution.

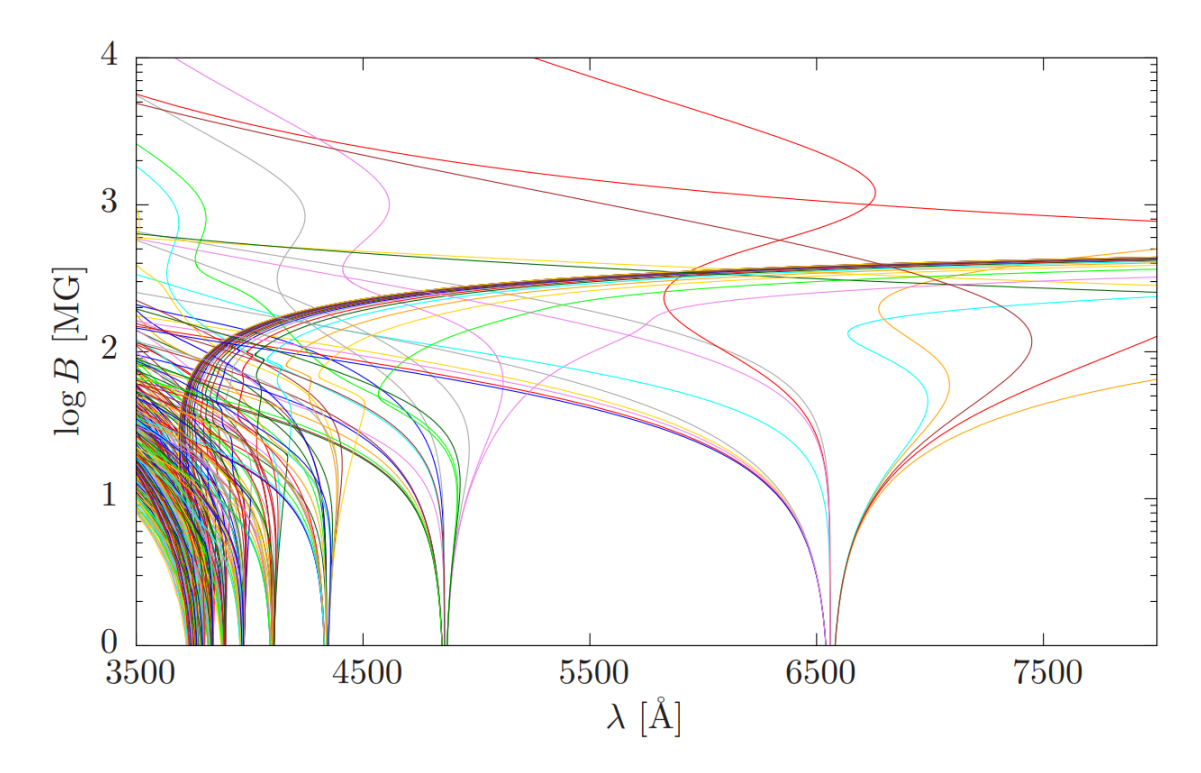


Figure 1.7: Magnetic field strength as a function of the wavelength for the first 325 transitions in the Balmer series is reproduced from Schimeczek & Wunner (2014). At magnetic field strengths greater than 100 MG, the transitions start to overlap significantly. This makes it challenging to obtain an accurate magnetic field estimate or even to identify the magnetic DA white dwarf as such. For magnetic field strengths less than 1 MG, the Zeeman splitting is relatively small, thus necessitating high-resolution spectroscopy and high S/N ratios.

such as SDSS (Kepler et al., 2021)³, there is a notable skew towards field strengths of 1 to 100 MG (Bagnulo & Landstreet, 2022). Fields below 1 MG require high-resolution spectroscopy or spectropolarimetry to detect Zeeman splitting or circular polarization of the continuum (Landstreet, 1992). Magnetic fields exceeding 100 MG result in position and components of lines altered to such an extent that it becomes difficult to recognise and classify the spectrum as belonging to a magnetic white dwarf and assign a reliable field strength (Wunner et al., 1985). This phenomenon of rapid divergence at B > 100 MG and overlap at B < 1 MG can be seen in Figure 1.7. An additional pile-up of known low field magnetic white dwarfs (1 < B < 10 MG) can be explained, at least to some extent, by magnitude limitations of such surveys, resulting in a disproportionately high number of younger white dwarfs (Bagnulo & Landstreet, 2022). Because magnetic fields are detected with a higher sensitivity in younger white dwarfs that tend to have lower field strengths, there is a resultant overrepresentation of lower fields (e.g. Figure 1.8).

Returning to the question of field formation, I begin by listing some of the theories before exploring them in-depth. In general, magnetic field formation mechanisms can be separated into two groups: formation in isolation or via binary interaction. Isolated theories include the fossil field theories (Woltjer, 1964; Landstreet, 1967; Angel et al., 1981; Tout et al., 2004; Kissin & Thompson, 2015; Stello et al., 2016) and crystallization (Isern et al., 2017; Ginzburg et al., 2022). Binary theories include: post common envelope dynamo (Tout et al., 2008; Briggs et al., 2018; Schreiber et al., 2021a) and merger dynamo (García-Berro et al., 2012) theories.

Starting with the fossil field theory, one of the earliest hypotheses suggested that magnetic Ap and Bp stars could be the precursors of magnetic white dwarfs (Woltjer, 1964; Landstreet, 1967; Angel et al., 1981). Due to magnetic flux conservation, weakly magnetic Ap and Bp stars could produce fields of observed intensities as they evolve and collapse to a much smaller radius (Tout et al., 2004). However, the expected birth rate of these stars is too low by a factor of 2-3 to explain all of the magnetic white dwarfs (Kawka & Vennes, 2004; Wickramasinghe & Ferrario, 2005; Külebi et al., 2009). Additionally, a fossil field would have to survive the turbulence associated with the RGB and AGB phases of stellar evolution, although field lines may be trapped and retained in non-convective core regions.

More recently, Stello et al. (2016) studied a sample of 3600 red giant stars using asteroseismology and concluded that a significant fraction could harbour strong magnetic fields in the core, undetectable at the star's surface. If the fossil field hypothesis is correct, volume-limited observations by Bagnulo & Landstreet (2022) suggest that the fields evolve and become stronger during the first 2 – 3 Gyr due to gradual relaxation (Fontaine et al., 1973; Braithwaite & Spruit, 2004). A recent study found three magnetic white dwarfs identified as members of open clusters, and firmly linked to single, intermediate-mass star evolution (Caiazzo et al., 2020). This result supports the idea of fossil field origin in at least some cases.

The idea of crystallization-driven dynamo was proposed by Isern et al. (2017) and can be used to account for magnetism not only in white dwarfs but in a number of other

³SDSS resolution is about 1800, resulting in $\Delta \lambda = 4 \,\text{Å}$ at Balmer H α (Stoughton et al., 2002). The Zeeman splitting at $B = 1 \,\text{MG}$ is 40 Å and 20 Å at $B = 0.5 \,\text{MG}$ (Schimeczek & Wunner, 2014). Under optimal conditions such splittings can be identified, but at low S/N< 10 a poorly-separated Zeeman triplet can be hard to resolve (Amorim et al., 2023). Fields below approximately $B \sim 0.25 \,\text{MG}$ cannot be identified with such resolution.

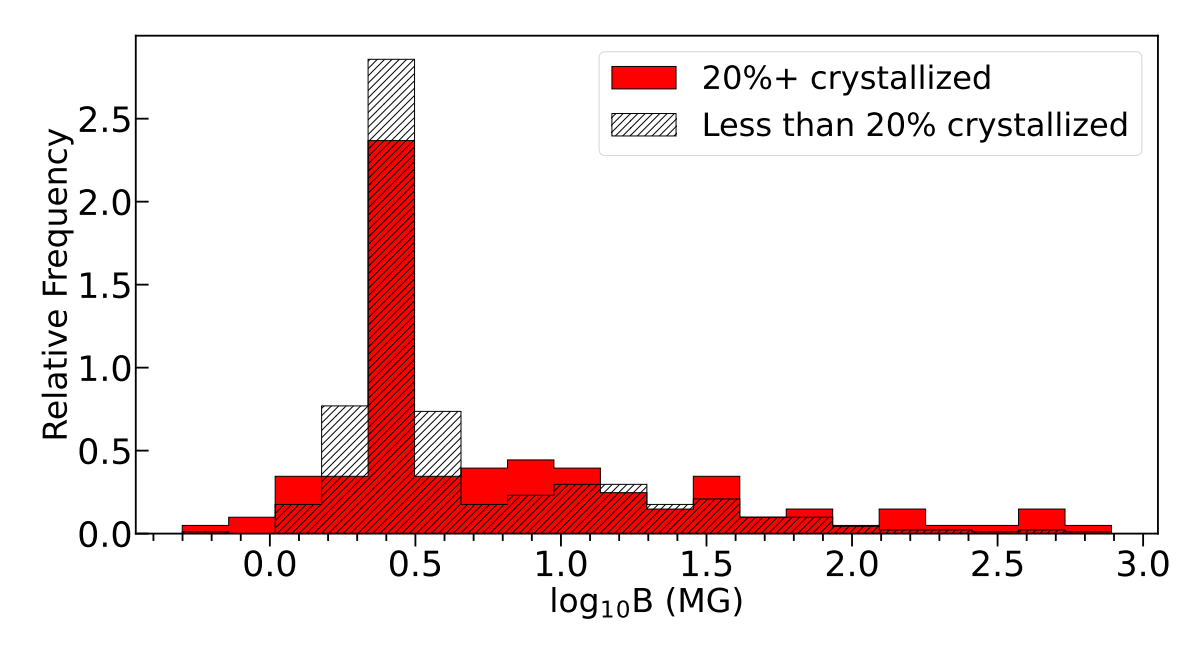


Figure 1.8: Histograms showing distributions of magnetic field strengths for two populations of white dwarfs. The shaded histogram represents white dwarfs that are less than 20 per cent crystallized, while the red histogram shows the distribution for white dwarfs that have completed at least 20 per cent of their crystallization process. The DAH sample is from Amorim et al. (2023) based on SDSS observations. The crystallization tracks used to divide the population are from Tremblay et al. (2019). There is a slight overabundance of stronger fields in more crystallized sample although the sample is heavily biased (see text).

stellar and substellar objects, all the way down to Earth-sized planets. This theory requires a rotating white dwarf that forms a dynamo in the core excited by convection. In turn, the convection is produced by sinking solids when crystallization begins (Isern et al., 2017; Ginzburg et al., 2022). Originally, Isern et al. (2017) proposed this mechanism as a formation pathway for fields of order 1 MG. However, Schreiber et al. (2021a) suggested that the energy flux scaling law used to estimate the maximum possible field strength via crystallization potentially underestimates the field strengths of slowly rotating single white dwarfs. Moreover, Ginzburg et al. (2022) advocated that the resulting convection is slower than originally estimated, requiring slower rotation rates to produce equivalent field strengths. Due to these modifications, a magnetic field of the order of 100 MG can be produced, implying that this mechanism can play a role in field generation after 2-3 Gyr in about 20 per cent of white dwarfs of typical mass (i.e. likely a non-merger product Bagnulo & Landstreet 2022). This mechanism is further backed up by observations that white dwarfs with a cooling age below 0.5 Gyr tend to have a lower prevalence of magnetic fields and smaller field strengths (Bagnulo & Landstreet, 2021, 2022). Although the SDSS sample is biased for the reasons outlined above, a histogram of less than 20 per cent crystallized and more than 20 per cent crystallized white dwarfs shown in Figure 1.8 supports this idea and shows that crystallized white dwarfs tend to have higher fields that non-crystallized counterparts.

As mentioned earlier, another field formation theory in white dwarfs involves close binary evolution. In this context, a dynamo can be excited during specific stages of the binary lifecycle. The most massive magnetic white dwarfs are often hypothesized to be the result of a merger between two white dwarfs initially formed through the evolution of a close binary system (Ferrario et al., 1997b; Dobbie et al., 2012). This merger has the potential to lead to the creation of an immensely strong magnetic field that would be almost immediately present at the white dwarf's surface (García-Berro et al., 2012). In this case, a dynamo would be driven by differential rotation (Briggs et al., 2018). An essential characteristic that further substantiates this theory is the rapid rotation found in several massive magnetic white dwarfs (Schmidt & Norsworthy, 1991; Barstow et al., 1995; Pshirkov et al., 2020). Moreover, studies have highlighted a difference in the average mass between magnetic and non-magnetic white dwarfs, where magnetic stars are often found to be more massive (Liebert, 1988; Kepler et al., 2013; McCleery et al., 2020).

Tout et al. (2008) originally proposed that high magnetic fields were generated by a dynamo between the common envelope and the white dwarf outer layers before the envelope's ejection in a common envelope system. If the cores merge, the resulting giant star eventually reveals a single high-field magnetic white dwarf. Conversely, if the cores are close but not merged when the envelope is ejected, a magnetic cataclysmic variable is formed. Potter & Tout (2010) identified issues with this scenario, noting that the timescale for diffusion of the field into the WD was longer than the expected common envelope lifetime. An alternative explanation by Wickramasinghe et al. (2014a) suggested that a weak seed field could be intensified through a dynamo created by differential rotation in the merged object. Another model by Nordhaus et al. (2011) proposed that magnetic fields could be generated in an accretion disc from a tidally disrupted low-mass companion and then advected onto the proto-white dwarf's surface. García-Berro et al. (2012) went further, suggesting that a field can be created from a massive, hot, and differentially rotating corona forming around a merged double degenerate.

In conclusion, this discussion has encompassed multiple theories behind magnetic field formation in white dwarfs. While volume-complete surveys are invaluable in discerning the mechanisms at play (Bagnulo & Landstreet, 2021, 2022), the question of magnetic field formation remains open. Magnetism, especially at the extremes observed in white dwarfs, can influence physical properties such as luminosity, cooling rate, internal structure, and evolutionary trajectory (Chamel et al., 2013; Das & Mukhopadhyay, 2013; Bera & Bhattacharya, 2014; Franzon & Schramm, 2017; Ferrario et al., 2020b). It also plays a pivotal role in binary interactions (Ferrario & Wickramasinghe, 1999; Ferrario et al., 2020b), potential planetary systems or asteroids (Li et al., 1998; Willes & Wu, 2004, 2005; Bromley & Kenyon, 2019; Veras et al., 2019), and disc material dynamics (Farihi et al., 2018a; Hogg et al., 2021). Given the significant proportion of magnetic white dwarfs, understanding these objects is essential.

Chapter 2

A test of the planet-star unipolar inductor for magnetic white dwarfs

This chapter is based on the paper of the same title (Walters et al., 2021). Spectropolarimetric observations, measurements and analysis were undertaken by my collaborators, and are described in sections 2.3.2, 2.4.4, and 2.5.2. All other work is my own.

2.1 Abstract

At the time of writing, despite thousands of spectroscopic detections, only four isolated white dwarfs exhibited Balmer emission lines. The temperature inversion mechanism is a puzzle over 30 years old that has defied conventional explanations. One hypothesis is a unipolar inductor that achieves surface heating via ohmic dissipation of a current loop between a conducting planet and a magnetic white dwarf. To investigate this model, new time-resolved spectroscopy, spectropolarimetry, and photometry of the prototype GD 356 are studied. The emission features vary in strength on the rotational period, but in antiphase with the light curve, consistent with a cool surface spot beneath an optically thin chromosphere. Possible changes in the line profiles are observed at the same photometric phase, potentially suggesting modest evolution of the emission region, while the magnetic field varies by 10 per cent over a full rotation. These comprehensive data reveal neither changes to the photometric period, nor additional signals such as might be expected from an orbiting body. A closer examination of the unipolar inductor model finds points of potential failure: the observed rapid stellar rotation will inhibit current carriers due to the centrifugal force, there may be no supply of magnetospheric ions, and no antiphase flux changes are expected from ohmic surface heating. Together with the highly similar properties of the four cool, emission-line white dwarfs, these facts indicate that the chromospheric emission is intrinsic. A tantalizing possibility is that intrinsic chromospheres may manifest in (magnetic) white dwarfs, and in distinct parts of the HRD based on structure and composition.

2.2 Introduction

In recent years, there has been a rapid rate of white dwarf discovery, ensuing from the advent of modern large-scale surveys. Currently, over 800 white dwarfs have been identified as magnetic from SDSS spectra alone (Kepler et al., 2015, 2016, 2019, 2021; Amorim et al., 2023), with field strengths ranging from as high as 1000 MG and down to a few kG, below which successful detection of magnetism via spectropolarimetry is challenging (Landstreet et al., 2012). From studies of the nearly complete 20 pc census it is estimated that 20 per cent of white dwarfs are magnetic above a few kG (Landstreet & Bagnulo, 2019; Bagnulo & Landstreet, 2019, 2020, 2021). Three-quarters of the known magnetic white dwarfs are thought to be isolated, or are members of non-interacting binary systems (Ferrario et al., 2020a). Research on magnetic white dwarfs that exhibit atypical properties remains crucial for the insight into the magnetic fields of this population. The origin and evolution of magnetism in white dwarfs is an outstanding astrophysical problem, and thus detailed studies of individual systems may shed light on their exact nature.

Two theories have been developed to account for the presence of magnetic fields in isolated degenerate stars: a fossil magnetic field (Tout et al., 2004; Wickramasinghe & Ferrario, 2005) and convective dynamo field driven either by a binary merger (Tout et al., 2008; Potter & Tout, 2010; Wickramasinghe et al., 2014a) or a core crystallisation (Isern et al., 2017; Ginzburg et al., 2022). An interplay of the two could also be a possible explanation (Featherstone et al., 2009; Schreiber et al., 2021a, 2022). More importantly, a recent volume-limited analysis of magnetic white dwarfs by Bagnulo & Landstreet (2022) showed that a single mechanism cannot be responsible for all instances of magnetism in white dwarfs. These theories have been discussed in Section 1.4.

The presence of a strong magnetic field can have a direct effect on the appearance of the stellar photosphere due to surface inhomogeneities, frequently manifested as photometrically inferred spots (Brinkworth et al., 2005; Holberg & Howell, 2011; Hermes et al., 2017b; Reding et al., 2018), as well as effects on accretion in binary systems (Ablimit & Maeda, 2019), and convective mixing (Tremblay et al., 2015b). Field-inhibited atmospheric convection can trigger the formation of dark spots (Valyavin et al., 2014), while a lower mixing rate between the outer layers and a convective envelope may result in a non-uniform chemical surface composition (Ferrario et al., 2020a). A combination of stellar rotation and variation in surface composition can produce continuum flux and polarimetric modulation via magnetic dichroism (Achilleos et al., 1992), thus resulting in photometric variability. Moreover, spectroscopic changes in the Zeeman-split components may appear due to variations in the surface field strength through a rotation cycle (Kilic et al., 2019).

GD 356 (=WD 1639+537) is an isolated and cool magnetic white dwarf (Greenstein & McCarthy, 1985) with fundamental parameters summarised in Table 2.1. Its highly unusual optical spectrum lacks absorption lines, but exhibits broad H α and H β emission features in Zeeman-split triplets, translating into a rare – and until only recently unique – DAHe spectral type (D: degenerate, A: Balmer lines strongest, H: magnetic line splitting, e: emission). However, the spectral energy distribution is best fitted by a helium atmosphere model, and interpreted as such (Bergeron et al., 2001). Analysis of the emission line profiles of GD 356 suggests a magnetic field described by a centred magnetic dipole with a polar field of 13 ± 2 MG (Ferrario et al., 1997a). This archetypal white dwarf exhibits brightness variations with amplitude ±0.2 per cent (V-band), and period 1.9272±0.00002 h that is interpreted as the white dwarf spin, where light curve modelling yields a polar (or

inclined equatorial) starspot which covers 10 per cent of the surface (Brinkworth et al., 2004). A similarly-sized spot is inferred as the source of emission lines in a temperature-inverted region based on spectropolarimetry and detailed modelling (Ferrario et al., 1997a).

The exact physical nature of such a spot and its origin remain unclear, despite extensive and multi-wavelength efforts to detect a companion, a corona or accretion (Ferrario et al., 1997a; Weisskopf et al., 2007; Wickramasinghe et al., 2010). At the time of writing this publication, at least two, and possibly three further examples of DAHe stars have been reported in 2020 (Reding et al., 2020; Gänsicke et al., 2020; Tremblay et al., 2020); all are isolated (i.e. not cataclysmic variables, no circumstellar disks), relatively fast rotators, and have cool atmospheres where $T_{\rm eff} < 10\,000\,{\rm K}$. More recent publications have extended the number of candidates to over 40 (Manser et al., 2023). Thus GD 356 became the prototype of a small class of DAHe stars, but the new discoveries only deepen the mystery. The only published and still viable theory for the nature of GD 356 prior to this publication is the unipolar inductor. In this model a conducting planet, orbiting within the magnetosphere, sets up a current loop that dissipates in the stellar atmosphere via ohmic dissipation and thus heating the outer layers into emission (Li et al., 1998).

Motivated by the unipolar inductor model, this work aimed to detect additional periodic signals from the influence of such a closely orbiting planet. This chapter presents rotation phase-resolved spectroscopy and spectropolarimetry of GD 356, which is then compared with the latest NASA *TESS* data release available at the time, and ground-based, time-series imaging to investigate the spectroscopic and photometric variability. The observations are described in Section 2.3, and in Section 2.4 the analytic approaches and results are outlined. The implications of the results are then discussed in Section 2.5, followed by conclusions in Section 2.6.

2.3 Observations and data

A combination of optical photometry, spectroscopy and spectropolarimetry was obtained. See Table 2.2 for details of these datasets which are detailed in the following sub-sections.

2.3.1 Time-series spectroscopy

Spectroscopic observations were carried out on the 4.2-m William Herschel Telescope (WHT) at Roque de los Muchachos, La Palma. Time-series data were obtained on 2018 July 29 and 2019 May 14 in service mode, using the Intermediate-dispersion Spectrograph and Imaging System (ISIS), a double-arm, low- to medium-dispersion, long-slit spectrograph. The instrument was used in the default service mode setup, including the EEV12 $2048 \times 4096 \,\mathrm{pixel^2}$ detector in the blue arm, and Red+ $2048 \times 4096 \,\mathrm{pixel^2}$ array in the red arm. On-chip binning of 3 pixels in the spatial direction was employed to increase signal-to-noise (S/N) in the case of potentially poor or variable seeing. A slit width of 1.2 arcsec was used together with the R600B and R600R gratings centred at 4500 Å and 6500 Å respectively. This resulted in an unvignetted wavelength range of approximately $3920 - 5150 \,\mathrm{Å}$ in the blue arm with resolving power $R \approx 1800$, and $5900 - 7100 \,\mathrm{Å}$ in the red arm with $R \approx 2700$. Exposures were taken in both arms simultaneously, with individual integration times of 120 s each. In this manner, both observing runs covered around 4.5 contiguous hours on-source, and yielded, on average, 116 frames of data in

Table 2.1: Published parameters of GD 356.

Parameter	Value
Spectral Type	DAHe
V (mag)	15.1
$B_{\rm dip}$ (MG)	13 ± 2
Distance (pc)	20.14 ± 0.01
$v_{\rm tan}~({\rm km~s^{-1}})$	21.47 ± 0.02
$T_{\rm eff}$ (K)	7560 ± 30
$\log g (\text{cm s}^{-2})$	8.19 ± 0.01
Mass (M_{\odot})	0.70 ± 0.01
Cooling Age (Gyr)	1.98 ± 0.04

References: Ferrario et al. (1997a); Bergeron et al. (2001); Fontaine et al. (2001); Gentile Fusillo et al. (2019).

each arm. Such a setup ensured full spectroscopic coverage of H α and H β emission lines (Fig. 2.1).

The target frames were obtained under bright conditions with lunar illumination of 96 and 81 per cent during the 2018 July and 2019 May runs, respectively. Weather conditions during the 2018 July run were dusty, but cloudless, and seeing ranged from 0.5 to 0.8 arcsec. The seeing in the 2019 May observational period varied from 0.8 to 2.0 arcsec, with an average of approximately 1.0 arcsec and no clouds. For both runs, the airmass ranged between 1.1 to 1.6. Multiple flat, bias, and arc lamp frames were taken on each night for calibration purposes, but only a single spectroscopic standard star was observed for the program (during the 2019 May run). These service-mode calibration data could not be reliably used for (relative) flux calibration, and wavelength calibration was also a challenge, especially in the blue arm, where a 2 Å shift is apparent between arcs taken at the start and the end of both nights.

Standard long-slit, single object reduction procedures were performed in IRAF (Tody, 1986, 1993) for spectral extraction. Because a bright standard star was not available, two-dimensional images of the science target were co-added to obtain the optimal trace for each observing night. This trace aperture was then used to extract the individual frames using the APALL package. Owing to the lack of reliable flux calibration data, it was decided to calibrate using continuum normalisation. Individual extracted spectra were continuum-normalised by fitting a polynomial over spectral regions that are free of emission or telluric features. A third-order polynomial function was used to normalise individual blue arm spectra, and a fourth order for individual red arm spectra. The overall accuracy of the normalisation was then verified by assessing trailed spectrograms to ensure relative homogeneity between the individual frames. The S/N was assessed for individual spectra in the regions $4500 - 4600 \,\text{Å}$ and $6600 - 6700 \,\text{Å}$, and found to be $\langle \text{S/N} \rangle = 23 \pm 2$ for the 2018 July run and $\langle \text{S/N} \rangle = 19 \pm 2$ for 2019 May.

2.3.2 Spectropolarimetry

The WHT ISIS instrument was also used to obtain a time series of circular spectropolarimetric measurements on 2019 October 9 over an entire rotational cycle of GD 356. This

strategy allowed a measurement of the polarisation averaged over almost the entire spin cycle, but can also detect variability of the magnetic field due to rotation. Simultaneous exposures were taken through the R600B grating in the blue arm, and the R1200R grating in the red arm, with central wavelengths 4400 Å and 6500 Å respectively. The slit width was set to 1.0 arcsec and spectral resolving powers of $R \approx 2350$ and $R \approx 7800$ were attained in the blue and the red arm, respectively. Twelve pairs of exposures were obtained with the retarder waveplate at position angles of $\pm 45^{\circ}$, thus exchanging the right- and left circularly polarised spectra on the CCDs. This beam-swapping procedure avoids most of the possibly serious systematic errors that arise from single integrations using a fixed waveplate position (e.g. Bagnulo et al., 2009). An exposure time of 300 s was adopted for each frame at each position, providing an effective cadence of 600 s in measuring Stokes V and V. For each exposure pair, a global peak S/N of V0 per Å was achieved in the blue arm, and V0 per Å in the red arm.

The details of the data reduction, and a discussion on the conventions adopted for Stokes V are described in Bagnulo & Landstreet (2018). In agreement with most recent literature on stellar magnetic fields, Stokes V is defined as right-handed circular polarisation minus left-handed circular polarisation (as seen from the observer). Notably, this is opposite the definition adopted by Ferrario et al. (1997a) in their study of GD 356. The average Stokes I and V/I over a full rotation are shown in Fig. 2.2.

In order to identify correctly the extent of the Zeeman σ and π components, and because later measurements require an accurately calibrated I spectrum for normalisation of measurements of the polarised (Stokes V or V/I) spectra, the instrumental wavelength sensitivity variations from the flux (Stokes I) spectra have been removed. This was done through the use of featureless DC white dwarf spectra taken with the same instrumental setting as for the science target. Each spectrum of GD 356 was normalised to 1.00 near the centre, at 6400 Å for the red spectra, and at 4500 Å for the blue spectra. The DC flat field standard was then normalised to 1.00 in the same region, and the slope of its continuum was adjusted by multiplication by a factor of $[1.00-C((\lambda-\lambda_0)/\lambda_0)]$, where C is a constant adjusted for each spectrum, with a value of around 0.4 for blue spectra flat-fielded with WD 1055–072 ($T_{\rm eff} = 7155 \, \rm K$), and a value around 2.0 for red spectra flat-fielded with WD 1820+609 ($T_{\rm eff} = 4865 \, \rm K$). This fitting procedure led to virtually identical spectra over several hundred Å of spectral data exterior to the extended Zeeman components of GD 356. The process was then completed by dividing the spectrum of GD 356 by the matched spectrum of the DC white dwarf, resulting in flux spectra accurately normalised to unity except within the Zeeman components.

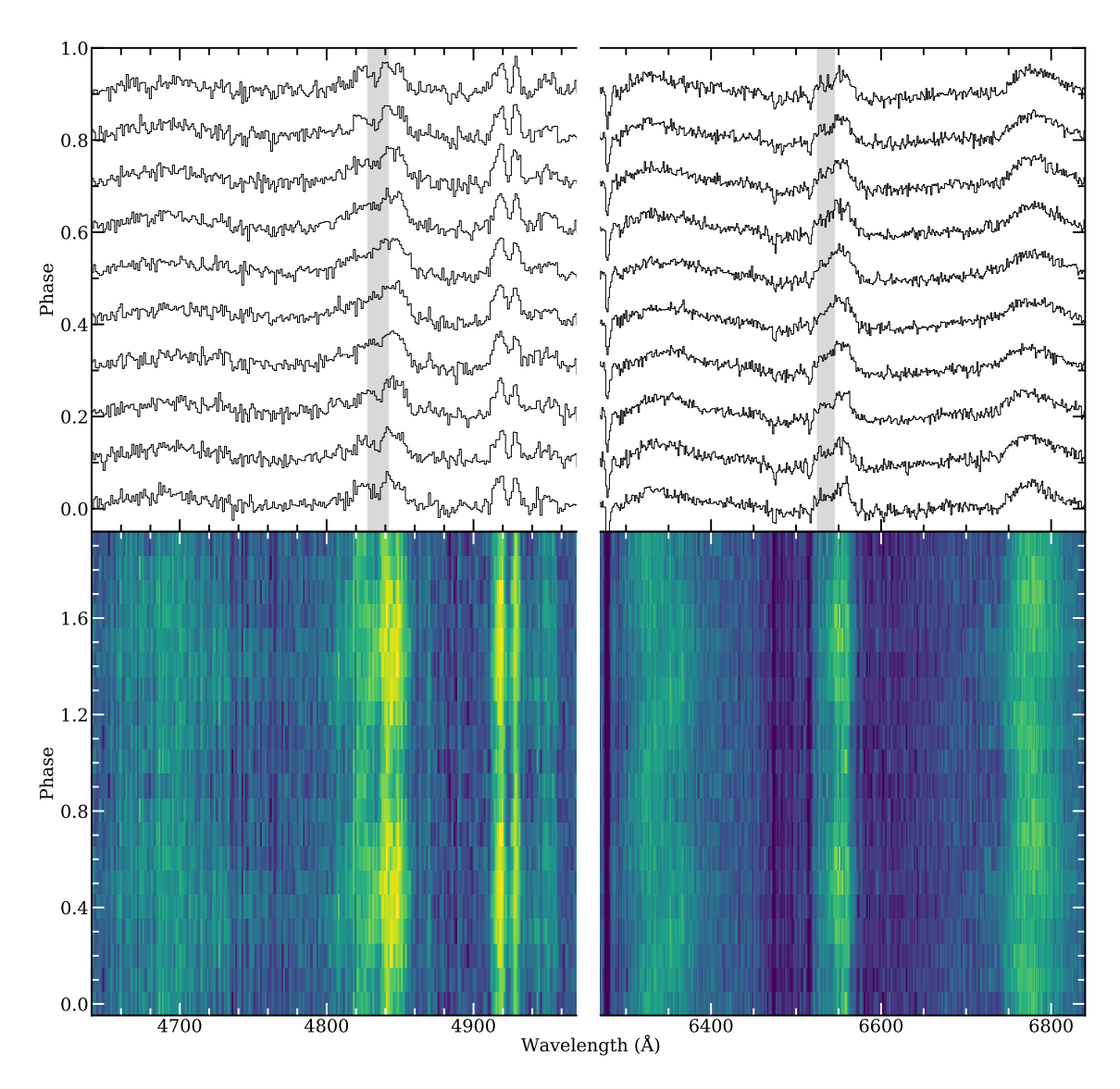


Figure 2.1: Upper panel: Phase-folded H β and H α normalised ISIS spectra. The spectra were folded on the established period where phase = 0 corresponds to photometric maximum at BJD_{TDB} ≈ 2458296.0255 . Shaded regions highlight (potential) periodic dips in both central π components, where this variation is clear in the H β component, and less certain in H α . The absorption feature near 6375 Å is telluric O₂. The red arm data were re-binned to 1.5 Å, and blue arm data to 1.3 Å for better visualisation. Lower panel: The data from the upper panel plotted as a trailed spectrogram. The maximum relative flux is indicated in yellow and the minimum in dark blue. Periodic variations in both the relative emission intensity and central wavelength are visible in multiple features, with the latter most clearly evident in the σ_b component of H α .

Table 2.2: Ground-based, time-series observations obtained for this study.

Telescope /	Obs	Obs	Duration	$t_{\rm exp}$	$n_{\rm exp}$
Instrument	Type	Date	(h)	(s)	•
WHT / ISIS	Spec	2018 Jul 29	4.4	120	113
WHT / ISIS	Spec	2019 May 14	4.6	120	120
WHT / ISIS	Spol	2019 Oct 09	2.0	300	24
LT / RISE	Phot	2020 Jul 09	2.0	6	1168
LT / RISE	Phot	2020 Jul 10	2.0	6	1168
LT / RISE	Phot	2020 Jul 14	2.0	6	1168
LT / RISE	Phot	2020 Jul 17	2.0	6	691
LT / RISE	Phot	2020 Jul 26	2.0	6	1168
LT / RISE	Phot	2020 Aug 08	2.0	6	1168
LT / RISE	Phot	2020 Aug 16	2.0	6	1168
PTO / PRISM	Phot	2020 Aug 15	3.3	10	784

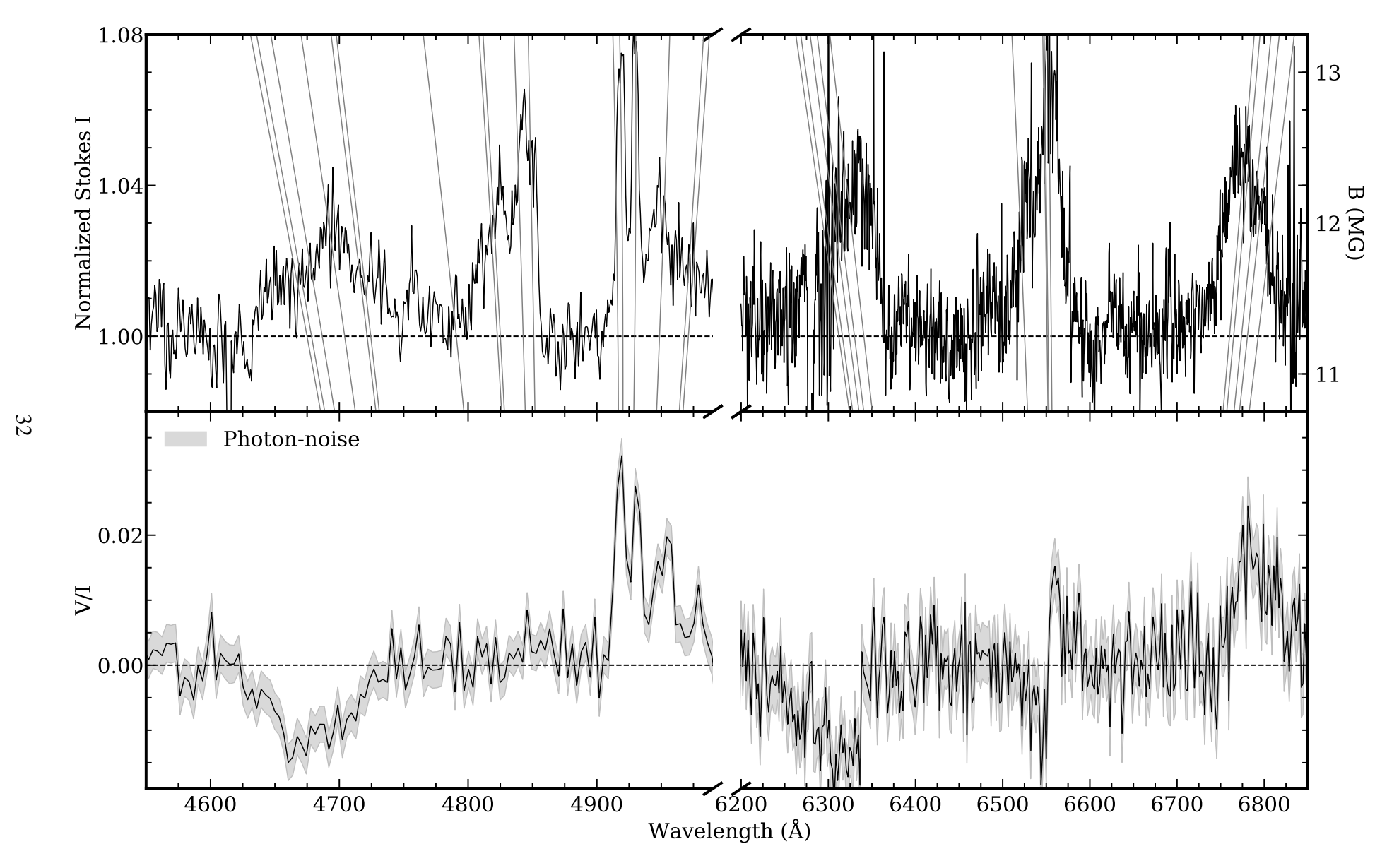


Figure 2.2: *Upper panel*: Integrated 2 h intensity (I) spectrum obtained via spectropolarimetry. Grey lines represent magnetic transitions as a function of field strength (Schimeczek & Wunner, 2014). *Lower panel*: The average V/I spectrum with estimated photon-noise overplotted in grey. The former has the opposite sign to that shown in Fig. 1 of Ferrario et al. (1997a), which is simply due to different definitions adopted in this work (see Sect. 2.3.2 and Bagnulo & Landstreet, 2018). The spectrum was re-binned for clarity to 2.0 Å and 3.5 Å in red and blue, respectively.

2.3.3 TESS observations

GD 356 was observed by *TESS* in Sectors 16, 23, 24, 25, and 26 under designation TIC 274239484 (*TESS* Mag = 14.8 mag; Stassun et al. 2018). Additional *TESS* observations took place after the publication and will be discussed in the next chapter. Data from Sector 16 were observed from 2019 September 12 until 2019 October 6. Data from Sector 23 onward span dates from 2020 March 19 until 2020 July 4. *TESS* utilises a red-optical bandpass covering roughly $6000 - 10\,000\,\text{Å}$, and each CCD has a $4096 \times 4096\,\text{pixel}^2$ on-sky area, which are read out at 2 s intervals. The on-board computer then produces $11 \times 11\,\text{pixel}^2$ postage stamps centred at the target, with flux averaged over 120 s. After a quality-flag cut, a total of 113.7 d of GD 356 observations at 2 min cadence were retained for photometric analysis. Only points with the nominal quality flag were analysed (94.4 per cent of the total recordings).

Data products from the outlined sectors were accessed from the *TESS* Mikulski Archive for Space Telescopes pages¹. Light curves were extracted from the 2 min target pixel files by the *TESS* Science Processing Operations Center pipeline (Jenkins et al., 2016). Presearch Data Conditioning Simple Aperture Photometry (PDCSAP) light curves were used, as these have systematic errors removed, including error sources from the telescope and the spacecraft (Smith et al., 2012; Stumpe et al., 2012). Flux values were divided by the mean for each sector and centred at zero. Aperture masks identified by the pipeline differed between the sectors, and to investigate possible effects of this, the LIGHTKURVE package was used to extract the data with a consistent aperture mask. No significant differences in the resulting light curves were found, and therefore, pipeline defined apertures were used throughout for reliability and reproducibility provided by the PDCSAP.

Gaia DR2 reveals a source that is 12.8 arcsec distant from GD 356 and fainter by $\Delta G = 3.2 \,\mathrm{mag}$, and $\Delta R_{\mathrm{P}} = 2.4 \,\mathrm{mag}$ (Gaia Collaboration et al., 2018a), thus on the order of ten times fainter in the region of the *TESS* bandpass. There appears to be no significant contamination from this source in the extracted data. From the *TESS* pipeline, an average ratio of target flux to total flux (CROWDSAP) in the aperture is 0.87 over five sectors. This is accounted for in the PDCSAP data. To confirm that any variability present in the aperture mask is due to GD 356 the TESS-LOCALIZE package was used (Higgins & Bell, 2023). As Fig. 2.3 shows, photometric variability in the data is due to GD 356 and not the nearby fainter object.

2.3.4 The Liverpool Telescope

Ground-based photometry was acquired on the fully robotic 2.0 m Liverpool Telescope (LT) at Roque de los Muchachos, La Palma. The fast-readout CCD imager, Rapid Imaging Search for Exoplanets (RISE; Steele et al. 2008) instrument was used on 2020 July 9, 10, 14, 17, and 26, as well as on 2020 August 8 and 16. The imaging data were taken with the in-house V + R filter, constructed from a 3 mm Schott OG515 bonded to 2 mm Schott KG3 filter, and with a central wavelength of approximately 5900 Å. The data were acquired in the 2×2 binning configuration, corresponding to 1.17 arcsec² per pixel² on an E2V CCD47-20 frame-transfer CCD with a 1024×1024 pixel² light-sensitive region. All but one observational group covered the 1.93 h rotational period of GD 356, including all overheads, with 6 s individual exposures, yielding a total of 1168 frames per group. The

¹https://mast.stsci.edu/

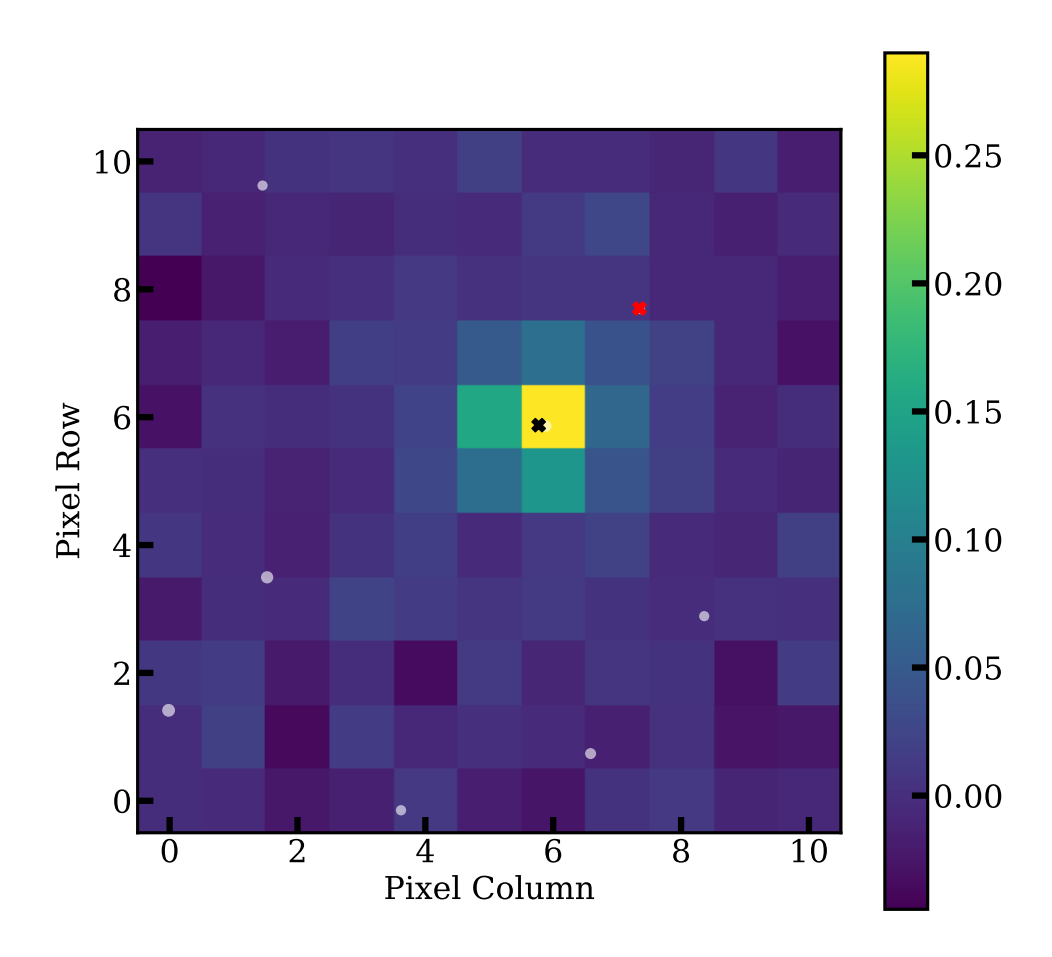


Figure 2.3: *TESS* target pixel file of GD 356 from Sector 16. The colourbar shows relative variability strength for a $12.45 \, d^{-1}$ signal. The estimated epicentre of this signal is marked with a black cross that overlaps well with GD 356 estimated position from *Gaia*. The second closest object is 12.8 arcsec away and is marked as a red cross.

remaining observational visit on 2020 July 17 was affected by the calima (dust) resulting in an early dome closure. The data were automatically reduced through the RISE pipeline which performs bias subtraction, removes a scaled dark frame, and generates the flat-field correction. Overall, a total of seven sets of data were obtained, six of which cover the full photometric cycle of GD 356 at a higher cadence, a finer spatial scale, and higher S/N compared to *TESS*.

Circular aperture photometry was performed in AstroImageJ (Collins et al., 2017) to obtain relative fluxes comprised of the net integrated counts of the target divided by the total integrated counts of all comparison stars. Three comparison stars were used for differential photometry, where the faintest was approximately three times brighter within the photometric aperture than GD 356. These comparison sources appear non-varying, with S/N always greater than the target, yet below the level where the CCD has a non-linear response. Aperture size was chosen empirically and individually for each visit based on uncertainty minimisation of the resulting amplitude of the photometric variability, where a typical aperture radius was 4 arcsec or roughly twice the typical seeing (2 – 2.5 arcsec). Finally, a barycentric correction was applied to the mid-points of the exposure time stamps to allow for a comparison with other photometric studies.

2.3.5 The Perkins Telescope Observatory

Additional ground-based photometry was acquired on the 1.8 m Perkins Telescope Observatory (PTO) on Anderson Mesa outside of Flagstaff, Arizona, on 2020 August 15, using the Perkins Re-Imaging SysteM (PRISM; Janes et al. 2004). Time-series photometry was performed in the SDSS g filter with no binning, with each exposure lasting 10 s. The readout times are typically slow (8.0 s) for PRISM, but they were reduced by using a $410 \times 410 \,\mathrm{pixel^2}$ subarray of the CCD, reduced from its full $2048 \times 2048 \,\mathrm{pixel^2}$. This strategy yielded 784 frames over 196 min, including overheads. The weather was clear, and the seeing ranged from $2.1 - 4.3 \,\mathrm{arcsec}$. The data were reduced with custom code written in PYTHON that corrects the data for bias, performs the flat field, and executes aperture photometry using Photutils version 0.7.2 (Bradley et al., 2019). Frame times were corrected to barycentric times using Astropy (Astropy Collaboration et al., 2013, 2018). At the end of the run, a roughly 3 s offset was found in the data-acquisition computer time compared to a Network Time Protocol time server, which was corrected by adding 3.0 s to each time in the light curve. Given these imprecise time stamps, 3.0 s was also added to the estimated phase uncertainty.

2.4 Analysis and results

First the photometric data are presented, as the known – now updated and highly precise – photometric period sets a foundation against which all observed variability may be compared. Owing to extensive *TESS* observations, the photometric period is sufficiently constrained to allow for comparisons of epochs multiple years apart. To assess the origins of the broad-band photometric variability in GD 356, the semi-amplitude of the light curves in several bandpasses are compared with that expected from changes in the emission lines alone. Following these results, both the time-series spectroscopy and spectropolarimetry are discussed.

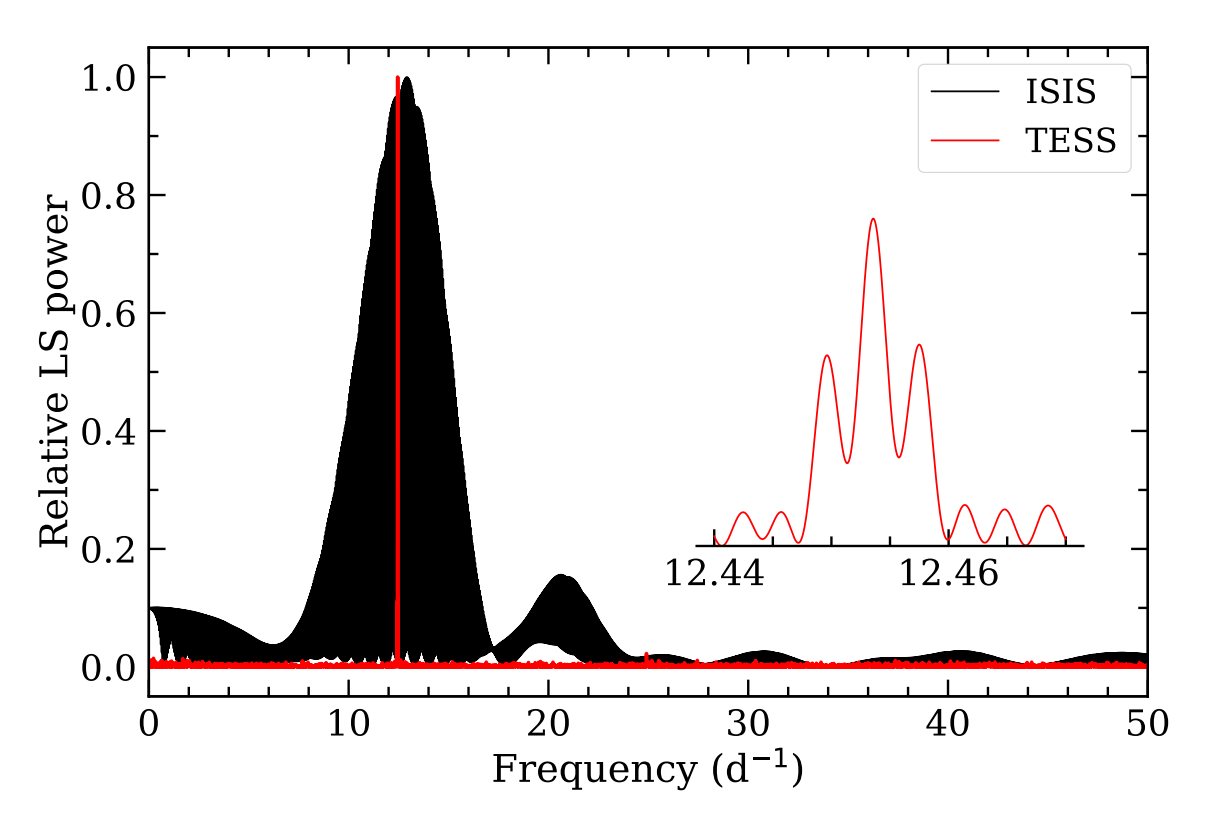


Figure 2.4: Lomb-Scargle (LS) periodogram of ISIS relative equivalent widths (W_{λ} , black) and *TESS* photometry (red). The *TESS* data show a clear peak at 12.45 d⁻¹ (zoomed panel) corresponding to the known period, and a less obvious but significant first harmonic of this frequency is also present at approximately 25 d⁻¹.

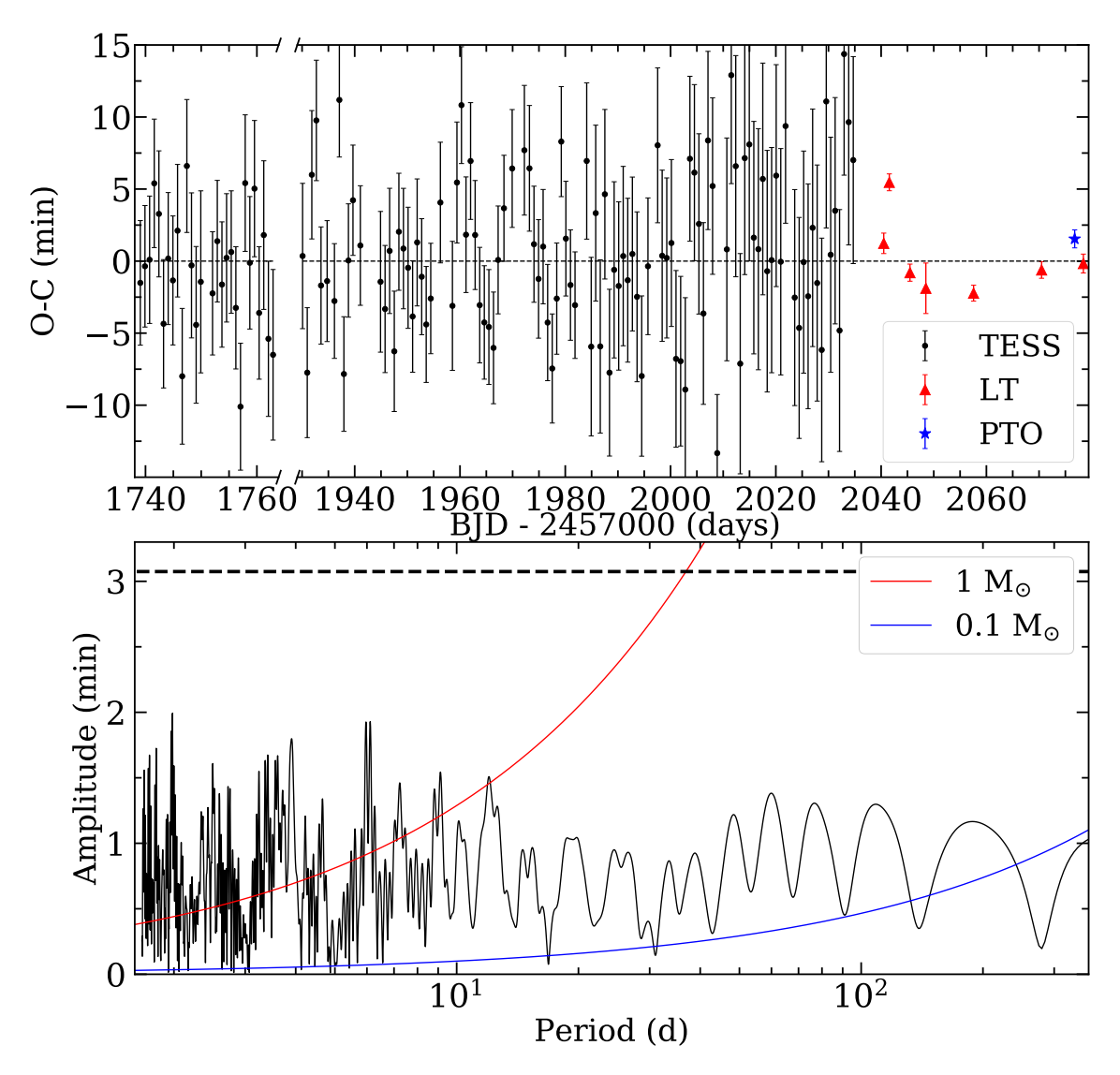


Figure 2.5: Upper panel: O - C diagram of TESS sectors 16, 23, 24, 25, and 26, and ground-based LT and PTO observations showing the arrival time of the rotational signal assuming a constant spin period. Each TESS data point is a time slice of approximately 20 h or roughly 10.5 rotational cycles. Modest discrepancies are seen between the expected and observed arrivals, in both space- and ground-based observations. Lower panel: LS periodogram of the O - C data plotted above, where the dotted line just above 3 min in amplitude is an empirical estimate of the 1 per cent false-alarm probability. Although the photometric data deviate somewhat from a constant in O - C, there is no statistically significant signal in the periodogram. Moreover, the expected amplitude of a variation induced by a planetary-sized companion would be much smaller than can be constrained by these data. This point is demonstrated by the blue and red lines which display the expected amplitudes from a 0.1 and 1.0 M_☉ companion for a range of orbital periods.

Table 2.3: Re-constructed spectral energy distribution of GD 356 convolved with the various light curve filters.

Facility				$A_{ m W}$	A_0	Year
		(Å)	(%)	(%)	(%)	
PTO	g	4750	0.69	0.13	1.28	2020
JKT	V	5510	0.11	0.02	0.20	2002-2003
LT	V+R	6170	0.27	0.05	0.83	2020
<i>TESS</i>	TESS	7900	0.18	0.03	0.65	2019–2020

Note. The third column is the flux-weighted, average wavelength, and the fourth column gives the fractional contribution of the emission lines relative to the continuum. The fifth column is the expected semi-amplitude $A_{\rm W}=f_{\rm em}\times 0.19$ from only the observed variation in W_{λ} (whose semi-amplitude is 0.19 for all emission lines). The sixth column is the observed light curve semi-amplitude, and is an order of magnitude larger than $A_{\rm W}$ in all cases.

2.4.1 Photometric variability

To establish a physical context for any and all spectroscopic or polarimetric variability, the *TESS* observations are examined. The star has unparalleled temporal coverage from a total of five sectors, four of which are consecutive, and together with the 2 min cadence provide an excellent opportunity to investigate the photometric variability in detail. The AstroPy implementation² of the Lomb-Scargle (LS; Lomb 1976; Scargle 1982) periodogram for the pipeline-processed light curves shows a strong signal at 1.92717 ± 0.00001 h (Fig. 2.4). The period determined from these data is within 2σ of the value established from *V*-band observations almost 20 years prior (Brinkworth et al., 2004). The observed semi-amplitude of the variation is 0.64 ± 0.02 per cent in the *TESS* filter, which fully covers all three H α emission components, whereas the *V*-band observations had a semi-amplitude of 0.2 per cent and this filter covers only a fraction of the H β emission. Despite the relatively small uncertainty in the period, the direct comparison of T_0 from *TESS* and Brinkworth et al. (2004) is not possible.

The unipolar inductor predicts that the hot emission region is the result of a current loop connecting the stellar surface with an orbiting and conducting planetary body. It is thus expected that such a signal would be present in photometric data, assuming the spot location is (even partly) modulated by its Keplerian orbit. First, the only significant signals seen in the photometric data analysed here are the rotational frequency and its first harmonic. Second, an observed (O) minus calculated (C) arrival time diagram is shown in Fig. 2.5, where both *TESS* and ground-based observations are plotted. Despite the profound temporal coverage of *TESS*, and higher accuracy of the ground-based arrival times, there are no clear trends or periodic signals in the O - C data – certainly nothing above the false alarm probability (Greiss et al., 2014). Therefore, evidence of a secondary modulation in the photometric period has not been detected in the extensive *TESS* or ground-based data, nor has the period appeared to change in more than 15 years.

The lack of additional frequencies does not support a unipolar inductor with planetary

²The AstroPy Lomb-Scargle documentation available at: https://docs.astropy.org/en/stable/timeseries/lombscargle.html

orbits that are well-sampled by the *TESS* light curves (on the order of hours to weeks). This includes both additional simple sinusoidal signals and beat frequencies. However, for hypothetical orbital periods exceeding approximately one month, the beat period becomes too close to the rotational period to be distinguished. Such orbital periods would be inconsistent with the unipolar inductor interaction. However, the O-C observations are hardly constraining in terms of orbital modulation. A maximum amplitude in the phase variation can be calculated for a potential companion (Hermes, 2018). As shown in Fig. 2.5, companions of sensible masses cannot be ruled out from these data, e.g. $1.0\,\mathrm{M}_\odot$ object on a 30 day orbit can be dismissed. Clearly, the existing $3-8\,\mu\mathrm{m}$ *Spitzer* constraint of $12\,\mathrm{M}_\mathrm{Jup}$ (Wickramasinghe et al., 2010) is far more informative. Potentially, future *TESS* observations might prove useful in a prospective O-C interpretation. However, there does appear to be at least one point based on LT observations that is more than 3σ from zero in Fig. 2.5, and may indicate some modest surface feature evolution. But from these analyses, it is the lack of additional frequencies that fails to indicate any significant emission region modulation by a conducting planetary companion, as in the unipolar inductor model.

Emission line variability seen in the ISIS spectra cannot be solely due to continuum variation, because the relative semi-amplitude of equivalent width variation 0.19 ± 0.01 (Fig. 2.6) is inconsistent with photometric semi-amplitudes (below 0.015 for PTO, LT and *TESS*). Thus, the emission must be contributing to the variability, albeit the antiphase relation between equivalent widths and photometry. To quantify the contribution of emission a synthetic spectrum was stitched up that includes H α to H γ emission. This spectrum was then continuum normalised and the most prominent telluric features were removed. Next the spectrum was multiplied by a normalised black body model at T = 8000 K. The processed spectrum was then multiplied by a transmission function of the photometric filters used in this investigation and the previous photometric study (Brinkworth et al., 2004). Results are summarised in Table 2.3. It appears that the dominant source of the photometric variability must be due to continuum variation, since the emission line variability is approximately an order of magnitude below the observed values. The continuum variation hypothesis is further supported by the fact that the variation is larger at shorter wavelengths, which is consistent with a blackbody at 8000 K.

2.4.2 Spectroscopic variability

The ISIS long-slit (non-polarimetric) spectra exhibit Balmer emission features at all rotational phases (Fig. 2.1). The known H α and H β features are split into Zeeman triplets, where the central π components exhibit a weak displacement relative to the zero-field position, and the side components σ_b (blueshifted) and σ_r (redshifted) are displaced approximately equally from the undisturbed spectroscopic location and carry opposite polarisation states (Fig. 2.2). There is also a single, weak emission feature observed at H γ (not shown), where other Zeeman components are not detected, even in a co-added spectrum of an entire night.

The equivalent widths (W_{λ} ; Vollmann & Eversberg 2006) are measured to investigate the emission activity of GD 356, using determinations for each H α and H β Zeeman component, corresponding to six total W_{λ} values per time-series spectra. The individual component W_{λ} are divided by the temporal mean, and all six spectral components are averaged into a single $\langle W_{\lambda} \rangle$ per time-series exposure, which is then passed to the periodogram algorithm.

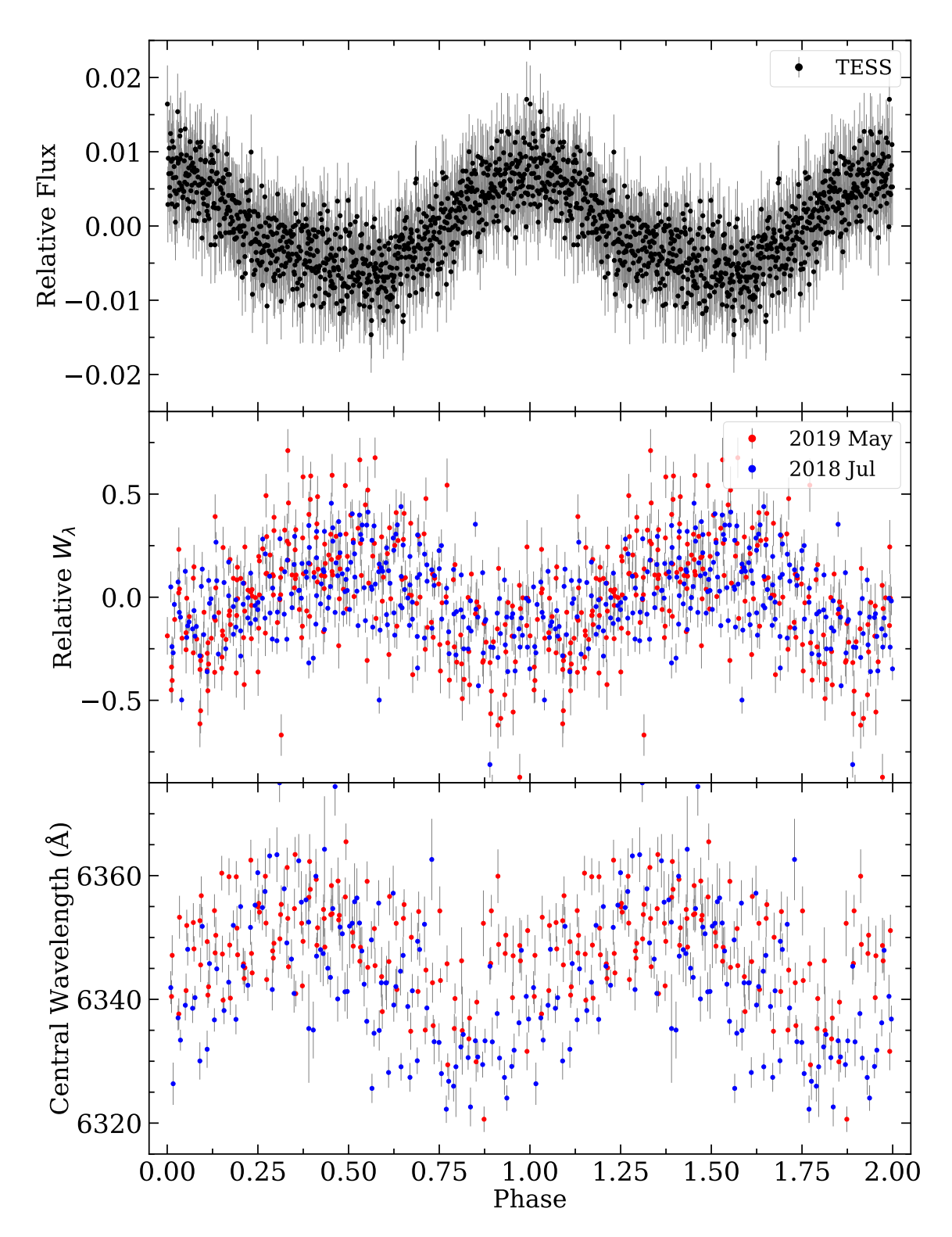


Figure 2.6: *Upper panel*: All five available *TESS* sectors combined and folded on the 1.92717 h period, where each point is an average of 100 phase-consecutive recordings. *Middle panel*: Relative W_{λ} estimates from ISIS spectra coloured by the observing run. *Lower panel*: Variation in the central wavelengths of the σ_b component of H α . A change in the central wavelength of $-22 \,\text{Å}$ corresponds to a change in the average magnetic field of $+1.0 \, \text{MG}$. Phase = 0 corresponds to photometric maximum in all three panels.

Computing the LS periodogram for the W_{λ} -time recordings shows a strong signal near the known photometric period (Fig. 2.4). Furthermore, a repeating, sinusoidal pattern is evident in W_{λ} for each of the six individual emission components, where the clarity of the pattern varies depending on the particular feature. To better quantify these time-dependent changes for individual features, a goodness of fit statistic is estimated for each emission component using the spin frequency, and confirms the same variability is present in all emission feature components, and above the typical noise level in each case. Variation is conspicuous in the π components of H α and H β , as well as the σ_r components of H α . The behaviour of W_{λ} values during the 2018 July and 2019 May observing runs are entirely consistent (Fig. 2.6).

Interestingly, when the $\langle W_{\lambda} \rangle$ of the emission is phase-folded on the photometric period, it displays a 180° phase shift; the photometric maximum occurs when $\langle W_{\lambda} \rangle$ is minimum and vice versa (Fig. 2.6). To quantify the phase shift, we fit the respective sinusoids to measure a relative phase and its uncertainty. A normalised phase discrepancy of 0.50 ± 0.01 is found between the *TESS* photometry and ISIS equivalent widths. This anti-phase behaviour between photometric flux and emission line strength is corroborated by the LT photometry, whose phase is consistent with that of *TESS* (Fig. 2.5).

From the visual inspection of co-added spectra that consist of five consecutive images (Fig, 2.1), there are some notable morphological changes in the central emission features over the spin period. These changes in the shape of the emission lines are most notable in the π component of H β , and possibly in the π component of H α , and appear periodic with rotation. Because each emission component is a combination of contributions from multiple magnetic-atomic transitions, the morphological modulation is likely due to periodic displacement of individual transitions in response to a changing view of the local magnetic field. It should be noted that this morphological variability alone is unlikely to be the primary source of W_{λ} modulation, because morphological changes are not detected in other emission components with clear W_{λ} periodicity. Thus, the observed variability in the equivalent widths is likely due to a variation in the emission strength rather than magnetically induced changes in the emission profile morphology.

A variation in the mean wavelength of the emission profiles is also apparent. Each emission feature has been fitted with a Gaussian by minimising the difference between the fit and the profile. The parameter that corresponds to the mean of the Gaussian fit is then used as a proxy for the centre of the emission, where the nature of the fitting method results in a more stable fit to broader emission components. Partly for this reason, the σ_b component of H α exhibits the clearest periodic variation in wavelength and is shown in the bottom panel of Fig. 2.6. Interestingly, while the variability is unsurprisingly periodic over a rotational cycle, there is a noticeable, normalised phase shift of -0.13 relative to the W_{λ} maximum (+0.37 relative to the photometric maximum).

These central wavelengths of the emission profiles act as an excellent indicator of the average magnetic field in the emission region, where the larger blueshift in the σ_b component of H α corresponds to a larger magnitude of the surface-averaged magnetic field. Hence, the higher field values approximately correspond to higher photometric amplitudes, although the 0.13 relative phase shift indicates that this correlation is likely accidental. This fact also suggests that the position of the emitting region does not favour the extremes of the magnetic field, at least in a context of the surface-averaged field. The lack of a direct relationship between the average magnetic field and photometry is potentially further supported by the spectroscopy of another DAHe star (Reding et al.,

2.4.3 Possible emission feature evolution

While it is clear that the π component of H β varies on the same timescale as the photometric flux, it is possible that the two ISIS data sets exhibit morphological dissimilarities in this feature at the same rotational phase (Fig. 2.7 and Fig. 2.8). The two observing runs are separated by nearly ten months, and in particular the 2019 May data display a dip in the π component for a larger part of the cycle, for example. Initially, these dissimilarities were considered from the viewpoint of the unipolar inductor model. To investigate this possibility further, W_{λ} are measured for the narrow region 4822 – 4844 Å where these superficial differences can be seen from visual inspection. These area estimates capture potential differences that are clearest near normalised phase 0.35 and 0.78 highlighted in the lower panel of the figure. There is a similar, modest difference between the 2018 July and 2019 May data W_{λ} of all three H β components (not shown), at the same phase. The data do not permit a more robust analysis and the reality of these possible feature evolution over many months is intriguing but uncertain.

Alternatively, assuming the variations presented in the O-C diagram (Fig. 2.5) are physical, then the morphological differences in the emission at the same rotational phase could be linked to small deviations in the photometric period. Given the exact anti-phase relationship between the photometric and emission intensity, the two quantities could be closely related. Therefore, judging by the fact that some inconsistencies are seen with the fixed period sinusoidal model in photometry, one might expect to see the same behaviour in the emission. Given that the emission profiles were analysed from co-added spectra with combined exposure of ten minutes, then a small alteration in phase of a few minutes could produce the observed behaviour and would be consistent with the O-C photometric analysis. This would indicate that the features are evolving, albeit modestly at most, on a timescale of days rather than months.

2.4.4 Spectropolarimetric measurements and variability

The spectropolarimetry of GD 356 simultaneously present both flux and circular polarisation spectra over a single complete rotation of GD 356, captured at 10 min intervals. The polarised spectra wavelength range includes H α from 6200 to 6900 Å and both H β and H γ from 4000 to 5100 Å. The new circular polarisation data have been integrated through the stellar rotation to be compared with the spectropolarimetry of Ferrario et al. (1997a). This juxtaposition can be viewed in Fig. 2.9. The 1997 data, which is not available in the tabulated form, has been extracted from Fig. 4 of Ferrario et al. (1997a). The resemblance between the two V/I spectra is notable, suggesting no significant changes in the average polarisation of GD 356 over a span of 25 years.

The $\langle |B| \rangle$ values are calculated by determining the average wavelength for each of the two σ components for both H α and H β . This is based on the excess flux over the continuum observed in the normalised spectra. The average longitudinal magnetic field $\langle B_z \rangle$ is ascertained using techniques established for magnetic Ap stars (Babcock, 1947; Mathys, 1989). Specifically, this involves estimating the wavelength shift of the entire emission feature in both right and left circularly polarised light, relative to its original

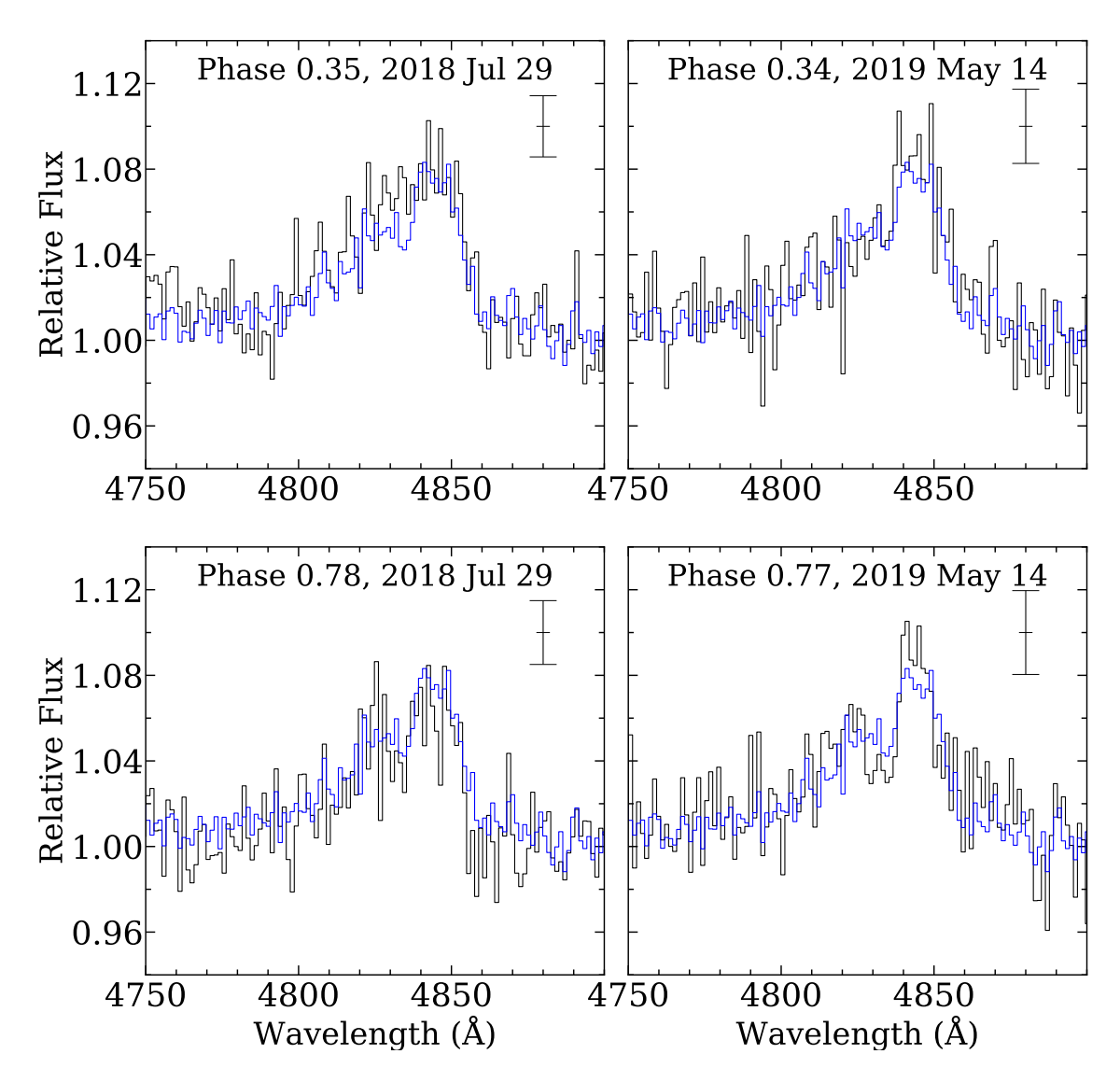


Figure 2.7: Potential morphological dissimilarities are observed in the π component of H β at approximately the same phase of rotation, based on different observing runs separated by ten months. Each panel represents 10 min of spectroscopy, where the spectra are re-binned for visual clarity. A blue line represents the average line profile across the entirety of the two observing runs for reference. Finally, one standard deviation is given as a black error bar for each panel.

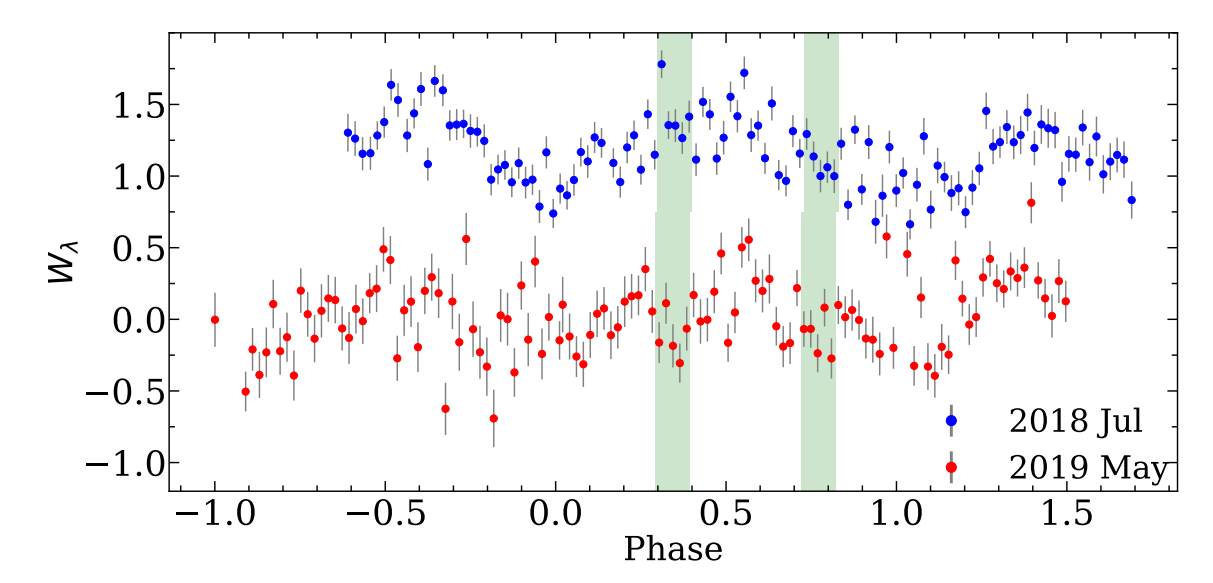


Figure 2.8: Relative W_{λ} for the region spanning 4822 – 4844 Å only, where the green shading highlights the rotation phase corresponding to the four phases shown in Fig 2.7, and the 2019 run is offset vertically downward for clarity.

position. This displacement can be described by the first wavelength moment of Stokes V centered around the average wavelength λ_0 :

$$\Delta \lambda_z = \frac{\int V(\lambda - \lambda_0) \, d\lambda}{\int I \, d\lambda} \tag{2.1}$$

Evaluation of this quantity and its uncertainty are discussed by Landstreet et al. (2015).

From prior research and as depicted in Fig. 2.2, the average field modulus is approximately 11 MG (Greenstein & McCarthy, 1985; Ferrario et al., 1997a). Based on the calculated wavelength positions of the various σ components, which are illustrated in Fig. 2.2 (Schimeczek & Wunner, 2014), it is determined that at this field strength, the average separation $\Delta\lambda$ between the two σ components of H α can be precisely represented by the equation $\Delta\lambda = 39.98B$. Here, $\Delta\lambda$ is in Å and B is in MG. The uncertainty in $\langle |B| \rangle$ is derived from the uncertainty in the calculated average position of the σ components. It is important to highlight that due to the shallow nature of the emission features, the primary challenge in accurately determining $\langle B_z \rangle$ lies in the continuum normalisation of the I spectrum, which is essential for the calculation in Eq. (2.1).

The calculated values of $\langle |B| \rangle$ and $\langle B_z \rangle$ can be found in Table 2.4. The top row corresponds to the integrated spectrum over 2 h. Subsequent rows detail the 10 min observations in sequential order throughout the entire observation period, presenting the average time for each exposure set. Additionally, the table provides measurements from the merged I and V polarised spectra, including the average wavelength shift, $\Delta \lambda_Z$, of the right or left circularly polarised spectra from their nominal values, the $\langle B_z \rangle$ values derived from this shift, and the equivalent width for each σ component, denoted as $W_{\lambda b}$ and $W_{\lambda r}$.

In addition to the mean field strength and mean longitudinal field, the range δB of B values in the emission region is also an interesting quantity. This range can be estimated from the excess width of each σ component over the width that the component would have in a uniform B field, due to line broadening and splitting of components by the quadratic Zeeman effect. As shown in Fig. 2.2, the individual σ components of the Balmer lines are

more widely separated in H β than in H α . This means that the most robust estimates of δB will be obtained from the analysis of H α . The range δB of field values is estimated using the dispersion of the intensity with wavelength of each σ feature within H α . This is done by using the same conversion between wavelength and field strength as above, for the full 2 h integrated spectrum.

The broadening of the σ components can be caused by a number of factors, including the variation of the magnetic field over the stellar surface, the intrinsic width of the emission components, and the dispersion in wavelength of the individual Zeeman components. The intrinsic width of a single emission σ component can be estimated from the widths of the two individual stationary red σ components of H β at 4920 and 4930 Å. This gives an intrinsic width of the order of 5 Å. Intrinsic broadening is thus unimportant. Another consideration is the dispersion in wavelength of the individual Zeeman components at 11.5 MG. Fortunately, the strongest of the five components in each σ pattern are in the middle, while the two outermost components are weakest.

For the H α , at a magnetic field strength of 11 MG, the dispersion in the calculated wavelengths of its five σ components – when adjusted for line strength – is roughly 7 Å. In comparison, the observed dispersions for the blue and red σ features of H α in the intensity spectrum measure approximately 26 Åand 19 Å, respectively. This disparity indicates that the observed width of each feature may stem from variations in magnetic field strengths across the emitting region.

Given the curvature noted in the relationship between wavelength and magnetic field strength for Zeeman components at 11.5 MG (see Fig. 2.2), the rate at which the wavelength broadens due to changes in the magnetic field is $-22.4 \,\text{Å}\,\text{MG}^{-1}$ for the dominant blue σ components. For the red components, this rate is $+17.1 \,\text{Å}\,\text{MG}^{-1}$. In both scenarios, this leads to a field variation, δB , of about $1.16 \,\text{MG}$. Consequently, the assessed range of magnetic field strengths, B, is approximated to be $11.5 \pm 1.2 \,\text{MG}$. This approximation aligns with prior estimates of field strength variations across the stellar surface.

Table 2.4: Magnetic field measurements of GD356 using H α and H β .

JD-2450000	Phase	λ_{b}	$\lambda_{\rm r}$	$\langle B \rangle$	$\Delta \lambda_{ m Z}$	$\langle B_{\rm z} \rangle$	$W_{\lambda \mathrm{b}}$	$W_{\lambda m r}$
(d)		(Å)	(Å)	MG	(Å)	(MG)	(Å)	(Å)
8766.357	Avg	6317.14 ± 0.86	6776.93 ± 0.76	11.50 ± 0.03	55.70 ± 2.74	2.79 ± 0.14	$\pmb{2.86 \pm 0.07}$	2.32 ± 0.06
8766.317	0.776	6311.51 ± 2.76	6773.77 ± 2.13	11.56 ± 0.09	58.57 ± 7.62	2.93 ± 0.38	2.86 ± 0.22	2.74 ± 0.21
8766.324	0.863	6321.19 ± 2.47	6784.60 ± 2.42	11.59 ± 0.09	36.73 ± 8.66	1.84 ± 0.43	3.11 ± 0.21	2.18 ± 0.19
8766.331	0.950	6318.21 ± 2.90	6774.98 ± 2.19	11.43 ± 0.09	63.51 ± 9.11	3.18 ± 0.46	2.56 ± 0.21	2.37 ± 0.19
8766.338	0.038	6316.74 ± 2.43	6777.79 ± 2.24	11.53 ± 0.08	65.45 ± 8.66	3.27 ± 0.43	3.16 ± 0.21	2.39 ± 0.19
8766.346	0.137	6317.17 ± 2.31	6774.31 ± 2.18	11.43 ± 0.08	42.14 ± 7.88	2.11 ± 0.39	3.63 ± 0.23	2.69 ± 0.21
8766.353	0.224	6324.37 ± 2.97	6775.31 ± 2.38	11.28 ± 0.10	47.69 ± 9.09	2.39 ± 0.45	2.84 ± 0.23	2.52 ± 0.22
8766.360	0.312	6315.75 ± 3.19	6776.97 ± 2.33	11.54 ± 0.10	51.17 ± 8.66	2.56 ± 0.43	2.65 ± 0.23	2.60 ± 0.22
8766.367	0.399	6322.98 ± 3.32	6774.14 ± 3.05	11.28 ± 0.11	64.79 ± 9.98	3.24 ± 0.50	2.69 ± 0.25	2.08 ± 0.23
8766.374	0.486	6312.64 ± 3.11	6776.17 ± 2.47	11.59 ± 0.10	35.08 ± 9.11	1.75 ± 0.46	2.95 ± 0.26	2.70 ± 0.24
8766.382	0.585	6316.77 ± 3.31	6781.08 ± 3.30	11.61 ± 0.12	55.90 ± 11.27	2.80 ± 0.56	2.97 ± 0.27	2.12 ± 0.25
8766.389	0.673	6314.37 ± 3.82	6778.68 ± 3.61	11.61 ± 0.13	74.07 ± 11.52	3.71 ± 0.58	2.52 ± 0.27	2.02 ± 0.27
8766.397	0.772	6312.33 ± 3.84	6779.07 ± 4.95	11.67 ± 0.16	83.90 ± 16.46	4.20 ± 0.82	2.67 ± 0.29	1.61 ± 0.29
8766.357	Avg	4688.50 ± 0.86	4938.65 ± 2.08	11.58 ± 0.10	36.83 ± 1.55	3.41 ± 0.14	$\boldsymbol{1.63 \pm 0.05}$	$\textbf{2.24} \pm \textbf{0.05}$
8766.317	0.776	4685.77 ± 4.85	4942.55 ± 8.07	11.89 ± 0.44	52.87 ± 7.09	4.90 ± 0.66	0.94 ± 0.17	1.95 ± 0.16
8766.324	0.863	4683.62 ± 2.86	4941.50 ± 8.16	11.94 ± 0.40	43.79 ± 6.49	4.06 ± 0.60	1.52 ± 0.16	1.85 ± 0.15
8766.331	0.950	4686.60 ± 2.80	4942.78 ± 8.17	11.86 ± 0.40	35.59 ± 5.92	3.29 ± 0.55	1.52 ± 0.16	1.81 ± 0.15
8766.338	0.038	4690.31 ± 3.10	4938.30 ± 6.74	11.48 ± 0.34	51.90 ± 5.33	4.81 ± 0.49	1.40 ± 0.16	2.26 ± 0.15
8766.346	0.137	4692.29 ± 3.22	4939.50 ± 8.66	11.45 ± 0.43	44.53 ± 6.82	4.12 ± 0.63	1.48 ± 0.17	1.91 ± 0.17
8766.353	0.224	4690.16 ± 3.56	4936.64 ± 7.08	11.41 ± 0.37	35.06 ± 5.99	3.25 ± 0.55	1.35 ± 0.18	2.35 ± 0.17
8766.360	0.312	4686.94 ± 2.38	4933.98 ± 6.30	11.44 ± 0.31	29.73 ± 4.38	2.75 ± 0.41	2.02 ± 0.18	2.65 ± 0.17
8766.367	0.399	4684.60 ± 2.49	4936.34 ± 6.67	11.65 ± 0.33	30.27 ± 4.53	2.80 ± 0.42	1.98 ± 0.18	2.55 ± 0.17
8766.374	0.486	4694.92 ± 3.82	4937.59 ± 6.33	11.23 ± 0.34	36.66 ± 4.82	3.39 ± 0.45	1.29 ± 0.18	2.73 ± 0.18
8766.382	0.585	4691.30 ± 2.31	4939.30 ± 6.11	11.48 ± 0.30	23.12 ± 4.24	2.14 ± 0.39	2.16 ± 0.18	2.86 ± 0.18
8766.389	0.673	4687.08 ± 2.28	4937.84 ± 8.27	11.61 ± 0.40	50.69 ± 5.15	4.69 ± 0.48	2.16 ± 0.18	2.07 ± 0.17
8766.397	0.772	4684.02 ± 3.36	4936.97 ± 7.87	11.71 ± 0.40	30.70 ± 5.60	2.84 ± 0.52	1.45 ± 0.18	2.19 ± 0.17

The data can be further examined for evidence of magnetic field variability during the rotation period of GD 356. A first assessment of variations may be obtained from Fig. 2.1. This figure suggests strongly that rotational variations do occur. Variability is particularly apparent in the red H β σ lines, in which two of the strongest magnetically split components are approximately stationary with changes of field strength, thus producing narrow emission features in which small changes (for example in amplitude) are particularly obvious to the eye. In contrast, the blue σ component of H β produces wide observable features because the wavelength vs. field strength dependence is stronger, and variability is not at all obvious by eye.

In addition the π components of H β include relatively strong transitions that are nearly but not quite stationary, and so also lead to sharp features in which variations are easier to see than in broad smooth features. In the sharp features of both the π and red σ components of H β , clear variability is visible. If one assumes that blue-shifted excursions of the π component at about 4825 Å are due to increasing field strength (see Fig. 2.2), then it appears from Fig. 2.1 that the $\langle |B| \rangle$ may be largest around phase 0.9 and weakest about phase 0.4.

In Fig. 2.10, the $\langle |B| \rangle$ and $\langle B_z \rangle$ values are shown as functions of the photometric period and zero point derived from the *TESS* observations detailed in Sections 2.3 and 2.4. Two key observations can be made from this figure. First, the $\langle |B| \rangle$ values obtained from H α and H β measurements are in remarkable alignment. Secondly, although the mean field modulus seems largely consistent, there is a noticeable variation, approximately in the range of 0.1–0.2 MG. This fluctuation is at its lowest around phase 0.3 and peaks between phase 0.8–0.9. This trend aligns with the data from Fig. 2.1, which indicates the most significant splitting of the H β π component occurs around phase 0.9.

In contrast, the measurements of $\langle B_z \rangle$ from the two Balmer lines diverge more than anticipated based on the calculated uncertainties. This discrepancy might arise from minor errors in the flat field corrections applied to the faint Zeeman components of the emission lines; these errors have not been factored into the uncertainty estimates. Setting aside this potential issue, the value of $\langle B_z \rangle$ is approximately constant at around 3.0–3.2 MG. It appears the mean longitudinal field may have slight variations, with the lowest value near phase 0.4 and a peak (or possibly two peaks) around phase 0.8 or 0.0. This fluctuation mirrors the trend hinted by the mean field modulus $\langle |B| \rangle$ as shown in Fig. 2.10, but the evidence for this trend is not definitive.

2.5 Discussion

The following section discusses the findings of all measurements, including inferences that can be made about the magnetic field and emission regions of the prototype DAHe star. Ample discussion is dedicated to the only model considered viable prior to this study, the unipolar inductor (Li et al., 1998). This model is re-examined in the context of observations of GD 356 and what is known from the two other DAHe stars SDSS J125230.93-023417.7 (J1252 hereafter; Reding et al. 2020) and SDSS J121929.45+471522.8 (J1219 hereafter; Gänsicke et al. 2020). A few issues that might cause this model to fail from a theoretical perspective are discussed, and an alternative hypothesis for the DAHe class is given based on collective stellar properties that make extrinsic mechanisms unlikely.

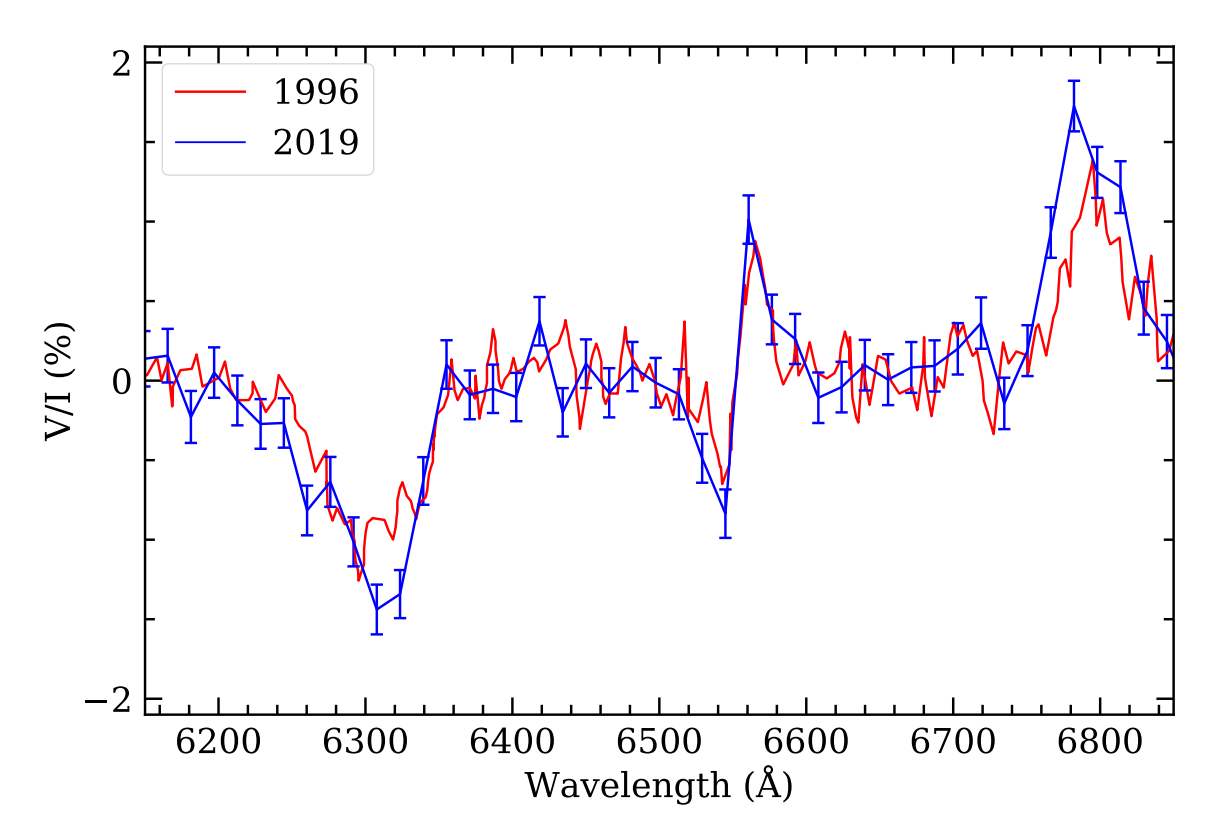


Figure 2.9: Comparison of circular spectropolarimetric data digitalised from Fig 4 of Ferrario et al. (1997a) and those presented in this work, re-binned at 16 Å. The sign of the data from Ferrario et al. (1997a) has been changed to make it consistent with the convention used here.

2.5.1 Implications of the photometric and spectroscopic variability

All data and periodicities identified to date are consistent with a single period previously identified as stellar rotation (Brinkworth et al., 2004). In addition to the broadband flux, the strength of the emission lines and their central wavelength both vary on the same period. The emission feature W_{λ} values vary in anti-phase with the *TESS* and ground-based photometry, suggesting that either the emission features intrinsically diminish at the photometric maximum, or the emission remains relatively constant and the W_{λ} variability is produced by continuum brightness fluctuations. However, the latter can be ruled out by pointing out that the continuum flux variation is at most on the order of ± 1 per cent (see Table 2.3), while the line fluxes vary by roughly ± 30 per cent.

It is important to emphasise that J1252 appears to exhibit the same anti-phase behaviour where the emission features manifest their maximum strength at the photometric minimum (Reding et al., 2020). There is not yet phase-resolved spectroscopy of J1219, but of the two spectra obtained for this star, it seems to also follow this pattern where emission is strongest when the total optical flux is lowest (Gänsicke et al., 2020). To avoid confusion, it is worth noting that for GD 356 and J1252 phase = 0 is defined at the light curve maximum, whereas for J1219 the authors use the opposite convention. Thus any successful model should account for the anti-phase behaviour, as it appears intrinsic to the DAHe population to date.

Detected morphological changes in the π components of H β and potentially H α (Fig. 2.1) appear periodic and follow the spin period, suggesting that rotation is responsible. Transformations in the emission profiles are consistent with a modest changes in the magnetic field across the surface as it rotates in and out of the view (more on this in Section 2.5.2). The broad-band photometric variability is clearly dominated by changes in the photospheric continuum (Table 2.3), and is almost certainly due to some type of magnetic field-dependent opacity, as seen in other high-magnetic field white dwarfs, such as Feige 7 or G183-35 (Achilleos et al., 1992; Kilic et al., 2019).

Previous modelling of spectropolarimetric and photometric data independently suggest a 0.1 covering fraction for the 1) polarised emitting region (Ferrario et al., 1997a), and 2) a dark star spot (Brinkworth et al., 2004). These two inferences can be reconciled with the anti-phase behaviour observed in GD 356 and other DAHe stars if a dark photospheric spot is located below an optically thin emission region, i.e. a chromosphere. These two regions – one hot, one cool – cannot be spatially independent or the anti-phase behaviour would not be observed. In terms of the unipolar inductor model, there is no a priori reason why a dark surface spot caused by magnetic dichroism should be coincident with an emission region caused by accretion along a current loop from an orbiting companion. There are no such additional signals in any data obtained to date, and despite the independent variations in broad-band flux, emission line strength, and emission line wavelength, only the spin period manifests with confidence. However, beyond the unipolar inductor model, it should be noted that such observed anti-phase behaviour might be plausible at certain wavelengths when a propagating electron beam is considered (Aboudarham & Henoux, 1987; Hallinan et al., 2015).

2.5.2 Interpretation of the magnetic measurements

Here, the possible interpretations of the magnetic measurements are considered. If the emission region is localised on the surface of the white dwarf, with a magnetic field that is roughly uniform in strength and approximately vertical in direction over the emission spot, then the small ratio of $\langle B_z \rangle/\langle |B| \rangle \approx 0.25-0.30$ suggests that the line of sight towards the spot is inclined at a large angle of perhaps 70° to the vertical direction. In other words, the spot is near the limb of the star as seen from Earth. In this case, for the spot to appear almost unchanging under rotation, the spot must be nearly centred on one of the two poles of stellar rotation, and thus the inclination angle of the rotational axis is similarly large. If correct, this implies the emission region itself is not responsible for the broad-band photometric variations, and consistent with the findings given in Table 2.3.

However, this picture depends strongly on the specific model of the emission as arising in a localised spot on the white dwarf. The localised spot model is supported by observations of the two other DAHe stars, J1252 and J1219, both of which exhibit strong rotational variations in the strength of the magnetised emission region (Reding et al., 2020; Gänsicke et al., 2020). In fact, the emission region of J1252 appears to vanish over the stellar limb for part of the rotation cycle, indicating that the emission is confined to a limited region of the stellar surface, while an H α absorption line region, in which the line may well be broadened by a weaker magnetic field, extends over a larger part of the white dwarf.

In a scenario where the distribution of emission over the surface of GD 356 is different from that deduced from the other two DAHe stars, it is still possible that emission arises

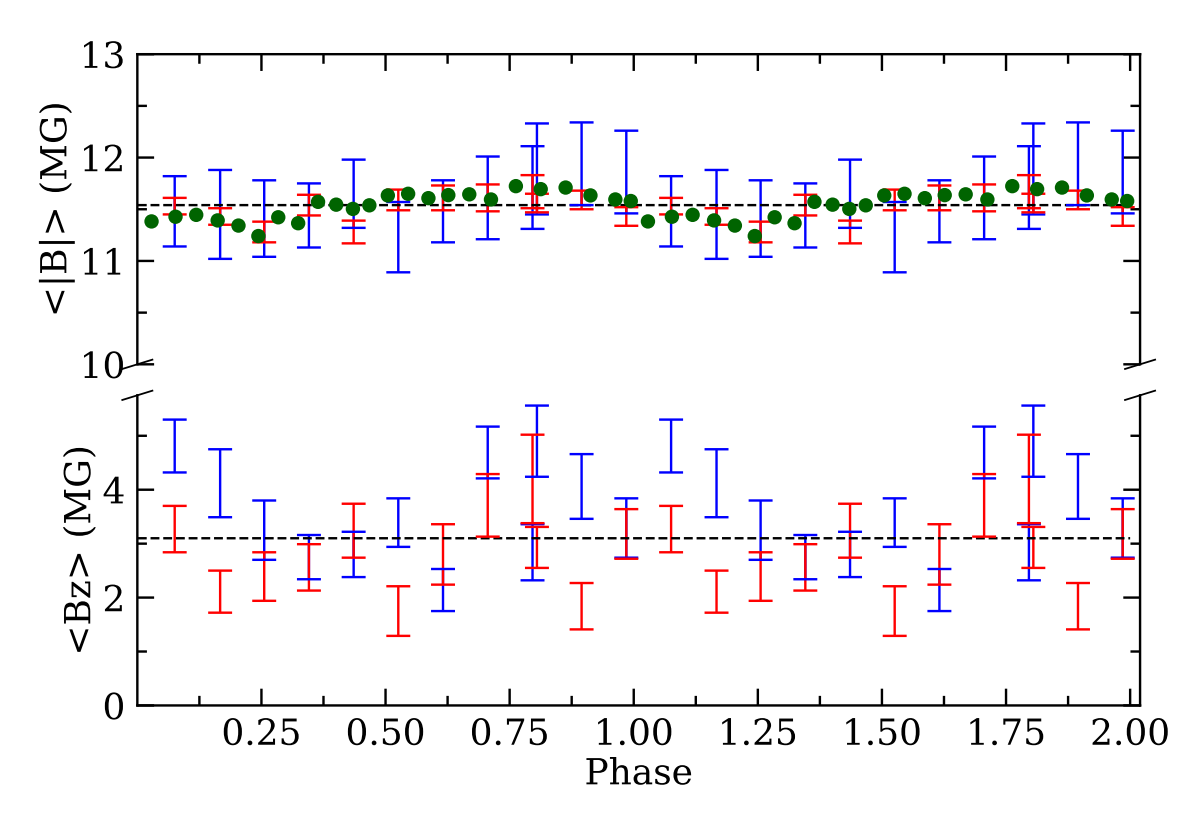


Figure 2.10: $\langle B_z \rangle$ and $\langle |B| \rangle$ as functions of *TESS* photometric phase. The spectropolarimetry measurements obtained using H α are shown in red symbols; those from H β are in blue. Dashed black lines represent the average value. In green are shown analogous results from the non-polarimetric spectroscopy, based on the measurements plotted in Fig, 2.4, where a small offset of +0.28 MG has been applied to account for calibration disparities between the two datasets. Each data point is the phase average of approximately 15 exposures in total, and the error bars are roughly the same size as the symbols. The scale of the two *y* axes are different, and highlight the greater precision of the $\langle |B| \rangle$ measurements.

from the bulk of the visible stellar disk. The observed, and limited, 1 MG dispersion of |B| indicates the whole emission region has a nearly uniform value of |B|. This has been proposed as an argument against a widely distributed emission region (e.g. by Ferrario et al., 1997a) on the grounds that an assumed global dipole magnetic field varies in strength by a factor of two between pole and equator. Nevertheless, little is known about the real global field distributions over magnetic white dwarfs, where only a few models based on phase-resolved magnetic measurements are available in the literature (e.g. Euchner et al. 2005; Valyavin et al. 2005; Euchner et al. 2006; Valyavin et al. 2008). And in fact for WD 2047+372, in which the two magnetic hemispheres become independently visible as the star rotates, the value of $\langle |B| \rangle$ remains virtually constant as the star rotates (Landstreet et al., 2017).

Exploring another possibility, if the magnetic emission region on GD 356 extends over much or all of the stellar surface, then the low-amplitude of variation of $\langle B_z \rangle$ suggests that the field structure is close to, but not precisely, axisymmetric about the rotation axis, and that the small value of $\langle B_z \rangle / \langle |B| \rangle$ merely reflects the variation in local field vector inclination over the visible stellar surface. One might suspect that the rotational axis makes a relatively small angle (say of the order of 30°) to the line of sight, as it seems probable that field cancellation over the surface in such a global model would reduce the mean projected field to a fairly small fraction of the value of the mean field modulus.

Despite all this, any interpretation of the nearly constant mean longitudinal field measurements implicitly assumes a production model for the line polarisation in the emission region. This model supposes that the polarisation in the line is produced essentially only in the emission region of inverted temperature and source function gradients, without any significant contribution from the underlying photosphere with a normal, negative temperature gradient. The spectroscopy of J1252 shows that for at least one DAHe star, the flux from the emission line region adds to flux emerging from a surrounding or underlying hydrogen-rich photosphere, producing absorption lines that seem to be broadened by a magnetic field comparable in strength to that in the emission line region (Reding et al., 2020).

If a region of Balmer absorption lies beneath the emission line region of GD 356, and shares the local magnetic field, the emergent flux from that absorption region into the overlying emission region will probably already carry a polarisation signature qualitatively like that of the emission lines, but of opposite sign. This should then be further polarised by the overlying emission, but the net emergent polarisation may be rather different than would emerge from the emission line region alone. This might, for example, reduce the net level of polarisation in σ components, and lead to deduced values of $\langle B_z \rangle$ that are substantially smaller than the physically correct values.

2.5.3 Challenges to unipolar inductor model

GD 356 has defied conventional models and here the reasons are briefly described. Because the emission cannot arise from the cool photosphere with a negative temperature gradient, a heating mechanism is required. Perhaps the most conventional model would be accretion from a mass-transferring companion, but ultraviolet through mid-infrared photometry rules out all unevolved companions down to $12\,M_{Jup}$ (Wickramasinghe et al., 2010). Furthermore, both radio observations and a deep X-ray pointing provide strong constraints on accretion from the interstellar medium and photospheric heating by a stellar corona,

where the latter observations set an upper limit of $L_X < 6 \times 10^{25}$ erg s⁻¹, nearly two orders of magnitude lower than the Balmer line emission luminosity (Greenstein & McCarthy, 1985; Ferrario et al., 1997a; Weisskopf et al., 2007).

Owing to these empirical challenges, the unipolar inductor model has been applied to GD 356 (Li et al., 1998). In this picture, the surface hot spot is electromagnetically induced by the orbital motion of a conducting planet through the stellar magnetosphere, similar to the Jupiter-Io system (Piddington & Drake, 1968; Goldreich & Lynden-Bell, 1969). An exoplanet in a sufficiently close orbit can induce a current loop between itself and the star, resulting in ohmic dissipation and heating in the stellar atmosphere. In principle, the induced potential and dissipated power could be significantly higher than in the Jupiter-Io system. From an observational point of view, the line of sight to the heated region is modulated by stellar rotation, and an additional displacement on the stellar surface due to the motion of the planet through the magnetosphere. The displacement of the spot should be periodic on the orbital period, and possibly further modulated by misalignment of stellar magnetic, rotational, and planetary orbital axes.

Despite the attractions of this model, especially in light of the ubiquitous nature of planetary systems orbiting white dwarfs, there are at least two fundamental flaws when applied to isolated stars such as GD 356. The first and perhaps less critical problem with the unipolar inductor is that there may be no actual magnetosphere associated with an isolated magnetic white dwarf. That is, there is no a priori reason to expect available ions to form a current sheet and thus enable the inductor to work in the first place. Li et al. (1998) speculate that the ions may be provided either by the interstellar or interplanetary medium, but that is far from certain, especially as the three published DAHe stars are all within the Local Bubble where little interstellar material is to be found. Even if present, it is not clear that passing interstellar material would be ionised and then incorporated into a stellar magnetosphere. While it may be attractive to invoke an interplanetary medium, it is worth pointing out that the heliosphere and some planetary magnetospheres (e.g. Mercury, Earth) are powered by plasma from the solar wind. Thus for the unipolar inductor to work at a white dwarf, it requires either a planet be *conducting and a source of ions*, or else these two requirements must be met independently.

The second and most damaging problem for the unipolar inductor when considered on an individual basis is stellar rotation, and within this framework there are two distinct ways in which the model can break down. In order for a steady DC circuit to be established (and form a single, localised spot) the Alfvén travel time between the planet and star has to be small compared to the time it takes the magnetic field lines (flux tube) to rotate past the companion (Goldreich & Lynden-Bell, 1969). This is a point of failure in the Jupiter-Io system due to the rapid planetary rotation, and this results in the appearance of multiple spots and leading and trailing emission regions on either side of the main Io spot (Bonfond 2013 and references therein). The Alfvén speed is expected to be substantially larger for GD 356 because of its large magnetic moment (Willes & Wu, 2005), and for an Earth-sized planet orbiting just outside the Roche limit at $1 R_{\odot}$, a flux tube requires only 20 s to rotate past the entire planet diameter in this best case scenario. In the model outlined by Li et al. (1998), where the planet is in a wider orbit of 10 h then the flux tube sweeps past the planet in just over 4 s. Assuming a 13 MG dipole field (admittedly uncertain, see previous Section) with a magnetospheric plasma of the same number density as the Io torus, an Alfvén speed faster than light is obtained, and the Alfvén mode practically becomes an electromagnetic mode, travelling at the speed of light. The resulting, round trip Alfvén

travel time between the white dwarf and the magnetically linked companion will be close to 15 s just outside the Roche limit, and over 30 s for the planetary orbit modelled by Li et al. (1998). Under such conditions, the system marginally fits the DC unipolar conditions if the companion is adequately large and orbits close to the Roche limit, but otherwise fails. Admittedly, a more thorough calculation would take into account the changing magnetic field along the flux tube, rather than assuming an unrealistic constant value for the field.

Another crucial factor in rapid rotation is the capacity of charge carriers to travel along the flux tube when subjected to substantial centrifugal forces. The equilibrium between the gradient of plasma pressure and the components of centrifugal force that are parallel to the magnetic field lines results in a characteristic plasma length scale, as described by (Caudal, 1986):

$$\ell = \sqrt{\frac{(Z+1)kT}{m_i\omega^2}} \tag{2.2}$$

where Z represents the ion charge, T is the plasma temperature, m_i denotes the ion mass, and ω is the rotational frequency. The efficiency of the resulting current carriers is indicated by the ratio of the plasma scale length ℓ to the orbital radius a of the conducting body. Considering a plasma temperature of $T \sim 10^5$ K and singly ionized sulfur in the Jupiter-Io system, the ratio ℓ/a is roughly 0.1. Consequently, it is suspected that the Io footprint in the aurora of Jupiter might be created by a hotter plasma source (perhaps with lighter ions) as the unipolar inductor is not very efficient. In this context, it is important to note that significant particle acceleration by Alfvén waves is needed based on the observed and modeled relationship between decametric radio emission and the auroral emission of the Io footprint (Zarka, 1998). Additionally, the intensity of the main auroral emission of Jupiter also demands substantial particle acceleration within the magnetospheric plasma to supply the necessary power input (Ray et al., 2009). Recent in situ plasma observations by the *Juno* spacecraft have revealed at least two distinct mechanisms for this particle acceleration (Mauk et al., 2018). Therefore, the study of this acceleration process, even at Jupiter, remains an active area of research.

The situation becomes worse when considering GD 356 and the DAHe stars, as their more rapid rotation results in even stronger centrifugal forces acting on ions. In a simplified scenario where the plasma consists solely of protons and electrons (hydrogen), with $T \sim 10^5$ K, and assuming a solid planet just outside the Roche limit at about $1\,\mathrm{R}_\odot$, the significantly higher rotation speed of GD 356 results in a ratio of $\ell/a \approx 0.06$, which is not favourable to efficient charge transport. However, the model becomes entirely untenable when applied to J1252, which rotates every 317 s according to (Reding et al., 2020)³, yielding a ratio of $\ell/a \approx 0.003$. As a result, it appears that the unipolar inductor cannot operate effectively in the presence of extreme differential rotation of the star relative to any planetary orbit, as these ratios are upper limits based on the closest possible orbiting planet. These ratios can be scaled by a factor of 43 when considering a pure electron plasma, although this aspect is beyond the scope of this work.

Lastly, the unipolar inductor predicts a single surface spot which is heated, rather than the conventional star spot which is cooler than the surrounding photosphere owing to the magnetic suppression of neighbouring convective cells. Thus the anti-phase behaviour of

³The rotational period was shown to be 634.6 s (Farihi et al., 2023), but this fact does not significantly affect the argument.

the light curve and emission-line strength in GD 356 and other DAHe stars does not appear consistent with this simple prediction. The results of the magnetic field measurements indicate the hot region is likely near one of the two *rotational* poles, and that is also not necessarily expected if the spot is due to an orbiting planetary body, where instead an unipolar-induced footprint should be near the *magnetic* pole, and these two may or may not coincide.

For all the above reasons, the unipolar inductor does not appear to be a successful description of these intriguing white dwarfs from either an observational or theoretical perspective. These calculations, however, do not rule out magnetic star-planet interactions as a whole; in particular, the Alfvén wing model might be more favorable under such conditions (Neubauer, 1998; Strugarek et al., 2015).

2.5.4 Intrinsic chromospheric activity in white dwarfs

It has been independently noted, as mentioned also in Gänsicke et al. (2020), that the three confirmed DAHe stars known at the time of publication all lie within a compact region of the HRD. The second example of this class is J1252, and with $B \approx 5$ MG and a 317 s photometric period, it was the fastest-rotating, isolated (magnetic) white dwarf at the time of writing (the current record holder is SDSS J221141.80+113604.4 (Kilic et al., 2021) with a rotational period of 70 s). As previously noted, at some photometric phases the emission lines from J1252 diminish to undetectable levels within complex H α and H β absorption features (Reding et al., 2020), but it is noteworthy that the light curve is consistent with a spot that is never fully out of view. The optical spectrum of the third example, J1219, is superficially similar to GD 356 but with $B \approx 18$ MG and a 15.3 h rotation period. All three stars exhibit light curves and emission line strengths consistent with anti-phase variation on the same period.

Also reported within the past year of the publication, there is a fourth DA star with Balmer emission lines, WD J041246.85+754942.3 (hereafter J0412; Tremblay et al. 2020). It is remarkably similar to the three known DAHe stars; it lies in precisely the same and compact region of the HRD, and it has rapid rotation. The *TESS* light curve of WD J0412+7549 shows photometric modulation with a period of 2.28910 \pm 0.00002 h with amplitude 2.58 \pm 0.07 per cent (Fig. 2.11) and thus potentially signals the presence of spectroscopic variability as seen in GD 356. This DAe white dwarf exhibits a much weaker emission feature in the core of an otherwise-normal looking H α absorption feature, and has an H β feature whose depth is likely diluted by emission. There are not yet any magnetic field constraints, nor significant changes in three observational epochs (Tremblay et al., 2020), but it is clearly worth further study.

From these four stars and their collective and highly similar properties, I hypothesise that the phenomenon of Balmer emission lines in these white dwarfs *is an intrinsic stellar property*. In Fig. 2.12 all four of these white dwarfs are plotted on an HRD, together with a sample of *Gaia* DR2-selected white dwarfs with $G < 19 \, \text{mag}$ (Gentile Fusillo et al., 2019). The position of these DA(H)e stars is truly remarkable, with $G = 13.23 \pm 0.20 \, \text{mag}$. Given their highly similar $G = 13.23 \pm 0.20 \, \text{mag}$. Given their highly similar $G = 13.23 \pm 0.20 \, \text{mag}$. Given their bolometric luminosities, suggesting they are all well within roughly a factor of $G = 13.23 \pm 0.20 \, \text{mag}$. This likelihood is substantiated by using the stellar parameter determinations based solely on *Gaia* bandpasses and distances (Gentile Fusillo et al., 2019), where mean stellar luminosities for these four

stars appear to be even more tightly correlated with $\langle \log(L_*/L_{\odot}) \rangle = -3.34 \pm 0.09.4$ Their collective properties of these stars include:

- 1. All four stars show emission lines of hydrogen, with no other species in emission.
- 2. All four stars are rotating faster than a typical white dwarf, and in three of four cases the rotation is rapid to extreme.
- 3. All four stars have a similar luminosity, approximated by $M_{\rm G}=13.2\,{\rm mag}$ and $\log(L_*/L_\odot)=-3.3$.
- 4. At least three of the stars are highly magnetic with field strengths on the order of MG.

An analysis of this magnitude-limited white dwarf population can provide a probability of finding all four stars in a narrowly-defined region of the HR diagram. For this analysis, in addition to the G < 19 mag requirement, the following conditions were imposed for white dwarfs to be drawn from the sample (Gentile Fusillo et al., 2019), in units of magnitude:

$$G_{abs} < 10: G_{abs} - 8 \times (G_{BP} - G_{RP}) > 10$$

 $10 < G_{abs} < 12: G_{abs} - 4 \times (G_{BP} - G_{RP}) > 10$
 $G_{abs} > 12: G_{abs} - 3 \times (G_{BP} - G_{RP}) > 10.5$ (2.3)

These cuts effectively remove a portion of white dwarf-main sequence systems, extremely-low-mass white dwarfs and cataclysmic variables. The resulting distribution is shown in Fig. 2.12.

Although such a small number of the DA(H)e stars prohibit meaningful statistical investigation, some inference can be made. Within a quadrangle where each vertex is one of the four emitting stars, there are 0.8 per cent of all sources. Alternatively, by converting the individual objects into a continuous distribution using kernel density estimation, and sampling it via a Monte Carlo method, it can be shown that such close clustering is rarely achieved. Only about 1.2 per cent of four randomly sampled objects end up within $\Delta(G_{\rm BP}-G_{\rm RP})<0.31$ and $\Delta G_{\rm abs}<0.84$ of each other anywhere on the presented HR diagram. These Δ values correspond to *twice the maximum spread* of $G_{\rm BP}-G_{\rm RP}$ and $G_{\rm abs}$ of the four DA(H)e white dwarfs. Even though these methods cannot provide a robust statistical characterisation, it should be nonetheless clear that extrinsic sources are highly unlikely to be the cause of their observed properties.

This fact suggests that these four stars each have an intrinsically activated chromosphere, one that appears dependent on rotation, magnetism, and temperature or luminosity. There are three independent reasons that suggest the observational phenomena are intrinsic. First, as detailed above, if the source of emission were extrinsic, there would be only a tiny chance of finding all four stars in the same position on the HRD. Second, if the emission were to become detectable only once these stars become sufficiently faint to unmask the chromosphere, then they would be free to populate the larger portion of the HRD. In contrast, the position of the stars in the HRD and their highly similar luminosities makes it clear that these stars occupy only a narrow range of phase space.

 $^{^4}$ CL Oct, a rapidly rotating DAH white dwarf, has $\log(L_*/L_\odot) = -2.00$ and is more than $20 \times$ intrinsically brighter than the DAHe stars, but may eventually enter an emission phase later in its evolution.

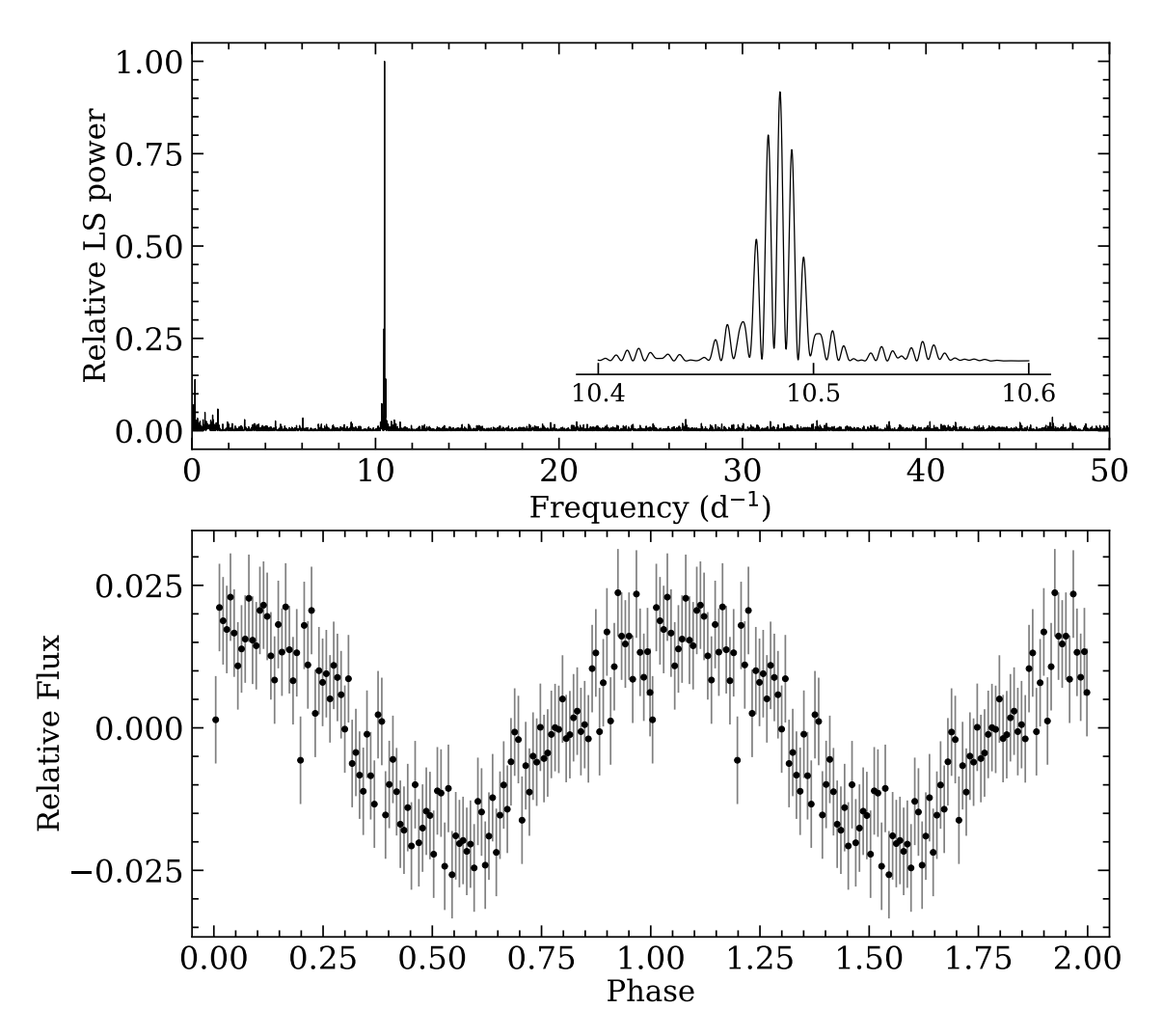


Figure 2.11: *Upper panel*: Normalised LS periodogram of *TESS* photometry of J0412. The peak value corresponds to $10.48437(7) \, d^{-1}$. The insert shows a zoomed in version of the periodogram. *Lower panel*: *TESS* photometry folded on the peak period. Each point is an average of 400 recordings. Phase = 0 corresponds to the photometric maximum at $T_{\rm BJD} = 2458816.031(5) \, d$.

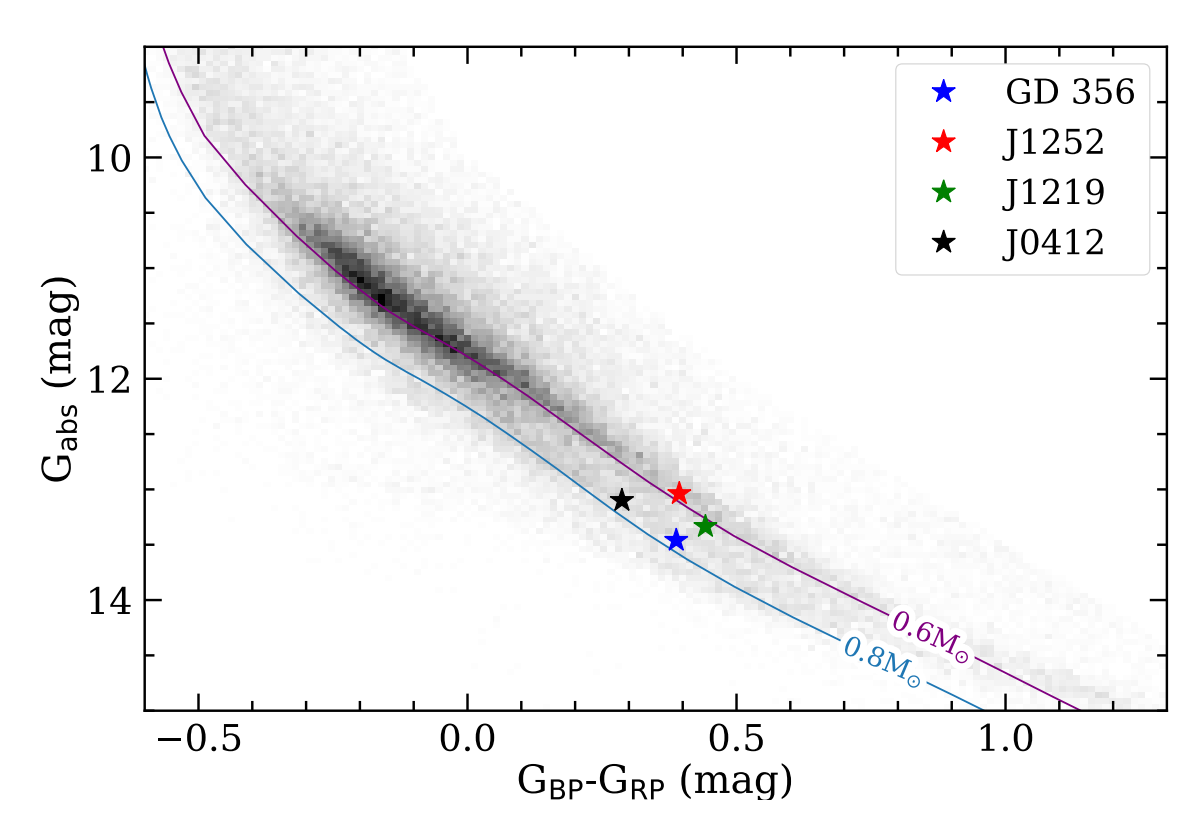


Figure 2.12: Magnitude-limited Hertzsprung-Russell diagram of *Gaia*-selected white dwarfs with G < 19 mag (Gentile Fusillo et al., 2019). Two cooling tracks are shown for pure-hydrogen atmosphere white dwarfs with 0.6 and 0.8 M_{\odot} . By defining a rectangular region with vertices corresponding to the positions of the four known DA(H)e stars, it is estimated that 0.8 per cent of white dwarfs are enclosed in this region. Therefore, such close clustering of the four objects is highly unlikely to be accidental.

Third, and something that has not yet been noted in the literature, an extrinsic source of matter or ions would be reflected in the composition of the accreted or conducted mass, and also in the chromospheric emission line species (e.g. CVs, convective stars like the Sun). Instead, these stars emit only in Balmer lines with no other species apparent. An interesting counter-example to the DA(H)e stars is the singular case of PG 1225–079, where the modest Ca II H and K emission features seen in a deep and high-resolution spectrum (Klein et al., 2011). The fact that Ca is present in the photosphere together with other heavy elements is well-understood as atmospheric pollution via the accretion of circumstellar, planetary material (Farihi, 2016), but in the case of the DA(H)e stars, the lack of other species argues against (planetary) accretion. Therefore, viewed as an intrinsic phenomenon, the Balmer emission lines arise in DAHe stars because their atmospheres are composed of hydrogen. Thus, the previous inference of a helium atmosphere for GD 356, based on optical through near-infrared photometry (Bergeron et al., 2001), is suspect. It is well known that highly magnetic white dwarfs have distorted spectral energy distributions, where sometimes not even a single temperature can be confidently assigned (Ferrario et al., 2015b).

It is tempting to speculate a bit further based on this potentially new insight into the white dwarf evolution, and include the only other two white dwarfs suspected to have chromospheric emission; the massive DQe stars G227-5 and G35-26. Both stars have emission lines seen only in the ultraviolet, where only the heavy elements C and O are seen towards both stars, with further lines of N (plus Mg and Si possibly) observed from G35-36 (Provencal et al., 2005). If the DAHe stars are emitting from intrinsic chromospheres and all have hydrogen atmospheres, it is tempting to co-identify these two as non-DA counterparts. Historically, DQ stars were modelled with helium atmospheres (e.g. Bues 1973; Grenfell 1974; Wegner & Yackovich 1984), but there is now a significant body of evidence that the warmer and hot DQ stars have little or no helium, and are instead bare stellar cores that just avoided detonation as supernovae, and thus have significant carbon and oxygen in their atmospheres (Dufour et al., 2007a, 2008). In this picture, the observed emission lines from G227-5 and G35-26 are intrinsic and reflect the composition of the atmosphere, and thus the composition of the outer layers of a stellar core.

Furthermore, the hot DQ stars in particular appear consistent with stellar mergers (Dunlap & Clemens, 2015; Cheng et al., 2019), which together with the above paints them as failed type Ia supernovae. But in common with the DAHe stars, many hot DQ stars are rapid rotators (Williams et al., 2016), magnetic (Dufour et al., 2010, 2013), and if so then they share multiple properties. The difference in the stellar parameters of these DQe and DAHe stars, such as luminosity, thus, may be down to their stellar structure and in particular their atmospheric compositions. While speculative, there may be a cluster of DQ(H)e stars awaiting to be found, but may require ultraviolet searches for emission lines. The two known DQe stars have nearly identical $M_G = 12.8$ mag, which is not too dissimilar to the DAHe stars, but total luminosities that are roughly an order of magnitude brighter and not tightly clustered based on *Gaia*-derived stellar parameters. Nevertheless, it is an intriguing prospect that intrinsic chromospheres may be present in white dwarfs, and in different regions of the HR diagram based on structure and composition.

In this picture of intrinsic chromospheres for DAHe stars, the following predictions and corollaries result:

⁵http://www.astro.umontreal.ca/~bergeron/CoolingModels/

- 1. J0412 will exhibit modulation of the emission features on the 2.29 h rotation period, but in anti-phase.
- 2. J0412 should be magnetic at a detectable level, and spectropolarimetry is ideal to test for this.
- 3. Periodic signals consistent with orbiting planets will not be forthcoming in continued photometric studies of DAHe stars.
- 4. Only species consistent with the stellar atmosphere will be found in emission, regardless of observational sensitivity.
- 5. All four DAHe stars have hydrogen-rich atmospheres, including GD 356.
- 6. A search of this region of the HRD will find further potential examples.

In closing, while this hypothesis does not invoke closely orbiting planetary bodies or second generation planets, it does not exclude them. If it is correct that the emission mechanism is intrinsic, then any system hosting planetary material can have potential interactions. For example, if and when a polluted white dwarf passes through this region of the HRD, and if it has a favourable magnetic field and rotation, it would be expected to exhibit emission features that reflect the surface compositions. Given that at least 1/3 to 1/2 of isolated white dwarfs host planetary systems (Koester et al., 2014), and thus if the unipolar inductor is not applicable, it does not put any significant dent in the number of evolved planetary systems to characterise in the near future.

2.6 Conclusions

This chapter reports periodic variations in the photometry and spectropolarimetry of GD 356, which are linked to the rotational period. The previously published rotation period of 1.93 h is in excellent agreement with the latest photometric data. The emission strength and the average magnetic field varies over the rotation, with the emission persisting at all rotational phases. An anti-phase relation between the relative strength of the emission and broad-band photometry has been demonstrated by the new data, and likely present in all known DAHe white dwarfs. By analysing the semi-amplitudes that would be produced from the observed emission variation, it has been shown that the photometric variability must be predominantly due to the continuum flux variation. Also noted are potential morphological dissimilarities in the emission profiles at the same rotational phase in observations separated by ten months, and although the evidence is weak it could be indicative of changes in the emission region. Importantly, *TESS* and LT light curve analysis highlighted no statistically significant photometric modulation or additional signals other than the known spin period, and thus no evidence for a unipolar inductor caused by an orbiting and conducting planetary body.

In the light of the unipolar inductor model, the absence of secondary signals in the photometry does not provide any support to the theory. Moreover, considering the three recently discovered white dwarfs that share a plethora of properties with GD 356, the likely mechanism behind chromospheric emission appears to be intrinsic. According to an existing model, acoustic waves generated by atmospheric oscillations can potentially

trigger chromospheric activity with the predicted luminosity change of less than one percent for a typical white dwarf surface gravity (Musielak et al., 2005). Although speculative, because GD 356 is magnetic, perhaps the temperature inversion is the result of thermal pressure overcoming magnetic pressure, but there are currently no such theoretical models.

Despite all the data accumulated to date, there is not yet a complete and consistent picture of such a potential mechanism. However, there are several testable predictions that could be used to evaluate the intrinsic hypothesis for the emission mechanism, and potentially provide additional DAHe candidates. Further study of this emerging population of white dwarfs will likely shed light on physics behind possible chromospheric activity in these magnetic stars.

Chapter 3

Reflections on GD 356

This chapter is *not* based on any previously published paper, and all the results presented here are solely my own. Since the analysis of GD 356 and the identification of the DAHe class, there have been significant advancements, necessitating a revisit to this work. This chapter aims to offer an in-depth follow-up discussion on white dwarfs with Balmer emission lines, exploring the latest intriguing developments in this field and deepening our understanding of these celestial objects. I will also briefly touch upon some of the current work underway.

3.1 DAHe predictions

Currently, the number of identified DAHe stars has grown substantially from the initial four to 30 published stars, with an additional 14 candidates (Reding et al., 2023; Manser et al., 2023; Farihi et al., 2023; Elms et al., 2023). Utilising the proposed DAHe region identified in Walters et al. (2021) and quantified in Manser et al. (2023) and their estimated occurrence rate of approximately 1.5 per cent of the white dwarf population, combined with the Gaia EDR3 white dwarf catalogue (Gentile Fusillo et al., 2019), it can be inferred that the population of DAHe stars with $G < 20 \,\mathrm{mag}$ is just below 400. All known and candidate DAHe stars are depicted on the HRD in Figure 3.1. A white dwarf with $M = 0.8 \,\mathrm{M}_{\odot}$, representative of the typical DAHe mass, spends about 2 Gyr of cooling time in the proposed emitting region. The cumulative distribution of DAHe stars by volume is illustrated in Figure 3.2. Assuming a uniform spatial distribution of DAHe stars, there is a lower limit of 3×10^{-5} of these white dwarfs per cubic parsec.

Given the significant increase in identified members of this class and the ongoing potential to discover more, it is pertinent to reevaluate the predictions outlined in Chapter 2. The initial prediction asserted that all stars of this type would exclusively show hydrogen emission lines, with no signs of emission from other atomic species. This prediction has held true, as no other atomic species have been detected in the observed spectra. However, it is crucial to note that spectral observations have mostly been confined to optical spectra, ranging from $3600 - 9824 \,\text{Å}$ for the DESI instrument (DESI Collaboration et al., 2022) and $3800 - 9200 \,\text{Å}$ for the SDSS instrument (York et al., 2000).

The second prediction pertains to the fast rotation rates exhibited by DAHe stars in comparison to typical white dwarfs. Investigating the distribution of magnetic white dwarf rotation rates remains an active field of research, with recent advancements expected from

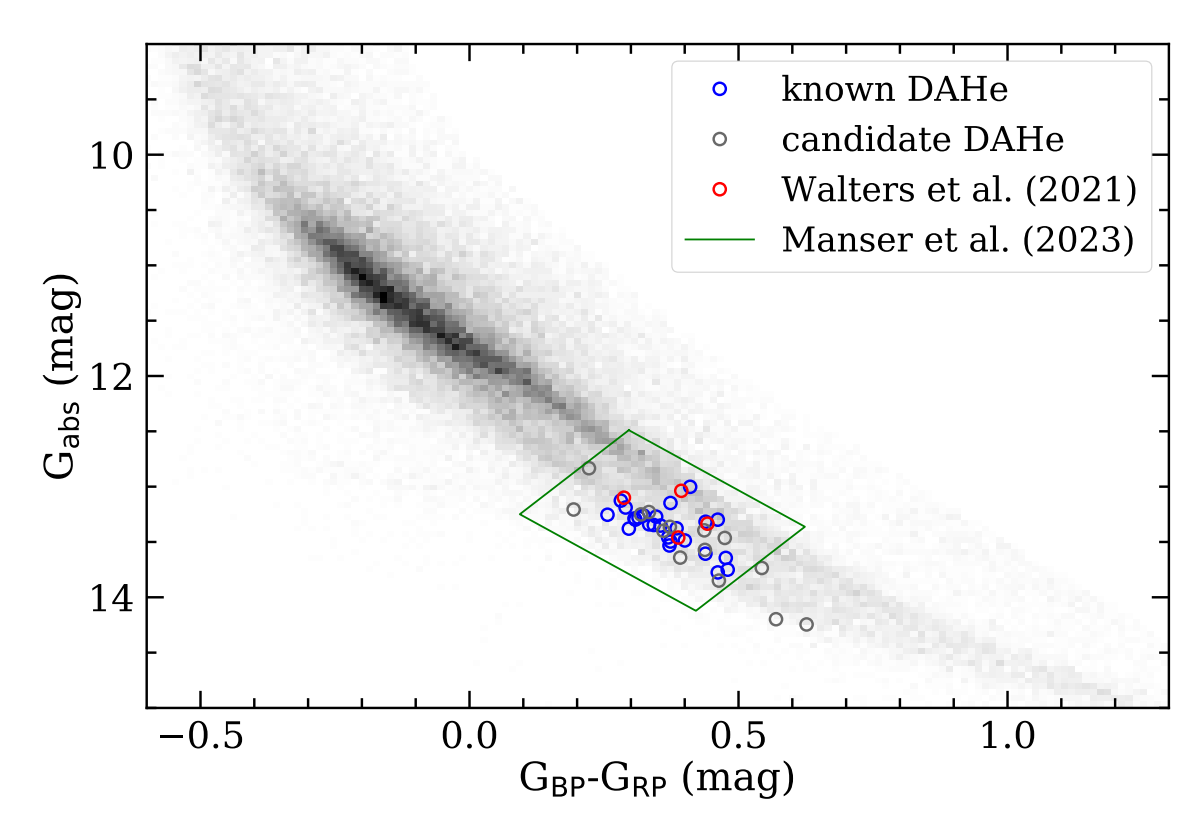


Figure 3.1: Colour-magnitude diagram of *Gaia*-selected white dwarfs with $G < 19 \,\mathrm{mag}$ (Gentile Fusillo et al., 2019). The DAHe stars previously reported in Walters et al. (2021) are shown in red, representing our knowledge of this class in 2021. All of the spectroscopically identified members of this class to date are shown in blue. Candidate stars of this type from Manser et al. (2023) are shown in grey, along with the proposed region boundaries encompassing the class in green.

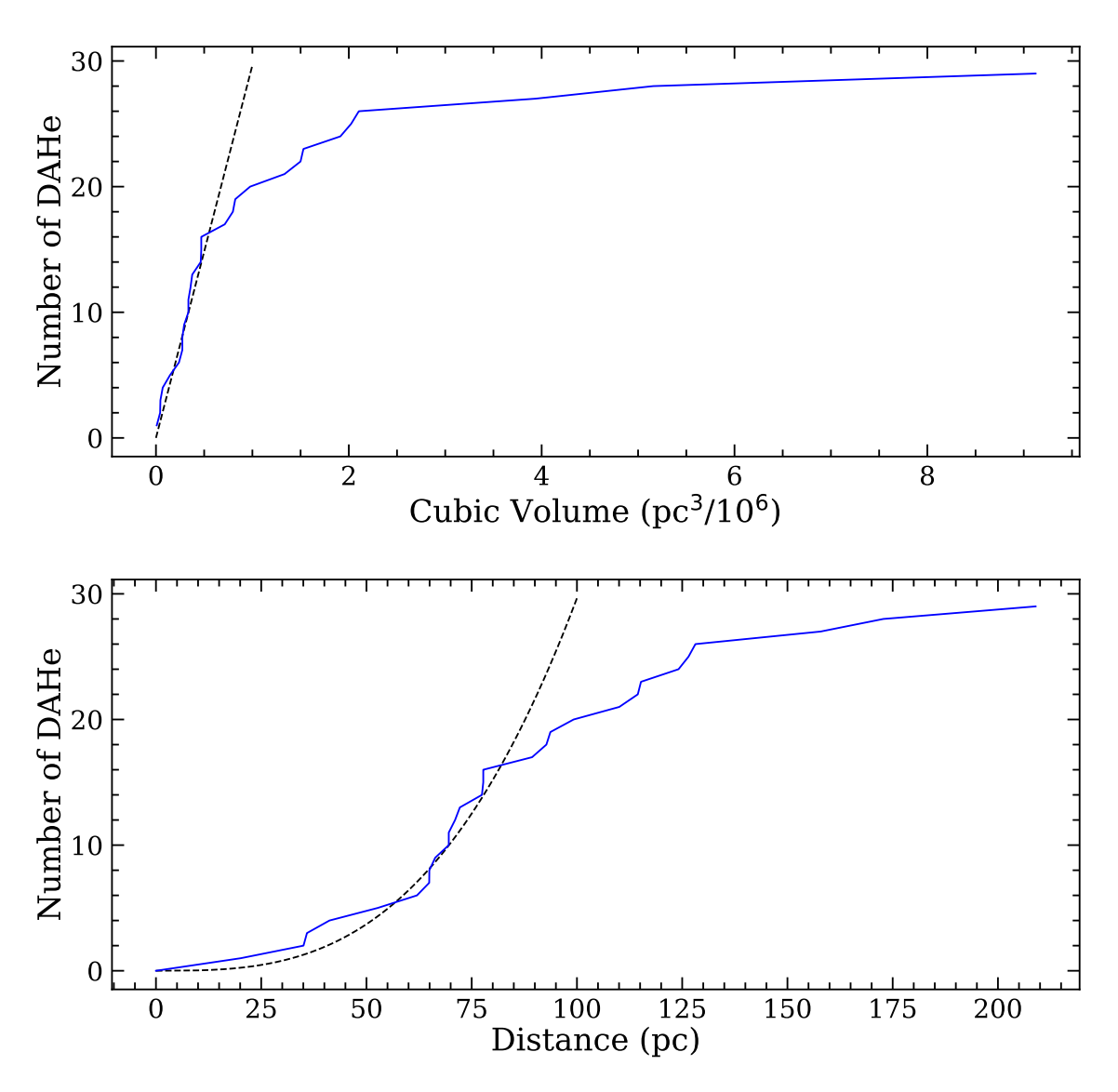


Figure 3.2: *Upper panel:* The cumulative distribution of the known DAHe stars as a function of cubic volume. By leveraging the assumption that this class is uniformly distributed in volume it is possible to model the linear part of the distribution to obtain lower limits on their space density, shown as a dashed black line. The distribution is approximately linear for objects within 80 pc. *Lower panel:* The same as above but transformed into a distribution as a function of distance by taking a cubic root of the volume.

comprehensive full-sky photometric surveys such as ZTF, TESS, and Gaia. Rotation rates of isolated magnetic white dwarfs range from a few hundred seconds to practically non-rotating ($P \approx 100\,\mathrm{yr}$; Ferrario & Wickramasinghe 2005). However, determining rotation rates in isolated, non-magnetic white dwarfs can be challenging. These stars are spotless and the rotational broadening of their lines is insignificant compared to pressure broadening (Kawaler, 2004). To streamline the discussion, I will solely consider isolated magnetic white dwarfs, as the majority of DAe stars appear to possess significant magnetic fields.

In their study, Ferrario & Wickramasinghe (2005) identified three clusters of magnetic white dwarfs based on their rotation: fast rotators ($P_{\text{rot}} \approx 700 \,\text{s}$), modest rotators with periods ranging from hours to days, and slow rotators ($P_{\text{rot}} > 50 \text{ yr}$). The average determined rotational rate for DAHe stars among all reported periods is 5 hours. Nevertheless, it is worth noting that only about half of these stars have had their periods estimated. Given that estimating extremely long periods might be especially challenging (leading to observational bias), it is worth questioning whether some DAHe stars have rotational periods that last several years. To date, the answer to this question appears to be negative. All of the reported DAHe stars without a determined rotational period are faint (G > 17.4 mag), rendering them difficult targets for high-cadence surveys like TESS. The slowest rotating emitting magnetic white dwarf, which also appears to be one of the most magnetic, has a reported period of 34.3 h (Manser et al., 2023). Thus, the link between fast rotators and DAHe class members appears to hold so far, potentially hinting at the conditions needed for a magnetic white dwarf to become emitting compared to DAH in the same region of HRD. However, the full picture is incomplete since some magnetic, rapidly rotating white dwarfs in the right area of the HRD do not show detectable emission (Tremblay et al., 2020).

The next observation made in Chapter 2 is that the DAHe stars appear to have similar luminosities, and their clustering on the HRD was used as evidence of emission being of intrinsic origin. This observation has withstood scrutiny and continues to serve as a crucial element in the quest for magnetic stars displaying emission. In their work, Manser et al. (2023) visually identified DAHe objects from DESI EDR and DR1 white dwarf spectra, as well as SDSS DC-classified white dwarfs. Based on their identifications, the authors proposed HRD constraints that define the DAHe region (shown in Figure 3.1). It is important to emphasise that the initial search was unrestricted to the region or its proximity (Cooper et al., 2023). Therefore there is scant evidence to suggest that DAHe stars also populate an additional region within the HRD beyond the already outlined cluster.

Another prediction noted that 3/4 of the known members of the class at the time are magnetic at a detectable level, and thus magnetism must play a role in the nature of these stars. Now that 30 objects are known, all of them appear strongly magnetic except for the previously discussed in Chapter 2 J0412 and the newly discovered DAe WDJ165335.21–100116.33 (J1653; O'Brien et al. 2023). The average magnetic field strength for the class is about 30 MG and forms a relatively symmetric distribution of values in logarithmic space (lower panel of Figure 3.3). The interesting thing to note is that the field strength distribution appears distinct to non-emitting magnetic white dwarfs in the region of the colour-magnitude diagram. There is only a handful of DAHe with field strength below 10 MG. It is unclear whether perhaps it is more challenging to sustain the emitting mechanism at lowfield strengths. However, there is definitely an observational bias in identifying such stars. Two such examples are J0412 and J1653 for which follow-up

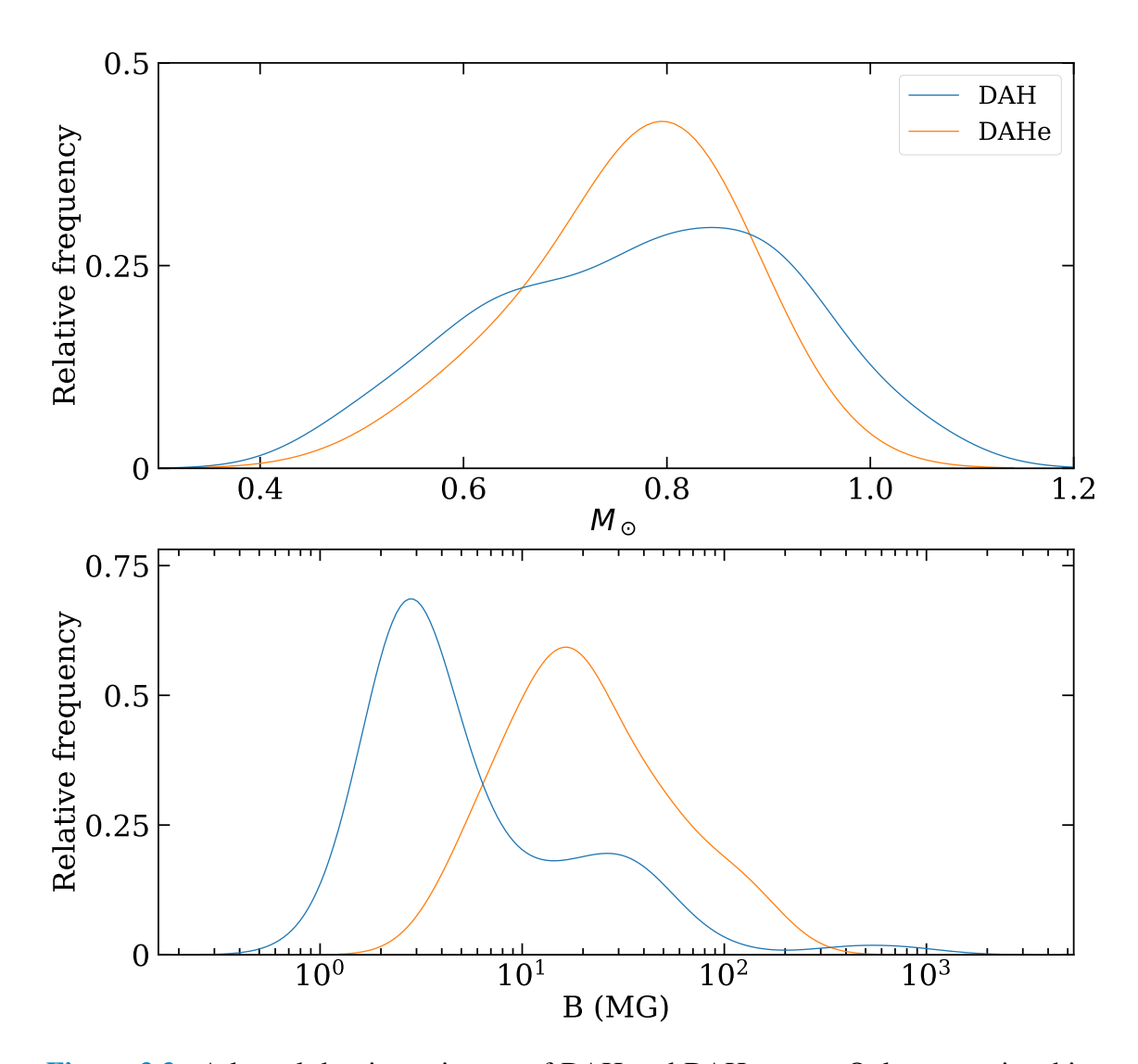


Figure 3.3: A kernel density estimates of DAH and DAHe stars. Only magnetic white dwarfs within the DAHe region were considered (Manser et al., 2023). The non-emitting magnetic white dwarfs were sourced from the SDSS catalogue (Amorim et al., 2023). Out of the total 804 sources in the catalogue, 99 are within the emitting region. *Upper panel*: Mass distribution. *Lower panel*: Mean magnetic field strength. Since there is currently no magnetic field estimate for J0412 and J1653 they were amended from the lower panel. Although the number of stars is small in both samples, the magnetic field distributions appear distinct.

spectroscopy could not identify Zeeman splitting of the emission lines, thus claiming a limit of $B < 0.05 \,\mathrm{MG}$ (Elms et al., 2023). Although spectropolarimetry was not acquired for these targets, their magnetic field strengths are notably below a representative DAHe value. However, this does not imply that the two stars are non-magnetic.

The upper panel of Figure 3.3 shows the mass distribution for emitting and non-emitting magnetic white dwarfs. In their crucial work on the nature of magnetism in white dwarfs, Bagnulo & Landstreet (2022) identified two distinct populations based on mass. Magnetic white dwarfs with mass below $0.75\,M_\odot$ with low field strengths that are thought to be products of single-star evolution and more massive white dwarfs with $B\approx 100\,MG$ which are almost certainly merger products.

Crystallization is thought to be the source of magnetism in lower-mass magnetic dwarfs with fields slowly growing in the first 2-3 Gyr of cooling. Crystallization is an attractive hypothesis given its internal nature for the magnetic field formation. As discussed previously, the emission mechanism in DAHe is also intrinsic and requires an internal trigger to switch on and then switch off the emission during further cooling. However, as can be seen in the figure, DAHe stars tend to be more massive than $0.75\,\mathrm{M}_\odot$ making them more consistent with the merger population.

Perhaps more importantly, the DAHe class is also in the region of the HRD that precedes crystallization (Tremblay et al., 2019). Although crystallization depends heavily on internal composition which is admittedly uncertain, Elms et al. (2023) showed that the process of crystallization has not started for members of this class for a range of possible compositions. There is also an expected delay between the onset of crystallization and the emergence of a surface magnetic field from a crystallisation dynamo (Ginzburg et al., 2022).

Based on these observations and the current knowledge of crystallization, this physical process appears to be an unlikely field-forming mechanism for this class of white dwarf. However, caution must be exercised in this case, not only because of the limited understanding of magnetic field formation in degenerate stars, but also because both kernel density estimates shown in Figure 3.3 rely on small numbers.

3.2 My continuation of the research

3.2.1 *Gaia*

In 2022, the *Gaia* Data Release 3 (DR3) took place, including tens of new data products. Two are worth outlining: the low-resolution ($R \approx 50$) BP/RP spectra and the epoch photometry. Spectra are generally available for objects with G < 17.65 mag. However, spectroscopic data could be available for white dwarfs as faint as $G \sim 21.4$ mag. Each spectrum covers a range of 3300 to 10500 Å and is a calibrated combination of the *Gaia* blue (BP) and red photometers (RP) (de Angeli et al., 2023; Montegriffo et al., 2023), although sometimes these spectra are referred to as the XP spectra (Gaia Collaboration et al., 2023). The target list included a catalogue of about 100 000 white dwarf candidates (Gaia Collaboration et al., 2022). The second data product is the epoch photometry for 11.8 million sources. From the photometry, a variability analysis was also performed by the *Gaia* collaboration that introduced a variability flag for variable sources. Since at the time, there were no estimates for the DAHe occurrence rate, BP/RP spectra offered a tantalising possibility of searching for additional candidates. In addition, epoch photometry would

provide almost simultaneous measurements in the G, BP, and RP bands that would be useful for variability amplitude analysis.

Unfortunately, the spectroscopic interpretation of BP/RP spectra proved challenging due to their low resolution and S/N (Vincent et al., 2023). DAHe stars are also a challenging target for this type of spectroscopy since due to the initially unknown magnetic field strength it is impossible to know the exact location of the emission. Even with moderately higher resolution spectra, they can be challenging to distinguish in some cases from DC white dwarfs. However, with BP/RP spectra, even DA stars with Balmer absorption lines can be tricky to distinguish. As an example, Figure 3.4 shows the GD 356 optical spectrum from the WHT and its corresponding BP/RP spectrum. It also shows a DA white dwarf LHS 1038 that is approximately similar to GD 356 in its G magnitude, $T_{\rm eff}$, and $\log g$ $(14.2 \text{ mag}, 6400 \text{ K}, \text{ and } 8.2 \text{ cm s}^{-2} \text{ against } 15.0 \text{ mag}, 7700 \text{ K}, \text{ and } 8.3 \text{ cm s}^{-2} \text{ for LHS } 1038 \text{ ms}^{-2})$ and GD 356, respectively)¹. The figure demonstrates that even for such relatively bright sources, identification can be challenging. Lastly, out of the 30 DAHe sources, only GD 356 has a BP/RP spectrum (mostly due to the faintness of other targets) making it difficult to distinguish Gaia BP/RP features of this class from other white dwarf spectra. Perhaps in future analysis, some white dwarf BP/RP spectra in the DAHe region could be automatically flagged that exhibit above-average uncertainty in the Balmer line vicinity, since emission lines are expected to be variable both in intensity and in precise wavelength (due to non-uniform magnetic field topology). Such uncertainty analysis could yield a few additional DAHe candidates, especially with epoch BP/RP spectra set to be released in Data Release 4 in 2025.

Regarding Gaia epoch photometry, the median number of measurements of G, BP, and RP is approximately 40 for each filter (Eyer et al., 2022). Due to the way the Gaia variability pipeline operates, the smallest number of valid measurements is five in the G band. Out of the 30 reported DAHe, six have epoch photometry. By itself, Gaia epoch photometry is not as impressive as some of the higher cadence surveys like ZTF or TESS but in combination with those, it can be rather powerful. In a publication by Farihi et al. (2023), it was noted that once the amplitude of variability of DAHe was standardised by dividing the amplitude from each photometric filter by the amplitude from the ZTF-g filter, a somewhat consistent set of ratios can be seen, apparently shared by all of the DAHe stars studied in this way. In other words, there is a strong wavelength-amplitude dependence that appears consistent for the members of the class, and can be standardised. Hence, one can envision a way to identify further candidates by first finding variable white dwarfs in the DAHe region and then utilising TESS, ZTF and Gaia photometry to estimate those photometric amplitude ratios and find promising candidates. In this case, the three bands of Gaia epoch photometry becomes a significant advantage. Such a method would be magnitude limited but benefits from the public availability of the data. In the future, the LSST, which will operate with ugrizy filters (LSST Science Collaboration et al., 2009), could be highly successful if the above method is validated.

Lastly, it could be interesting to explore the *Gaia* variability flag, in particular the distribution of flagged white dwarfs in the DAHe region. Figure 3.5 shows *Gaia* and *TESS* variable sources on the white dwarf cooling sequence. *TESS* sources were identified as variable if they exhibited a LS false alarm probability below 0.01 (Greiss et al., 2014).

 $^{^{1}}$ LHS 1038 is weakly magnetic at $B = 0.25 \,\mathrm{MG}$ (Bagnulo & Landstreet, 2021) but does not show sufficient Zeeman splitting to be visually identifiable as such from its displayed optical spectrum due to low resolution.

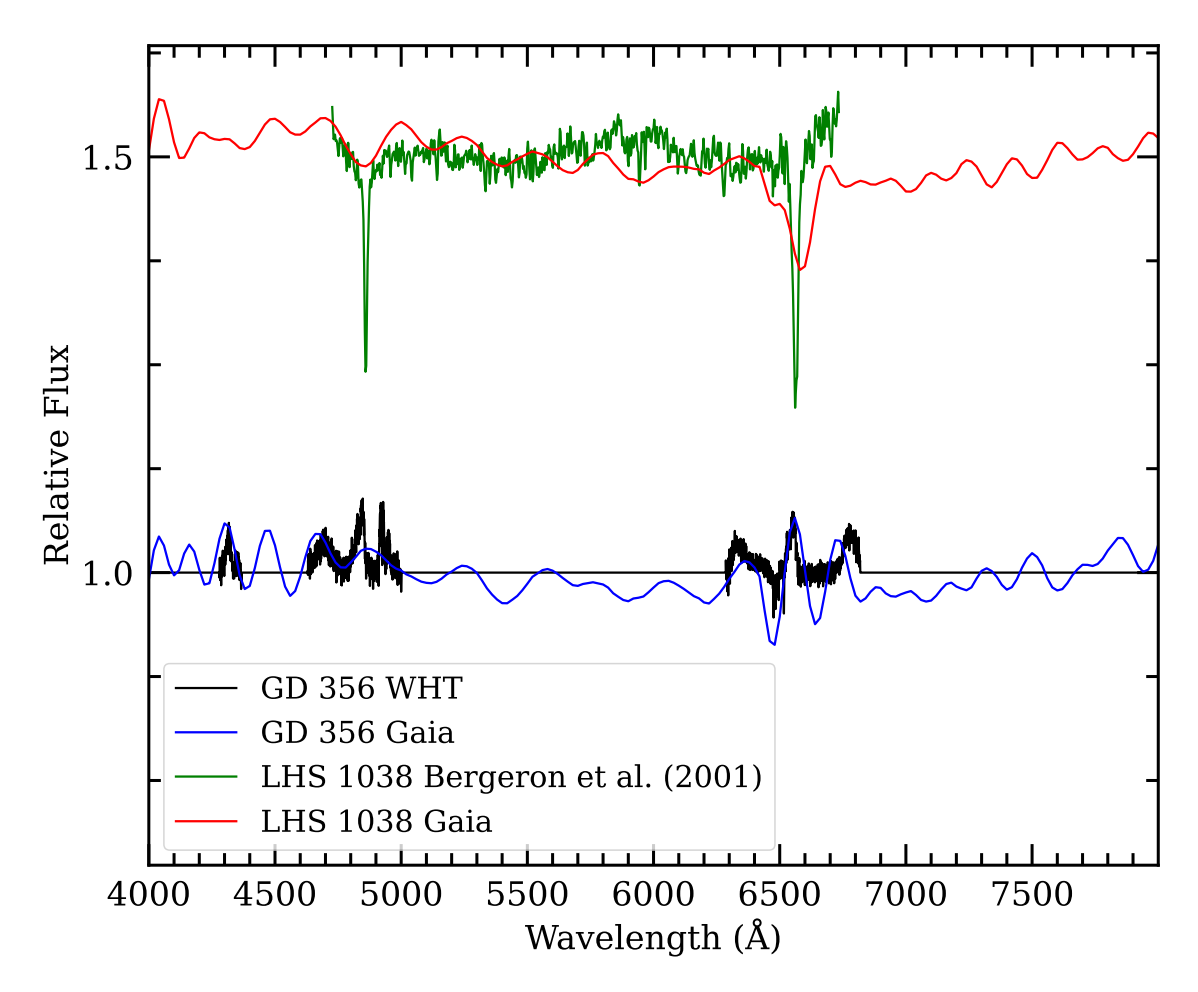


Figure 3.4: A comparison plot between typical low resolution optical spectra ($R \sim 1000$) contrasted to *Gaia* BP/RP spectra. The lower spectra show GD 356 Balmer features from WHT and *Gaia*. The upper spectra belong to LHS 1038 (Bergeron et al., 2001), a representative DA white dwarf with similar intrinsic parameters and G magnitude to GD 356. Although the H α absorption can be distinguished in LHS 1038, the figure demonstrates that identification of DAHe stars from BP/RP spectra can be challenging even for the brightest candidates.

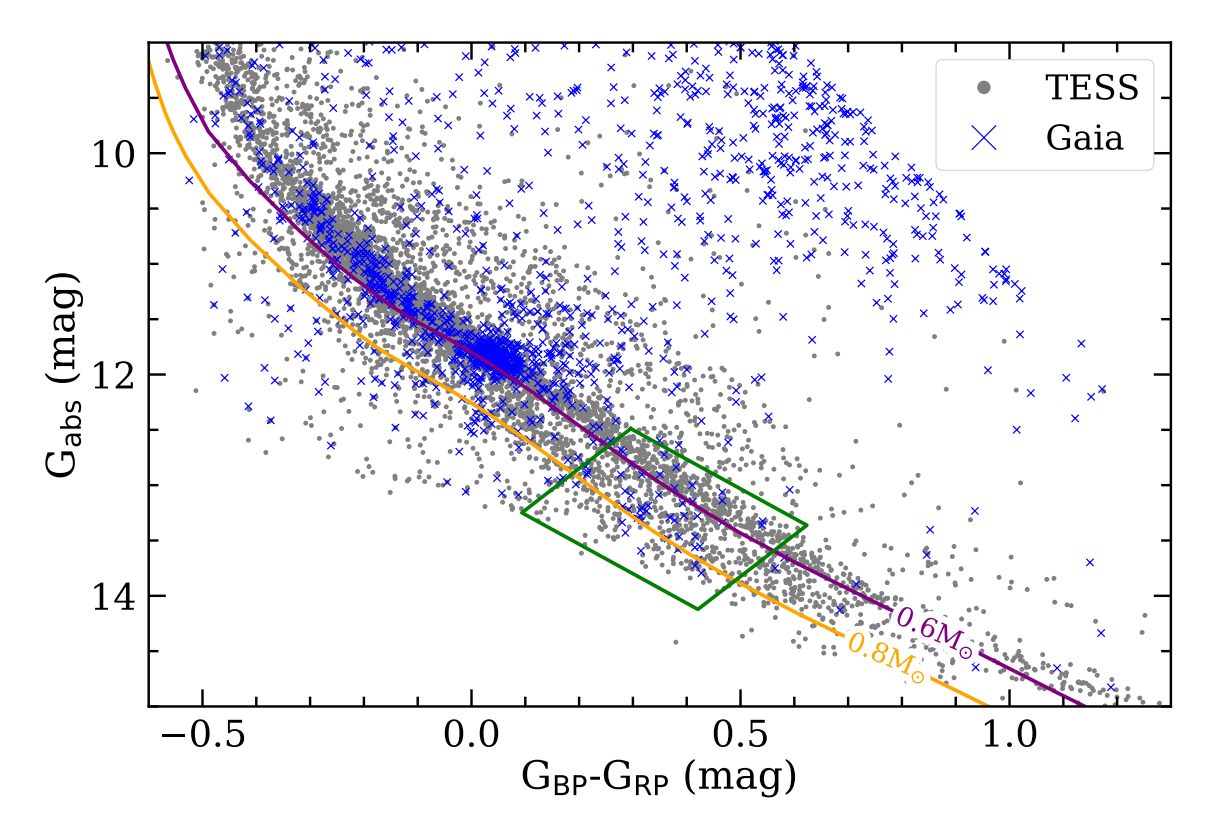


Figure 3.5: Colour magnitude diagram of Gaia white dwarf sample with G < 19 mag from Gentile Fusillo et al. (2019) catalogue that display photometric variability. Two cooling tracks are shown for 0.6 and $0.8 \, \mathrm{M}_{\odot}$ pure-hydrogen atmosphere white dwarfs. In grey are TESS-variable white dwarfs based on the LS analysis and false alarm probabilities. In blue are the Gaia pipeline-processed white dwarfs that were flagged as variable (any variability type). The DAHe region proposed by Manser et al. (2023) is outlined in green.

The underlying data set consisted of all of the PDCSAP TESS light curves. The interesting thing to note is that DAHe stars do not appear to form a visual cluster on the HRD based purely on variability indicators, unlike the ZZ Ceti stars that form a clear clump at $G_{BP} - G_{RP} \approx 0$ and $G_{abs} \approx 12$ mag. This fact appears consistent with a relatively low occurrence rate estimated by Manser et al. (2023) of one per cent. For context, inferred from this TESS data, approximately 18 per cent of white dwarfs are variable at one per cent or lower false alarm probability in the frequency range of 1 to 50 cycles per day.

3.2.2 Further GD 356 observations

Beyond the many exciting discoveries that significantly broadened the DAHe class of white dwarfs, its prototype, GD 356, remains an important object to study. Being the brightest and the most well-studied emitting magnetic white dwarf, it could be an important key to understanding this class. This section outlines some of the follow-up observations of this enigmatic star.

3.2.3 WHT

Photometric observations in the u-band of GD 356 were acquired on the WHT under the proposal SW2021a20 (principal investigator (PI): Walters). The photometry was acquired on 2021 June 20 in a single night covering two consecutive rotational cycles of GD 356. The data were acquired on the PF-QHY test camera that was available during the WEAVE integration from 2021 May 10 to July 12 only. The instrument is a QHY600L camera with 9576×6388 3.8 µm pixels resulting in a field of view of $10.7' \times 7.1'$. A total of 1128 exposures were acquired, each 10 s long and with a 13.7 s cadence that includes readout and overheads. Overall, this setup produced a total time coverage of 15 800 s but included a small pause due to the rotator limit. A 4×4 binning was used resulting in a scale of 0.267" per pixel. The exposures were acquired through the Sloan-u filter, covering approximately 3200 to 3900 Å. The observing conditions were satisfactory with a seeing of 0.7 – 1.0 arcsec. The data were reduced in the same fashion as the LT photometric observations described in detail in Section 2.3.4. The median S/N achieved per extracted photometric point of the light curve was 162 (upper pannel of Figure 3.6).

3.2.4 *HST*

GD 356 was selected for *HST* observations under the proposal 16719 (PI: Walters) to constrain the physical properties of the emitting region. Two sets of Near Ultraviolet (NUV) and one set of Far Ultraviolet (FUV) time-resolved spectra were acquired for this purpose. The FUV visit took place on 2022 December 30. The first NUV visit was on 2023 January 2, and the second NUV observation set was on 2023 April 20. In general, all three runs proved problematic due to guide star acquisition via the fine guidance sensors and were completed on gyroscope pointing control. The instrument used was the Space Telescope Imaging Spectrograph with the Multianode Microchannel Array 2048×2048 detector (Woodgate et al., 1998). All observations were obtained in the TIME-TAG mode, meaning each detector event has a time stamp, so the data can be sliced into shorter exposures of a specified length. The G140L grating with a resolving power $R \approx 1000$ and covering 1150 to 1700 Å was used for FUV observations. For NUV the G230L with $R \approx 3000$ and coverage extending from 1650 to 3200 Å was employed. In total, almost 8 and 5 hours of data were acquired in NUV and FUV, respectively.

The spectra were extracted and re-binned in the time dimension using the stistools Python package. The exposure time for each spectrum was re-binned to 50 s for NUV and FUV using the integration and the event list with a _tag suffix. This resulted in 559 NUV and 329 FUV exposures, compared to the original ten and six. Due to a low signal in 50 s FUV exposures, instead of estimating the extraction position for each exposure a custom position was specified that was set to the extraction position derived from the full dataset. In NUV, noisy data from the detector edges were not considered, resulting in 1631–3145 Å wavelength coverage. Due to airglow emission, FUV coverage is less uniform. Useful regions include 1148–1206 Å, 1223–1293 Å and 1311–1710 Å. Due to excellent calibration and space conditions, the acquired spectra could be used as time-series photometry by integrating the total flux. This was done over the specified wavelength ranges resulting in light curves with a median S/N of 144 and 17 in NUV and FUV, respectively. This flux integration excluded negative values. The resulting, phase-folded light curves are shown in Figure 3.6.

The light curves obtained from optical observations and those acquired from the ultraviolet spectra are in phase. This phase agreement leads to the conclusion that the emitting region maintains its opacity even in the ultraviolet range. It is worth noting the nuanced nature of sunspots, as they are not merely two-dimensional structures and exhibit distinct characteristics in various layers of the solar atmosphere, including the photosphere, chromosphere, transition region, and corona. Nevertheless, it is interesting to compare the variability in their light curves to the dark spot of GD 356. In the visible light range, sunspots appear darker when contrasted with their surrounding regions. However, at specific wavelength ranges, such as 1600-1700 Å, the sunspot flux is observed to be higher (Toriumi et al., 2020), resulting in an anti-phase relationship between the optical and ultraviolet light curves.

In order to gain deeper insights into the physical characteristics of the emitting region, it proves valuable to examine the amplitudes of photometric variations across different spectral bands. This analysis could capture the region's intrinsic properties, including its temperature, as the variability is primarily driven by this emitting region. Figure 3.7 illustrates the amplitudes obtained from previously published optical light curves (Walters et al., 2021), as well as the amplitudes derived from the WHT *u*-band, and the *HST* NUV and FUV bands.

Since the UV amplitudes are obtained from spectra, it becomes possible to further dissect them into smaller wavelength bins, as demonstrated in Figure 3.8. GD 356 is a relatively cool white dwarf with a limited emerging flux in the FUV range. It is noteworthy that the emitting region exhibits a substantial contrast with the stellar photosphere at shorter wavelengths within the FUV range, resulting in an amplitude of variability that reaches nearly 20 per cent. In contrast, the amplitude observed in the *TESS* band, which covers the region where the majority of the stellar flux emerges, is a mere 0.6 per cent. This stark contrast in amplitudes offers an avenue for further exploration to ascertain the geometry and temperature of the emitting region to be done in future work.

TESS

In Section 2.3.3 I outlined *TESS* photometric observations of GD 356. However, since the publication, the white dwarf was observed in additional four sectors: 50, 52, 56, and 59. More recent data are similar to the previous observations and were acquired and extracted in the same fashion. One notable difference, however, is that these sectors now offer a 20 s cadence data, compared to the previously available 120 s data. The higher cadence data allows for higher frequency signals to be identified in the time series. However, LS analysis identified no additional significant signals in the data at frequencies higher than the known rotational frequency.

Lastly, these extra four sectors can be used to update the O-C diagram in Chapter 2. The updated version is shown in Figure 3.9, along with O-C predictions from the new WHT u-band and HST FUV and NUV data. As mentioned before, one clear conclusion from the diagram is that there is no anti-phase relationship in the photometric flux between any of the filters. Overall, there seems to be no change in the established photometric period during the three years of observations. This is consistent with the predictions made in Walters et al. (2021) forecasting that periodic signals consistent with orbiting planets will not be forthcoming in continued photometric studies.

Finally, the vast amount of data from the TESS mission allows for the investigation of

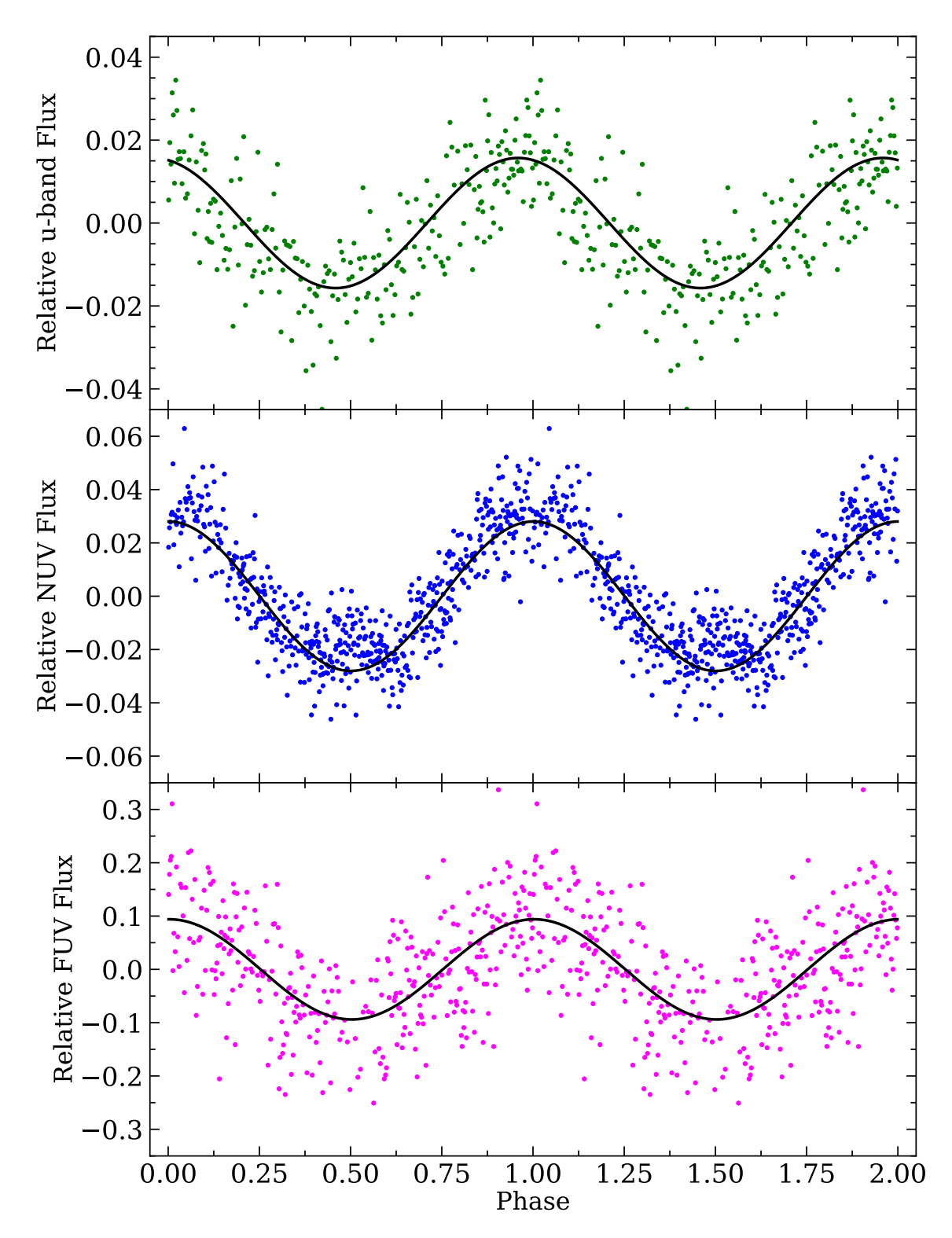


Figure 3.6: Phase-folded light curves of GD 356 folded on the most significant *TESS* photometric period ($P = 1.92717\,h$) determined in Section 2.4.1. Phase = 0 corresponds to *TESS* photometric maximum in all three panels. From top to bottom: WHT SDSS-u band, HST NUV, and HST FUV observations. The light curves appear to be in phase with each other and the previous optical photometric observations. The amplitude of light curve variability increases from top to bottom. The best-fit lines in black were estimated for each phase-folded light curve individually and consisted of a simple sine model.

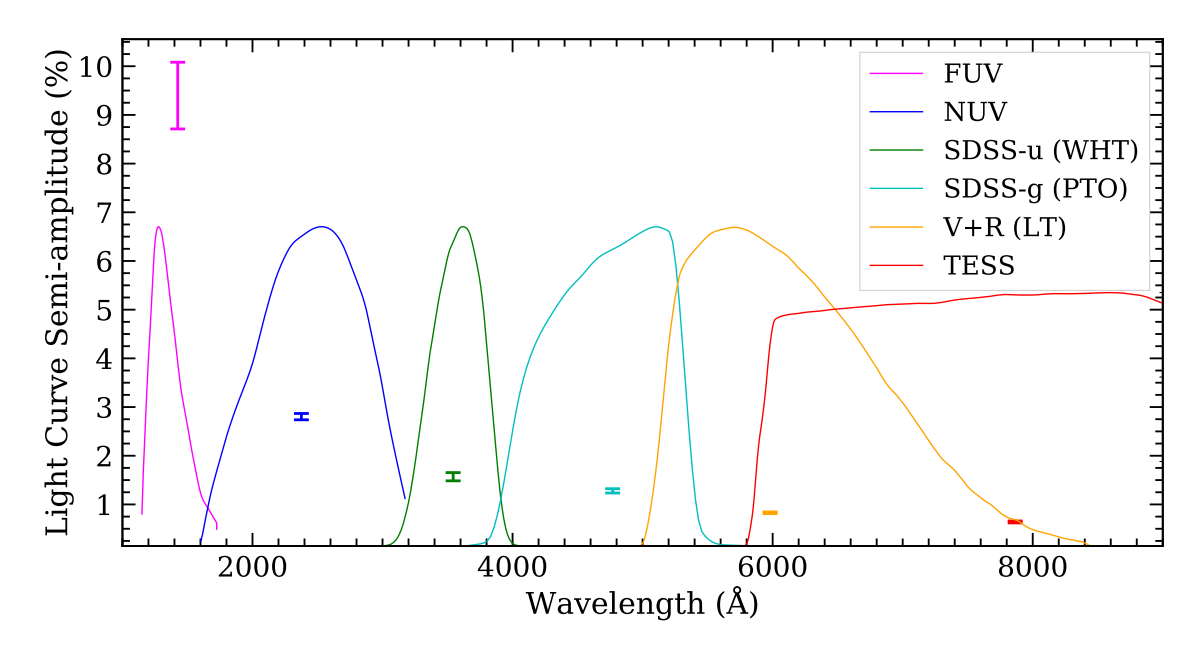


Figure 3.7: Semi-amplitudes of GD 356 variability in different filters. There is a clear increase in the variability towards the blue, implying a higher contrast between the spot and the photosphere.

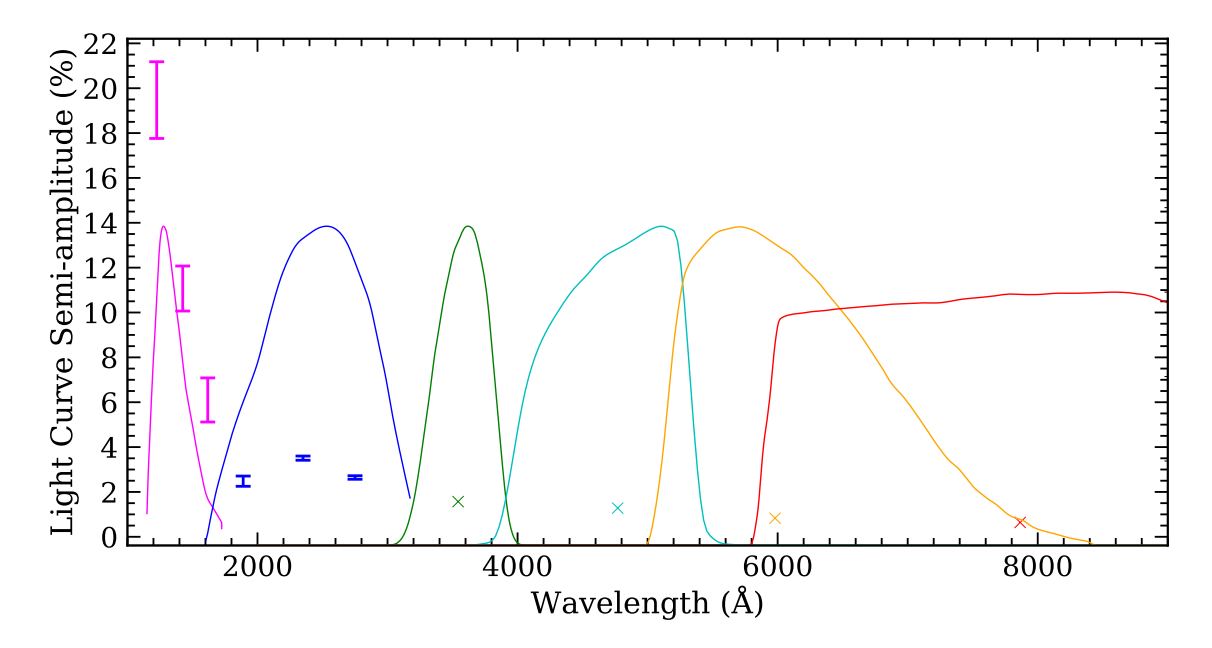


Figure 3.8: The same as the above figure (Figure 3.7) but in this instance the *HST* spectra were subdivided into smaller wavelength ranges before integrating the total flux, resulting in multiple points per filter. The plot shows a similar pattern to the previous figure, but this time the extreme end of FUV reaches a variability amplitude of almost 20 per cent. Note that the uncertainties on some points have been removed due to their small size for clarity.

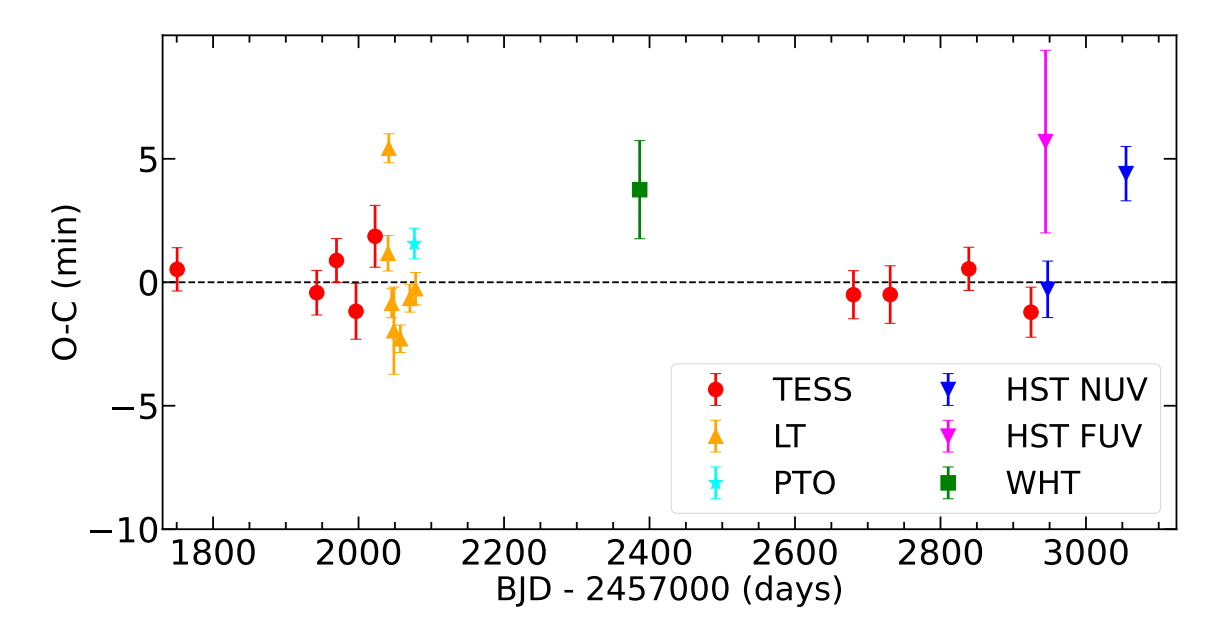


Figure 3.9: O - C diagram of GD 356 photometry. Each *TESS* point represents a whole sector. A barycentric correction was applied to each point. Despite some scatter, there is clearly no anti-phase relationship between any of the points (resulting in an O - C estimate of ≈ 60 min). The first five sectors of *TESS* were used to generate the zero line. Hence, over a three-year baseline, there appears to be no change in the O - C value. In the previous work on GD 356, short-term change in the period (and thus in O - C value) was ruled out. This diagram shows that this is also the case over a longer time range as well.

amplitude variation over time. Canonical star spots are dynamic structures characterized by short lifetimes, which are likely constrained by shear resulting from surface differential rotation. However, unlike main-sequence stars that possess convective envelopes, the outermost shell of most white dwarfs comprises a thin convective layer. While differential rotation in white dwarfs is still an active area of research (Calcaferro et al. 2023 and references therein), it is generally understood that white dwarfs rotate as solid bodies. This may extend the lifetime of a spot. In the case of GD 356, some of the earliest photometric data indicating its variability dates back to 2002 (Brinkworth et al., 2004), while the earliest spectra showing emission from GD 356 go as far back as 1973 (Greenstein & McCarthy, 1985). Given the correlation between emission and photometric variability, it is conceivable that the spotted region on GD 356 could be over 50 years old. An intriguing question arises: has this spot undergone any evolution? Analyzing *TESS* data on the amplitudes of variability for different sectors, as depicted in Figure 3.10, reveals no statistically significant variation over a three-year baseline.

However, there is a puzzling aspect that seems to contradict the current understanding. The V band photometric amplitude of GD 356 was reported to be 0.2 per cent in 2002-2003 data (Brinkworth et al., 2004), while observations in the V + R filter in 2020 exhibited an amplitude of 0.8 per cent (Walters et al., 2021). Although the V + R filter is not identical to the V filter, considering the trend of increasing amplitude towards the blue, one would expect a slightly higher amplitude in 2020 if it were acquired using the V filter. This discrepancy raises the question of whether the spotted region has evolved over the course of several decades. Future monitoring of GD 356, including O - C analysis and amplitude measurements, could provide valuable insights into this matter. In fact, any long-term

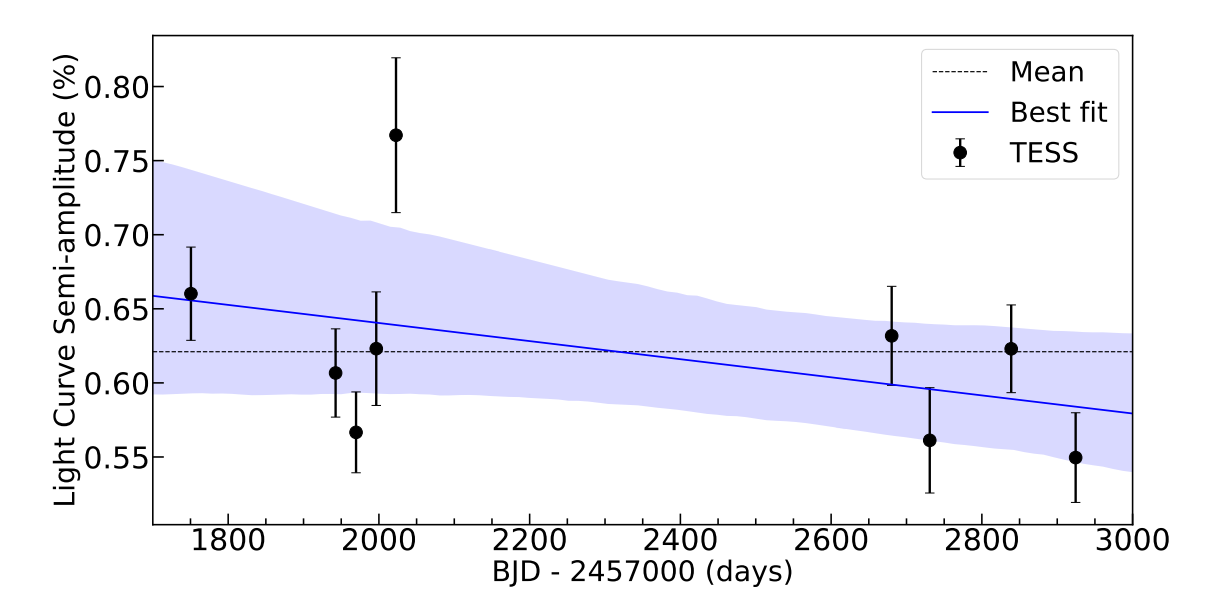


Figure 3.10: *TESS* light curve-semi amplitudes of GD 356. Each point represents a whole sector. The best-fit line is shown in blue, while a fixed, mean amplitude value is shown as a dotted black line. A 95 per cent confidence region is shaded in light blue. The constant amplitude value, corresponding to an undetectable change in the *TESS* amplitude is within the mentioned confidence region. Thus, there is no statistically significant evidence to suggest an amplitude change over three years of measurements.

photometric observations and analysis of spotted white dwarfs spanning several decades would be of great interest, as the lifetimes of spots on magnetic white dwarfs, even beyond the DAHe class, remain poorly understood.

3.3 Conclusions

Although the unipolar inductor model does not appear applicable to GD 356 or other DAHe stars, the model is by no means obsolete outside of the Jupiter-Io system. A recent review on star-planet magnetic interactions can be found in Strugarek (2021), as well as a number of suspected cases (e.g. Shkolnik et al. 2003, 2008; Walker et al. 2008; Pagano et al. 2009; Saur et al. 2013; Moutou et al. 2016; Cauley et al. 2019; Loyd et al. 2023; Trigilio et al. 2023). These studies highlight the continued exploration and understanding of magnetic field interactions in the realm of the exoplanetary systems, emphasizing the relevance and potential applicability of the unipolar inductor model in diverse astrophysical contexts, independent of the DAHe phenomenon.

The nature of white dwarf stars with active chromospheres raises several questions. One prominent line of inquiry pertains to the selective occurrence of DAHe within the magnetic DA subset. Could this be indicative of an evolutionary pathway followed by the emitting stars or be related to the fundamental source of magnetism? Deciphering the underlying mechanisms behind this emission phenomenon carries profound implications for any theoretical modelling of these stellar objects. Additionally, directing future work towards GD 356 offers an avenue to establish crucial empirical constraints on the physical attributes associated with the spotted region. By doing so, observationally-derived parameters can be tested against forthcoming theoretical models. One thing is clear: this class

represents a pathway to bridge existing gaps in the current understanding of magnetism, white dwarfs, and stellar phenomena.

Chapter 4

Two substellar survivor candidates; one found and one missing

This chapter is based on the paper of the same title (Walters et al., 2022). Some of the data presented in this chapter are from archival observations. *HST* and Keck NIRC2 adaptive optics observations were obtained and analysed by Jay Farihi (described in section 4.3.1). The physical parameters of the two stars were estimated using the BASE-9 software and are discussed in sections 4.4.1 and 4.5.1. PG 0010+281 infrared spectra were reduced and analysed by Jay Farihi, as well as PG 0010+281 SED fitting and L5 brown dwarf models, and are both discussed in section 4.5.5. PG 0010+281 Keck HIRES, INT IDS, MMT Blue Chan, WHT ISIS, and Gemini GRACES observations were reduced by the co-authors. All other work is my own.

4.1 Abstract

This chapter presents observations of two possible substellar survivors of post-main sequence engulfment currently orbiting white dwarf stars. Infrared and optical spectroscopy of GD 1400 reveal a 9.98 h orbital period, where the benchmark brown dwarf has $M_2 = 68 \pm 8 \,\mathrm{M_{Jup}}$, $T_{\mathrm{eff}} \approx 2100 \,\mathrm{K}$, and a cooling age under 1 Gyr. A substellar mass in the lower range of allowed values is favoured by the gravitational redshift of the primary. Synthetic brown dwarf spectra are able to reproduce the observed CO bands, but lines below the bandhead are notably overpredicted. The known infrared excess towards PG 0010+281 is consistent with a substellar companion, yet no radial velocity or photometric variability is found despite extensive searches. Three independent stellar mass determinations all suggest enhanced mass loss associated with binary evolution, where the youngest total age for an isolated star is 7.5 ± 2.5 Gyr. A possible solution to this conundrum is the cannibalization of one or more giant planets, which enhanced mass loss post-main sequence, but were ultimately destroyed. PG 0010+281 is likely orbited by a debris disk that is comfortably exterior to the Roche limit, adding to the growing number of non-canonical disks orbiting white dwarfs. At present, only L-type (brown) dwarfs are known to survive direct engulfment during the post-main sequence, whereas T- and Ytype substellar companions persist at wide separations. These demographics indicate that roughly 50 M_{Jup} is required to robustly avoid post-main sequence annihilation, suggesting all closely-orbiting giant planets are consumed, which may contribute to mass loss and magnetic field generation in white dwarfs and their immediate progenitors.

4.2 Introduction

It is now well established that white dwarfs often host planetary systems (e.g. Veras 2016), largely demonstrated by metal pollution and circumstellar matter (Farihi, 2016), and more recently transiting debris clouds as well as a few giant planet candidates (Vanderburg et al., 2015; Gänsicke et al., 2019; Vanderburg et al., 2020; Farihi et al., 2022). And while sun-like (FGK) stars are well characterized over a wide range of planetary masses and orbital radii (Millholland et al., 2017; Hsu et al., 2019; Kunimoto & Matthews, 2020; Jin, 2021), main-sequence stars of intermediate mass (A-type and similar) are generally not amenable to conventional exoplanet detection techniques such as precision radial velocities and transits. However, their white dwarf descendants, which can be formed within 1 Gyr for stars above 2 M_☉ (Mowlavi et al., 2012), are – at least in some ways - easier substellar companion search targets. For example, in addition to the powerful sensitivity of atmospheric pollution (Zuckerman et al., 2007), brown dwarf and high-mass planetary companions can be detected through infrared excess (Rebassa-Mansergas et al., 2019), and transit depths can be enhanced by a factor of over 100. Moreover, statistically speaking, extant white dwarf planetary system hosts likely outnumber their progenitors systems; there are 20 white dwarfs within 10 pc, and only 12 stars earlier than G-type (Reylé et al., 2021). Complicating the picture somewhat, is the evolution of planetary systems from the main sequence through the two giant branches, and into the white dwarf phase. What survives, and are the substellar survivors altered?

Low-mass stellar and substellar companions to white dwarfs provide important insight into the above question, albeit at the higher mass end of possible survivors. Because brown dwarfs are not expected to be altered during common envelope evolution, low-mass ratio binaries carry information on the initial (and companion) mass functions, including an avenue for exploration of the known deficit of brown dwarf companions to main-sequence stars (McCarthy & Zuckerman, 2004; Grether & Lineweaver, 2006). Furthermore, the study of bound companions provides more information than isolated objects, as a binary is the smallest possible 'cluster'. For systems with a white dwarf primary, there will be a clear age constraint from its cooling age, which can be applied directly to the secondary, and where state-of-the-art Bayesian methods can provide a decent constraint on the total system age (von Hippel et al., 2006; Moss et al., 2022).

The frequency of white dwarfs hosting a brown dwarf companion is also low, where an extensive near-infrared imaging survey measured the fraction to be below 0.5 per cent (Farihi et al., 2005b). This estimate agrees with later, near-infrared photometric surveys covering a large fraction of the sky (Steele et al., 2011; Girven et al., 2011), and a subsequent *WISE* study (Debes et al., 2011). Although possibly incomplete in terms of its low-mass brown dwarf companion census, the 40 pc sample of white dwarfs contains only two substellar companions; the prototype L dwarf GD 165B (Becklin & Zuckerman, 1988), and the first sub-T dwarf candidate WD 0866-661B (Luhman et al., 2011)¹. This

¹These astrophysical firsts were detected as companions to white dwarfs, underscoring their utility and impact. Combined with the prototype T dwarf Gl 229B, discovered as a companion to an M dwarf (Oppenheimer et al., 1995), low-luminosity stars have been paramount in the discovery and establishment of substellar spectral classes.

yields a fraction of brown dwarf companions close to 0.2 per cent (Gentile Fusillo et al., 2019).

From both theory and observation, low-mass stellar and substellar companions to white dwarfs form two distinct populations, differentiated by orbital separation and separated by a period gap (Farihi et al., 2006; Nebot Gómez-Morán et al., 2011). The existence of the two populations is consistent with the expectations of stellar evolution (Nordhaus et al., 2010), where close pairs have experienced a phase of common envelope evolution (Paczynski, 1976) that has dramatically decreased their initial orbits at formation. In wide binaries, the secondary has migrated outwards by a factor directly proportional to the mass lost during the RGB and AGB phases of the host (Jeans, 1924).

In the case where a substellar companion persists, after the engulfment by its first ascent giant or asymptotic giant host star, the brown dwarf is expected to be strongly irradiated during the first few Gyr of white dwarf cooling. Such systems can provide empirical data that can be compared to existing models of irradiated hot Jupiter atmospheres (Lee et al., 2022; Tan & Showman, 2020). The lowest-mass survivors of the common envelope provide direct testimony of planetary survival under these conditions and thus provide useful benchmarks. An example might be the recently reported giant planet candidate transiting a white dwarf (Vanderburg et al., 2020), where the expected effects of a common envelope (e.g. atmospheric ablation, orbital dissipation) may imply the transiting object migrated much later to its current orbital position, or was originally more massive. Despite almost a thousand candidate post-common envelope systems (Kruckow et al., 2021), this phase of binary evolution remains a major modelling challenge (Ivanova, 2011).

This chapter presents observations of GD 1400 and PG 0010+281, where both are suspected of being white dwarf - brown dwarf binaries that underwent post-common envelope evolution. Orbital and binary parameters are successfully obtained for both components of GD 1400, whereas only companion limits are obtained for PG 0010+281. In Section 4.3 new and archival observations are described, followed by two sections of analysis and results focussing on the separate science targets: Section 4.4 for GD 1400, and Section 4.5 for PG 0010+281, including all findings, followed by concluding remarks.

4.3 Observations and data

This section is divided over the two science targets, and describes new and archival observations of GD 1400 and PG 0010+281, where a summary is provided in Table 4.1.

4.3.1 GD 1400

GD 1400 was observed with five instruments to constrain its binary orbit and companion mass. The order presented below follows the chronology of these various datasets.

High-resolution imaging

Following the spectroscopic discovery of GD 1400B in 2004, which was the second known substellar companion to any white dwarf (Farihi & Christopher, 2004), efforts were made to spatially resolve the brown dwarf from its white dwarf primary through high-resolution imaging observations. As part of Cycle 13 Snapshot program 10255 (Farihi et al., 2006),

HST observed GD 1400 on 2005 June 5 using the Advanced Camera for Surveys (ACS; Ford et al. 1998). The observation consisted of a four-position imaging sequence using the High Resolution Camera and the F814W filter (analogous to the Cousins I band), with a total exposure time of 1080 s. The resulting fully-processed and multidrizzled science image did not show any evidence of the companion, including any elongation of the stellar image, though point spread function subtraction was not carried out. While these space-based observations are sensitive to sub-arcsecond spatial separations, the anticipated $\Delta I \sim 6$ mag difference between the white dwarf and its L dwarf companion leaves open the possibility that such a binary system could remain unresolved even at the 0.1 arcsec level (Dahn et al., 2002; Farihi et al., 2005a).

On 2005 September 10, laser guide star adaptive optics observations of GD 1400 were conducted on Mauna Kea using the Keck II telescope and the Near-Infrared Camera 2 (NIRC2; van Dam et al. 2006; Wizinowich et al. 2006), as part of the H26aN2 program. Four images of GD 1400 were captured in the *K* band with the narrow field camera (0.01 arcsec² pixels), each consisting of 20 s exposures with 2 co-adds. As the white dwarf and brown dwarf are expected to have roughly equal flux density at this wavelength (Farihi & Christopher, 2004), the image with the best corrections and highest Strehl ratio was examined for any signs of duplicity. The contours of this S/N > 300 image are displayed in Figure 4.1. The point spread function is sufficiently symmetric to rule out an equally luminous binary separated by 1/3 the full width at half maximum (FWHM), implying a projected separation of less than 0.02 arcsec. The latest *Gaia* DR3 observations place the system at a distance of 46.3 pc, thereby limiting the projected separation on the sky to under 0.9 AU (Gaia Collaboration et al., 2022). In light of this evidence suggesting a probable orbital period of less than about 1 yr, a program to monitor the radial velocity of GD 1400A was initiated in 2006.

Optical spectroscopy of GD 1400A

High-resolution optical spectroscopy of the white dwarf was performed using the Ultraviolet and Visual Echelle Spectrograph (UVES; Dekker et al. 2000) mounted at the European Southern Observatory (ESO) Very Large Telescope (VLT). A total of 34 spectra were obtained covering H α and the higher Balmer lines; two of these spectra were acquired under the ESO SPY survey (Napiwotzki et al., 2003) several years prior to the dedicated follow up observations. The remaining 32 spectra were observed as part of programme 077.D-0673 between 2006 July 06 and September 03, using the same UVES setup as the SPY survey: a 2.1 arcsec slit and 2 × 2 binning on the array. The setup provided spectral resolving power of $R \approx 18\,500$ (Napiwotzki et al., 2001).

The 2006 observations were performed in service mode, in seeing no worse than 1.4 arcsec, for a total exposure time of 1200 s per visit. Each observing visit was split into 2×600 s exposures to avoid orbital smearing in case the period was shorter than a few hours. On 2006 July 18, no data in the blue arm were taken, resulting in four missing exposures covering 3250 to 4500 Å, which is attributed to human or instrumental error (no reasons are provided in the night log). All data were extracted in a semi-automatic way using the ESO Reflex Environment (ESOREFLEX; Freudling et al. 2013) and UVES pipeline version 6.1.6 (Ballester et al., 2000). The standard recipes were used to optimally extract and wavelength calibrate each spectrum. The resulting average S/N was estimated to be 31 in the H β region and 29 in the H α .

Table 4.1: Journal of new and archival observations with approximate dates.

Telescope &	Data Type	Dates of
Instrument		Observation
GD 1400:		
HST ACS	F814W imaging	2005 Jun 5
Keck NIRC2	K-band AO imaging	2005 Sep 10
VLT UVES	Optical spectroscopy	2000, 2006 Jul – Sep
VLT ISAAC	K-band spectroscopy	2010 Oct
TESS	Optical photometry	2018, 2020 Sep – Oct
PG 0010+281:		
Keck HIRES	Optical spectroscopy	2013 Sep
INT IDS	"	2015 Jul
MMT Blue Chan	"	2016 Jan 15
VLT UVES	"	2017 Oct – Nov
WHT ISIS	"	2018 Aug – Sep
Gemini GRACES	"	2019 Nov
Keck NIRSPEC	K-band spectroscopy	2015 May 26
IRTF SpeX	Near-infrared spectroscopy	2019 Oct 20
TESS	Optical photometry	2019 Oct – Nov
ZTF	"	2018 May – 2021 Jan
WISE	Infrared photometry	2010 - 2020

Infrared spectroscopy of GD 1400B

To measure the radial velocity of GD 1400B, K-band time-series spectroscopy was carried out using the Infrared Spectrometer and Array Camera (ISAAC; Moorwood et al. 1999), a low- to medium-resolution, infrared spectrograph and imager previously mounted on the VLT. The spectra were obtained over two consecutive nights under proposal 086.D-0030 on 2010 October 29 and 30 on a Rockwell 1024×1024 pixel² Hawaii array, using the short wavelength arm in spectroscopic mode with the medium-resolution grating. The slit width was set to the narrowest available option of 0.3 arcsec, resulting in $R\approx8900$ over the spectral range $1.82-2.50\,\mu\text{m}$. Based on the discovery spectrum of the brown dwarf (Farihi & Christopher, 2004), this setup was chosen to resolve individual transitions within the CO bands, and provide robust cross-correlation across velocity-shifted spectra. A total of 62 exposures were obtained over the two nights, using 600 s integrations and following the standard infrared ABBA pattern on the slit, i.e. nodding the object along the slit between two positions.

Spectral reduction was performed in IRAF. A bad pixel mask was constructed by identifying hot pixels in dark frames and cold pixels in flat field frames; this mask was then used to interpolate across all affected pixels in all science and calibration frames. The two-dimensional data were flat fielded, then A–B and B–A pairs were created to remove the bright infrared sky, and for subsequent spectral extraction. An A0V standard star (HD 9132) was observed in a similar manner as the science target, and its strong spectral trace was used to extract the spectra of GD 1400B. For wavelength calibration, XeAr arcs were acquired multiple times throughout both nights to correct for any flexure

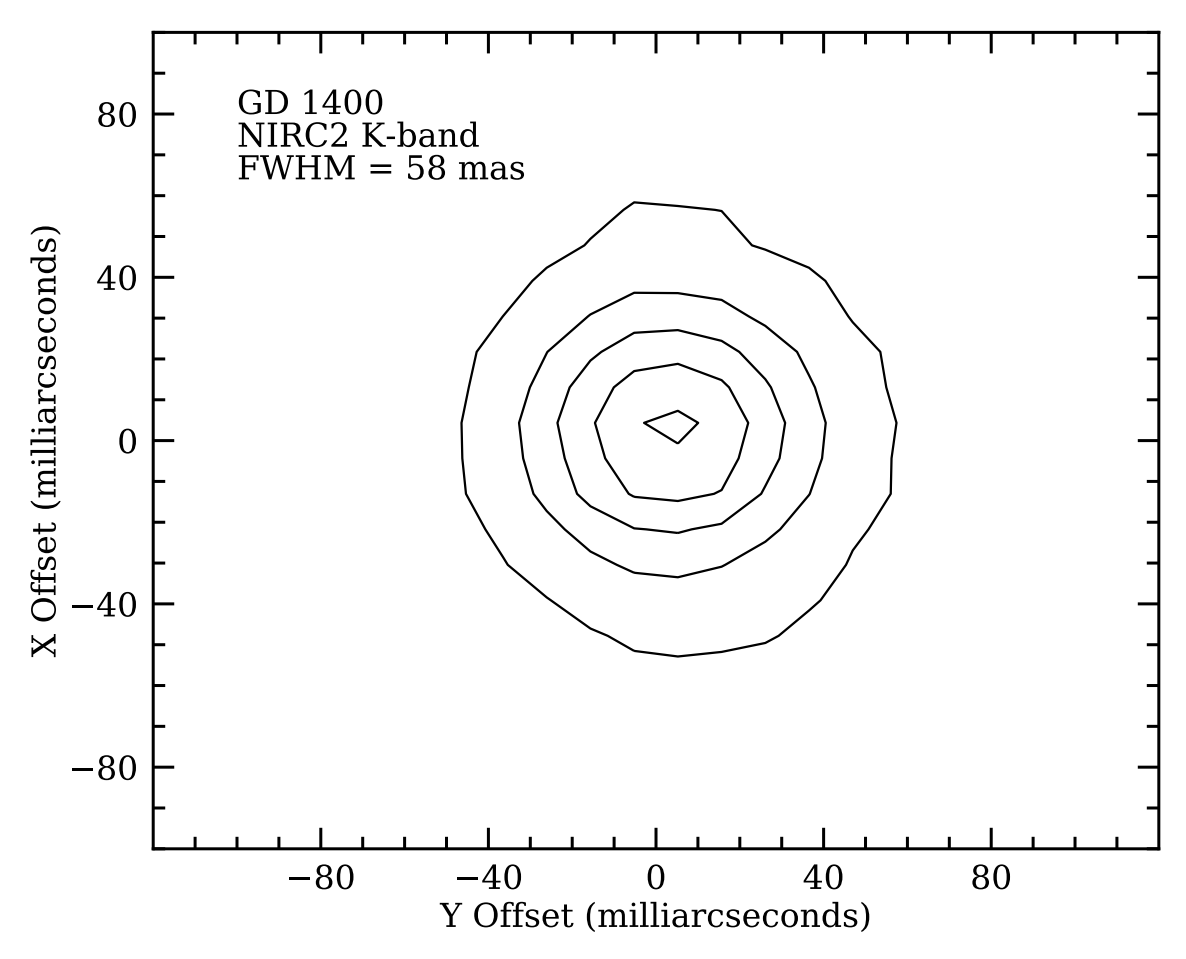


Figure 4.1: Flux density contours for the Keck NIRC2, K-band adaptive optics image with the highest Strehl ratio. The five evenly-spaced contours are plotted from 1000 to 5000 counts, and the FWHM is measured to be 58 mas. For a pair of equally luminous binary components, a separation of approximately 20 mas (≈ 0.9 au) can be ruled out.

in the optics, and to provide the best wavelength solution as a function of time. Telluric correction and flux calibration were applied using the XTELLCOR_GENERAL routine within SPEXTOOL (Vacca et al., 2003; Cushing et al., 2004). The resulting spectra had an average S/N of 15.

Time-series photometry

GD 1400 was observed by *TESS* in Sector 3 from 2018 September 21 until 2018 October 17, and again in Sector 30 from 2020 September 23 until 2020 October 20. The star was observed with camera 2, and on CCD chip number 3 in both sectors, under designation TIC 164772507 (*TESS* Mag = 15.2 mag; Stassun et al. 2018). In some cases (for approximately 1000 targets per sector), data that are flux averaged over 20 s are also available along with the usual 120 s, as was the case for Sector 30 observations of GD 1400.

The availability of this higher cadence data is due to the white dwarf being specifically targeted as a known ZZ Ceti pulsator (Fontaine et al., 2003). This is a stellar evolutionary phase common to all white dwarfs with hydrogen atmospheres, where an atmospheric instability results in non-radial pulsations (see Romero et al. 2022 and references therein). Given the approximate effective temperature and mass from prior publications, the star

should be in the middle of the ZZ Ceti instability strip (Tremblay et al., 2015a), where some stars have pulsation periods shorter than the standard 120 s cadence (Mukadam et al., 2006).

Data products from both sectors were accessed from the *TESS* Mikulski Archive for Space Telescopes. Light curves were extracted from the target pixel files by the *TESS* Science Processing Operations Center pipeline (Jenkins et al., 2016). PDCSAP light curves were used, since they have systematic errors removed, including error sources from the telescope and the spacecraft using co-trending basis vectors (Smith et al., 2012; Stumpe et al., 2012). It should be noted that the pipeline corrects the flux of each target to account for crowding from other sources, where the flux of GD 1400 is modelled as 0.97 of the total on average, so the corrections are minor. Pipeline defined apertures were used throughout for reliability and reproducibility provided by the PDCSAP. Across the two sectors 38 259 120 s measurements are available and 29 552 of these have no anomalous flags.

4.3.2 PG 0010+281

Three independent approaches were considered to identify or rule out possible substellar companions to PG 0010+281 as suggested by its infrared excess (Xu et al., 2015).

Optical spectroscopy

Optical spectra were acquired (or extracted from archives) from several facilities as summarized in Table 4.1, and are detailed below in chronological order.

Spectra of PG 0010+281 were obtained with the High Resolution Echelle Spectrometer (HIRES; Vogt et al. 1994) on the Keck I telescope on Mauna Kea 2013 September 17 and 20 with different setups (Xu et al., 2015). The program ID for these observations is U067Hr. On the first night, the C5 decker was employed, which has a slit width of 1.15 arcsec and a nominal resolving power of $R \approx 36\,000$. Two exposures were taken with integration times of 2400 s each, using the red cross disperser (HIRESr) and covering 4960 – 6730 Å. This resulted in a S/N of 31 in the H α order. On the second night, the C1 decker was used with a slit width of 0.86 arcsec². Using this setup, two further exposures were obtained at a higher resolving power of $R \approx 48\,000$, but with exposures of 1800 s and 426 s, with the blue cross disperser (HIRESb) covering 3050 – 5940 Å. The average S/N for these two exposures in the H β region is 39. These data were reduced using the HIRES REDUX package³.

Spectroscopic observations were also carried out on the 2.5 m Isaac Newton Telescope (INT) at Roque de los Muchachos under program P2. Fourteen spectra were obtained with grating R400V on 2015 July 22 and 23 using 420 s exposures, and on-chip binning of 2 pixels in the spatial direction. Six additional spectra were acquired with grating R1200R on three consecutive nights starting 2015 July 29 and using 1500 s exposures. Both data sets were obtained with the Intermediate Dispersion Spectrograph (IDS), a double arm, long-slit spectrograph mounted at the Cassegrain Focal station. The REDPLUS2 detector was used in both cases, with wavelength coverage 3800 – 7150 Å for R400V, and

²This value, confirmed using the Keck archive, disagrees with the setup reported in Xu et al. (2015)

³https://www.ucolick.org/~xavier/HIRedux/index.html

6050 – 7050 Å for R1200R. The data were processed and extracted using MOLLY⁴, where typical S/N values were 20 and 15, respectively, for the R400V and R1200R grating data.

Further spectroscopic data were acquired on the Multiple Mirror Telescope (MMT), located on the summit of Mount Hopkins. A total of four exposures were obtained on 2016 January 15 using the Blue Channel spectrograph in cross-dispersed mode with the Echellete grating (Schmidt et al., 1989). Exposure times were set to 600 s and cover a wavelength range from around 3100 to 7200 Å. The average seeing was 1.4 arcsec and the airmass ranged between 1.3 and 1.8 during the observations. These data were reduced without a pipeline, using the echelle data package within IRAF. An average S/N of 20 was achieved.

PG 0010+281 was observed with VLT UVES instrument under proposal 0100.D-0133 in service mode. A total of eight high-resolution, echelle spectra were acquired between 2017 October 22 and 2017 November 18. Observations were split into four sets of two exposures, with each set done on separate nights to reduce the probability of observing a (candidate) binary system at the same phase. A 1.0 arcsec slit was used resulting in $R \approx 40\,000$. The integrations were 600 s each and 2×2 on-chip binning was employed. Spectra were extracted similarly to GD 1400 as described above using ESOREFLEX, but with one important difference; there are numerous, residual sky emission lines⁵ in four out of the eight spectra, including one at H α . To effectively minimize these residual emission lines, the sky subtraction method (the reduce.extract.skymethod parameter) was changed from optimal to median. In the end product S/N varied from 15 to 20 in the H α region with a representative S/N of 17.

The ISIS instrument, on the 4.2 m WHT, at Roque de los Muchachos was employed to obtain 13 spectra of PG 0010+281. A total of 11 spectra were obtained on 2018 August 29, and two further spectra on the nights of 2018 September 1 and 3 under program P8/N13. This observing cadence provided good sensitivity to short orbital periods of several hours, as well as variations beyond one day. ISIS has two spectrographic arms, where the blue side used the R600B grating centred at 4400 Å, while the red side used R1200R centred at 6560 Å, and where a resolving power of $R \approx 7200$ was estimated. The spectra were binned on-chip, using 3×2 spectral vs. spatial pixels in the blue arm, and 3×1 binning in the red arm. The exposure time was consistently 1200 s for both arms. The spectra were extracted using IRAF standard procedures. The resulting spectra had an average S/N of 24 in the red arm.

High-resolution spectroscopy was also acquired under program 2019B-0162 with the Gemini Remote Access to CFHT ESPaDOnS Spectrograph (GRACES; Chene et al. 2014) located at the Gemini North Observatory on Mauna Kea. The spectra were collected in two-fibre mode for superior sky subtraction. A total of 12 exposures were collected, consisting of four observational blocks with three exposures per block, where one block each was observed on 2019 November 10 and 11, and two blocks executed on 2019 November 12. Individual exposures were 1800 s, with the aim to achieve S/N > 20 at H α and $R \approx 40\,000$. The spectral data have some modest wavelength gaps, and span optical wavelengths redward of 3950 Å (including H ϵ), below which the silver mirror coating on Gemini has little reflectivity. The Gemini spectra were reduced using the

⁴MOLLY was written by T. R. Marsh and is available at http://www.warwick.ac.uk/go/trmarsh/software

⁵All residuals were robustly confirmed to be stationary and of telluric origin. This shortcoming in the UVES pipeline reduction (and Phase 3 products) for this target was reported to ESO but not resolved.

Data Reduction and Analysis for GRACES (DRAGRACES; Chené 2020; Chené et al. 2021) software package. Automated steps include overscan correction, bias subtraction, order rectification, slit tilt correction, background illumination correction, order extraction, and wavelength calibration. The software does not include a cosmic ray removal procedure, and such artefacts were removed by identifying features not present in all three exposures in a single block. The sky was subtracted by scaling the sky spectra by a fixed factor of 1.25 and applying a small wavelength shift (below ±1 pixel) that minimises the root mean square statistic of the resulting spectra using the IRAF task SKYTWEAK.

Infrared spectroscopy

To better characterise the infrared excess of PG0010+281, data from the Near-Infrared Echelle Spectrograph (NIRSPEC; Martin et al. 2018) were extracted from the Keck II telescope archive, and additional spectra were obtained at the NASA Infrared Telescope Facility (IRTF), both on Mauna Kea.

The NIRSPEC observations were carried out using the Keck II telescope on 2015 May 26 as part of program 15B/U049NS⁶. The NIRSPEC-6b filter configuration was used together with a 0.57 arcsec slit, resulting in approximate wavelength coverage of $1.94 - 2.32 \,\mu\text{m}$ (McLean et al., 2003) and resolving power $R \approx 2000$. A total of 16 exposures of 300 s each were taken, in an ABBA nodding pattern along the slit. These data were reduced via the REDSPEC package (Kim et al., 2015), including a telluric correction routine that enables interpolation over real spectral features, such as the Br γ line in the observed telluric standard star HD 9711. Each AB pair of spectra were extracted and combined, resulting in eight individual spectra, and these were further combined into a single spectrum using an unweighted mean. The resulting combined spectrum had an estimated S/N of 49.

At the IRTF, spectroscopy of PG 0010+281 was obtained on 2019 October 20 using the SpeX near-infrared spectrograph (Rayner et al., 2003), under program 2019B030. The spectra were taken in prism mode with a 0.5 arcsec slit width, covering $0.80-2.52~\mu m$ at a resolving power of $R\approx 130$, obtaining 16 exposures of 120 s each. The spectra were extracted and combined using a robust weighted mean, with telluric correction and flux calibration performed using SPEXTOOL (Cushing et al., 2004) and with HD 222749 as an A0V standard star. The S/N of the combined spectrum is 15.

Time-series photometry

PG 0010+281 was observed by *TESS* in Sector 17 from 2019 October 8 until 2019 November 2 under designation TIC 437743290 (*TESS* Mag = 16.0 mag; Stassun et al. 2018). The target was observed with spacecraft's camera number 1 and CCD chip number 2. Unlike in the case of GD 1400, PG 0010+281 is fainter and is surrounded by relatively bright objects, resulting in a low ratio of PG 0010+281 flux to total flux of 0.69. The data were accessed similarly to GD 1400 and 120 s PDCSAP light curve was obtained. Out of 18 012 data points, 5139 have non-zero (anomalous) quality flags, and further scrutiny showed these data to be of lesser quality and were thus rejected from analysis.

⁶These data were taken prior to the instrument upgrade in 2018 and thus some of the old configurations noted are obsolete or altered.

Two additional sources of photometry were retrieved to search for possible variations caused by an orbiting companion. Publicly available infrared light curves obtained by the *Wide-field Infrared Survey Explorer (WISE*; Wright et al. 2010) were downloaded from NASA/IPAC Infrared Science Archive, using the AllWISE Multiepoch Photometry Table for the 3.4 µm *W1* and 4.6 µm *W2* bands only. The same archive provides access to optical photometry for PG 0010+281 ZTF observations, where all available data were downloaded with the exception of observations with non-zero catflags values, which were dropped.

4.4 Analysis and results: GD 1400

4.4.1 Stellar parameters

Stellar parameters for GD 1400A were estimated using the Bayesian Analysis for Stellar Evolution with Nine Parameters (BASE-9; von Hippel et al. 2006; O'Malley et al. 2013), determined from the *Gaia* DR3 parallax measurement and Pan-STARRS *griz* photometry. The *y*-band flux was not used due to contamination from the companion. The posterior distributions are non-Gaussian, with means and 68 percentile credible intervals $T_{\rm eff} = 11\,000\pm100\,{\rm K}$, $M=0.592\pm0.009\,{\rm M}_{\odot}$. These temperature and mass estimates include formal errors that reflect only the precision within the adopted methodology. To obtain more realistic uncertainties, the standard deviation of recently published results (Gianninas et al., 2011; Leggett et al., 2018; Napiwotzki et al., 2020; Bergeron et al., 2021; Gentile Fusillo et al., 2021b) and BASE-9 estimates was calculated and adopted as the final uncertainty. This results in $T_{\rm eff}=11\,000\pm500\,{\rm K}$ and $M=0.59\pm0.07\,{\rm M}_{\odot}^{7}$.

For radial velocity measurements of GD 1400, the infrared and optical data were processed in a distinct manner. The ISAAC spectra are feature-rich due to CO molecular bands from the brown dwarf companion. These individual transitions are resolved, sharp, cover almost the whole spectral range, and remain identifiable even in the lowest S/N spectrum. Therefore, cross-correlation is well-suited to calculate radial velocity changes in this case.

However, cross-correlation methods are less effective for extracting radial velocity estimates from optical spectra of white dwarf Balmer lines, which are pressure broadened and few (Napiwotzki et al., 2001). Instead, radial velocities can be measured by fitting the relatively narrow Balmer line cores using Gaussian and Lorentzian profiles (e.g. Maxted & Marsh 1999). These functions individually may describe the line profile only approximately and so, for accurate modelling, a combination of multiple functions may be necessary. In general, the more pronounced core of H α , and to a lesser extent H β , can be fitted more exactly by a combination of a Lorentzian, plus a Gaussian for the wings, while higher Balmer lines can be modelled by Gaussian profiles alone. The line cores originate from the low density, non-local thermodynamic equilibrium (NLTE) regions in the upper layers of white dwarf atmospheres and thus undergo diminished pressure broadening, where H α and H β have the strongest NLTE features for fitting. The optical spectra of GD 1400 (and PG 0010+281 in Section 4.5 below) were fitted by minimising residuals between a combination of these functions and the spectra.

⁷The gravitational redshift is consistent with a mass in the lower part of this range, see Table 4.2 and Section 4.4.5

4.4.2 Optical radial velocities of GD 1400A

The UVES spectra cover several Balmer absorption lines, but only H α and H β were used for radial velocity estimation of the white dwarf. H α displays a sharp NLTE core in every spectrum, while relatively narrow cores can only be distinguished in about 2/3 of H β lines. Because of this, both H α and H β were fitted simultaneously. To fit the lines, two dependent functions were used, each function being a combination of a Gaussian (for wider wings) and a Lorentzian (for the core). The logarithm of the wavelength was used to ensure the value of the shifts from the known air wavelength positions would be the same for both H α and H β during the fitting process. The fitted parameters were obtained from non-linear, least-square minimisation algorithm implemented by the LMFIT python package (Newville et al., 2016). The log wavelength range supplied to the fitting model varied from spectrum to spectrum, determined by first fitting H α and H β with a Gaussian over $\log[\lambda(A)] = 3.8169 - 3.8173$ and 3.6866 - 3.6869, respectively. The wavelength range passed to the final fitting model would then be equal to the estimated position of the centre ± 0.0004 dex. In other words, the length of the fitted range would be the same as in the first case but centred on the NLTE core from the initial Gaussian fits. The fitted wavelength range thus corresponded to approximately $\pm 6 \,\text{Å}$ for H α , and $\pm 5 \,\text{Å}$ for H β. The final wavelength central positions were then converted into velocity shifts, and barycentric corrections were applied using the ASTROPY package.

4.4.3 Infrared radial velocities of GD 1400B

Cross-correlation for radial velocity information requires a template spectrum. For the template, it was found that using a synthetic template provided notably superior results compared to using the highest S/N spectrum or a velocity-adjusted co-add of multiple spectra. As an initial guess, a synthetic model of a substellar, cloud-free atmosphere was picked with $T_{\rm eff} = 1500\,\rm K$, $\log{[g({\rm cm\,s^{-2}})]} = 5.5$, and solar metallicity from a grid of Sonora Bobcat models (Marley et al., 2021). The wavelength range used for cross-correlation was $2.28-2.34\,\mu \rm m$ for both the synthetic and science spectra. The resolution of the synthetic template was reduced to the same value as the ISAAC spectra by convolution with a Gaussian kernel, and applying a flux-conserving re-sampler. To obtain the radial velocities, the IRAF cross-correlation task FXCOR was used.

After obtaining velocity estimates based on the model template, barycentric velocities were calculated using the ASTROPY package. The resulting velocities were then fitted with a simple sinusoidal model. Velocity shifts, derived from this model, were then applied to the ISAAC data to produce individual spectra that have zero velocity in the brown dwarf rest frame. These brown dwarf rest frame spectra were then co-added into a single spectrum that was used to perform a grid search for the best fitting synthetic spectrum via residual minimisation. Two model grids were explored: the aforementioned cloud-free, Sonora Bobcat theoretical spectra, and the BT-Settl cloudy models (Baraffe et al., 2015).

The Sonora Bobcat search grid covered $T_{\rm eff}$ from 1400 to 2400 K in steps of 100 K, and log g from 3.5 to 5.5 in steps of 0.25 dex. The BT-Settl grid is coarser, and was searched from $T_{\rm eff} = 1400$ K to 3000 K, and from log g = 3.5 to 5.5 in steps of 0.5 dex. For the Sonora Bobcat models, the search included metallicities [Z/H] = -0.5, 0, +0.5. However, the theoretical spectra were insufficiently distinct in the narrow region of the ISAAC spectra, and thus unable to meaningfully constrain the metallicity of the brown

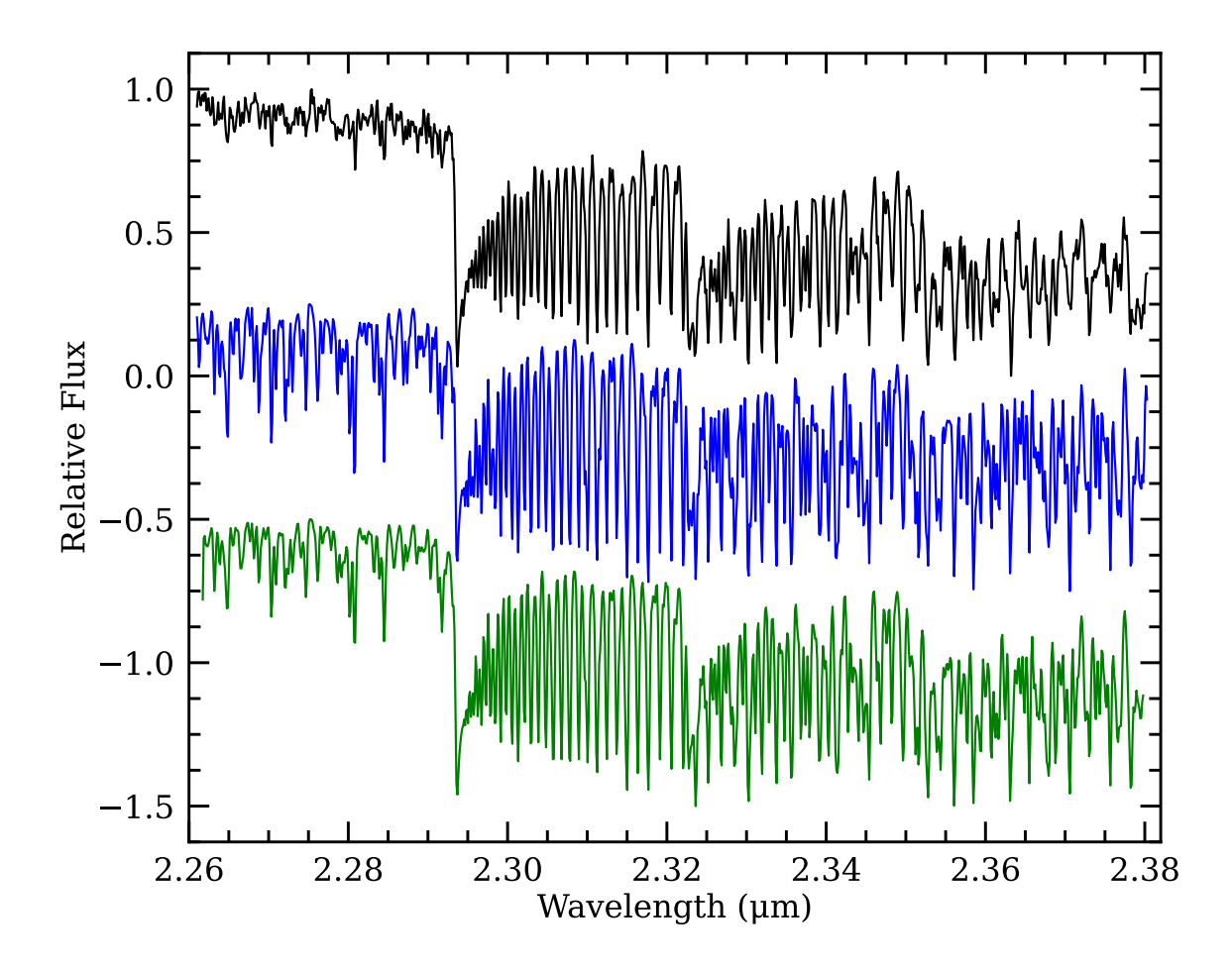


Figure 4.2: In black is the infrared spectrum of GD 1400, shown as the rest-frame co-add of all ISAAC exposures, where velocity shifts were determined from the sinusoidal model fit to the radial velocities (see Figure 4.3). In blue is a synthetic brown dwarf template with solar metallicity, $T_{\rm eff} = 1900$ K, and log g = 5.25 from the grid of Sonora Bobcat models (Marley et al., 2021). In green is another solar metallicity template at $T_{\rm eff} = 2300$ K, and log g = 5.5 from BT-Settl model spectra (Baraffe et al., 2015). The resolutions of both synthetic spectra were adjusted to match the $R \approx 8900$ resolving power of the data. Of all models tested, these two templates best match the ISAAC data, yet both fail to reproduce the notably weak-lined 2.26 - 2.29 μm region. At these wavelengths, spectral lines should betray only modest dilution by the white dwarf photosphere.

dwarf.

The Sonora Bobcat grid search identified the best fitting model with parameters $T_{\rm eff}$ = 1900 K and log g=5.25, where this template was then used to repeat the radial velocity cross-correlation. The co-added, rest frame spectrum of GD 1400B is plotted in Figure 4.2, together with the Sonora Bobcat synthetic template that provides the best match. It should be noted, however, that all of the templates within the model-grid search were adequate for cross-correlation with the science data, and effectively produce similar radial velocity estimates. This is further supported by the R^2 correlation scores, with the second best matching template ($T_{\rm eff}=1900$ K and log g=5.0) having a score only 0.3 per cent lower. Similarly, the second best synthetic spectrum, at the fixed log g=5.25 of the best match, has $T_{\rm eff}=1800$ K and a 1.0 per cent lower score.

A warmer result is obtained using the BT-Settl models, where the best cross-match predicts $T_{\rm eff} = 2300\,\rm K$ and log g = 5.5, also shown in Figure 4.2. Established on the average residual error, this model provides a decent improvement of 28 per cent compared to the best fitting Sonora Bobcat template, and notably predicts weaker lines in the $2.26-2.29\,\mu \rm m$ region. Nevertheless, both sets of atmospheric models exhibit lines that are visibly too strong compared to the weak lines observed at the blue end of the spectra. The results from both models were averaged, yielding $T_{\rm eff} = 2100 \pm 200\,\rm K$ and log g in the range 5.25-5.5.

4.4.4 Orbital period determination

The bulk of UVES spectra for GD 1400A were taken sparsely over a period of three months, yielding an orbital period of $9.978 \pm 0.002 \,\mathrm{h}$. Based on the initial determination of this period with UVES, the ISAAC data for GD 1400B were obtained more efficiently, using continuous observations over two consecutive nights, resulting in a period of 9.99 ± 0.01 h. Both independent results were obtained from a mean value of the most significant peaks within 1000 LS periodograms run on bootstrapped samples. The uncertainties quoted are two standard deviations of the set of most significant peaks. Another period inference was made using both the UVES and ISAAC data as follows. The radial velocity estimates from each instrument were fitted individually with a sine curve, resulting in a semiamplitude and period for each binary component. The radial velocities were then offset by the fitted y value, and divided by their respective, fitted velocity semi-amplitudes for normalization (ISAAC data were divided by negative semi-amplitude of the radial velocity of the secondary star $(-K_2)$ $-K_2$ because of the anti-phase relationship between the white dwarf and brown dwarf velocities). Then the two normalized datasets were combined and another period was calculated, again using the bootstrapping method, but this time taking into account uncertainties associated with each instrument (for ISAAC data the measurement weight is approximately 4.5× greater than UVES). This combined analysis results in $P = 9.976 \pm 0.006 \,\mathrm{h}$. All three period values are consistent, and the UVES estimate of $9.978 \pm 0.002 \,\mathrm{h}$ is adopted as the final value, on the basis of the highest precision. This period was then used for all subsequent analyses, namely to re-fit the radial velocity curves for each instrument individually, to obtain the final amplitude and y estimates while keeping the period fixed.

The radial velocity curves for both binary components of GD 1400 are shown in Figure 4.3 and the derived orbital and binary parameters are summarised in Table 4.2. Of particular note is the impressive performance of the cross-correlation on the infrared

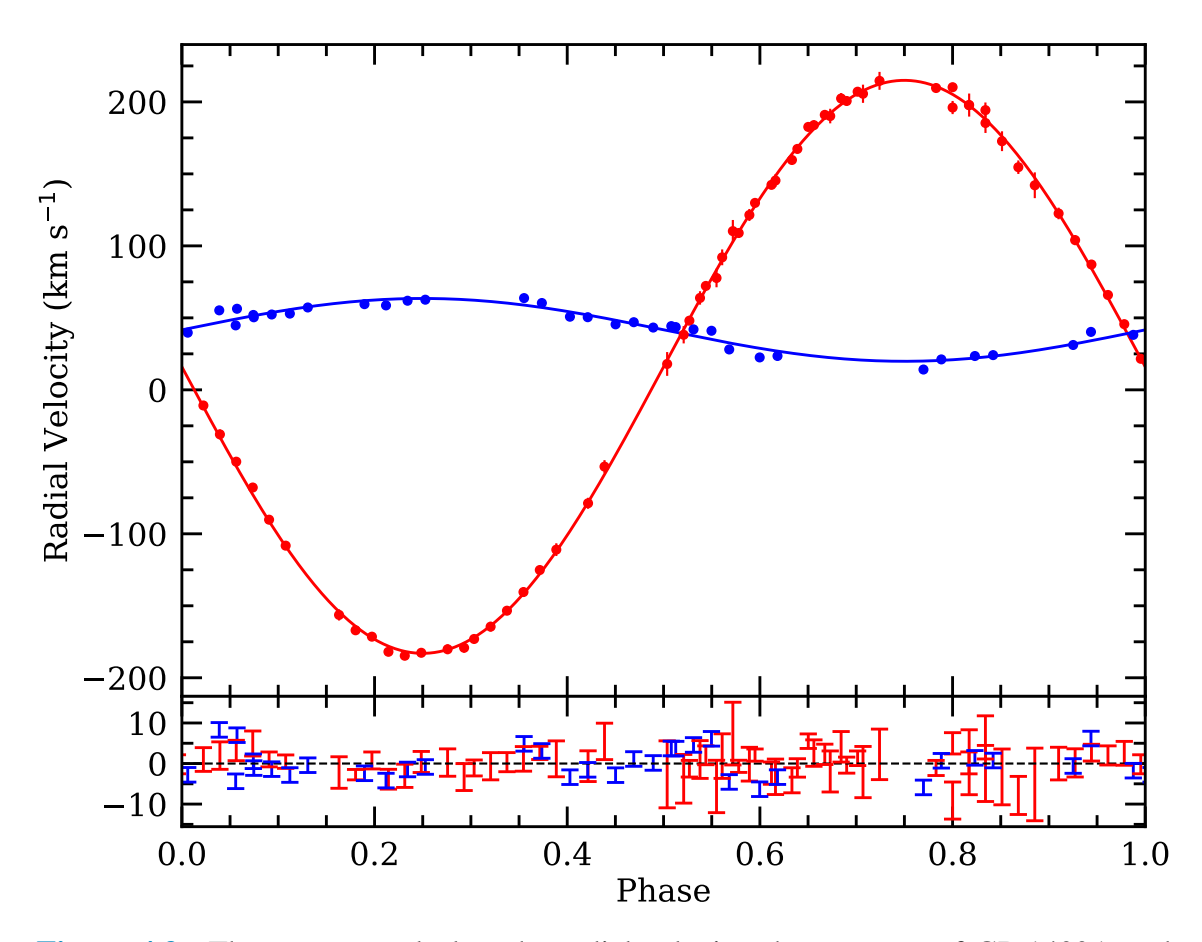


Figure 4.3: The upper panel plots the radial velocity phase curves of GD 1400A and GD 1400B in blue and red, respectively. The measurements for both components are well described by sine functions that have been fitted to the data (circular orbits are expected post-common envelope). The lower panel plots the residuals between the measurements and the simple model.

Table 4.2: Orbital and (sub)stellar parameters of the GD 1400 binary.

<i>P</i> (h)	9.978 ± 0.002
T_0 (MJD)	55498.389 ± 0.002^a
$K_1 ({\rm km s^{-1}})$	21.8 ± 1.1
$K_2 ({\rm km s^{-1}})$	199.2 ± 0.6
$\gamma_1 (\mathrm{km} \mathrm{s}^{-1})$	41.7 ± 0.7
$\gamma_2 (\mathrm{km} \mathrm{s}^{-1})$	16.0 ± 0.4
$M_1~({ m M}_\odot)$	0.59 ± 0.07^b
$M_2 (M_{Jup})$	68 ± 8
$i\stackrel{\circ}{(\circ)}$	60 ± 10
$ \gamma_1 - \gamma_2 (\text{km s}^{-1})$	25.7 ± 0.8
$GM_1/R_1c~(\mathrm{km}\mathrm{s}^{-1})$	28.9 ± 4.0

^a T_0 is provided for phase = 0 (see Figure 4.3).

spectra, where the final uncertainty on K_2 is less than $1 \,\mathrm{km}\,\mathrm{s}^{-1}$ (cf. the instrumental resolution $33 \,\mathrm{km}\,\mathrm{s}^{-1}$). This can further be appreciated in Figure 4.2, where the match between the synthetic templates and the empirical spectrum of CO bandheads is striking.

The mass of GD 1400B is calculated from Kepler's law in the form of $M_2 = M_1(K_1/K_2) = 68 \pm 8 \, \mathrm{M_{Jup}}$ (0.065 \pm 0.008 $\mathrm{M_{\odot}}$), which places it at the more massive end of substellar objects, not just those that are companions to white dwarfs. The BASE-9 estimate of M_1 with formal errors yields $M_2 = 68 \pm 4 \, \mathrm{M_{Jup}}$, and is modestly below the hydrogen-burning limit of approximately 75 $\mathrm{M_{Jup}}$ (Burrows et al., 1997) for solar metallicity. For a circular orbit, the semimajor axis is 0.009 AU or about 1.9 $\mathrm{R_{\odot}}$, and is outside of the distance required for the substellar companion to fill its Roche lobe. The difference between the measured binary component velocities, γ_1 and γ_2 , is 25.7 \pm 0.8 km s⁻¹, and is in agreement with the lower range of gravitational redshifts $28.9 \pm 4.0 \, \mathrm{km \, s^{-1}}$ expected for a $0.59 \pm 0.07 \, \mathrm{M_{\odot}}$ white dwarf. At face value, the measured $|\gamma_1 - \gamma_2|$ corresponds to a white dwarf mass of 0.54 $\mathrm{M_{\odot}}$, and suggests the actual masses of GD 1400A and B are towards the lower ends of the ranges of values allowed by their uncertainties.

4.4.5 Discussion

Despite being a well-known pulsator (Fontaine et al., 2003) with numerous frequencies reported using Sector 3 TESS observations (Bognár et al., 2020), any day-night side or irradiation effect, if present, should be detectable in time-series photometry. However, in two sectors of TESS data, which are by far the most sensitive photometric data available, there is no signal present at the orbital period of the binary. Neither is there any indication of photospheric heating (e.g. emission lines) in the day-side co-add of ISAAC spectra for GD 1400B, nor any notable differences in the day- and night-side co-added spectra. It may be that the 10 h orbital period (to which the brown dwarf should be tidally locked) and the modest $T_{\rm eff}$ of the primary are simply insufficient to give rise to an observable modulation. Lastly, a co-add of UVES spectra in the brown dwarf rest frame also failed to reveal any emission lines that could be associated with irradiation, thus strengthening the idea that

^b M_1 derived from photometry and parallax is in mild tension with the gravitational redshift implied by $|\gamma_1 - \gamma_2|$ (see Section 4.4.5).

surface heating is mild or absent at all wavelengths considered here.

A similar lack of observed irradiation was reported for ZTF J0038+2030 (van Roestel et al., 2021), a 10 900 K white dwarf with a brown dwarf companion in a 10.4 h orbit. GD 1400 is 10× brighter than ZTF J0038+2030, and thus the spectroscopic data as well as *TESS* photometry, are more sensitive. These two white dwarfs have similar effective temperatures, but the radius of GD 1400A is around 10 per cent smaller, owing to a mass that is 15 per cent higher, and the expected temperature increase on the surface of GD 1400B is likely no more than 10 K (Littlefair et al., 2014). Thus, the lack of any observed photometric modulation or emission lines is consistent with expectations.

Of additional interest, given that GD 1400 is a ZZ Ceti, stellar rotation may split the pulsation frequencies into $2\ell+1$ azimuthal components. Such equally-spaced triplets in a periodogram, provided they are associated with the dipole ($\ell=1$) mode, could help uncover the rotation period of the white dwarf. No such triplets or quintuplets (for the case of $\ell=2$) could be confidently identified in either the 120 and 20 s *TESS* data. However, the white dwarf may not be tidally locked (unlike the brown dwarf), thus the orbital period may not equate to the white dwarf rotation rate.

The brown dwarf in this system is an excellent benchmark for existing models, where the temperature, mass, and age of GD 1400B can all be estimated. Although the system experienced a common envelope, the mass of the white dwarf suggests that single star evolution was not drastically truncated, and provides a lower limit on the system age via white dwarf cooling at around 0.5 Gyr. The white dwarf mass is consistent with a CO-core remnant that completed the RGB and where the common envelope was initiated further out during the AGB. However, the current white dwarf mass is almost certainly lower than would have resulted for a single star, and thus a total age for the binary system, using initial-to-final mass relations (IFMRs) and main-sequence lifetimes, will be overpredicted and unreliable. Independent from evolutionary considerations of the primary, the 3D space motion of GD 1400 is $(U, V, W) = (3, -1, -6) \text{ km s}^{-1}$, and consistent with a relatively young, thin disk star with a likely age less than around 2 Gyr.

Based on brown dwarf evolutionary models, at an age of $1.0\,\mathrm{Gyr}$, a $68\,\mathrm{M_{Jup}}$ object should have an effective temperature near $1800\,\mathrm{K}$ and surface gravity $\log g \approx 5.3$ (Baraffe et al., 2015). Of the spectral templates tested above, a Sonora Bobcat model with $T_{\rm eff} = 1800\,\mathrm{K}$, $\log g = 5.25$ (Marley et al., 2021) provides an adequate fit to the ISAAC spectrum over the CO bandheads. However, if GD 1400B has $T_{\rm eff} \approx 2100\,\mathrm{K}$, as inferred by considering both cloudy and cloud-free model fits to the K-band ISAAC spectrum, then it has a brown dwarf cooling age of only $0.6\,\mathrm{Gyr}$. If the actual substellar companion mass is within the lower range of values allowed by the uncertainties, as suggested by the gravitational redshift for M_1 , then its cooling age will be somewhat younger.

The white dwarf cooling age is 0.48 ± 0.01 Gyr and can thus accommodate a total system age less than 1 Gyr via binary evolution, consistent with the relatively warm brown dwarf temperature implied by the theoretical model fits. An alternative history is that the total age is somewhat older, but that GD 1400B has been re-heated during circularization and tidal synchronization. This possibility has yet to be explored from a theoretical perspective, and is beyond the scope of this work, but a potentially useful speculation because at least one substellar companion to a white dwarf appears to be unexpectedly inflated (i.e. has a radius too large for its evolutionary age; Casewell et al. 2020a).

It should be emphasized that the T_{eff} for GD 1400B has been derived in an unconventional way, by fitting spectral templates to a K-band spectrum covering a narrow

wavelength range, and at moderately high spectral resolution. Essentially, only the CO bands have been fitted, and while these features are distinctive, providing excellent anchor points for model comparison, this atypical determination of brown dwarf parameters may result in systematic errors. To underscore this possibility, as pointed out earlier, Figure 4.2 demonstrates that neither of the synthetic spectral grids can provide a decent match to the absorption lines in the $2.26-2.29~\mu m$ region of the ISAAC data.

The cause of this line strength mismatch between models and observations of GD 1400B is unclear. First, it cannot be caused by dilution from the light of the primary. The substellar companion is comparably bright at these wavelengths, and any significant dilution would similarly weaken the depths of its CO features, which is not observed. Second, and ignoring the young disk kinematics and the likely youth of the warm brown dwarf, the weak lines cannot be due to metal poverty. Owing to increased collision-induced absorption in the *K*-band, metal-poor L subdwarfs, and even warmer M subdwarfs, display spectra where the CO bands are typically absent or notably weaker than their solar metallicity counterparts (Burgasser, 2004; Burgasser et al., 2009; Zhang et al., 2017, 2018). Third, the significantly weaker lines in the observations are unlikely to be due to clouds. The BT-Settl models exhibit moderately weaker absorption lines than the cloud-free Sonora Bobcat grid, and thus provide a better overall match to the data, but clouds are not a known source of line obscuration (Baraffe et al., 2015).

Remaining possibilities include a particularly dusty atmosphere or current modelling deficits. In at least some cases, atomic line profiles in brown dwarfs can be significantly affected by dust, but dusty spectral models are currently limited, available only for a few optical lines (Johnas et al., 2008). Comparing contemporary models with data covering a broader range of wavelengths may help shed light on this apparent discrepancy in line depths for GD 1400B. While there are no other L dwarfs with $R \approx 9000~K$ -band spectra, available low- to medium resolution spectra reveal few or no features in the region blueward of the first CO bandhead (McLean et al., 2003; Cushing et al., 2005; Rojas-Ayala et al., 2012), in contrast to the strong and feature-rich models in Figure 4.2. Thus, the spectrum of GD 1400B may not be unusual, but the models which remain at odds with observed L dwarf spectra.



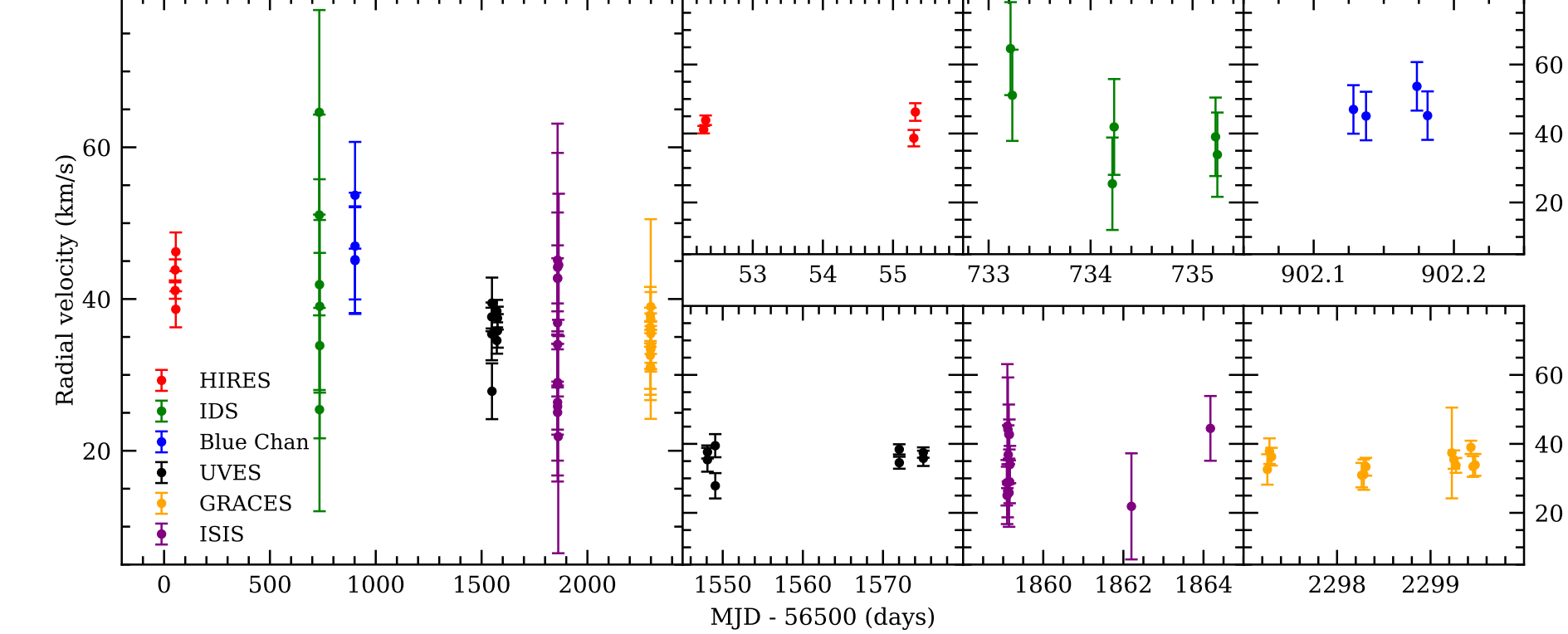


Figure 4.4: All radial velocities and their errors for PG 0010+281 as determined from H α line fitting. The six panels on the right show zoomed-in regions of the left panel. The observations span just over six years, and have been acquired with six different instruments, each designated in the plot legend with a distinct symbol colour (see Table 4.1). Measurements are plotted as a function of MJD both for the overall, multi-instruments dataset, as well as for individual instruments. The plotted data are uncorrected for any systematic offsets between instruments.

4.5 Analysis and results: PG 0010+281

4.5.1 Stellar parameters

Physical parameters and ages were constrained from *Gaia* DR3 parallaxes and Pan-STARRS photometry using BASE-9. As for GD 1400, the posterior distributions are non-Gaussian with means and 68 percentile credible intervals yielding $T_{\rm eff} = 26\,500 \pm 1000$ K, $M = 0.569 \pm 0.005\,{\rm M}_{\odot}$, and a total age $7.5 \pm 2.5\,{\rm Gyr}$ assuming isolated stellar evolution. Similarly to GD 1400, a standard deviation of recently published results (Liebert et al., 2005b; Gianninas et al., 2011; Xu et al., 2020; Gentile Fusillo et al., 2021b) and the BASE-9 estimate modestly increases the uncertainties to $T_{\rm eff} = 26\,500 \pm 1100\,{\rm K}$, $M = 0.569 \pm 0.027\,{\rm M}_{\odot}$. These are the adopted mass and effective temperature for this work.

The kinematics of PG 0010+281 do not support such an old age as suggested by single star evolution. Using *Gaia* DR3 astrometry, together with an estimated radial velocity from the weighted mean radial velocity (36.1 km s⁻¹), corrected for the gravitational redshift (24.7 km s⁻¹) of a $M = 0.569 \, \mathrm{M_\odot}$ white dwarf, yields three dimensional space velocities $(U, V, W) = (28, 1, -10) \, \mathrm{km \, s^{-1}}$. In accordance with chemo-kinematical models of the local solar neighbourhood, the white dwarf is 80× more likely to be a thin disk star than a member of the thick disk (Bensby et al., 2014), and thus likely to have an age below 5 Gyr. Kinematics are not conclusive by any means, as any star of any age can have any space velocity, where Galactic kinematical populations are established primarily by their dispersions, and to a much lesser degree their mean space velocities. However, the mismatch between kinematics, mass and total age suggests the possibility of binary evolution.

Because of this unexpectedly low mass and total age conflict, three further age and mass determinations were considered, two of which are fully independent. First, instead of Pan-STARRS grizy fluxes, SDSS ugriz photometry was used as input for BASE-9. This yields an even lower white dwarf mass, with a most probable total age of 9.8 ± 1.9 Gyr, and was therefore discounted in favour of the results using Pan-STARRS photometry. Second, the Gaia eDR3 catalogue of white dwarfs gives $M = 0.52 \pm 0.02$ M $_{\odot}$ calculated on a combination of parallax and Gaia colours, which are then fitted using a grid of atmospheric models using synthetic photometry (Gentile Fusillo et al., 2021b). From published IFMRs (e.g. Cummings et al. 2018, the same as used for the BASE-9 calculations), such a low white dwarf mass would yield a progenitor that should remain on the main sequence over a Hubble time, and is thus unphysical, instead requiring truncated (binary) stellar evolution. Third, there is a spectroscopic determination of $T_{\rm eff}$ and log g proceeded from Balmer line fitting, which yields $M = 0.57 \pm 0.02$ M $_{\odot}$ (Gianninas et al., 2011), in excellent agreement with the BASE-9 results based on Pan-STARRS. Thus, all available mass estimates for PG 0010+281 are sufficiently low that binary evolution is a possibility.

4.5.2 Radial velocities

The radial velocities of PG 0010+281 were determined as described for GD 1400A in Sections 4.4.1 and 4.4.2, and are plotted as a whole and centred on individual instruments in Figure 4.4.

Instrument	Year	$v_{\rm rad}$	$N_{ m obs}$	<i>p</i> -value	
		$(km s^{-1})$			
HIRES ^a	2013	42.1 ± 0.8	4	0.068	
IDS	2015	42.2 ± 5.2	6	0.378	
Blue Channel	2016	47.7 ± 3.5	4	0.801	
UVES	2017	36.6 ± 0.7	8	0.177	
ISIS	2018	34.8 ± 4.2	13	0.996	
GRACES	2019	35.1 ± 0.8	12	0.646	

^a Wavelength calibration and science frames not taken concurrently.

Notes. The p- value gives the likelihood the measurements are consistent with a single star with a constant radial velocity given by the weighted mean. A value p < 0.0027 indicates that the star is binary at 3σ confidence.

Uncertainties on the radial velocities of this target were estimated using the bootstrapping method. In detail, a number of points corresponding to the total number of points in a spectrum are selected at random with replacement, and the resulting Balmer profiles are refitted 1000 times per spectrum. The standard deviation of the resulting radial velocities was then estimated. In general, error estimation from bootstrapping provides a more robust result if there are imperfections in the input data, but the method performed less well for low resolution spectra. The NLTE core of H α in a low resolution spectrum would consist of only a few points which can be difficult to fit if any of these points were not selected by the algorithm.

To quantify the presence of any variability or excessive scatter in the radial velocities, beyond what would be expected from a constant radial velocity, the χ^2 statistic and the resulting probability are calculated (Maxted et al., 2000). Briefly, this includes calculating a weighted mean radial velocity, then performing a goodness-of-fit test between the observed radial velocities and the calculated mean. If the constant mean value provides a poor fit to a potentially varying signal, then the signal is judged as variable. This is quantified by calculating the probability p of observing such a signal from random radial velocity fluctuations where a low p value signifies high scatter and thus probable variability. The individual instrument means and resulting p-values are given in Table 4.3.

The calculated, weighted mean radial velocities for the individual spectrographs can identify systematic offsets between the sets of observations. To ascertain whether or not such observed velocity offsets can be corrected, individual sky line velocities in raw spectra were measured. Depending on availability, one or both of the sky lines at 5577.34 Å and 6300.30 Å were fitted, and any velocity shifts were calculated, based on their expected air wavelengths. In the case of the MMT Blue Channel observations, and despite the fact that arc lamps were taken either immediately before or after each exposure, the sky lines varied notably between frames and the measured velocity shifts were poorly behaved. In the case of the HIRES data, significant positive shifts were detected in all exposures; around 5 and $10\,\mathrm{km\,s^{-1}}$ for the HIRESr and HIRESb observations, respectively. However, it should be noted that wavelength calibration frames were not taken concurrently with science frames, and thus the effects of telescope flexure cannot be corrected.

4.5.3 Companion limits

Owing to significant instrumental offsets in velocities of skylines, as described above, the Blue Channel and HIRES observations were analysed individually, and were not combined with data from the other instruments. In contrast, and using the velocity offsets derived from sky lines, the data from IDS, UVES, ISIS, and GRACES all have an average systematic offset of $\lesssim 1 \, \mathrm{km \, s^{-1}}$.

To quantify the sensitivity of the observations to potential orbital periods, a number of simulations were run that take into account the calculated physical parameters of PG 0010+281 and a simulated companion of a specified mass. The simulated signal is a sine curve with a fixed period, random inclination (sampled uniformly from arccos(i)function) and random orbital phase. The resulting signal is sampled using the time stamps of the actual observations. Time stamps from IDS, UVES, ISIS, and GRACES were used in the simulations since these instruments do not show any significant systematic offsets $(\le 1 \,\mathrm{km \, s^{-1}})$ as determined from the sky line measurements. To assess if such a signal would be detected, a χ^2 goodness-of-fit statistical test is performed to identify whether the generated signal is statistically similar to a constant radial velocity with Gaussian uncertainties determined from the actual radial velocity measurement errors. A generated signal is deemed recoverable or significantly variable if its p-value < 0.0027 (3 σ in a normal distribution). For each specified period, 100 000 simulations were performed, consisting of 100 random phases for 1000 randomly sampled inclinations. Periods from 1 h to 2 d were sampled in step sizes just under 3 min, and the resulting sensitivities are plotted in Figure 4.5.

The radial velocity observations provide excellent sensitivity to orbital periods within 12 h. Observations by UVES and GRACES are the most powerful, and although if treated separately there are some gaps in the sensitivity at certain periods, by combining these observations together such gaps become practically non-existent. The small systematic offsets of IDS, UVES, ISIS, and GRACES should allow these datasets to be combined as if from a single instrument (albeit with different errors). Overall, it can be concluded that the temporal sensitivity of the data is adequate for substellar companions that experienced common envelope evolution.

A slight and superficial long-term trend is present in the radial velocity, which is reflected in the mean radial velocity values for each instrument. As can be seen in Table 4.1, the first three datasets were acquired from 2013 to 2016, while the latter three were taken from 2017 to 2019. The higher mean values from 2013 to 2016 followed by lower values from 2017 to 2019 might be construed to signify an orbital period of the order of years. However, such an interpretation is unlikely for two reasons. First, the sky line analysis showed that the radial velocities from HIRES and Blue Channel are less reliable. Moreover, the actual systematic offsets cannot be fully pinned down just from the sky line measurements, and would require radial-velocity standard observations, which were not acquired. Second, unlike radial velocity data, astrometric wobbles are relatively insensitive to orbital inclination, and periods on timescales near a year should be revealed by *Gaia*. However, the DR3 renormalised unit weight error is 1.044 (Gaia Collaboration et al., 2022), indicating that a single-star model provides a good fit to the observed precision astrometry. Long term variability cannot be ruled out but appears unlikely.

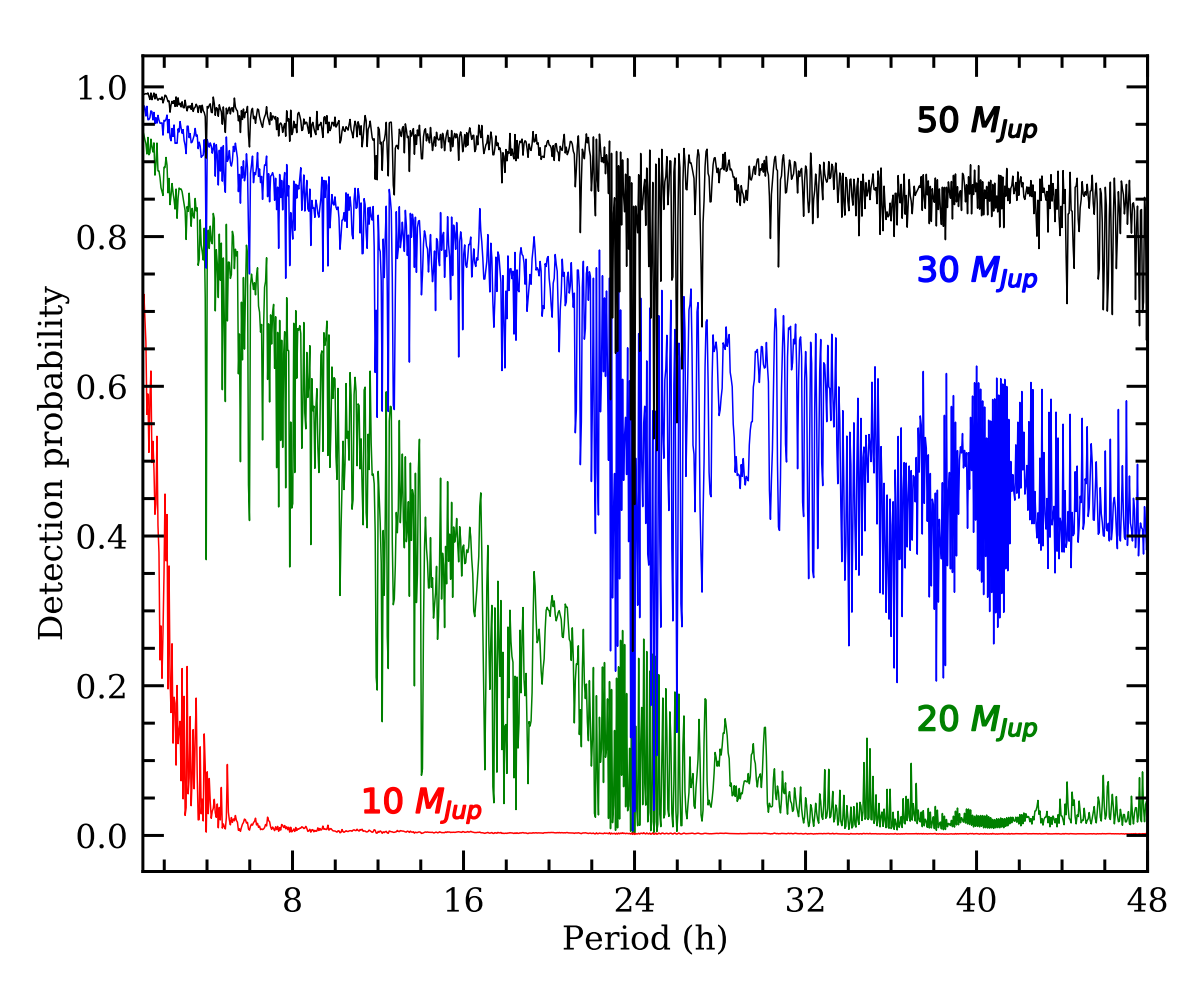


Figure 4.5: Detection probabilities as a function of orbital period for a range of substellar companion masses, based on a χ^2 test and the combined radial velocity data from IDS, UVES, ISIS, and GRACES. Of particular interest is the region below 12 h, which spans the orbital periods of all known white dwarf - brown dwarf binaries (Zorotovic & Schreiber, 2022). These brown dwarf companions to white dwarfs have masses in the range 50 – 70 M_{Jup} , for which the detection probabilities are typically above 0.9.

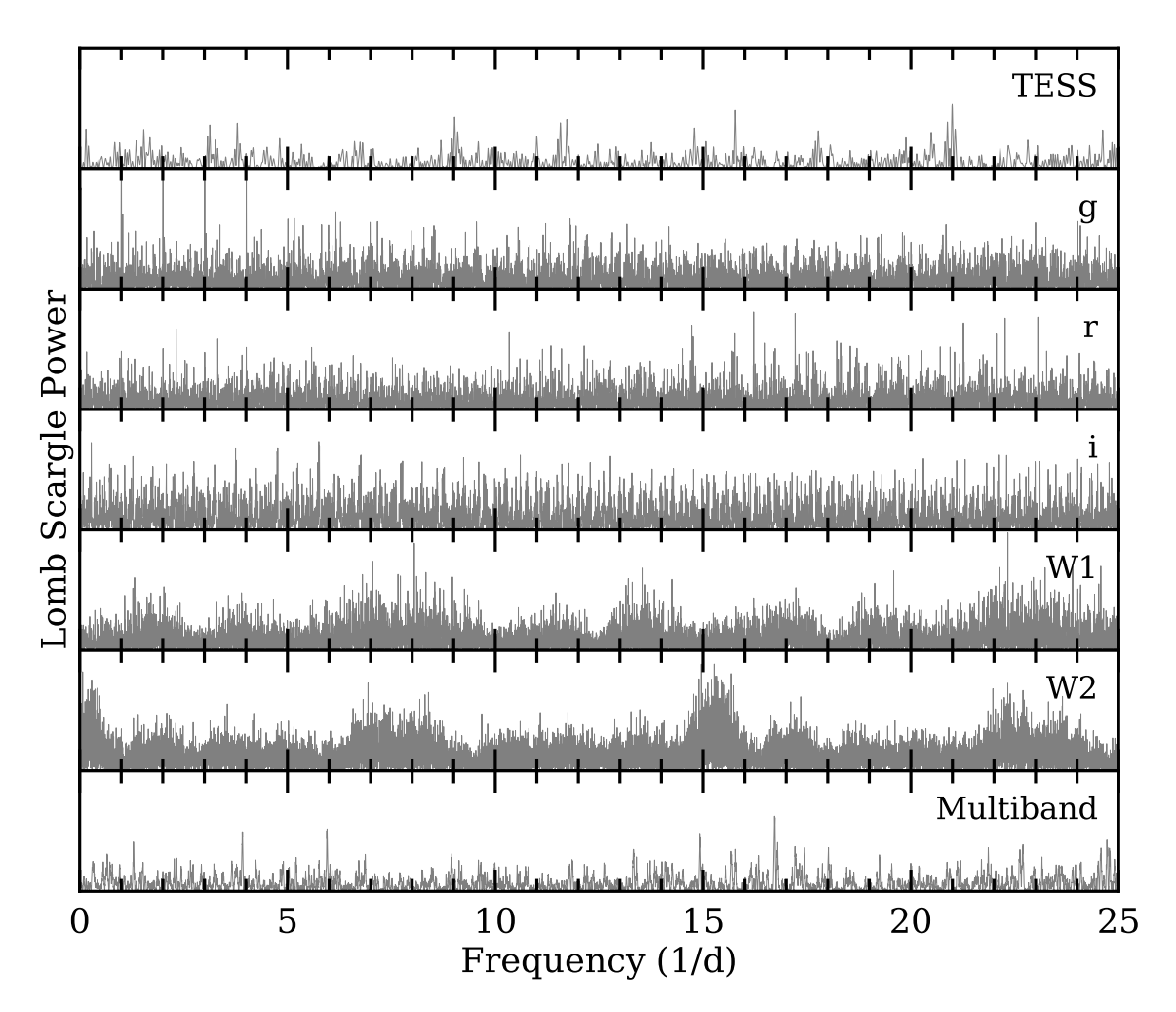


Figure 4.6: LS periodograms for PG 0010+281 photometry. From top to bottom, the panels correspond to: *TESS*, ZTF *gri*, *WISE W*1 and *W*2, and a multi-band periodogram that combines all of the aforementioned photometry. There are no significant periods except at aliases expected from ground-based observations, where the top of the y-axis range corresponds to a 1 per cent false alarm probability level in each panel.

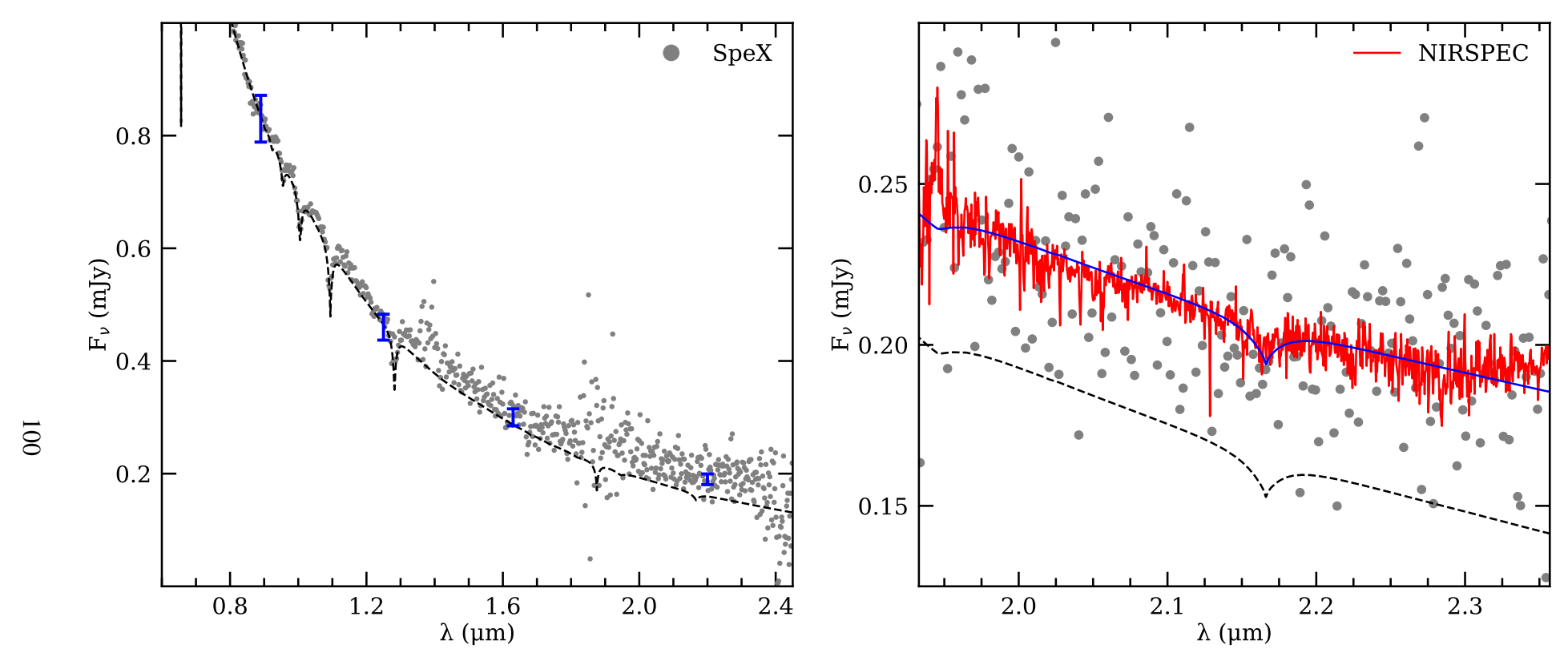


Figure 4.7: Infrared spectra of PG 0010+281. The left panel shows the SpeX prism spectrum (grey points), together with the same photometry (blue error bars) and white dwarf atmospheric model (black dashed line) as shown in Figure 4.8. The right panel shows the NIRSPEC spectrum in red, offset to match the K-band photometric flux, and with a weak but clear detection of Br γ from the stellar photosphere. The SpeX data and the white dwarf model atmosphere are also plotted as on the left, where the blue solid line includes the addition of a 1000 K blackbody. The upturn near 2.3 μm in the NIRSPEC data are not seen in the SpeX data, and thus may be an artefact of the reduction process or instrument settings.

4.5.4 Time-series photometry

The available photometric monitoring of PG 0010+281 with TESS, ZTF, and WISE were analysed using the ASTROPY package implementation of the LS periodogram. These results are plotted in Figure 4.6, including a single collective light curve analysis, using the multiband implementation of the periodogram (VanderPlas & Ivezić, 2015). As can be seen in the plot, no significant frequencies have been identified at any wavelength, and where TESS is by far the most sensitive in terms of cadence. The lack of statistical significance was determined using a standard false alarm probability (VanderPlas, 2018), estimated via a bootstrapping method. The analysis shows that there are no frequencies in any of the surveys or their combination with a false alarm probability below 1 per cent, except the aliases expected from the ground-based observations in ZTF g band.

While the radial velocity analysis is sensitive to the secondary mass, a heating or day-night side effect is primarily driven by the size and temperature of any irradiated spot. The radii of low-mass stars, brown dwarfs, and giant planets are all roughly equal down to M_{Jup} , and thus the heating effect might still be pronounced for a wide range of substellar secondary masses. Furthermore, the white dwarf has $T_{\rm eff} \approx 26\,500\,\rm K$ which is more than sufficient to drive such a variation for a range of short-period orbits and companion properties. For a brown dwarf temperature near 1700 K, and orbital periods within 1 d, irradiation should raise the surface temperature by at least 100 K, and increase to over 200 K for periods within 12 h (Littlefair et al., 2014). The fact that no photometric modulation is observed is in agreement with the radial velocity data, and there is likely no substellar companion consistent with post-common envelope evolution.

As with radial velocities, an orbital inclination that is face-on will not produce any variations from a day-night side effect, and such a signal will diminish with increasing inclination angle. However, this requires a finely-tuned orientation, and while it cannot be ruled out, this is unlikely.

4.5.5 Infrared flux excess

In Figure 4.7 are shown the two infrared spectra taken of PG 0010+281. The SpeX data are consistent with a modest excess in the H and K bands, but are otherwise too noisy to discern any possible features. The higher resolution and higher S/N spectrum taken with NIRSPEC exhibit two features that are possibly noteworthy. The first is the upturn near 2.3 μ m, which is rather abrupt and angular in the data. While the SpeX data are noisy, the data extend to 2.55 μ m and there is no upturn evident in that spectrum. At present, a reduction or instrumental artefact cannot be ruled out. The second feature is the weak but clear detection of Br γ , consistent with a partial detection of the white dwarf photosphere, possibly diluted by another source, such as a thermal continuum from warm dust as modelled and plotted. Overall, the infrared spectra fail to reveal any significant slope or features associated with a companion (e.g. Casewell et al. 2020b) or a gradual upturn associated with the rise of thermal dust emission (e.g. Kilic et al. 2006), but are far from conclusive based on the available combinations of wavelength coverage and S/N.

A substellar survivor?

The constraints from the previous Sections 4.5.2 and 4.5.4 have direct bearing on one of the hypotheses for the excess infrared emission observed with *Spitzer* IRAC (Xu et al., 2015). An irradiated companion would necessarily be in a close orbit, which should most often result in radial velocity variations, emission lines and photometric variation as the heated side changes viewing configuration, especially from a relatively hot white dwarf such as PG 0010+281. While both radial velocity changes and photometric variations should be zero for a binary inclined by 90°, emission lines from a low-mass companion might still be visible at all orbital phases. Despite this fact, there is no evidence for emission lines in any of the numerous spectra obtained for PG 0010+281 (see Section 4.3, and UVES footnote).

A more widely separated, self-luminous companion is possible, as it would not lead to photometric or radial velocity variability. The existing K-band image of PG 0010+281 (Xu et al., 2015) should rule out an equally luminous companion at a projected separation beyond roughly 33 AU, which is 1/3 of the 0.8 arcsec FWHM reported in the observation, at a distance of 134 pc based on the *Gaia* DR3 parallax of 7.47 ± 0.06 mas. Figure 4.8 shows the spectral energy distribution of PG 0010+281 from the ultraviolet through the infrared, including *Spitzer* IRAC photometry performed and analysed here independently. The data at $5.7 \,\mu$ m are ignored as the errors are too large to be reliable, and furthermore the IRAC image appears possibly extended, and thus may contain light from a background galaxy. Models for an irradiated and non-irradiated L5 dwarf are broadly consistent with the observed photometry, given an uncertain companion temperature and radius. Keeping in mind that the two, shorter-wavelength IRAC observations are non-simultaneous, and the fact that the effects of irradiation are likely to be diverse across individual systems (Lee et al., 2022), this model seems plausible solely on the basis of the infrared photometric excess.

However, as discussed in the previous sections, the constraints on radial velocity, photometric modulation, and astrometry only allow a narrow and finely-tuned range of orbital configurations. A substellar companion, such as those known to orbit white dwarfs, would have to be in a nearly face-on (and short-period) orbit to eschew detection in all three of these observable metrics, and is therefore unlikely.

A debris disk?

While substellar companions cannot be completely ruled out, if the relatively low white dwarf mass is set aside, then the results favour a debris disk as the cause of the infrared excess. In this case, the thermal emission signature is subtle compared to many white dwarfs that reprocess up to 3 per cent of the incident stellar radiation (Rocchetto et al., 2015), but such faint disks are well represented in the population of metal-polluted white dwarfs observed with *Spitzer* (Farihi et al., 2010c; Bergfors et al., 2014).

It is now well understood that circumstellar material orbiting white dwarfs is not always contained within the Roche radius, nor always or only in an optically thick configuration (Farihi et al., 2018b; Swan et al., 2020). At the time of discovery, Xu et al. (2015) interpreted the infrared excess towards PG 0010+281 as a viable dust disk within the Roche limit using the older, canonical model of a flat and opaque configuration, as in the rings of Saturn. That study appealed to the shielding of dust within a vertically flat structure, to argue that $1200\,\mathrm{K}$ grains can be present near $0.5\,\mathrm{R}_{\odot}$, and concluding such

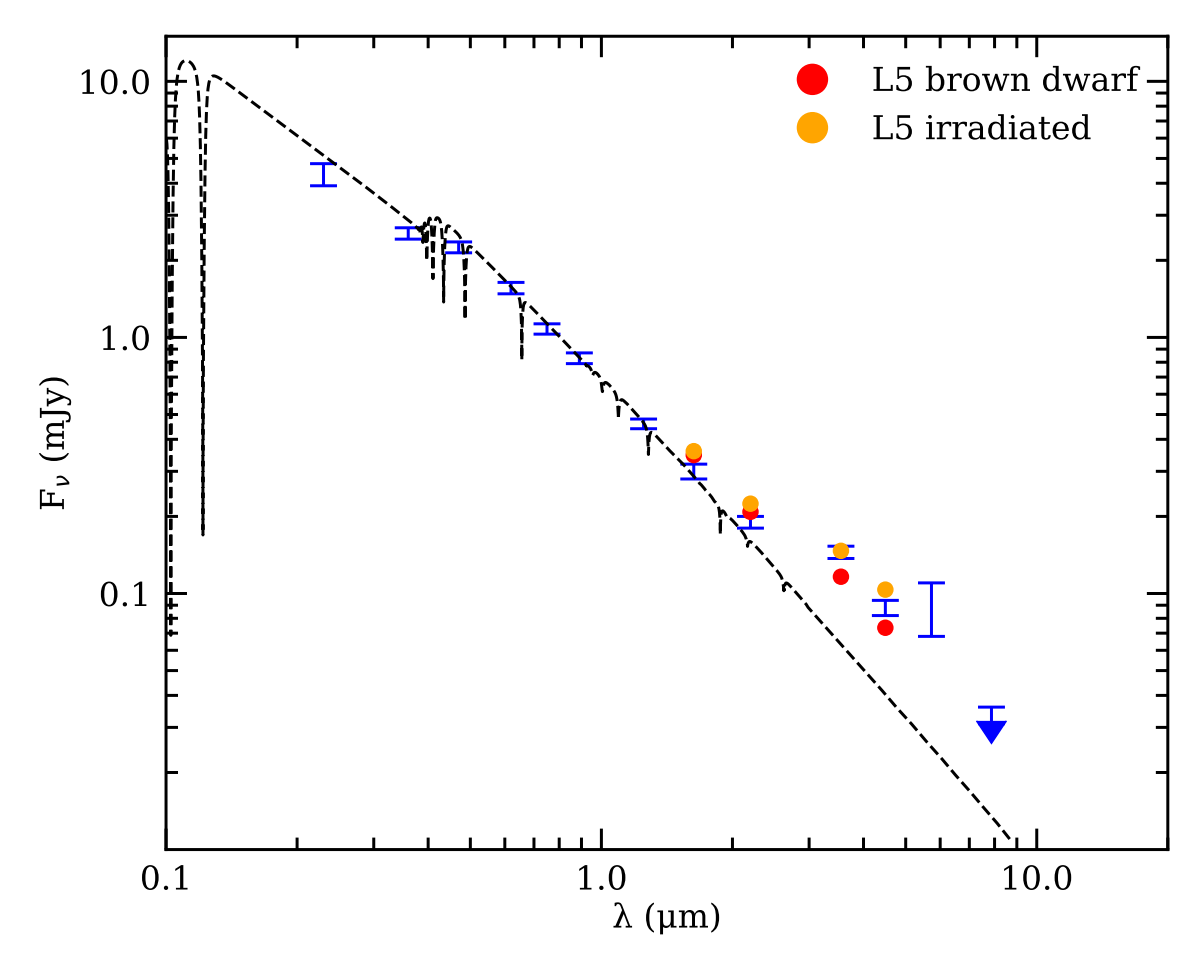


Figure 4.8: The photometric spectral energy distribution of PG 0010+281. Blue error bars show *GALEX* near-ultraviolet, optical SDSS *ugriz*, and *Spitzer* IRAC fluxes (measured here independently). The stellar photosphere is plotted as a black dashed line, and modelled using a 27 000 K pure hydrogen atmosphere white dwarf (Koester, 2010). Also plotted are models that include the addition of flux from an L5-type brown dwarf, both without (red circles) and with (orange circles) the influence of stellar irradiation. The brown dwarf fluxes are derived from an extensive study of M, L, and T dwarfs using *Spitzer* IRAC (Patten et al., 2006), and the effects of irradiation were estimated based on the observed IRAC variability for WD 0137–349 (Casewell et al., 2015). The IRAC 3.6μm and 4.5μm data for PG 0010+281 were 10–15 min apart, where an irradiated companion could change aspect somewhat for relatively short orbital periods.

a disk was possible. However, fully-exposed blackbody grains would attain $T > 2200 \, \mathrm{K}$ at $1 \, \mathrm{R}_{\odot}$ from the white dwarf, and thus there can be no solids present to provide the hypothesized shielding (Rafikov & Garmilla, 2012). An independent study has concluded that, in general, all material within the Roche limit would be rapidly sublimated by a 26 500 K white dwarf because no dust can arrive intact or otherwise be produced in this region (Steckloff et al., 2021).

For an infrared excess with emission temperatures in the range 1000–1300 K, a white dwarf temperature 26500 K, and a stellar radius 0.0146 R_☉, blackbody dust should be located at radii 3.0–5.1 R_☉, and thus orbit comfortably distant from the Roche limit. This debris disk model can be interpreted in a rather straightforward manner, where all material closer to the star is gaseous and thus unseen in the infrared. Poynting-Robertson drag on the inner portion of the disk near $3 R_{\odot}$ would remove typical $1 - 10 \mu m$ grains on roughly 4 – 40 yr timescales and a pileup should occur until fully depleted. If confirmed, such a debris disk would be yet another example of dust orbiting well outside the Roche limit (Farihi et al., 2017; Vanderbosch et al., 2020; Guidry et al., 2021; Farihi et al., 2022), and thus another example that the canonical model of flat and opaque rings (Jura, 2003) is either incorrect or not the whole picture for those stars with prominent infrared excess in Spitzer and WISE (Farihi et al., 2018b; Swan et al., 2020). And while heavy elements are not detected in optical spectra of PG 0010+281, it is not surprising given the relatively high temperature and corresponding opacity in the white dwarf atmosphere. A prediction of the debris disk model supported here, is that metal pollution should be apparent in ultraviolet observations, which are more sensitive for stars of similar temperature (Koester et al., 2014).

Observations with *JWST* MIRI can in principle confirm the dust with the detection of solid-state features such as those typical of planetary silicates (Jura et al., 2009). However, if there is both dust and a (wide or otherwise hidden) substellar companion, as in SDSS J155720.77+091624.6, then the interpretation of the infrared spectra may be complicated.

A cannibalized companion?

There is tension between the low white dwarf mass and the old total age it implies, versus the expectations of single star evolution, where known white dwarfs hosting debris disks are essentially a single star (or distant binary) population (Wilson et al., 2019). And although these are not mutually exclusive possibilities in terms of the circumstellar architecture, the disparate age indicators cannot be reconciled easily. One possible way to resolve this tension, is if the white dwarf destroyed one or more giant planets on the AGB, which enhanced mass loss during their final death spiral (i.e. a fatal common envelope Mustill & Villaver 2012; Nordhaus & Spiegel 2013; Soker 2013).

The cooling age for a $0.57\,\mathrm{M}_\odot$ white dwarf with $T_\mathrm{eff}=27\,000\,\mathrm{K}$ is negligible (< 15 Myr). Under an assumption of single star evolution for such a low remnant mass, however, there are essentially no reliable empirical constraints on the zero-age main-sequence progenitor. As mentioned above, IFMRs for a $0.57\,\mathrm{M}_\odot$ white dwarf predict main-sequence progenitors with hydrogen-burning lifetimes approaching or exceeding a Hubble time, thus suggesting the stellar evolution of PG 0010+281 was not typical of isolated stars.

While somewhat speculative, it would be beneficial to simulate the effects of planetary

engulfment on post-main sequence evolution, especially in terms of mass loss. It is well known that main-sequence stars commonly host multiple planets that orbit sufficiently close to be engulfed during the post-main sequence. The basic properties of white dwarfs, such as atmospheric composition, structure and mass of the outer layers, total remnant mass, and magnetism might all be dependent on such processes. Thus, the effect of planets on stellar evolution may be a key issue in white dwarf formation and subsequent evolution.

4.6 L dwarf survivors of giant encounters

To date, the only substellar survivors of one or both phases of giant stellar evolution appear to be brown dwarfs with masses in the range of roughly 50 – 70 M_{Jup}, and with spectral types consistent with L dwarfs (nine currently known, including GD 1400B; Zorotovic & Schreiber 2022). In contrast, at wider orbital separations, there is a small number of substellar companions to white dwarfs that are unambiguously cooler or less massive, in addition to widely bound L-type dwarfs. A possibly incomplete list of wide substellar companions to white dwarfs, where a common envelope would not have developed, includes: the prototype L dwarf GD 165B (Becklin & Zuckerman, 1988), the L dwarf PHL 5308B (Steele et al., 2009), the T dwarfs LSPM J1459+0851B (Day-Jones et al., 2011) and PSO J058.9855+45.4184B (Zhang et al., 2020), the likely Y-type dwarf WD 0806-661B (Luhman et al., 2012, 2014), and an old, metal-poor T dwarf Wolf 1130C, which is bound to a post-common envelope (11.9 h) binary consisting of an M subdwarf and an unseen, massive white dwarf Wolf 1130AB (Mace et al., 2018).

One possible exception to this is the Jupiter-sized body in a 1.4 d orbit around WD 1856+534 (Vanderburg et al., 2020), assuming that it did actually emerge from a common envelope. That scenario is uncertain for a few reasons, one of which is the fact that post-common envelope, low-mass stellar or substellar companions at these longer orbital periods are rare or non-existent (Nebot Gómez-Morán et al., 2011). Another potential complication is that there are not one, not two, but three stars in this system (McCook & Sion, 1999; Vanderburg et al., 2020), and more than one study has suggested this object arrived recently by Kozai-Lidov migration (Lagos et al., 2021b; O'Connor et al., 2021; Stephan et al., 2021). Other solutions that invoke the common envelope require fine tuning (Lagos et al., 2021a) and are thus far less likely.

Therefore, at face value, the evidence suggests that a mass of around $50\,M_{Jup}$ is a robust benchmark for survival of the common envelope. This strongly implies that all objects of planetary masses as represented by the solar system, are destroyed during the RGB or AGB if engulfed, and merge with the central star. These merging events, of objects up to a few tens of M_{Jup} , may have observational implications for the final mass and properties of the white dwarf remnant, including the potential emergence of a magnetic field.

4.7 Summary and conclusions

New data are presented and analysed for GD 1400 and PG 0010+281, both white dwarfs where closely-orbiting substellar companions were previously suspected. The radial velocity and photometric search for a substellar companion to PG 0010+281 did not identify any candidates, and relatively good constraints are established for short periods that are typical of post-common envelope binaries. The infrared spectroscopy presented here does

not conclusively distinguish between a cool companion and dust emission, but photospheric Br γ is detected which likely favours the latter. As a result, it appears the infrared excess measured for PG 0010+281 is more consistent with a single star and circumstellar dust, but its mass and age appear potentially inconsistent with isolated stellar evolution.

In contrast, GD 1400A and B are successfully characterised in this chapter, including orbital parameters, substellar companion mass, and its $R \approx 9000~K$ -band spectrum. Derived from comparisons with synthetic templates, the benchmark brown dwarf appears relatively warm at $T_{\rm eff} \approx 2100~{\rm K}$, and also rather young with an implied age of less than around 1 Gyr according to evolutionary models for the calculated mass of $68~{\rm M_{Jup}}$. The chapter notes a dearth of T-type and later brown dwarfs as companions to white dwarfs in post-common envelope systems, whereas cooler and less massive brown dwarfs clearly form and survive at wide separations. This suggests a crude benchmark of $50~{\rm M_{Jup}}$ for a companion to survive engulfment on the RGB (or both RGB and AGB) common envelope evolution.

Chapter 5

Measurement of stellar and substellar winds using white dwarf hosts

This chapter is based on the paper of the same title (Walters et al., 2023). Data for this publication were obtained from publicly available data archives, with proposal IDs and PIs clearly stated. Abundances were determined by P. Dufour in Section 5.4.3. Calculations related to the irradiation of brown dwarf atmospheres were performed by L. Fossati, S. Mohanty, and J. E. Owen. These calculations are mentioned in Section 5.6.4. All other work is my own.

5.1 Abstract

White dwarfs stars are known to be polluted by their active planetary systems, but little attention has been paid to the accretion of stellar and substellar wind from low-mass companions. The capture of stellar or substellar wind by white dwarfs is one of few methods available to astronomers which can assess mass-loss rates from unevolved stars and brown dwarfs, and the only known method to extract their chemical compositions. In this work, four white dwarfs with closely-orbiting, L-type brown dwarf companions are studied to place limits on the accretion of a substellar wind, with one case of a detection, and at an extremely non-solar abundance $m_{\text{Na}}/m_{\text{Ca}} > 900$. The mass-loss rates and upper limits are tied to accretion in the white dwarfs, based on limiting cases for how the wind is captured, and compared with known cases of wind pollution from close M dwarf companions, which manifest in solar proportions between all elements detected. For wind captured in a Bondi-Hoyle flow, mass-loss limits $\dot{M} \lesssim 5 \times 10^{-17} \,\mathrm{M_{\odot} \, yr^{-1}}$ are established for three L dwarfs, while for M dwarfs polluting their hosts, winds in the range $10^{-13}-10^{-16}\,\mathrm{M}_\odot\,\mathrm{yr}^{-1}$ are found. The latter compares well with the $\dot{M}\sim10^{-13}-10^{-13}$ $10^{-15} \,\mathrm{M}_{\odot} \,\mathrm{yr}^{-1}$ estimates obtained for nearby, isolated M dwarfs using Ly α to probe their astropsheres. These results demonstrate that white dwarfs are highly-sensitive stellar and substellar wind detectors, where further work on the actual captured wind flow is needed.

5.2 Introduction

Stellar wind can be defined as the flow of plasma or gas that is ejected from the upper atmosphere of stars. Such released material plays a crucial role in enriching the interstellar medium which in turn will be assimilated into the next generation of stars and planets. Despite extensive studies of the solar wind (e.g., Vidotto 2021) and AGB stars that have an exceptional mass-loss rate due to stellar wind (Höfner & Olofsson, 2018), relatively little is known about the mechanism, composition, and mass-loss rates in cool, sub-solar and low-mass stars.

The most common stars in the Milky Way are M dwarfs, numbering approximately 60 billion in total (van Vledder et al., 2016), where a handful of the nearest and brightest have mass-loss estimates derived from astrospheric Ly α absorption (Wood et al., 2002, 2005, 2021). While M dwarf winds are virtually negligible compared to those of massive stars, their mass loss plays a vital role in the context of exoplanet habitability (Khodachenko et al., 2007; Mesquita & Vidotto, 2020; Ridgway et al., 2023), and is a key observable for models of their interior, rotation, and magnetic field evolution (Reiners & Mohanty, 2012; Vidotto et al., 2014).

At the bottom of the main sequence and across the substellar boundary, there is little empirical information on intrinsic mass loss from ultracool dwarfs. It is well known that brown dwarfs tend to be fast rotators (Joergens et al., 2003; Scholz et al., 2015; Tannock et al., 2021), show signs of activity (Hawley et al., 2000; Mohanty & Basri, 2003; Reiners & Basri, 2008; Schmidt et al., 2016), and can be strongly magnetic (Berger et al., 2009; Route & Wolszczan, 2012; Kao et al., 2018). However, magnetic braking in ultracool dwarfs appears to be inefficient. Observational data suggest that the time required for spin-down extends from 5 to over 10 Gyr within the upper half of the L dwarf sequence (Reiners & Basri, 2008). These long braking times are indicative of the changes in the entirety of the magnetosphere, suggesting a transition in angular momentum evolution.

A clear decline in X-ray emissions into the L dwarf regimes suggests a lack of coronae, and hence non-existent winds (Pineda et al., 2017). Coupled with changes in topology (Schrijver, 2009), this suggests that ultracool dwarfs have magnetospheric environments distinct from those of warmer stars. In other words, despite the overlap of observable stellar properties between warmer M dwarfs and ultracool dwarfs, the former likely have coronae and winds, while the latter have such features strongly diminished. Previous studies (e.g. Pineda et al. 2016), have proposed that the cutoff point for brown dwarf chromospheres lies around spectral type L5.

The photospheres of white dwarfs can act as detectors for any heavy elements accreted from their circumstellar environments, including wind from close stellar or substellar companions. Owing to the high surface gravities in these compact stars, any primordial heavy elements can only be sustained for a brief period in the photosphere, and only to a certain degree while $T_{\rm eff} \gtrsim 25\,000\,\rm K$ (Chayer et al., 1995; Barstow et al., 2014). At cooler temperatures, any metals rapidly sink from white dwarf atmospheres on timescales that are always short compared to their evolutionary ages (Fontaine & Michaud, 1979; Vauclair et al., 1979). The diffusion of metals in white dwarf atmospheres is well understood, as is the strict requirement for an external source, and thus the presence of any heavy elements can be interpreted directly as ongoing accretion (Dupuis et al., 1992, 1993a,b).

In pioneering work on the nature of white dwarf pollution, Zuckerman et al. (2003) found that photospheric metals were over-represented in a sample of ten, spatially-

unresolved binaries with M dwarf companions; 60 per cent versus 25 per cent for isolated white dwarfs. Because M dwarfs should undergo mass loss via stellar wind, and those in potentially close pairs appeared to often have a polluted white dwarf host, it was postulated that mass transfer is occurring via stellar wind, and that the mass-loss rate could in principle be estimated. Based on this scenario, M dwarf winds have been estimated using white dwarf hosts (Debes, 2006), although in some cases with highly uncertain orbital separations (Farihi et al., 2010c). Nevertheless, the capture of stellar – and possibly substellar – wind by white dwarfs remains one of only two known methods to measure intrinsic mass-loss rates in unevolved stars.

This chapter analyzes four known white dwarfs with brown dwarf companions; specifically GD 1400, WD 0137–349, NLTT 5306, and SDSS J141126.20+200911.1 (hereafter SDSS J1411). In this work, I perform a sensitive search for atmospheric metals using deep co-adds of archival spectra, which in turn constrains any mass loss of the substellar companions through intrinsic winds. The data and methodology are outlined in Section 5.3, while Section 5.4 describes the framework in which the companion mass loss is calculated. Section 5.5 presents the results, with evidence of wind capture found in NLTT 5306, and upper limits provided for the three others. The discussion in Section 5.6 compares the mass-loss rates for M and L dwarfs, contextualises it with prior work on stellar wind determinations, and finishes with an examination of the mass-losing L dwarf NLTT 5306B.

5.3 Observations and data

Archival data from 8-m class observatories were searched for optical spectra of known white dwarf + brown dwarf, short-period binaries, with useful data described below in detail. The aim was to construct a sample of close substellar companions that might pollute their white dwarf hosts with any intrinsic mass loss (wind) in the same manner as occurs for close M dwarf companions to white dwarfs (Zuckerman et al., 2003). For this reason, the search was limited to white dwarfs with $T_{\rm eff} \lesssim 25\,000\,\rm K$, so that any photospheric heavy elements could be confidently attributed to ongoing pollution (as opposed to selective radiation pressure; Koester & Wilken 2006). It was also required that individual spectra have S/N > 5 in the region of H α and H β so these lines could be confidently fitted and shifted to the white dwarf rest frame for co-adding spectra.

These selection criteria resulted in four targets for which archival data were extracted and analysed¹: GD 1400 (Section 4.4), WD 0137–349 (Maxted et al., 2006), NLTT 5306 (Steele et al., 2013), and SDSS J1411 (Beuermann et al., 2013; Littlefair et al., 2014). Previous work indicates these targets are substellar survivors of at least one common envelope stage, and their white dwarf hosts are susceptible to wind accretion established on the orbital and stellar parameters. All archival data were reduced from raw files, even in the cases where reduced data products were available. While the focus was initially to look for the Ca π K line at 3934 Å, it was necessary to correct for the white dwarf radial velocity using the H α line cores, and thus the full optical range was extracted for all available data sets.

¹The binary SDSS J155720.77+091624.6 has been shown to be highly polluted by a circumbinary debris disk and thus cannot be used to search for substellar companion wind accretion.

5.3.1 GD 1400

A total of 34 spectra were available for GD 1400 that were obtained with the ESO VLT UVES. The spectra cover H α and higher Balmer lines at resolving power $R \approx 18\,500$ (Napiwotzki et al., 2001), with the vast majority of exposures acquired under programme 077.D-0673 (PI: Burleigh) in 2006 July. All data were extracted in a semi-automatic way using ESOREFLEX UVES pipeline version 6.1.6. The standard recipes were used to optimally extract and wavelength calibrate each spectrum. The average S/N was estimated to be 30 in the H α and H β regions. These are the same spectra that were discussed in the preceding chapter.

5.3.2 WD 0137-349

For this binary, 70 archival optical spectra acquired with UVES were analysed. Originally, these spectra were obtained as part of programme 276.D-5014 (PI: Maxted) and 079.C-0683 (PI: Burleigh) between 2005 and 2007. The spectral resolving power varies across arms and setups but is usually between 20000 and 30000. All data were retrieved and reduced similarly to GD 1400, with a representative S/N of 15 per spectrum. Additional medium-resolution optical spectra were also downloaded from the ESO archive, for observations made with X-shooter on the VLT (Vernet et al., 2011), under program 093.C-0211 (PI: Casewell) in 2014 August. The data were reduced using the ESOREFLEX X-shooter pipeline v3.5.3 (Modigliani et al., 2010) in STARE mode to avoid the automatic co-addition of multiple frames. The estimated S/N is 30 in the VIS arm and 75 in the UVB arm, per average exposure.

5.3.3 NLTT 5306

There are 24 X-shooter spectra of this target in the ESO archive, which were taken in the NODDING observing mode but reduced in the STARE mode for the same reason as discussed above. These spectra were acquired under two programmes, 085.D-0144 (PI: Steele; Steele et al. 2013) and 093.C-0211 (PI: Casewell; Longstaff et al. 2019), where the first obtained four exposures on 2010 September 5, and the second acquired the remaining 20 spectra on 2014 August 30. For this work, both the UVB and VIS arms were reduced, and cover Balmer lines with spectral resolving power 5400 and 8900, respectively. The average S/N is estimated to be 20 in the UVB arm and 17 in the VIS arm, per typical exposure. Further details on these observations can be found in the literature (Steele et al., 2013; Longstaff et al., 2019).

5.3.4 SDSS J141126.20+200911.1

A total of 37 UVB and 28 VIS X-shooter spectra were retrieved for this white dwarf + brown dwarf system. The data were acquired on 2014 April 19–20 under ESO programme 192.D-0270 (PI: Parsons; Littlefair et al. 2014). The UVB exposure time was 450 s, whereas a longer integration of 600 s was used in the VIS arm, resulting in fewer of these spectra. The resolving power is approximately 5400 in the UVB and 8900 in the VIS arm. The S/N averages around 12 across the UVB spectra and 10 for the VIS data.

5.4 Data analysis

5.4.1 Fitting Balmer features

To obtain radial velocity information from each spectrum, Balmer lines were fitted using a non-linear, least-square minimisation algorithm from the LMFIT python package (Newville et al., 2016). The fitting function for every absorption feature was a Gaussian, or a combination of a Gaussian and a Lorentzian profile if the sharp non-local thermodynamic equilibrium core could be distinguished. Where possible, up to three Balmer features (H α , H β , and H γ) were fitted simultaneously by keeping the velocity parameter shared across the fits. Once velocities were obtained for each target, a barycentric correction was applied using the ASTROPY package, where resulting values were fitted with a sine curve. The radial velocity amplitude and relative phase were determined using the residual minimisation routine, but the period was manually set to the orbital period from the literature. The fitted sine model was then used to make relative phase predictions and velocity offsets for individual spectra. A sine fit was deemed sufficient as the orbits should have circularised during the common envelope phase.

5.4.2 Construction of white dwarf rest-frame co-added spectra

Owing to the close proximity of the binary components studied here, illumination by the white dwarf can lead to significant temperature differences between the irradiated (day) and non-irradiated (night) hemispheres of any low-mass companion. Examples include the brown dwarf companions of interest in this chapter, WD 0137–349B (Burleigh et al., 2006a), SDSS J1411B (Casewell et al., 2018b), and possibly NLTT 5306B, but to a much weaker degree (Steele et al., 2013; Amaro et al., 2023). Of particular relevance to the objectives of this study, the day-side of M and L dwarf companions can be heated into line emission at precisely the same transitions that indicate metal accretion. Thus, an irradiated day-side can interfere with any search for wind pollution, even precluding abundance determinations or upper limits at wavelengths as short as Ca II K (Zuckerman et al. 2003; examples therein). Numerous emission lines are known to vary from the day-to night-side of the L dwarf WD 0137-349B, possibly including Ca II K (Longstaff et al., 2017). Intrinsic brown dwarf emission is also plausible, but unlikely for the older, late L dwarfs examined here (Schmidt et al., 2015).

In order to minimise or eliminate the effects of companion emission lines resulting from irradiation, only those spectra corresponding to night-side phases were utilised. As described above, after obtaining a radial velocity model, each spectrum was velocity shifted to place it into a white dwarf rest frame. The resulting spectra were then resampled with a consistent wavelength range and grid spacing. Next, the S/N ratios of individual exposures were estimated and used as weights to co-add all spectra for each star. Only spectra corresponding to orbital phases 0.3-0.7 were co-added, where phase 0.5 corresponds to the total (or maximum) obscuration of the irradiated side. This orbital phase range was judged appropriate by inspecting the H α emission in the highly irradiated companion to WD 0137-349 as a function of the orbital phase, and is a compromise between (little to no) emission line strength and the S/N of the phase-combined spectra.

It is also important to avoid any H α emission velocities that may overlap with the white dwarf absorption velocity at phases 0.9–0.1. The phases from 0.3 to 0.7 provide an uncontaminated (emission line-free) wavelength region, within which the white dwarf velocity can be readily obtained by absorption line fitting.

An alternative method of creating rest-frame co-adds, that are free of contamination by emission lines was considered. Combining spectra with phases near maxima and minima of radial velocities would, in principle, shift any (day-side) emission lines beyond $\pm 100 \, \mathrm{km \, s^{-1}}$ of the white dwarf velocity. This method was applied to the UVES spectra of WD 0137–349, but was found to offer no significant improvement in terms of S/N or range of wavelengths unaffected by emission lines. Therefore, the night-side-only method was applied throughout, for all four white dwarf + brown dwarf binaries.

These co-added, night-side, rest frame spectra achieved three goals: 1) a region with a minimised day-side emission contribution from the companion, 2) a rest frame in which to search for any weak absorption lines at the same velocity as the white dwarf, and 3) a co-added spectrum with a S/N substantially greater than any individual exposure, in line with \sqrt{N} improvement expectations. Note that because of the phase range requirement of 0.3–0.7 only \approx 40 per cent of the total available spectra were used in the night-side co-adds. Regions of interest of these co-adds are shown in Figure 5.1.

The orbital phases were determined using the periods from the following publications: NLTT 5306 (Steele et al., 2013), GD 1400 (Section 4.4), WD 0137–349 (Longstaff et al., 2017) and SDSS J1411 (Littlefair et al., 2014) with the periods given in Table 5.1. These values were verified by identifying the most significant photometric period from the *TESS* light curves. This was not possible for GD 1400 owing to a lack of significant signal at the expected orbital frequency. However, for the remaining three binaries, the *TESS* periods were found to be within 0.02 per cent agreement with the published values.

5.4.3 Abundance determinations and upper limits

These rest-frame co-adds were then used to search for heavy element absorption lines, such as those that might be captured as wind from the substellar companion. The entire available optical wavelength range was scrutinized for any possible photospheric absorption, with particular attention given to Ca II K, as this transition is well known to be the most prominent optical line in polluted white dwarfs for a wide range of effective temperatures, and across both hydrogen- and helium-rich atmospheres (Zuckerman et al., 2003; Koester et al., 2005). Perhaps surprisingly, while the Na ID doublet is not often seen in polluted white dwarfs (Hollands et al., 2017; Swan et al., 2019), the archival X-shooter spectra of NLTT 5306 exhibits these lines, which are always observed at the velocity of the white dwarf (Longstaff et al., 2019). Because of this unexpected pollution signature, this element and wavelength region also received special attention.

The four white dwarfs with substellar companions were fitted with atmospheric models to obtain $T_{\rm eff}$ and log g following the standard technique of Balmer line fitting (Tremblay & Bergeron, 2009). As a precaution in the case that emission from the secondary was present, the H α region was not used in the fitting procedure, but instead H β to H 8 were fitted. The resulting stellar parameters are listed in Table 5.1.

To determine abundances or upper limits for both Na and Ca, white dwarf atmospheric models were used (Coutu et al. 2019 and references therein) to produce a grid of synthetic spectra with the derived physical parameters of the observed stars. The limits (or

determinations) were made by fitting the expected positions (or detections) of the Ca II K and Na I D lines using a standard methodology (Dufour et al., 2012), where upper limits are established by simulating an absorption line that should have been detected at the photospheric velocity, for the corresponding S/N and spectral resolution. This work was done by my collaborator, P. Dufour.

5.4.4 Brown dwarf mass-loss rates

In this section, Ca is used as a typical example of observed white dwarf pollution, but the same methodology applies to all photospheric metals considered in this work. The accretion rate for any heavy element is calculated by considering its total mass in the outer, fully mixed layer of the star, which corresponds to the convection zone in cases where the star is sufficiently cool. Here, M_{cvz} is used for convenience, but for stars with radiative or stable atmospheres, it is simply the mass of the atmosphere above a Rosseland optical depth of 5 (Koester, 2009). This layer has a characteristic diffusion or sinking timescale for Ca (τ_{Ca}), which will be within a factor of a few of the sinking times for other heavy elements (Koester et al., 2020). In the case of a steady-state balance of accretion and diffusion, where the sinking timescale is much shorter than the ongoing accumulation of heavy elements, the accretion rate can be expressed as:

$$\dot{M}_{\rm Ca} = \frac{X_{\rm Ca} M_{\rm cvz}}{\tau_{\rm Ca}} \tag{5.1}$$

where X_{Ca} is the mass fraction of Ca atoms relative to the dominant atmospheric species (hydrogen is used here, but it could also be helium). The quantities M_{cvz} and τ_{Ca} come from diffusion models based on an individual set of stellar parameters. In the case of a hydrogen-dominated atmosphere, the Ca mass fraction is:

$$X_{\text{Ca}} = \frac{40.078 \, n_{\text{Ca}}}{1.008 \, n_{\text{H}}} = \frac{40.078 \times 10^{[\text{Ca/H}]}}{1.008}$$
 (5.2)

where n_{Ca} and n_{H} are the number of calcium and hydrogen atoms, respectively, and $[\text{Ca/H}] = \log(n_{\text{Ca}}/n_{\text{H}})$ is determined directly from the fitting of atmospheric models to the spectroscopic data.

To estimate a total mass accretion rate from a single element, a reasonable assumption about the nature of the material must be made (e.g. solar, interstellar medium, rocky, icy), so that its relative abundance can be estimated. For example, by mass, Ca is 1.6 per cent of the bulk Earth (Allègre et al., 1995), but only 7×10^{-5} of the solar photosphere (Lodders, 2003). In this work, solar proportions are assumed as this should broadly reflect the bulk abundances of stars and brown dwarfs at formation. The total mass accretion rate is estimated by dividing the steady-state accretion rate for Ca by its overall abundance in the infalling material. Here, \dot{M}_1 refers to this total accretion rate onto the white dwarf primary, while \dot{M}_2 refers to the corresponding total mass lost from the secondary via (sub)stellar wind onto M_1 .

For captured stellar wind with an \dot{M}_1 determination (or limit), a few reasonable assumptions can be made to approximate the mass-loss rate from the companion. The first is a simple model of spherically-symmetric mass loss, which provides a density via the mass continuity equation:

$$\dot{M}_2 = 4\pi\rho v_2 r^2 \tag{5.3}$$

where ρ is the mass density, and v_2 is the velocity of material at a distance r from M_2 . It is assumed here that v_2 is the escape speed of the companion and is a constant. This is approximately true for the bulk of the solar wind that emerges near the escape speed. However, for the objects studied here, the terminal velocity would likely be similar to the escape speed but reached at a distance of hundreds of R_{\odot} . If the wind is still accelerating this may lead to an overestimation by a significant factor. The precise wind speed profile is beyond the scope of this work, but future modelling would better constrain the actual mass-loss rates for low-mass stars and brown dwarfs.

The M_2 radius for a low-mass star or brown dwarf is non-negligible relative to the semimajor axis in close binaries such as those studied here. For a spherical wind² that originates at the surface of such a companion, only material emanating from a narrow range of solid angles (i.e. only near the sub-stellar point) has any chance of being captured by the white dwarf, so that $r \approx a - R_2$, where a is the semimajor axis and R_2 is the radius of the companion. The velocity of the flow relative to the white dwarf can be approximated as $v_1^2 = v_2^2 + v_{\text{orb}}^2$, where the latter term is the Keplerian speed of the white dwarf.

The remaining quantity to be estimated is the density at the accretion radius R_A , where two models are considered here: the ideal case of Bondi-Hoyle-Littleton accretion (Bondi, 1952), and simple gravitational capture, also known as Eddington accretion (Eddington, 1926). In each case, the model describes a distinct R_A , within which all material is captured; a Bondi-Hoyle flow is an ideal fluid case where there is zero transverse momentum downstream of the accreting source, whereas an Eddington geometry is simply where gravity is sufficient to alter the flow trajectory onto the star. A detailed discussion on the application of these models to white dwarf accretion can be found in Farihi et al. (2010c).

Starting with the Bondi-Hoyle accretion, the material density at R_A is given by

$$\rho_{\rm BH} = \frac{\dot{M}_1 v_1^3}{4\pi G^2 M_1^2} \tag{5.4}$$

where G is the gravitational constant. By making appropriate substitutions in Equation (5.3), the following mass-loss estimate is obtained:

$$\dot{M}_2 = \frac{\dot{M}_1 v_1^4 r^2}{G^2 M_1^2} \tag{5.5}$$

For Eddington accretion, the material density at R_A depends on R_1 as:

$$\rho_{\rm Edd} = \frac{\dot{M}_1 v_1}{2\pi G M_1 R_1} \tag{5.6}$$

where appropriate substitutions lead to the following mass-loss rate:

$$\dot{M}_2 = \frac{2\dot{M}_1 v_1^2 r^2}{GM_1 R_1} \tag{5.7}$$

²The precise flow structure should be addressed with future modelling.

Using NLTT 5306 as an example, $\rho_{\rm Edd}/\rho_{\rm BH} \approx 40$, which is the same ratio between the two corresponding mass-loss estimates. All resulting mass-loss and accretion rates, as well as upper limits, are provided in three columns of Table 5.1.

The diffusion timescales and fully-mixed, atmospheric mass fractions were determined using bilinear interpolation of hydrogen-rich model grids with convective overshoot (Koester et al., 2020), where all four stars in the sample have been characterised as hydrogen atmosphere white dwarfs that manifest as spectral type DA. Steady-state accretion is a safe assumption, as the wind accretion timescales are the white dwarf cooling ages ($\sim 10^8 - 10^9$ yr), while the heavy element sinking timescales are at least $1000 \times$ shorter.

Evolutionary models for brown dwarfs (Baraffe et al., 2015) were employed to estimate parameters of the potentially mass-losing substellar secondaries, such as R_2 and $\log g$. The age of 2 Gyr was chosen for this purpose, as brown dwarfs should be effectively fully contracted by then. However, determining the ages of brown dwarfs from their white dwarf companions is not feasible, as the white dwarfs have undergone binary (non-isolated) evolution. In this scenario, the white dwarf cooling ages act as the minimum ages for the systems.

In the case that the system is still young and the radius is not fully contracted there would be a modest increase in the mass-loss rate. For example, a 500 Myr brown dwarf would have a 10 per cent larger radius than a fully contracted older counterpart (Baraffe et al., 2015). Such a larger radius would result in a 40 per cent increase in the mass-loss rate in the case of a Bondi-Hoyle flow, or a 60 per cent increase in the case of gravitational capture.

5.5 Results

The results section is organized as follows. First, metal pollution resulting from substellar wind is evaluated in terms of upper limit or determined accretion rates. Second, corresponding mass-loss rates and limits are derived for the four systems with brown dwarf companions detailed in Section 5.3. Third, these substellar wind estimates are then compared to that of several M dwarfs known to be polluting their host white dwarfs via wind capture.

Table 5.1: Adopted stellar parameters, abundance determinations, accretion and mass-loss rates for (sub)stellar winds captured by white dwarfs.

	Adopted		Estimated		Orbital	Abundances		Accretion	BH Capture	Edd Capture	
Binary	$T_{ m eff}$	$\log g$	M_2	SpT	Period	[Ca/H]	[Na/H]	\dot{M}_1	$-\dot{M}_2$	$-\dot{M}_2$	Refs
	(K)	(cgs)	(M_{Jup})		(h)			$(M_{\odot}yr^{-1})$	$(M_{\odot}yr^{-1})$	$(M_{\odot}yr^{-1})$	
Low-mass stars:											
Case 1	15 500	8.07	380	M3	16.0	-8.1		2.6×10^{-17}	1.9×10^{-15}	1.0×10^{-13}	1,2,3,4
PG 1026+002	17 200	7.96	380	M5	14.3	-8.6		6.0×10^{-18}	4.4×10^{-16}	2.0×10^{-14}	1,2,3,5,6
LHS 1660	7500	7.70	190	M5	7.3	-9.3		3.1×10^{-16}	9.9×10^{-15}	3.2×10^{-13}	1,2,7,8
PG 2257+162	24 300	7.51	190	M5	7.7			3.1×10^{-17}	1.3×10^{-16}	3.2×10^{-15}	1,9,8
BPM 6502	22 600	7.84	150	M5	8.1			1.4×10^{-17}	2.6×10^{-16}	1.3×10^{-14}	1,3,10
LTT 560	7500	7.75	150	M6	3.5	-7.5		8.5×10^{-15}	9.4×10^{-14}	3.1×10^{-12}	1,11
Rubin 80	8200	7.75	100	M7	4.0	-8.3		8.7×10^{-16}	1.0×10^{-14}	3.7×10^{-13}	1,2,3,6,12
GD 448	19 700	7.49	100	M7	2.5			1.2×10^{-17}	7.0×10^{-17}	1.9×10^{-15}	1,9,13
Brown dwarfs:											
NLTT 5306	7700	7.49	60	L5	1.7	< -11.0	-7.7	3.3×10^{-15}	5.6×10^{-15}	2.1×10^{-13}	1,14
GD 1400	11 400	8.17	70	L6	10.0	< -9.8	< -7.3	$< 2.4 \times 10^{-18}$	$< 5.5 \times 10^{-17}$	$< 4.3 \times 10^{-15}$	1,15
WD 0137-349	17 600	7.58	60	L7	1.9	< -7.9	< -5.7	$< 2.2 \times 10^{-17}$	$< 5.1 \times 10^{-17}$	$< 2.0 \times 10^{-15}$	1,16,17
SDSS J1411	11 800	8.01	50	L8	2.0	< -8.2	< -6.2	$< 3.9 \times 10^{-17}$	$< 4.6 \times 10^{-17}$	$< 4.1 \times 10^{-15}$	1,18,19

Notes. The Ca abundance limits for GD 1400 and WD 0137–349 were determined from night-side UVES spectra, while those for NTT 5306 and SDSS J1411 were obtained using night-side X-shooter data. Stellar parameters and abundances for M dwarf hosts are taken from the literature, where GD 448 and PG 2257+162 have only Si and C abundances from ultraviolet observations. Spectral types and masses for the companions were estimated from the literature, and from the absolute *K*-band magnitude in some cases. For the low-mass stars, accretion and mass-loss rates are averages based on all available abundances, including a few not shown here or in the left panel of Figure 5.2. For the brown dwarfs, the rate limits are founded on the more constraining Ca abundances, with the exception of NLTT 5306, for which a Na abundance was determined and used to estimate the rates. All (single-element) accretion rates assume the metal is present in solar proportions.

References: (1) This work; (2) Zuckerman et al. (2003); (3) Gianninas et al. (2011); (4) Lanning (1982); (5) Saffer et al. (1993); (6) Farihi et al. (2005b); (7) Maxted et al. (2007); (8) Parsons et al. (2017a); (9) Koester et al. (2014); (10) Kawka et al. (2008); (11) Tappert et al. (2011b); (12) Ashley et al. (2019); (13) Maxted et al. (1998); (14) Steele et al. (2013); (15) Farihi & Christopher (2004); (16) Maxted et al. (2006); (17) Longstaff et al. (2017); (18) Beuermann et al. (2013); (19) Littlefair et al. (2014).

5.5.1 Brown dwarf winds

It should be emphasized that conventional *mass transfer* is not considered here as intrinsic mass loss analogous to the stellar wind. As shown in Table 5.1, a typical estimated upper limit for the accretion onto the white dwarf is $\dot{M}_1 < 5 \times 10^{-17} \, \rm M_{\odot} \, yr^{-1}$. This is at least three orders of magnitude lower than the solar value of $2 \times 10^{-14} \, \rm M_{\odot} \, yr^{-1}$ (Cohen, 2011). For all but NLTT 5306, there is a lack of detected pollution and thus only corresponding upper limits for any substellar winds. There is a clear Na I doublet detection in the coadded spectrum of NLTT 5306, but only weak upper limits for Na in the other three binary systems. Moreover, there are no detections of Ca (only upper limits) in all four white dwarfs with close substellar companions (Figure 5.1). Based on these non-detections, the presented accretion and mass capture constraints are calculated from the more constraining Ca limit rather than Na. The only exception is NLTT 5306, for which the determined Na abundance was used instead of the Ca upper limit.

For additional context, polluted white dwarfs with infrared detections of their circumstellar disks have typical, total inferred mass accretion rates $\dot{M} \gtrsim 10^{-18}\,\rm M_\odot\,yr^{-1}$ (Farihi et al., 2009), where a common assumption is that Ca is 0.016 of the total accreted mass as it is in the Earth (Farihi, 2016). But while accretion rates for white dwarfs polluted by (sub)stellar winds have been calculated using the same steady-state formalism as done for planetary debris pollution, the limits established here are higher for wind capture, despite the fact that similar abundance sensitivities have been established using the same large telescopes and sensitive spectrographs. Owing to the dominance of hydrogen, Ca has a mass fraction that is roughly 220× smaller in the sun than in the rocky material of the inner solar system, and thus a fixed Ca abundance translates to a total accretion rate that is commensurately higher for solar composition as opposed to terrestrial abundances.

Unlike Ca, there is a clear detection of Na in the spectrum of NLTT 5306, with a determined abundance [Na/H] = -7.7. The radial velocities of these lines rule out interstellar medium absorption. It is important to note that the lack of Na ID detections in GD 1400, WD 0137–349, and SDSS J1411 are not highly constraining. For a fixed abundance, the Na ID transition is significantly stronger in $T_{\rm eff} \lesssim 10\,000\,\rm K$ and cooler white dwarfs (Hollands et al., 2021, 2022). Thus, for these three warmer white dwarfs with substellar companions, the high S/N spectroscopy is insensitive to the Na abundance detected in NLTT 5306. Because the Na abundance upper limits are two orders of magnitude less stringent than those placed on Ca, the latter element provides more sensitive \dot{M}_1 and \dot{M}_2 limits in accordance with a solar composition wind.

5.5.2 Stellar winds

To provide independent main-sequence mass-loss benchmarks, the methodology described in the previous section is also applied to several known white dwarfs that are polluted by the wind of their M dwarf companions, and where metal abundances are available in the literature. For four of these sources (Case 1, PG 1026+002, LHS 1660, and Rubin 80) Ca and other heavy element abundances were derived from optical spectroscopy, as described in Zuckerman et al. (2003). In addition, C and Si abundances for two sources (PG 2257+162 and GD 448) were determined using ultraviolet data, as reported in Koester et al. (2014). The adopted physical parameters from the literature are listed in Table 5.1; in cases where multiple sources were available a preference was given to more recent work

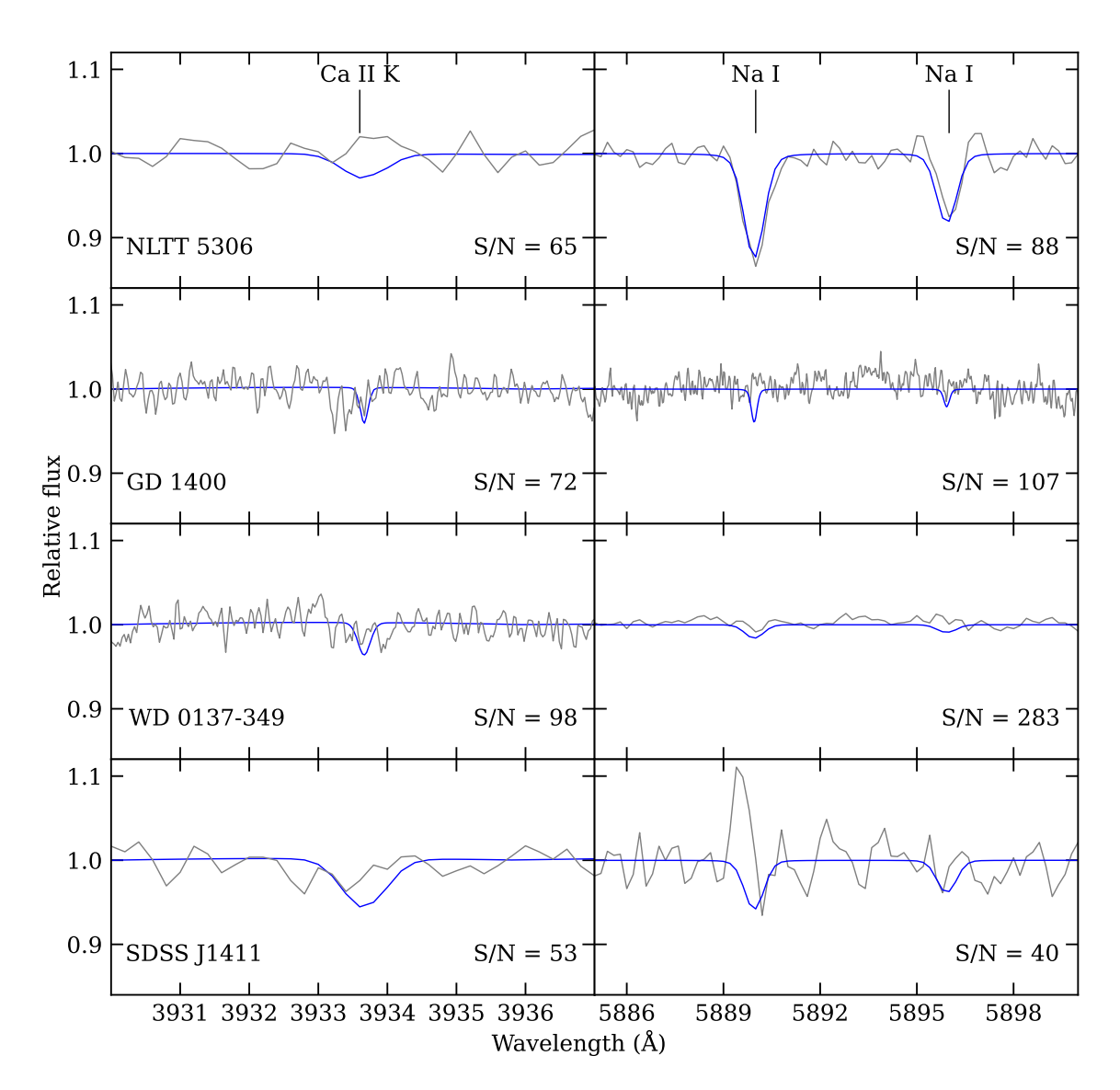


Figure 5.1: The night-side co-added spectra (in grey) of all four white dwarfs hosting L dwarf companions, plotted in the regions of the Ca II K line (left panels), and Na I D doublet (right panels), with relevant S/N estimates given in each panel. Atmospheric models (in blue) are overplotted in each case to determine the upper limit abundances of these two elements, with the sole exception of the Na detection in NLTT 5306. There are continuum imperfections in some cases (e.g. GD 1400), but these have little effect on the modelling outcomes. All co-added spectra were scrutinised for any additional absorption features, but none were found.

and studies that account for the binary nature of the system.

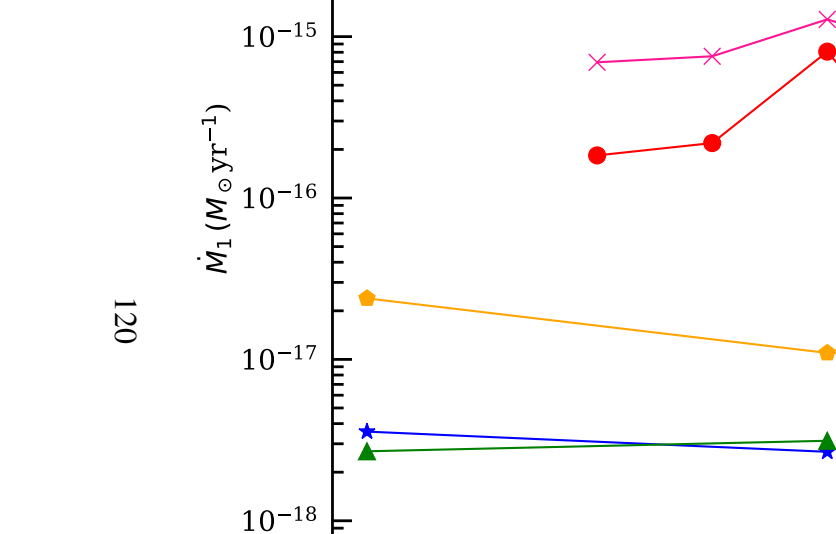
There are two additional, close M dwarf companions to white dwarfs in the literature, where pollution from stellar wind has been detected. The close binary BPM 6502 has FUSE ultraviolet spectroscopy, from which photospheric abundances have been derived for C, N, Si, and Fe (Kawka et al., 2008). Based on these abundances, the white dwarf is likely too warm to exhibit metal absorption via optical spectroscopy. Indeed, an examination of archival UVES observations from the SPY survey (Napiwotzki et al., 2003) reveals a DA spectrum with no clear metal absorption, but strong emission lines of Ca II H & K from the irradiated companion. Remarkably, one of the most metal-rich white dwarfs known is LTT 560, which is highly polluted by the wind of its M dwarf companion and shows strong H α emission. There are even photospheric detections of the elements Sc and Co (Tappert et al., 2011b), where otherwise these two rare elements have only been detected together in extremely polluted white dwarfs with infrared-bright debris disks (Zuckerman et al., 2007; Dufour et al., 2012).

All eight aforementioned white dwarfs that are polluted by close M dwarf companion winds were re-analysed based on their published heavy element abundances, but with state-of-the-art diffusion parameters (Koester et al., 2020)³. As in Section 5.4.4, each detected element was assumed to be present in solar abundance, and in this way each metal species present provides an independent estimate of the total accretion rate. For the M dwarf secondaries, stellar parameters were obtained from the model grids of Baraffe et al. (2015), while white dwarf parameters were generally taken from the literature (N.B. the *Gaia* eDR3 white dwarf catalogue entries for these targets are likely inaccurate because of the optical red flux of the companion).

The resulting accretion and mass-loss estimates are summarised in Table 5.1, where an average across all detected elements is given in the ninth column (with upper limits established on Ca for L dwarf hosts). The inferred accretion and mass-loss rates for M dwarfs and the L dwarf and NLTT 5306 are plotted together in Figure 5.2, where for each element, \dot{M}_1 is calculated assuming it is present in solar proportions. With a few minor exceptions, the left-hand panel demonstrates that distinct metal species yield broadly similar estimates for \dot{M}_1 when solar abundances are assumed, thus indicating the captured M dwarf winds are approximately solar in composition.

5.6 Discussion

³The average percentage difference between this work and Debes (2006) for convection zone mass ratio and Ca diffusion timescale is 3 and 32 per cent, respectively.



Na

Mg

C

Al

Element

Si

Ca

 10^{-14}

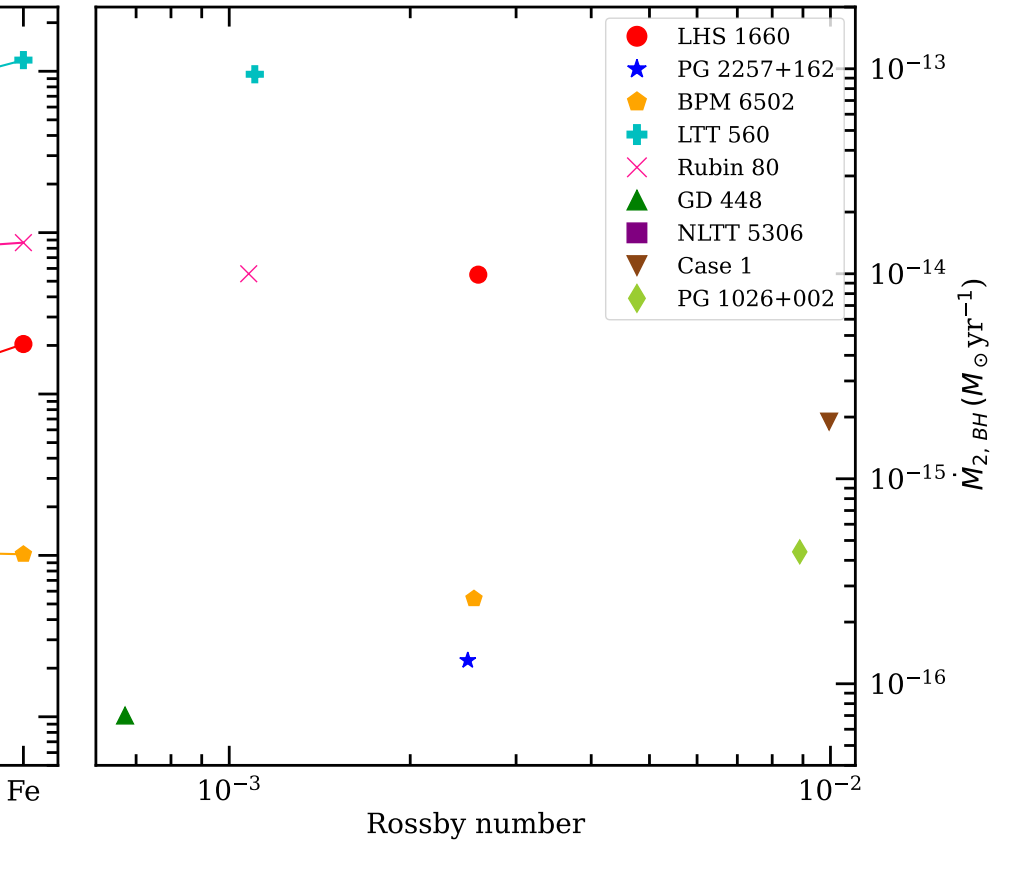


Figure 5.2: On the left are white dwarf accretion rate inferences for all M dwarf hosts in Table 5.1 with multiple heavy element abundances, where all elements are assumed to be present in solar ratios. Case 1 and PG 1026+002 are not plotted since only the Ca abundance was available. For the L-dwarf host NLTT 5306, the ratio of Na accretion rate and Ca upper limit provide a stark contrast to the M dwarf wind accreting stars. On the right are shown Rossby numbers for the M dwarfs against their mass-loss rates estimated using the Bondi-Hoyle formalism.

5.6.1 Prior work and measurements

The first work that attempted to estimate M dwarf mass-loss rates using polluted white dwarfs relied on existing Ca abundances in suspected close binary systems and assumed that the wind is captured in a Bondi-Hoyle flow (Debes, 2006). Of the six binaries in that study, there are four here in common: Case 1, PG 1026+002, LHS 1660, and Rubin 80.

While there is an order-of-magnitude agreement between the prior estimates and those made here using the Bondi-Hoyle prescription in two cases, the other two are notable exceptions. First, the binary orbit of Rubin 80 was only recently characterized (Ashley et al., 2019), and thus the prior mass-loss estimate suffered from a poorly constrained orbital separation. Second, the stellar parameters of Case 1 differ significantly between the new and prior work, with the sinking timescale used here 40× shorter and implying a commensurately higher white dwarf accretion rate, and thus mass-loss rate in the M dwarf. Third, it should be noted that the remaining two systems in Debes (2006) are now known to be wide binaries (Farihi et al., 2010a), and thus wind cannot be responsible for any atmospheric pollution (which is unconfirmed for PG 1210+464, but clearly detected in PG 1049+103; Zuckerman et al. 2003).

According to some studies, M dwarf stellar wind measurements can be obtained from low accretion rate polars (magnetic cataclysmic variables; Schwope et al. 2002). In this scenario, the donor star is underfilling its Roche lobe, and thus mass transfer would only be possible via wind accretion (Schwope et al., 2009). However, in contrast to the M dwarf companions studied here, a strongly magnetic white dwarf may couple to the magnetic field lines of the secondary, and thus have the potential to influence stellar wind, which is itself an intrinsically magnetic process. Above a critical magnetic field strength $B \sim 60 \, \text{MG}$, a white dwarf is capable of collecting the global mass loss from a donor star out to at least several R_{\odot} (Li et al., 1994; Webbink & Wickramasinghe, 2002, 2005). In low accretion rate polars with M dwarf secondaries, the total accretion rates range from around 5×10^{-14} to $6 \times 10^{-13} \, \text{M}_{\odot} \, \text{yr}^{-1}$ (Schmidt et al., 2005, 2007b; Kafka et al., 2010; Parsons et al., 2021).

These accretion rate inferences are 2 – 4 orders of magnitude larger than the M dwarf wind capture rates determined here in Table 5.1, and are therefore unlikely to represent intrinsic, unenhanced mass loss from low-mass stars. Such high corresponding mass-loss rates have been questioned previously, especially in similar systems where the donor is substellar, and where they notably exceed the solar mass-loss rate (e.g. Farihi et al. 2008; Stelzer et al. 2017). Although the surface magnetic field and rotational rates tend to be higher in M dwarfs, the general trend is that activity decreases towards lower stellar temperatures and masses (Cranmer & Saar, 2011; Kumar et al., 2023). Therefore, low accretion rate polars are not representative of unassisted mass loss, but rather mass transfer that is modulated in the presence of strong white dwarf magnetism. However, these mass transfer rates provide a useful, high benchmark to which the estimates calculated here for completely detached, non-magnetic binaries can be compared.

The only other successful mass-loss estimates for M dwarfs are made using astrospheric signatures of interactions between their stellar winds and the interstellar medium near their respective astropauses (Wood et al., 2005). The confluence of wind and interstellar medium can produce detectable Ly α absorption, which can be modelled to constrain the mass-loss rate, where estimates span nearly three orders of magnitude $0.1-60\times10^{-14}\,\mathrm{M}_{\odot}\,\mathrm{yr}^{-1}(\mathrm{Wood}$ et al., 2021). It is noteworthy that the solar wind value lies in the middle of this range, and that winds an order of magnitude stronger are implied by this methodology. In contrast

to the M dwarfs studied here, astrospheric observations target nearby, bright, and well-studied stars with constraints on X-ray luminosity, and some indications of magnetic field strength as well as topology.

5.6.2 New M dwarf wind estimates

To interpret the results of this work, it must first be asked whether a Bondi-Hoyle flow or gravitational capture is more realistic, or perhaps another accretion geometry (e.g. influenced by white dwarf magnetism). Based on the previously discussed examples of accretion in low-state polars, it is well-known that strong magnetic fields can redirect mass transfer. Magnetic fields can do work on an incoming flow, and effectively remove transverse momentum downstream, as well as capture material from a wider radius. While none of the white dwarfs in this chapter are known to be magnetic, that does not rule out weak magnetism on the order of a few kG or lower (Bagnulo & Landstreet, 2021), and which may play a role in assisting the capture of stellar wind.

Comparing the newly-obtained M dwarf wind estimates with the solar value, the Bondi-Hoyle estimates are all lower or similar to the solar wind mass-loss rate. In contrast, the pure gravitational capture model results in many mass-loss rates that exceed the solar value, and thus suggest that a Bondi-Hoyle flow is the more realistic model. An important caveat is that the close M dwarf companions to white dwarfs are all tidally locked, thus rotating rapidly and highly active. Instead, comparing the Table 5.1 mass-loss estimates with those of the most active M dwarfs in Wood et al. (2021), gravitational capture estimates appear to be a closer match. Further investigation into the flow geometry, especially the influence of weak white dwarf magnetism, is beyond the scope of this work but would better constrain stellar wind measurements using atmospheric pollution.

There are no indications that the white dwarfs studied here have any influence on the winds of their companion stars, irrespective of the mechanism of wind capture. However, there is a sensitivity bias, where photospheric heavy elements in white dwarfs are far easier to detect in the ultraviolet than in the optical (e.g. Koester et al. 2014); the three lowest mass-loss estimates in Table 5.1 and Figure 5.2 are the result of ultraviolet observations. Overall, the rates of mass loss estimated from white dwarf pollution are not significantly different from those measured for isolated M dwarf stars using astrospheric Ly α absorption (Wood et al., 2021). However, the M dwarf companions studied here are all tidally locked and have rotation periods of hours, and thus are somewhat distinct from the isolated M dwarfs studied by Wood et al. (2021).

5.6.3 Mass loss and activity across the substellar boundary

Limits on substellar winds are a new constraint on the activity and structural changes that occur as mass and temperature decrease along the ultracool dwarf sequence, from low-mass stars to brown dwarfs. While instances of high stellar activity are commonly linked to fast rotational velocities (Skumanich, 1972; Wright et al., 2011), and spectroscopic observations have shown that many brown dwarfs are indeed fast rotators (e.g. Mohanty & Basri 2003; Blake et al. 2010) – in some cases rotating at \approx 30 per cent of their break-up speed (Konopacky et al., 2012) – ultracool dwarfs of spectral type M9 and later

exhibit low activity levels (Gizis et al., 2000; Mohanty & Basri, 2003; Reiners & Basri, 2008). This deterioration in the rotation-activity relationship is further supported by X-ray observations of late M-type stars (Williams et al., 2014; Cook et al., 2014). This may be an empirical indication that, in general, L-type brown dwarfs do not generate substantial winds.

This observed change in the rotation-activity relation at the M/L transition could be due to a fundamental change in the dynamo mechanism within ultracool dwarfs, reducing dynamo efficiency and decoupling field generation from rotation rate (Reiners & Basri, 2010). Another possibility is the growing atmospheric neutrality which weakens the coupling between the ionized atmosphere and magnetic field, consequently rendering magnetic heating ineffective (Reiners, 2012). As a result, there might be more similarities in the underlying magnetic field generation between brown dwarfs and giant planets (Christensen et al., 2009; Morin et al., 2011) than in solar-mass stars. In this sense, brown dwarf activity can exhibit itself in the form of an auroral-planet framework rather than conventional stellar winds (Pineda et al., 2017). However, this auroral population is likely distinct from those ultracool dwarfs exhibiting coronal or chromospheric behaviour (Stelzer et al., 2012). Some activity indicators, such as X-rays (Tsuboi et al., 2003; Stelzer et al., 2006), imply chromospheric activity, and thus potentially, some mass loss in their outermost layers.

The right-hand panel of Figure 5.2 is an attempt to contextualize the mass-loss rates of M dwarf companions to white dwarfs, in a manner similar to astrospheric wind estimates, by accounting for the rotation rate (assumed to be identical to the orbital period owing to tidal locking). The figure displays the inferred mass-loss rates for M dwarf companions to white dwarfs, in the Bondi-Hoyle approximation, as a function of the Rossby number (the ratio of the spin period to the convective turnover timescale, following Wright et al. 2018). In this diagram, there is a distinct lack of correlation between mass-loss rates and the Rossby number, which should be a reliable indicator of magnetic field strength and stellar activity (Reiners et al., 2022).

A dependence between mass-loss rates and Rossby number would only be expected in an unsaturated regime of stellar activity. However, almost all of the M dwarf companions studied here are in the coronally-saturated regime, where stellar winds no longer correlate with rotation (Johnstone, 2017), similar to magnetic field saturation and other activity indicators (Reiners et al., 2022). One potential exception is Case 1 which would require a rotational period of $\sim 5\,\mathrm{h}$ or less to be fully saturated (Reiners et al., 2014). Further comparison is not possible without detailed information on the properties of the M dwarf companion magnetic fields.

Comparing the results obtained here with those for nearby, bright, and active M dwarfs (Wood et al., 2021), the astrospheric technique has a typical sensitivity to $\dot{M} \gtrsim 10^{-15} \, \mathrm{M}_\odot \, \mathrm{yr}^{-1}$, and identifies mass-loss rates centred near $10^{-14} \, \mathrm{M}_\odot \, \mathrm{yr}^{-1}$, comparable to the solar value. On the one hand, these astrospheric wind determinations are broadly consistent with the Table 5.1 inferences for Eddington capture. On the other hand, roughly half of the Table 5.1 wind estimates made using a Bondi-Hoyle flow are notably near or below the sensitivity for astrospheric wind detection. It is therefore possible that those M dwarfs with detected astropheres are outliers within a distribution that, for the most part, are more sedate and similar to the Table 5.1 results for the Bondi-Hoyle wind capture model. However, it is important to note that the nearby M dwarfs from Wood et al. (2021) exhibit significantly lower and more typical rotational rates, with the shortest period just

under 3 d. This complicates a direct comparison since the two samples are likely to be operating in different activity regimes. Finally, the upper limit of $5\times 10^{-17}\,\mathrm{M}_\odot\,\mathrm{yr}^{-1}\,$ found for the L-dwarfs using the Bondi-Hoyle formalism, when translated into a mass loss per unit surface area, is comparable to the most sensitive measurements presented in Wood et al. (2021). In other words, the white dwarf pollution technique has a similar sensitivity to the more instrumentally demanding Ly α monitoring that is generally limited to within 7 pc (due to being outside of cooler, partially neutral material within the Local Bubble). It should also be noted, that the astrospheric technique inherits systematic uncertainties associated with the methodology that could skew this comparison.

The binary orbital motion may play an underestimated role in determining the actual geometric structure of the wind outflow. This is plausible, as the bulk of unevolved, low-mass companions have orbital velocities that are the same order of magnitude as their escape velocities. However, if the wind capture were strongly dependent on orbital velocity, then a correlation between accretion rate and binary period might be seen, yet no such trend is evident. Because the binary mass ratios are not greatly dissimilar (all should have $q = M_2/M_1 \lesssim 0.6$; Pecaut & Mamajek 2013), these are unlikely to influence the flow and wind capture mechanism between individual systems. Such considerations underscore the benefit of further work on the wind flow geometry toward white dwarfs from their low-mass stellar and substellar companions, and which will result in more accurate comparisons to stellar wind estimates obtained for isolated stars.

5.6.4 The detection of Na in NLTT 5306

The translation of the photospheric Na in NLTT 5306 into a mass-loss rate from an L dwarf is a first. Because the measurement derives from detectable white dwarf pollution, it is perhaps unsurprising that the nominal mass-loss rate for the brown dwarf is comparable to those estimated for M dwarf companions, under a model that each detected element is present in solar abundance.

In the case of NLTT 5306, however, the detected Na and upper limit Ca abundances cannot be reconciled with material that is ejected and accreted in solar elemental ratios. This is made strikingly apparent in the left panel of Figure 5.2, where there is more than three orders of magnitude disparity between the two accretion rates as inferred for solar composition. In contrast, all other wind-polluted white dwarfs appear to be accreting matter with element-to-element ratios broadly consistent with solar abundance material, insofar as the available data allow.

The steady-state accretion rate for Na and upper limit for Ca yield $m_{\rm Na}/m_{\rm Ca} > 900$ for the matter falling onto NLTT 5306. This highly unusual mass ratio can be directly compared to the solar and chondritic values where both are $m_{\rm Na}/m_{\rm Ca} \approx 0.5$ (Lodders, 2003), and three orders of magnitude smaller. Therefore, the material being accreted by the white dwarf cannot be the result of conventional mass transfer via Roche lobe overflow, as gravity would not differentiate between neutral atoms, molecules, or dust grains. Moreover, even if Ca is locked up in dust it will be accreted, as radiation pressure on small grains is negligible at the luminosity of most white dwarfs. Lastly, while the metallicity of many brown dwarfs may be subsolar, their bulk compositions are expected to reflect formation by gravitational collapse and thus be of broadly solar ratios.

Therefore, the pollution in this white dwarf is by a weak substellar wind, and where the observed, intrinsic H α emission is a hallmark of accretion similar to that observed in

other white dwarfs capturing M dwarf winds (Maxted et al., 1998; Tappert et al., 2011a,b; Ribeiro et al., 2013). In fact, this telltale sign is prominent in only two cases (NLTT 5306 and LTT 560) and detectable but at weaker strength in a third system (RR Cae = LHS 1660); all of which are relatively low-luminosity white dwarfs with $T_{\rm eff}$ < 8000 K. These modest signatures of accretion luminosity via H α emission may be difficult or impossible to detect against the higher intrinsic brightness of white dwarfs that are warmer, and against the intrinsic or irradiatively-driven, chromospheric emission lines of the secondary (precisely the case for GD 448; Maxted et al. 1998).

The extreme Na/Ca ratio cannot be planetary debris of any known origin, nor can it be material remaining from previous stages of stellar evolution. Post-AGB stars in binaries can have metal-poor surfaces and non-solar abundances because they accrete material from a circumbinary disc (Waters et al., 1992; Oomen et al., 2019, 2020), where a well-known example is the Red Rectangle (Waelkens et al., 1996). In this scenario, the accreted material is reduced in refractory elements owing to the formation of dust grains that are expelled by radiation pressure. Nonetheless, even in those systems $m_{\rm Na}/m_{\rm Ca} \ll 900$, and typically enhanced only by a factor of 10-20 (van Winckel et al., 1992, 1998). Owing to the sinking timescale of heavy elements in white dwarfs, these short-lived post-AGB system signatures cannot persist to the present epoch, over the cooling age of NLTT 5306 (Zijlstra et al., 2001; Steele et al., 2013; Amaro et al., 2023).

Some elemental fractionation is observed in the solar wind and corona, as well as M dwarf coronae. In the case of the sun, low first ionization potential (FIP) elements, such as sodium, can be typically enhanced in abundance by a factor of two to five (Laming, 2015), where more pronounced fractionation can be observed locally during solar flares (Doschek et al., 2015). In contrast, in M dwarfs with $T_{\rm eff} < 4000$ K, low-FIP elements are coronally depleted by a factor of three to four (Wood et al., 2018). Although such changes in coronal abundances, relative to solar, may produce some scatter in the left-hand panel of Figure 5.2, none of the observed ratios are as extreme as the $m_{\rm Na}/m_{\rm Ca}$ lower limit in NLTT 5306.

At face value, this highly non-solar ratio implies that the outer layers of the brown dwarf are depleted in Ca, which acts as an empirical indicator that the atmosphere of NLTT 5306B is differentiated (as expected) and distinct from a low-mass star. Speculating somewhat, and assuming the brown dwarf atmosphere is cloudy, Ca could be locked up in molecules as simple as CaH, or perovskite (CaTiO₃), which starts condensing below 1700 K, forming clouds (Fegley & Lodders, 1996; Burrows et al., 2001; Lodders, 2002). In contrast, Na would not be locked up in any molecule and should remain atomic, consistent with spectroscopy and atmospheric modelling appropriate for L dwarf temperatures (Kirkpatrick et al., 1999a; Lodders, 1999; Cushing et al., 2005; Line et al., 2017). At least superficially, these simple expectations of brown dwarf atmospheres are consistent with the data for NLTT 5306.

On the hypothesized inflation and magnetism

Before further discussion, previous work and assertions made for NLTT 5306 are critically examined. In particular, it has been claimed that the brown dwarf is inflated, and that white dwarf magnetism plays a fundamental role in the binary properties (e.g. mass transfer).

At first glance, an inflated radius may have relevance to the detection of mass loss. However, the single infrared spectrum on which the inference is based is not only model dependent (from where the gravity indicators originate), but also sensitive to the accuracy of the modelled and subtracted white dwarf photosphere at infrared wavelengths (Casewell et al., 2020b). Apart from the inferred shape of its infrared spectrum, there is no empirical support for an inflated radius in NLTT 5306B.

In contrast, WD 1032+011 is a similar (white dwarf + brown dwarf) system, with a radius determined from eclipse measurements, but even in this case, the radius is within $2\sigma - 3\sigma$ of several reasonable models (Casewell et al., 2020a), where the binary can be younger than suggested by single-star kinematics⁴. But more importantly, there is no suggestion of mass transfer in the WD 1032+011 system, despite indications of an enlarged brown dwarf radius. There are a small number of eclipsing brown dwarf companions to white dwarfs, and only in the case of WD 1032+011 is there an indication of inflation (Littlefair et al., 2014; Parsons et al., 2017b). Perhaps similarly, there is a well-documented scatter in radii for M dwarfs which extends down to $90 \, \text{M}_{\text{Jup}}$ (Parsons et al., 2018). As these radii are derived primarily via eclipses with both main-sequence and white dwarf primaries, the cause cannot be any influence from a white dwarf host, and L-type brown dwarfs may simply exhibit a similar pattern (see next Section).

In the case of NLTT 5306B, for a 55 M_{Jup} brown dwarf of age greater than 1 Gyr, evolutionary models predict the radius should be smaller than $0.096\,R_\odot$, whereas the Roche lobe is $0.125\,R_\odot$. While neither the age nor mass are tightly constrained, for any reasonable range of parameters, the brown dwarf should be far from filling its Roche lobe (Baraffe et al., 2015). Moreover, as previously mentioned, if NLTT 5306B were abnormally enlarged and *transferring* mass gravitationally, the accreted m_{Na}/m_{Ca} ratio should be mundane, and not the anomalous value observed. Lastly, a wind Roche lobe overflow mechanism exists which lies in between the standard Roche lobe overflow and Bondi-Hoyle accretion (Mohamed & Podsiadlowski, 2007; de Val-Borro et al., 2009), but has so far only been applied to AGB stars with dusty and massive winds, and requires a significant wind acceleration zone. AGB wind speeds range from 5 to 30 km s⁻¹ (Mayer et al., 2014; Goldman et al., 2017), and are at least an order of magnitude slower than the wind speeds expected of M and L dwarfs, and that observed from the Sun. Thus, it is currently unclear if wind Roche lobe overflow applies to mass loss in main-sequence stars, and further research would clarify if the flow diverges significantly from Bondi-Hoyle.

Separately but related, previous work on NLTT 5306 has repeatedly suggested that the white dwarf might be weakly magnetic, with a field strength below the currently detectable threshold of Zeeman splitting in the optical (Longstaff et al., 2019; Casewell et al., 2020b; Buzard et al., 2022). The motivation for a putative white dwarf magnetism appears to be twofold: to account for the mass accretion onto the white dwarf, and to sustain the claimed brown dwarf inflation.

First, magnetic funnelling of infalling material was inferred for NLTT 5306 based on "the lack of any observational evidence for a substantial accretion disc" (Longstaff et al., 2019), but the same is true for non-magnetic white dwarfs accreting stellar wind from their M dwarf companions. All eight white dwarf + M dwarf pairs in Table 5.1 have neither detected magnetic fields (via Zeeman splitting or cyclotron emission) nor any indications of accretion discs, yet are nevertheless profusely polluted from intrinsic mass loss from their companions. The same can be true for NLTT 5306.

⁴Any one star of any given age can have any space motion; it is only the dispersions exhibited by populations that yield deterministic ages based on non-kinematically selected benchmark populations (e.g. Nordström et al. 2004; Bensby et al. 2014).

Second, in the case of NLTT 5306, there has been speculation regarding the potential role of magnetic interactions between the brown dwarf and the primary star, although no specific models or underlying physical mechanism have been proposed (Casewell et al., 2020b). A follow-up study searched for a high metallicity and cloudy brown dwarf atmosphere that might result in a sizeable radius enhancement (Burrows et al., 2011), but was discounted in favour of inflation via white dwarf magnetism, albeit without referencing models or prototypes where such phenomena have been observed (Buzard et al., 2022).

It is not clear if there are any existing models or prototypical examples of magnetic white dwarfs that cause stellar or substellar companions to become inflated. A strongly magnetic white dwarf ($B \sim 100\,\mathrm{MG}$) might heat an asteroid or possibly a dwarf planet-sized body via Ohmic dissipation (Bromley & Kenyon, 2019), but the energy required to inflate a brown dwarf is many orders of magnitude larger. Brown dwarfs are degenerate and have the highest density of unevolved astrophysical objects (not stellar remnants), and to inflate the radius requires an energy source comparable to their internal energy. To accelerate NLTT 5306B to its current rotation rate (from zero) requires around 1 per cent of its gravitational potential, and, assuming there is actually any inflation, tidal synchronization may be better suited to the task, but this is speculation.

On the origin of the substellar mass loss

In the previous sections, it was discussed that the accreted material cannot be from a debris disk or a case of Roche lobe overflow based on the material composition. This conclusion is robust even against the pathological cases that the white dwarf atmosphere is observed either in the increasing or decreasing phase of accretion. In the increasing phase where accretion has been ongoing for less than a sinking timescale of roughly 10^4 yr, the material being accreted would have $m_{\rm Na}/m_{\rm Ca} > 1000$ by mass. If the system is observed in the decreasing phase so that the material originally had solar (or chondritic) abundance, then accretion should have ceased approximately 1.1 Myr prior, or roughly 20 sinking timescales for Na and nearly 30 timescales for Ca. This implies unphysical masses of pollutants (e.g. 10^{20} times the mass of Na observed today).

It can also be reasoned that the interstellar medium cannot be the source of the observed Na pollution in NLTT 5306. First, while highly refractory Ca may be locked up in dust grains more often than Na in the interstellar medium, the extreme ratio is incompatible, as Ca will sublimate into a gas at sufficiently close distances to the white dwarf and accrete. Second, the H α emission line would have to be supported by a sufficiently high interstellar accretion rate, and it would be expected in other stars but has only been seen in a small number of white dwarfs with close companions where wind accretion is suspected or known (Zuckerman et al., 2003; Debes, 2006; Tappert et al., 2011b). Furthermore, the density of the interstellar medium implied by the observed accretion rate onto the white dwarf, based on its tangential speed, suggests densities higher than observed in a molecular cloud. In accordance with these reasons, the interstellar medium can be discounted as a viable source of Na pollution.

All data indicate the white dwarf is currently accreting in a steady state from a source with a high degree of chemical differentiation, as observed between Na and Ca. A plausible source for this material is the outermost layers of the brown dwarf, lost in an intrinsic wind, which acts as the source of pollution. The immediate cause of this differentiated wind is unknown, but by default is presumed to be the acceleration of Na ions along the magnetic

field lines of the rapidly rotating brown dwarf. To account for this inference, there must be a mechanism to preferentially ionise Na atoms. The atmospheric chemistry of brown dwarfs certainly plays a crucial role, with Ca predicted to be locked up in molecules or cloud particles, whereas Na will be in an atomic state.

In this picture, the alkali metals Li and K might be similarly expected, as they should remain atomic for a range of the warmest dwarf temperatures (Lodders, 1999; Burrows et al., 2001). The co-added spectrum of NLTT 5306 does not exhibit absorption from these elements, where the estimated upper limits [Li/H] < -8.5 and [K/H] < -7.0 translate into abundance upper limits in the captured wind of $m_{\rm Li}/m_{\rm Na}$ < 0.03 and $m_{\rm K}/m_{\rm Na}$ < 10. Unfortunately, both these limits are two orders of magnitude higher than the solar values (Lodders, 2003), and thus no further inferences can be drawn at present.

Grounded in the detection of Na in one case, one might expect analogous pollution in the other three white dwarfs with similar brown dwarf companions in close orbit. However, as mentioned above and shown in Table 5.1 those observations are *insensitive to the Na abundance detected for NLTT 5306*. Future observations of physically similar systems, but with more favourable detection sensitivities, may be able to uncover analogous signs of chemically-peculiar pollution from differentiated winds in ultracool dwarfs.

A priori, isolated brown dwarfs are unlikely to have significant wind due to their low atmospheric ionisation levels, resulting in weak atmosphere-field coupling (Mohanty et al., 2002). However, in a post-common envelope binary system, the white dwarf may raise the ionisation fraction in the brown dwarf atmosphere via irradiation, potentially facilitating a stronger flow. To determine the contribution of ionisation to wind liberation, a recombination-limited case was considered using an appropriate DA model white dwarf spectrum (following the methodology from Owen & Alvarez 2016). Assuming the recombination limit, the resulting maximum mass outflow rate was estimated to be $10^{-23}\,\mathrm{M}_\odot\,\mathrm{yr}^{-1}$, drastically lower than the empirically estimated mass-loss rate. Given the trivial ionising photon flux in a 7700 K white dwarf, the recombination limit approximation is unlikely to hold. However, the correct energy-limited value would be even lower, thus making no qualitative difference.

Other externally-driven mass loss mechanisms were considered for NLTT 5306B but discounted. Non-thermal mass loss and Jeans escape are negligible, and atmospheric boil-off (Owen & Wu, 2016) would require the brown dwarf to significantly overfill its Roche lobe and is hence ruled out. The mass loss from the brown dwarf caused by X-ray and extreme ultraviolet ionising radiation emitted by the white dwarf (Erkaev et al., 2007) is also calculated to be negligible for all four systems studied here. In summary, the radiation fields of these cool white dwarfs should have no significant effect on the coronal activity of the brown dwarf. Those calculations were done by my collaborators.

5.7 Conclusions

The goal of this work is to obtain sensitive limits to mass loss via substellar winds using white dwarf hosts. Using archival data for four known white dwarfs with closely-orbiting brown dwarf companions, upper limits for intrinsic mass loss are found to be three orders of magnitude lower than the solar value, concluded from the absence of Ca II K absorption. On the one hand, this methodology demonstrates similar sensitivity to the mass-loss estimates obtained from Ly α observations of M dwarfs, but only requires optical spectra and is not limited to bright stars within 7 pc. On the other hand, only post-common

envelope binaries with a (polluted) white dwarf can be studied this way. The brown dwarf mass-loss limits are then compared to M dwarfs for which abundances of at least two elements are known. It is found that L dwarf wind upper limits are approximately an order of magnitude below the \dot{M} values calculated for the M dwarfs.

The sole exception is the detection of Na in NLTT 5306, where a white dwarf accretion rate and corresponding L dwarf mass-loss rate are estimated, but uncertain owing to the highly unusual composition. The accreted material is shown to have $m_{\rm Na}/m_{\rm Ca} > 900$ based on the Na detection and Ca upper limit (cf. $[m_{\rm Na}/m_{\rm Ca}]_{\odot} \approx 1$). This extreme ratio rules out planetary debris of any known origin, as well as the interstellar medium. Notably, the composition appears consistent with atomic abundance predictions for a warm brown dwarf upper atmosphere. Derived from such models, the alkali elements Li and K might also be incorporated into a wind (Line et al., 2017; Gharib-Nezhad et al., 2021), but the observations are currently insensitive to these elements at solar ratios. This differentiated material cannot have reached the white dwarf via Roche lobe overflow, and instead an intrinsic wind must be the source of pollution, making it the first detection of mass loss in a substellar object. An important caveat is that the 1.7 h spin period of NLTT 5306B may suggest that its substellar wind is not representative of most L dwarfs.

This chapter demonstrates that the complex atmospheres of brown dwarfs, which may reflect multiple formation pathways and chemical diversity (Apai et al., 2013; Helling & Casewell, 2014; Madhusudhan et al., 2016), can be probed to some degree using polluted white dwarf hosts. Importantly, it is demonstrated that the white dwarf hosts cannot radiatively induce significant mass loss in their companions. However, some intrinsic binary features are not necessarily representative of all isolated ultracool dwarfs, such as rapid rotation, and may influence mass loss. At present, these effects are difficult to quantify with the existing data. Further work on the captured wind flow would better constrain low-mass stellar and substellar mass-loss rates, and a sensitive search for Na, Li, and K in cooler white dwarfs with ultracool dwarf companions could prove fruitful (e.g. WISEA J061543.91–124726.8; Fajardo-Acosta et al. 2016).

Chapter 6

Conclusions

In the early stages of my PhD, I conducted an extensive literature review. During this review, I came across a seminal paper on GD 356 by Ferrario et al. (1997a). Despite my limited knowledge of atypical white dwarf spectra, I was truly fascinated by its magnetically split emission lines. Eager to share my excitement, I discussed the paper with my supervisor, who revealed that he possessed time-series spectroscopic data of GD 356. This marked the beginning of the study of this unique DAHe star, which has since evolved into a significant and relatively novel class of white dwarfs.

Chapter 2 of my thesis focuses on the analysis of the aforementioned time-series spectra of GD 356, in conjunction with spectropolarimetry and optical photometry. The analysis revealed a correlation between emission line variability and photometric variability, albeit with a striking anti-phase relationship. Specifically, the photometric maximum coincides with the emission minimum. This finding led to the deduction that the source of emission must be a dark photospheric spot situated beneath an optically thin emission region.

During the preparation of the publication that serves as the foundation for Chapter 2, the discovery of three additional emitting white dwarfs emerged (Reding et al., 2020; Gänsicke et al., 2020; Tremblay et al., 2020). The clustering of these objects on the HRD prompted the proposal of a new class of white dwarfs with chromospheres. The close proximity of these objects on the diagram suggests an intrinsic emission mechanism linked to white dwarf evolution. Furthermore, the nature of the emitting region as a dark spot, theoretical analysis, and the absence of O-C variation led to the conclusion that the unipolar inductor mechanism cannot account for this phenomenon.

The intriguing discoveries within the DAHe class led to new research avenues. A series of observing proposals were made, focusing on both the prototype object and other members of this class. In Chapter 3, I presented new data on GD 356 that will contribute to a better understanding of the physical properties associated with the emitting region. This includes UV light curves, which surprisingly did not exhibit the expected anti-phase relationship with the optical photometry, as commonly observed in typical starspots. Additionally, I incorporated semi-amplitudes of photometric light curves from various bands and expanded the O-C analysis to encompass all the new data.

The consistent O-C trend indicates not only the absence of short-term variability (as discussed in Chapter 2) but also the absence of long-term variability over a four-year baseline. Notably, the amplitude analysis of the *TESS* light curves did not reveal any statistically significant changes. This observation is particularly intriguing given the dynamic nature typically associated with starspots. Presently, there is limited research on

spot lifetimes within the context of white dwarfs.

Through an analysis of publicly available data, I aimed to address some of the predictions put forth in the original paper and further characterise the DAHe class. I also investigated *Gaia* BP/RP spectra within the context of DAHe stars and discussed the challenges associated with confidently identifying them using low-resolution spectra. Furthermore, I examined *TESS* and *Gaia* variabilities to demonstrate that DAHe stars do not form a visually identifiable 'variable' cluster on the HRD. On the same diagram the ZZ Ceti cluster is easily identifiable. Consequently, the number density of white dwarfs with active chromospheres must indeed be relatively small, consistent with the recently published findings (Manser et al., 2023).

Chapter 4 of my thesis focused on two potential white dwarf binary systems: GD 1400 and PG 0010+281. GD 1400 was already known to be a binary system (Farihi & Christopher, 2004), but its orbital parameters were poorly constrained, relying solely on optical spectroscopy (Burleigh et al., 2011). By analysing the infrared spectroscopy data obtained from ISAAC, the radial velocity behaviour of the companion was tightly constrained. Furthermore, the physical parameters of the companion were determined through modelling its infrared spectrum.

On the other hand, PG 0010+281 is a white dwarf that exhibits an infrared excess. The SED could be fitted well with an L5-type brown dwarf companion. However, a thorough analysis involving multiple observatories failed to reveal any significant radial velocity variations. Additionally, no photometric variability was observed for the star. Based on these findings, I conducted simulations to establish mass and orbital period constraints for a plausible substellar companion. Although inconclusive, it appears that PG 0010+281 is more consistent with a single star and circumstellar dust rather than a close companion.

Subsequently, the chapter delves into an investigation of known short orbital period white dwarf-brown dwarf binaries. It was noted that the secondary substellar companions in these types of systems tend to have masses within the range of $50-70\,M_{Jup}$ and exhibit spectral types consistent with L-type dwarfs. As a result of this empirical observation, it is proposed that a companion must possess a minimum mass of $50\,M_{Jup}$ to survive the common envelope evolution process. This benchmark holds significant importance for the survival of any substellar or exoplanetary object within a white dwarf system. Notably, masses below $50\,M_{Jup}$ may have observational implications for the final mass and properties of the white dwarf remnant, including magnetism.

In chapter 5, I explored wind capture in binary systems consisting of a degenerate primary and stellar or substellar companion. The companions considered consisted of brown dwarfs and M dwarf stars. The study relied on the fact that white dwarfs in close binary systems are capable of accreting wind from the secondary, resulting in photospheric pollution. It is understood that heavy elements cannot be sustained in the photospheres of white dwarfs with $T_{\rm eff} < 25\,000\,{\rm K}$. I utilised this temperature constraint and estimated photospheric abundances to establish limits on white dwarf accretion rates from their companions. It was assumed that in these systems the mass loss via wind from the secondary is the only source of material that can be accreted by the primary. To estimate the mass loss rates for the companions, I employed two different accretion formalisms. For the brown dwarf sample only the upper limits of mass-losses could be obtained for all but one system. In the case of M dwarf systems, definite mass-loss values were obtained. These calculated values were then compared to existing estimates based on a more observationally demanding astrospheric Ly α technique, and they were found to be

comparable while being easier to obtain.

The second part of the chapter centred around NLTT 5306, a white dwarf+brown dwarf binary system exhibiting Na absorption in its optical spectra. Previous work had suggested that this absorption originated from Roche lobe overflow from the possibly inflated brown dwarf companion (Casewell et al., 2020b). However, based on the evidence examined, this scenario seems unlikely. A more plausible explanation is the accretion of substellar wind from the companion. The highly non-solar composition of the accreted material and its likely source were discussed in the context of the atmospheric composition of brown dwarfs. Although NLTT 5306B may not be a representative field brown dwarf due to its rapid rotation rate and potentially enhanced wind activity, great care is taken to demonstrate that the mass-loss is not driven by irradiation from the white dwarf primary. These observations are significant as they mark the first instance of detecting mass loss via wind from an L-type brown dwarf.

The thesis endeavours to investigate white dwarf systems exhibiting unusual features across a broad range of wavelengths, from ultraviolet to infrared. By studying GD 356, a white dwarf displaying enigmatic Balmer emission, a novel class of white dwarfs with active chromospheres was discovered. Additionally, the investigation of GD 1400 and PG 0010+281 yielded valuable empirical constraints on the process of common envelope evolution, including the first observational mass requirement for a close companion to survive this stage of the binary evolution. Furthermore, the most recent investigation focusing on white dwarf accretion from close binary companions contributed to the establishment of pioneering mass-loss limits for substellar objects.

By exploring these exotic white dwarf systems and conducting comprehensive investigations across various wavelengths, this thesis makes a significant contribution to the advancement of knowledge in the field. The unravelling of intriguing phenomena within these systems not only adds to our understanding of white dwarfs but also sheds light on the complexities associated with these astrophysical objects. The three avenues explored in the chapters lay the foundation for future work, holding the potential to yield even more fruitful results. The research conducted in this study underscores the astrophysical significance of white dwarf stars in examining a range of phenomena.

Bibliography

- Abate C., Pols O. R., Izzard R. G., Mohamed S. S., de Mink S. E., 2013, Wind Roche-lobe overflow: Application to carbon-enhanced metal-poor stars, A&A, 552, A26
- Ablimit I., Maeda K., 2019, Evolution of Magnetized White Dwarf Binaries to Type Ia Supernovae, ApJ, 871, 31
- Ablimit I., Maeda K., Li X.-D., 2016, Monte Carlo Population Synthesis of Post-commonenvelope White Dwarf Binaries and Type Ia supernova Rate, ApJ, 826, 53
- Aboudarham J., Henoux J. C., 1987, Non-thermal excitation and ionization of hydrogen in solar flares. II Effects on the temperature minimum region Energy balance and white light flares, A&A, 174, 270
- Achilleos N., Wickramasinghe D. T., Liebert J., Saffer R. A., Grauer A. D., 1992, *Exploring the Peculiar Magnetic Field of Feige* 7, ApJ, 396, 273
- Adams W. S., 1915, *The spectrum of the companion of Sirius*, Publications of the Astronomical Society of the Pacific, 27, 236
- Aguilera-Gómez C., Chanamé J., Pinsonneault M. H., Carlberg J. K., 2016, *On Lithium-rich Red Giants: Engulfment on the Giant Branch of Trumpler 20*, ApJ, 833, L24
- Allard F., Homeier D., Freytag B., 2012, *Models of very-low-mass stars, brown dwarfs and exoplanets*, Philosophical Transactions of the Royal Society of London Series A, 370, 2765
- Allègre C. J., Poirier J.-P., Humler E., Hofmann A. W., 1995, *The chemical composition of the Earth*, Earth and Planetary Science Letters, 134, 515
- Althaus L. G., Panei J. A., Romero A. D., Rohrmann R. D., Córsico A. H., García-Berro E., Miller Bertolami M. M., 2009, Evolution and colors of helium-core white dwarf stars with high-metallicity progenitors, A&A, 502, 207
- Althaus L. G., Córsico A. H., Isern J., García-Berro E., 2010, Evolutionary and pulsational properties of white dwarf stars, A&ARv, 18, 471
- Althaus L. G., Córsico A. H., Torres S., Lorén-Aguilar P., Isern J., García-Berro E., 2011, *The evolution of white dwarfs with a varying gravitational constant*, A&A, 527, A72
- Amaro R. C., et al., 2023, Hotter Than Expected: HST/WFC3 Phase-resolved Spectroscopy of a Rare Irradiated Brown Dwarf with Strong Internal Heat Flux, arXiv e-prints, p. arXiv:2303.07420
- Amorim L. L., Kepler S. O., Külebi B., Jordan S., Romero A. D., 2023, *Catalog of Magnetic White Dwarfs with Hydrogen Dominated Atmospheres*, ApJ, 944, 56
- Andrews J. J., Price-Whelan A. M., Agüeros M. A., 2014, *The Mass Distribution of Companions to Low-mass White Dwarfs*, ApJ, 797, L32
- Angel J. R. P., Borra E. F., Landstreet J. D., 1981, *The magnetic fields of white dwarfs.*, ApJS, 45, 457
- Anguiano B., et al., 2022, White Dwarf Binaries across the H-R Diagram, AJ, 164, 126 Anthony F., et al., 2022, Activity and Rotation of Nearby Field M Dwarfs in the TESS

- Southern Continuous Viewing Zone, arXiv e-prints, p. arXiv:2204.04700
- Apai D., Radigan J., Buenzli E., Burrows A., Reid I. N., Jayawardhana R., 2013, HST Spectral Mapping of L/T Transition Brown Dwarfs Reveals Cloud Thickness Variations, ApJ, 768, 121
- Ashley R. P., Farihi J., Marsh T. R., Wilson D. J., Gänsicke B. T., 2019, Evidence for bimodal orbital separations of white dwarf-red dwarf binary stars, MNRAS, 484, 5362
- Astropy Collaboration et al., 2013, *Astropy: A community Python package for astronomy*, A&A, 558, A33
- Astropy Collaboration et al., 2018, The Astropy Project: Building an Open-science Project and Status of the v2.0 Core Package, AJ, 156, 123
- Babcock H. W., 1947, Zeeman Effect in Stellar Spectra., ApJ, 105, 105
- Baglin A., Vauclair G., 1973, Evolutionary Sequence for DA, DB, DC White Dwarfs, A&A, 27, 307
- Bagnulo S., Landstreet J. D., 2018, Searching for the weakest detectable magnetic fields in white dwarfs. Highly-sensitive measurements from first VLT and WHT surveys, A&A, 618, A113
- Bagnulo S., Landstreet J. D., 2019, Discovery of weak magnetic fields in four DZ white dwarfs in the local 20 pc volume. Implications for the frequency of magnetic fields with cooling age, A&A, 630, A65
- Bagnulo S., Landstreet J. D., 2020, *Discovery of six new strongly magnetic white dwarfs in the 20 pc local population*, arXiv e-prints, p. arXiv:2010.05795
- Bagnulo S., Landstreet J. D., 2021, New insight into the magnetism of degenerate stars from the analysis of a volume-limited sample of white dwarfs, MNRAS, 507, 5902
- Bagnulo S., Landstreet J. D., 2022, Multiple Channels for the Onset of Magnetism in Isolated White Dwarfs, ApJ, 935, L12
- Bagnulo S., Landolfi M., Landstreet J. D., Landi Degl'Innocenti E., Fossati L., Sterzik M., 2009, *Stellar Spectropolarimetry with Retarder Waveplate and Beam Splitter Devices*, PASP, 121, 993
- Balick B., Frank A., 2002, *Shapes and Shaping of Planetary Nebulae*, ARA&A, 40, 439 Ballester P., Modigliani A., Boitquin O., Cristiani S., Hanuschik R., Kaufer A., Wolf S., 2000, *The UVES Data Reduction Pipeline*, The Messenger, 101, 31
- Baraffe I., Chabrier G., Barman T. S., Allard F., Hauschildt P. H., 2003, Evolutionary models for cool brown dwarfs and extrasolar giant planets. The case of HD 209458, A&A, 402, 701
- Baraffe I., Homeier D., Allard F., Chabrier G., 2015, New evolutionary models for premain sequence and main sequence low-mass stars down to the hydrogen-burning limit, A&A, 577, A42
- Barstow M. A., Jordan S., O'Donoghue D., Burleigh M. R., Napiwotzki R., Harrop-Allin M. K., 1995, *RE J0317-853: the hottest known highly magnetic DA white dwarf*, MNRAS, 277, 971
- Barstow M. A., Barstow J. K., Casewell S. L., Holberg J. B., Hubeny I., 2014, Evidence for an external origin of heavy elements in hot DA white dwarfs, MNRAS, 440, 1607
- Basri G., Mohanty S., Allard F., Hauschildt P. H., Delfosse X., Martín E. L., Forveille T., Goldman B., 2000, *An Effective Temperature Scale for Late-M and L Dwarfs, from Resonance Absorption Lines of Cs I and Rb I*, ApJ, 538, 363
- Bear E., Merlov A., Arad Y., Soker N., 2021, Rapid expansion of red giant stars during core helium flash by waves propagation to the envelope and implications to exoplanets,

- MNRAS, 507, 414
- Becklin E. E., Zuckerman B., 1988, *A low-temperature companion to a white dwarf star*, Nature, 336, 656
- Bédard A., Bergeron P., Fontaine G., 2017, Measurements of Physical Parameters of White Dwarfs: A Test of the Mass-Radius Relation, ApJ, 848, 11
- Bédard A., Bergeron P., Brassard P., Fontaine G., 2020, On the Spectral Evolution of Hot White Dwarf Stars. I. A Detailed Model Atmosphere Analysis of Hot White Dwarfs from SDSS DR12, ApJ, 901, 93
- Bédard A., Brassard P., Bergeron P., Blouin S., 2022, On the Spectral Evolution of Hot White Dwarf Stars. II. Time-dependent Simulations of Element Transport in Evolving White Dwarfs with STELUM, ApJ, 927, 128
- Bell K. J., Hermes J. J., Montgomery M. H., Winget D. E., Gentile Fusillo N. P., Raddi R., Gänsicke B. T., 2017, in Tremblay P. E., Gaensicke B., Marsh T., eds, Astronomical Society of the Pacific Conference Series Vol. 509, 20th European White Dwarf Workshop. p. 303 (arXiv:1609.09097), doi:10.48550/arXiv.1609.09097
- Bellm E. C., et al., 2019, The Zwicky Transient Facility: System Overview, Performance, and First Results, PASP, 131, 018002
- Bensby T., Feltzing S., Oey M. S., 2014, Exploring the Milky Way stellar disk. A detailed elemental abundance study of 714 F and G dwarf stars in the solar neighbourhood, A&A, 562, A71
- Bera P., Bhattacharya D., 2014, Mass-radius relation of strongly magnetized white dwarfs: nearly independent of Landau quantization, MNRAS, 445, 3951
- Berger E., et al., 2009, *Periodic Radio and Hα Emission from the L Dwarf Binary 2MASSW J0746425+200032: Exploring the Magnetic Field Topology and Radius Of An L Dwarf*, ApJ, 695, 310
- Bergeron P., Ruiz M. T., Leggett S. K., 1997, *The Chemical Evolution of Cool White Dwarfs and the Age of the Local Galactic Disk*, ApJS, 108, 339
- Bergeron P., Leggett S. K., Ruiz M. T., 2001, Photometric and Spectroscopic Analysis of Cool White Dwarfs with Trigonometric Parallax Measurements, ApJS, 133, 413
- Bergeron P., Dufour P., Fontaine G., Coutu S., Blouin S., Genest-Beaulieu C., Bédard A., Rolland B., 2019, *On the Measurement of Fundamental Parameters of White Dwarfs in the Gaia Era*, ApJ, 876, 67
- Bergeron P., et al., 2021, Hot Degenerates in the MCT Survey. III. A Sample of White Dwarf Stars in the Southern Hemisphere, AJ, 162, 188
- Bergfors C., Farihi J., Dufour P., Rocchetto M., 2014, Signs of a faint disc population at polluted white dwarfs, MNRAS, 444, 2147
- Bertone G., Fairbairn M., 2008, *Compact stars as dark matter probes*, Phys. Rev. D, 77, 043515
- Bessel F. W., 1844, On the variations of the proper motions of Procyon and Sirius, MNRAS, 6, 136
- Beuermann K., et al., 2013, The eclipsing post-common envelope binary CSS21055: a white dwarf with a probable brown-dwarf companion, A&A, 558, A96
- Blackett P. M. S., 1947, The Magnetic Field of Massive Rotating Bodies, Nature, 159, 658
 Blake C. H., Charbonneau D., White R. J., 2010, The NIRSPEC Ultracool Dwarf Radial Velocity Survey, ApJ, 723, 684
- Blouin S., Dufour P., Allard N. F., 2018, A New Generation of Cool White Dwarf Atmosphere Models. I. Theoretical Framework and Applications to DZ Stars, ApJ, 863,

- Blouin S., Daligault J., Saumon D., 2021, ²²Ne Phase Separation as a Solution to the Ultramassive White Dwarf Cooling Anomaly, ApJ, 911, L5
- Blouin S., Kilic M., Bédard A., Tremblay P.-E., 2023, *The ubiquity of carbon dredge-up in hydrogen-deficient white dwarfs as revealed by GALEX*, arXiv e-prints, p. arXiv:2307.14295
- Bognár Z., et al., 2020, TESS first look at evolved compact pulsators. Known ZZ Ceti stars of the southern ecliptic hemisphere as seen by TESS, A&A, 638, A82
- Bognár Z., Kalup C., Sódor Á., 2021, Exploring the pulsational properties of two ZZ Ceti stars, A&A, 651, A14
- Bond G., 1862, On the Companion of Sirius, by Prof. G. Bond, Director of the Observatory of Harvard College, Astronomische Nachrichten, 57, 131
- Bondi H., 1952, On spherically symmetrical accretion, MNRAS, 112, 195
- Bonfond B., 2013, When Moons Create Aurora: The Satellite Footprints on Giant Planets. American Geophysical Union (AGU), pp 133–140 (https://agupubs.onlinelibrary.wiley.com/doi/pdf/10.1029/2011GM001169),
 - doi:10.1029/2011GM001169, https://agupubs.onlinelibrary.wiley.com/doi/abs/10.1029/2011GM001169
- Boothroyd A. I., Sackmann I. J., 1999, *The CNO Isotopes: Deep Circulation in Red Giants and First and Second Dredge-up*, ApJ, 510, 232
- Borucki W. J., et al., 2010, Kepler Planet-Detection Mission: Introduction and First Results, Science, 327, 977
- Bradley L., et al., 2019, astropy/photutils: v0.7.2, doi:10.5281/zenodo.3568287
- Braithwaite J., Spruit H. C., 2004, A fossil origin for the magnetic field in A stars and white dwarfs, Nature, 431, 819
- Briggs G. P., Ferrario L., Tout C. A., Wickramasinghe D. T., Hurley J. R., 2015, *Merging binary stars and the magnetic white dwarfs*, MNRAS, 447, 1713
- Briggs G. P., Ferrario L., Tout C. A., Wickramasinghe D. T., 2018, *Origin of magnetic fields in cataclysmic variables*, MNRAS, 481, 3604
- Brinkworth C. S., Burleigh M. R., Wynn G. A., Marsh T. R., 2004, *Photometric variability of the unique magnetic white dwarf GD 356*, MNRAS, 348, L33
- Brinkworth C. S., Marsh T. R., Morales-Rueda L., Maxted P. F. L., Burleigh M. R., Good S. A., 2005, *Rotational period of WD 1953-011- a magnetic white dwarf with a star-spot*, MNRAS, 357, 333
- Brinkworth C. S., Gänsicke B. T., Marsh T. R., Hoard D. W., Tappert C., 2009, A Dusty Component to the Gaseous Debris Disk Around the White Dwarf SDSS J1228+1040, ApJ, 696, 1402
- Bromley B. C., Kenyon S. J., 2019, *Ohmic Heating of Asteroids around Magnetic Stars*, ApJ, 876, 17
- Brown W. R., Kilic M., Allende Prieto C., Kenyon S. J., 2010, *The ELM Survey. I. A Complete Sample of Extremely Low-mass White Dwarfs*, ApJ, 723, 1072
- Bues I., 1973, Carbon Abundance in the Atmospheres of Hydrogen-poor White Dwarfs, A&A, 28, 181
- Burgasser A. J., 2004, Discovery of a Second L Subdwarf in the Two Micron All Sky Survey, ApJ, 614, L73
- Burgasser A. J., Witte S., Helling C., Sanderson R. E., Bochanski J. J., Hauschildt P. H., 2009, Optical and Near-Infrared Spectroscopy of the L Subdwarf SDSS J125637.13-

- 022452.4, ApJ, 697, 148
- Burleigh M. R., Clarke F. J., Hodgkin S. T., 2002, *Imaging planets around nearby white dwarfs*, MNRAS, 331, L41
- Burleigh M. R., Hogan E., Dobbie P. D., Napiwotzki R., Maxted P. F. L., 2006a, *A near-infrared spectroscopic detection of the brown dwarf in the post common envelope binary WD0137-349*, MNRAS, 373, L55
- Burleigh M. R., et al., 2006b, *The nature of the close magnetic white dwarf + probable brown dwarf binary SDSSJ121209.31+013627.7*, MNRAS, 373, 1416
- Burleigh M. R., et al., 2011, in Schuh S., Drechsel H., Heber U., eds, American Institute of Physics Conference Series Vol. 1331, Planetary Systems Beyond the Main Sequence. pp 262–270 (arXiv:1102.0505), doi:10.1063/1.3556209
- Burrows A., et al., 1997, A Nongray Theory of Extrasolar Giant Planets and Brown Dwarfs, ApJ, 491, 856
- Burrows A., Hubbard W. B., Lunine J. I., Liebert J., 2001, *The theory of brown dwarfs and extrasolar giant planets*, Reviews of Modern Physics, 73, 719
- Burrows A., Hubeny I., Budaj J., Knutson H. A., Charbonneau D., 2007, *Theoretical Spectral Models of the Planet HD 209458b with a Thermal Inversion and Water Emission Bands*, ApJ, 668, L171
- Burrows A., Heng K., Nampaisarn T., 2011, *The Dependence of Brown Dwarf Radii on Atmospheric Metallicity and Clouds: Theory and Comparison with Observations*, ApJ, 736, 47
- Busso M., Gallino R., Wasserburg G. J., 1999, Nucleosynthesis in Asymptotic Giant Branch Stars: Relevance for Galactic Enrichment and Solar System Formation, ARA&A, 37, 239
- Buzard C., Casewell S., Lothringer J., Blake G., 2022, Near-infrared spectra of the inflated post-common envelope brown dwarf NLTT 5306B, arXiv e-prints, p. arXiv:2204.05330
- Caiazzo I., et al., 2020, Intermediate-mass Stars Become Magnetic White Dwarfs, ApJ, 901, L14
- Calcaferro L. M., Córsico A. H., Althaus L. G., Lopez I. D., Hermes J. J., 2023, *Exploring the internal rotation of the extremely low-mass He-core white dwarf GD 278 with TESS asteroseismology*, A&A, 673, A135
- Campos F., et al., 2016, A comparative analysis of the observed white dwarf cooling sequence from globular clusters, MNRAS, 456, 3729
- Caplan M. E., 2020, Black dwarf supernova in the far future, MNRAS, 497, 4357
- Carlberg J. K., Majewski S. R., Arras P., 2009, *The Role of Planet Accretion in Creating the Next Generation of Red Giant Rapid Rotators*, ApJ, 700, 832
- Casewell S. L., et al., 2015, Multiwaveband photometry of the irradiated brown dwarf WD0137-349B, MNRAS, 447, 3218
- Casewell S. L., et al., 2018a, The first sub-70 min non-interacting WD-BD system: EPIC212235321, MNRAS, 476, 1405
- Casewell S. L., Littlefair S. P., Parsons S. G., Marsh T. R., Fortney J. J., Marley M. S., 2018b, *The direct detection of the irradiated brown dwarf in the white dwarf-brown dwarf binary SDSS J141126.20+200911.1*, MNRAS, 481, 5216
- Casewell S. L., et al., 2020a, WD1032 + 011, an inflated brown dwarf in an old eclipsing binary with a white dwarf, MNRAS, 497, 3571
- Casewell S. L., Debes J., Braker I. P., Cushing M. C., Mace G., Marley M. S., Kirkpatrick J. D., 2020b, *NLTT5306B: an inflated, weakly irradiated brown dwarf*, MNRAS, 499,

- Castellani V., Chieffi A., Tornambe A., Pulone L., 1985, *Helium-burning evolutionary phases in population II stars. I Breathing pulses in horizontal branch stars*, ApJ, 296, 204
- Catelan M., 2009, Horizontal branch stars: the interplay between observations and theory, and insights into the formation of the Galaxy, Ap&SS, 320, 261
- Caudal G., 1986, A self-consistent model of Jupiter's magnetodisc including the effects of centrifugal force and pressure, J. Geophys. Res., 91, 4201
- Cauley P. W., Shkolnik E. L., Llama J., Lanza A. F., 2019, Magnetic field strengths of hot Jupiters from signals of star-planet interactions, Nature Astronomy, 3, 1128
- Chabrier G., 1993, Quantum Effects in Dense Coulombic Matter: Application to the Cooling of White Dwarfs, ApJ, 414, 695
- Chabrier G., Ashcroft N. W., Dewitt H. E., 1992, White dwarfs as quantum crystals, Nature, 360, 48
- Chabrier G., Baraffe I., Allard F., Hauschildt P., 2000, *Deuterium Burning in Substellar Objects*, ApJ, 542, L119
- Chamandy L., Blackman E. G., Nordhaus J., Wilson E., 2021, Successive common envelope events from multiple planets, MNRAS, 502, L110
- Chamel N., Fantina A. F., Davis P. J., 2013, *Stability of super-Chandrasekhar magnetic white dwarfs*, Phys. Rev. D, 88, 081301
- Chandrasekhar S., 1931, The Maximum Mass of Ideal White Dwarfs, ApJ, 74, 81
- Chayer P., Fontaine G., Wesemael F., 1995, *Radiative Levitation in Hot White Dwarfs:* Equilibrium Theory, ApJS, 99, 189
- Chené A.-N., 2020, DRAGraces: Reduction pipeline for GRACES spectra (ascl:2012.024)
- Chene A.-N., et al., 2014, in Navarro R., Cunningham C. R., Barto A. A., eds, Society of Photo-Optical Instrumentation Engineers (SPIE) Conference Series Vol. 9151, Advances in Optical and Mechanical Technologies for Telescopes and Instrumentation. p. 915147 (arXiv:1409.7448), doi:10.1117/12.2057417
- Chené A.-N., Mao S., Lundquist M., Gemini Collaboration Martioli E., Opera Collaboration Carlin J. L., Usability Testing 2021, *DRAGraces: A Pipeline for the GRACES High-resolution Spectrograph at Gemini*, AJ, 161, 109
- Cheng S., Cummings J. D., Ménard B., 2019, *A Cooling Anomaly of High-mass White Dwarfs*, ApJ, 886, 100
- Christensen U. R., Holzwarth V., Reiners A., 2009, Energy flux determines magnetic field strength of planets and stars, Nature, 457, 167
- Ciddor P. E., 1996, *Refractive index of air: new equations for the visible and near infrared*, Appl. Opt., 35, 1566
- Clayton D. D., 1968, Principles of stellar evolution and nucleosynthesis
- Cohen O., 2011, The independency of stellar mass-loss rates on stellar X-ray luminosity and activity level based on solar X-ray flux and solar wind observations, MNRAS, 417, 2592
- Collins K. A., Kielkopf J. F., Stassun K. G., Hessman F. V., 2017, AstroImageJ: Image Processing and Photometric Extraction for Ultra-precise Astronomical Light Curves, AJ, 153, 77
- Cook B. A., Williams P. K. G., Berger E., 2014, Trends in Ultracool Dwarf Magnetism. II. The Inverse Correlation Between X-Ray Activity and Rotation as Evidence for a Bimodal Dynamo, ApJ, 785, 10

- Cooper A. P., et al., 2023, Overview of the DESI Milky Way Survey, ApJ, 947, 37
- Córsico A. H., 2020, White-dwarf asteroseismology with the Kepler space telescope, Frontiers in Astronomy and Space Sciences, 7, 47
- Córsico A. H., Benvenuto O. G., Althaus L. G., Isern J., García-Berro E., 2001, *The potential of the variable DA white dwarf G117-B15A as a tool for fundamental physics*, New Astron., 6, 197
- Córsico A. H., Althaus L. G., Miller Bertolami M. M., Kepler S. O., 2019, *Pulsating white dwarfs: new insights*, A&ARv, 27, 7
- Coutu S., Dufour P., Bergeron P., Blouin S., Loranger E., Allard N. F., Dunlap B. H., 2019, Analysis of Helium-rich White Dwarfs Polluted by Heavy Elements in the Gaia Era, ApJ, 885, 74
- Cowan N. B., Agol E., Charbonneau D., 2007, Hot nights on extrasolar planets: mid-infrared phase variations of hot Jupiters, MNRAS, 379, 641
- Cranmer S. R., Saar S. H., 2011, Testing a Predictive Theoretical Model for the Mass Loss Rates of Cool Stars, ApJ, 741, 54
- Cropper M., 1990, The Polars, Space Sci. Rev., 54, 195
- Cummings J. D., Kalirai J. S., Tremblay P. E., Ramirez-Ruiz E., Choi J., 2018, *The White Dwarf Initial-Final Mass Relation for Progenitor Stars from 0.85 to 7.5 M* _⊙, ApJ, 866, 21
- Cummings J. D., Kalirai J. S., Choi J., Georgy C., Tremblay P. E., Ramirez-Ruiz E., 2019, A Novel Approach to Constrain Rotational Mixing and Convective-core Overshoot in Stars Using the Initial-Final Mass Relation, ApJ, 871, L18
- Cushing M. C., Vacca W. D., 2006, The Schizophrenic Spectrum of LSR 1610-0040: A Peculiar M Dwarf/Subdwarf, AJ, 131, 1797
- Cushing M. C., Vacca W. D., Rayner J. T., 2004, Spextool: A Spectral Extraction Package for SpeX, a 0.8-5.5 Micron Cross-Dispersed Spectrograph, PASP, 116, 362
- Cushing M. C., Rayner J. T., Vacca W. D., 2005, *An Infrared Spectroscopic Sequence of M, L, and T Dwarfs*, ApJ, 623, 1115
- D'Angelo C., van Kerkwijk M. H., Rucinski S. M., 2006, Contact Binaries with Additional Components. II. A Spectroscopic Search for Faint Tertiaries, AJ, 132, 650
- D'Antona F., Mazzitelli I., 1989, The Fastest Evolving White Dwarfs, ApJ, 347, 934
- de Angeli F., et al., 2023, Gaia Data Release 3. Processing and validation of BP/RP low-resolution spectral data, A&A, 674, A2
- de Jong R. S., et al., 2019, 4MOST: Project overview and information for the First Call for Proposals, The Messenger, 175, 3
- de Marco O., Izzard R. G., 2017, *Dawes Review 6: The Impact of Companions on Stellar Evolution*, Publ. Astron. Soc. Australia, 34, e001
- de Rosa R. J., et al., 2014, *The VAST Survey III. The multiplicity of A-type stars within* 75 pc, MNRAS, 437, 1216
- DESI Collaboration et al., 2016, *The DESI Experiment Part I: Science, Targeting, and Survey Design*, arXiv e-prints, p. arXiv:1611.00036
- DESI Collaboration et al., 2022, Overview of the Instrumentation for the Dark Energy Spectroscopic Instrument, AJ, 164, 207
- de Val-Borro M., Karovska M., Sasselov D., 2009, Numerical Simulations of Wind Accretion in Symbiotic Binaries, ApJ, 700, 1148
- Dahn C. C., et al., 2002, Astrometry and Photometry for Cool Dwarfs and Brown Dwarfs, AJ, 124, 1170

- Dahn C. C., et al., 2008, Trigonometric Parallaxes for Two Late-Type Subdwarfs: LSR 1425+71 (sdM8.0) and the Binary LSR 1610-00 (sd?M6pec), ApJ, 686, 548
- Dalton G., et al., 2014, in Ramsay S. K., McLean I. S., Takami H., eds, Society of Photo-Optical Instrumentation Engineers (SPIE) Conference Series Vol. 9147, Ground-based and Airborne Instrumentation for Astronomy V. p. 91470L (arXiv:1412.0843), doi:10.1117/12.2055132
- Das U., Mukhopadhyay B., 2013, New Mass Limit for White Dwarfs: Super-Chandrasekhar Type Ia Supernova as a New Standard Candle, Phys. Rev. Lett., 110, 071102
- Day-Jones A. C., et al., 2011, Discovery of a T dwarf + white dwarf binary system, MNRAS, 410, 705
- Debes J. H., 2006, Measuring M Dwarf Winds with DAZ White Dwarfs, ApJ, 652, 636
- Debes J. H., Hoard D. W., Wachter S., Leisawitz D. T., Cohen M., 2011, *The WIRED Survey. II. Infrared Excesses in the SDSS DR7 White Dwarf Catalog*, ApJS, 197, 38
- Dekker H., D'Odorico S., Kaufer A., Delabre B., Kotzlowski H., 2000, in Iye M., Moorwood A. F., eds, Society of Photo-Optical Instrumentation Engineers (SPIE) Conference Series Vol. 4008, Optical and IR Telescope Instrumentation and Detectors. pp 534–545, doi:10.1117/12.395512
- Dobbie P. D., Baxter R., Külebi B., Parker Q. A., Koester D., Jordan S., Lodieu N., Euchner F., 2012, *Two new young, wide, magnetic + non-magnetic double-degenerate binary systems*, MNRAS, 421, 202
- Donati J. F., Catala C., Landstreet J. D., Petit P., 2006, in Casini R., Lites B. W., eds, Astronomical Society of the Pacific Conference Series Vol. 358, Solar Polarization 4. p. 362
- Dorschner J., Henning T., 1995, Dust metamorphosis in the galaxy, A&ARv, 6, 271
- Doschek G. A., Warren H. P., Feldman U., 2015, Anomalous Relative Ar/Ca Coronal Abundances Observed by the Hinode/EUV Imaging Spectrometer Near Sunspots, ApJ, 808, L7
- Doyle A. E., et al., 2023, New chondritic bodies identified in eight oxygen-bearing white dwarfs, arXiv e-prints, p. arXiv:2303.00063
- Drake A. J., et al., 2010, Discovery of eclipsing white dwarf systems in a search for Earth-size companions, arXiv e-prints, p. arXiv:1009.3048
- Drake J. J., Cohen O., Yashiro S., Gopalswamy N., 2013, *Implications of Mass and Energy Loss due to Coronal Mass Ejections on Magnetically Active Stars*, ApJ, 764, 170
- Dreizler S., 1999, *Hubble Space Telescope spectroscopy of hot helium-rich white dwarfs: metal abundances along the cooling sequence*, A&A, 352, 632
- Dreizler S., Heber U., 1998, Spectral analyses of PG 1159 star: constraints on the GW Virginis pulsations from HST observations, A&A, 334, 618
- Drewes M., McDonald J., Sablon L., Vitagliano E., 2022, Neutrino Emissivities as a Probe of the Internal Magnetic Fields of White Dwarfs, ApJ, 934, 99
- Duffy C., Ramsay G., Wu K., Mason P. A., Hakala P., Steeghs D., Wood M. A., 2022, Short-duration accretion states of Polars as seen in TESS and ZTF data, MNRAS, 516, 3144
- Dufour P., Bergeron P., Fontaine G., 2005, *Detailed Spectroscopic and Photometric Analysis of DQ White Dwarfs*, ApJ, 627, 404
- Dufour P., Liebert J., Fontaine G., Behara N., 2007a, White dwarf stars with carbon atmospheres, Nature, 450, 522

- Dufour P., et al., 2007b, On the Spectral Evolution of Cool, Helium-Atmosphere White Dwarfs: Detailed Spectroscopic and Photometric Analysis of DZ Stars, ApJ, 663, 1291
- Dufour P., Fontaine G., Liebert J., Schmidt G. D., Behara N., 2008, *Hot DQ White Dwarfs: Something Different*, ApJ, 683, 978
- Dufour P., Fontaine G., Bergeron P., Béland S., Chayer P., Williams K. A., Liebert J., 2010, in Werner K., Rauch T., eds, American Institute of Physics Conference Series Vol. 1273, 17th European White Dwarf Workshop. pp 64–69, doi:10.1063/1.3527891
- Dufour P., Kilic M., Fontaine G., Bergeron P., Melis C., Bochanski J., 2012, Detailed Compositional Analysis of the Heavily Polluted DBZ White Dwarf SDSS J073842.56+183509.06: A Window on Planet Formation?, ApJ, 749, 6
- Dufour P., Vornanen T., Bergeron P., Fontaine Berdyugin A., 2013, in Krzesiński J., Stachowski G., Moskalik P., Bajan K., eds, Astronomical Society of the Pacific Conference Series Vol. 469, 18th European White Dwarf Workshop., p. 167
- Dufour P., Blouin S., Coutu S., Fortin-Archambault M., Thibeault C., Bergeron P., Fontaine G., 2017, in Tremblay P. E., Gaensicke B., Marsh T., eds, Astronomical Society of the Pacific Conference Series Vol. 509, 20th European White Dwarf Workshop. p. 3 (arXiv:1610.00986)
- Dunlap B. H., Clemens J. C., 2015, in Dufour P., Bergeron P., Fontaine G., eds, Astronomical Society of the Pacific Conference Series Vol. 493, 19th European Workshop on White Dwarfs. p. 547
- Dunlap B. H., Barlow B. N., Clemens J. C., 2010, A New Small-amplitude Variable Hot DQ White Dwarf, ApJ, 720, L159
- Dupuis J., Fontaine G., Pelletier C., Wesemael F., 1992, A Study of Metal Abundance Patterns in Cool White Dwarfs. I. Time-dependent Calculations of Gravitational Settling, ApJS, 82, 505
- Dupuis J., Fontaine G., Pelletier C., Wesemael F., 1993a, A Study of Metal Abundance Patterns in Cool White Dwarfs. II. Simulations of Accretion Episodes, ApJS, 84, 73
- Dupuis J., Fontaine G., Wesemael F., 1993b, A Study of Metal Abundance Patterns in Cool White Dwarfs. III. Comparison of the Predictions of the Two-Phase Accretion Model with the Observations, ApJS, 87, 345
- Duquennoy A., Mayor M., 1991, Multiplicity among Solar Type Stars in the Solar Neighbourhood Part Two Distribution of the Orbital Elements in an Unbiased Sample, A&A, 248, 485
- Eddington A. S., 1926, *The Internal Constitution of the Stars*. Cambridge Science Classics, Cambridge University Press, doi:10.1017/CBO9780511600005
- Edwards J. L., Cox E. G., Ziurys L. M., 2014, Millimeter Observations of CS, HCO⁺, and CO toward Five Planetary Nebulae: Following Molecular Abundances with Nebular Age, ApJ, 791, 79
- El-Badry K., Rix H.-W., Weisz D. R., 2018, *An Empirical Measurement of the Initial-Final Mass Relation with Gaia White Dwarfs*, ApJ, 860, L17
- Elms A. K., et al., 2023, An emerging and enigmatic spectral class of isolated DAe white dwarfs, arXiv e-prints, p. arXiv:2307.09186
- Engels D., 2005, AGB and post-AGB stars., Mem. Soc. Astron. Italiana, 76, 441
- Erkaev N. V., Kulikov Y. N., Lammer H., Selsis F., Langmayr D., Jaritz G. F., Biernat H. K., 2007, Roche lobe effects on the atmospheric loss from "Hot Jupiters", A&A, 472, 329
- Euchner F., Reinsch K., Jordan S., Beuermann K., Gänsicke B. T., 2005, Zeeman to-

- mography of magnetic white dwarfs. II. The quadrupole-dominated magnetic field of <ASTROBJ>HE 1045-0908</ASTROBJ>, A&A, 442, 651
- Euchner F., Jordan S., Beuermann K., Reinsch K., Gänsicke B. T., 2006, Zeeman to-mography of magnetic white dwarfs. III. The 70-80 Megagauss magnetic field of <AS-TROBJ>PG 1015+014</ASTROBJ>, A&A, 451, 671
- Eyer L., et al., 2022, Gaia Data Release 3. Summary of the variability processing and analysis, arXiv e-prints, p. arXiv:2206.06416
- Fabrycky D., Tremaine S., 2007, Shrinking Binary and Planetary Orbits by Kozai Cycles with Tidal Friction, ApJ, 669, 1298
- Fajardo-Acosta S. B., et al., 2016, Discovery of a Possible Cool White Dwarf Companion from the AllWISE Motion Survey, ApJ, 832, 62
- Fantin N. J., et al., 2019, The Canada-France Imaging Survey: Reconstructing the Milky Way Star Formation History from Its White Dwarf Population, ApJ, 887, 148
- Farihi J., 2016, Circumstellar debris and pollution at white dwarf stars, New Astron. Rev., 71, 9
- Farihi J., Christopher M., 2004, A Possible Brown Dwarf Companion to the White Dwarf GD 1400, AJ, 128, 1868
- Farihi J., Zuckerman B., Becklin E. E., 2005a, Mid-Infrared Observations of the White Dwarf-Brown Dwarf Binary GD 1400, AJ, 130, 2237
- Farihi J., Becklin E. E., Zuckerman B., 2005b, *Low-Luminosity Companions to White Dwarfs*, ApJS, 161, 394
- Farihi J., Hoard D. W., Wachter S., 2006, White Dwarf-Red Dwarf Systems Resolved with the Hubble Space Telescope. I. First Results, ApJ, 646, 480
- Farihi J., Burleigh M. R., Hoard D. W., 2008, A Near-Infrared Spectroscopic Study of the Accreting Magnetic White Dwarf SDSS J121209.31+013627.7 and Its Substellar Companion, ApJ, 674, 421
- Farihi J., Jura M., Zuckerman B., 2009, *Infrared Signatures of Disrupted Minor Planets at White Dwarfs*, ApJ, 694, 805
- Farihi J., Hoard D. W., Wachter S., 2010a, White Dwarf-Red Dwarf Systems Resolved with the Hubble Space Telescope. II. Full Snapshot Survey Results, ApJS, 190, 275
- Farihi J., Barstow M. A., Redfield S., Dufour P., Hambly N. C., 2010b, *Rocky planetesimals* as the origin of metals in DZ stars, MNRAS, 404, 2123
- Farihi J., Jura M., Lee J. E., Zuckerman B., 2010c, Strengthening the Case for Asteroidal Accretion: Evidence for Subtle and Diverse Disks at White Dwarfs, ApJ, 714, 1386
- Farihi J., Gänsicke B. T., Wyatt M. C., Girven J., Pringle J. E., King A. R., 2012, Scars of intense accretion episodes at metal-rich white dwarfs, MNRAS, 424, 464
- Farihi J., Parsons S. G., Gänsicke B. T., 2017, *A circumbinary debris disk in a polluted white dwarf system*, Nature Astronomy, 1, 0032
- Farihi J., et al., 2018a, Magnetism, X-rays and accretion rates in WD 1145+017 and other polluted white dwarf systems, MNRAS, 474, 947
- Farihi J., et al., 2018b, Dust production and depletion in evolved planetary systems, MNRAS, 481, 2601
- Farihi J., et al., 2022, Relentless and complex transits from a planetesimal debris disc, MNRAS, 511, 1647
- Farihi J., Hermes J. J., Littlefair S. P., Howarth I. D., Walters N., Parsons S. G., 2023, *Discovery of Dipolar Chromospheres in Two White Dwarfs*, arXiv e-prints, p. arXiv:2307.02543

- Farmer A. J., Phinney E. S., 2003, *The gravitational wave background from cosmological compact binaries*, MNRAS, 346, 1197
- Faulkner J., 1971, Ultrashort-Period Binaries, Gravitational Radiation, and Mass Transfer. I. The Standard Model, with Applications to WZ Sagittae and Z Camelopardalis, ApJ, 170, L99
- Featherstone N. A., Browning M. K., Brun A. S., Toomre J., 2009, Effects of Fossil Magnetic Fields on Convective Core Dynamos in A-type Stars, ApJ, 705, 1000
- Fegley Bruce J., Lodders K., 1996, Atmospheric Chemistry of the Brown Dwarf Gliese 229B: Thermochemical Equilibrium Predictions, ApJ, 472, L37
- Feng F., et al., 2022, 3D Selection of 167 Substellar Companions to Nearby Stars, ApJS, 262, 21
- Fernandes R. B., Mulders G. D., Pascucci I., Mordasini C., Emsenhuber A., 2019, *Hints for a Turnover at the Snow Line in the Giant Planet Occurrence Rate*, ApJ, 874, 81
- Ferrario L., Wickramasinghe D. T., 1999, *The power of intermediate polars*, MNRAS, 309, 517
- Ferrario L., Wickramasinghe D. T., 2005, Magnetic fields and rotation in white dwarfs and neutron stars, MNRAS, 356, 615
- Ferrario L., Wickramasinghe D. T., Liebert J., Schmidt G. D., Bieging J. H., 1997a, The magnetic field and emission-line spectrum of the remarkable white dwarf GD356, MNRAS, 289, 105
- Ferrario L., Vennes S., Wickramasinghe D. T., Bailey J. A., Christian D. J., 1997b, *EUVE J0317-855: a rapidly rotating, high-field magnetic white dwarf*, MNRAS, 292, 205
- Ferrario L., Melatos A., Zrake J., 2015a, *Magnetic Field Generation in Stars*, Space Sci. Rev., 191, 77
- Ferrario L., de Martino D., Gänsicke B. T., 2015b, *Magnetic White Dwarfs*, Space Sci. Rev., 191, 111
- Ferrario L., Wickramasinghe D. T., Kawka A., 2020a, *Magnetic fields in isolated and interacting white dwarfs*, arXiv e-prints, p. arXiv:2001.10147
- Ferrario L., Wickramasinghe D., Kawka A., 2020b, *Magnetic fields in isolated and interacting white dwarfs*, Advances in Space Research, 66, 1025
- Fontaine G., Brassard P., 2008, The Pulsating White Dwarf Stars, PASP, 120, 1043
- Fontaine G., Michaud G., 1979, Diffusion time scales in white dwarfs., ApJ, 231, 826
- Fontaine G., Thomas J. H., van Horn H. M., 1973, *On the Evolution of Magnetic White Dwarfs*, ApJ, 184, 911
- Fontaine G., Brassard P., Bergeron P., 2001, *The Potential of White Dwarf Cosmochronology*, PASP, 113, 409
- Fontaine G., Bergeron P., Billères M., Charpinet S., 2003, A Confirmation of the Optical Spectroscopy Approach: Discovery of Two More Pulsating DA (ZZ Ceti) White Dwarfs, ApJ, 591, 1184
- Ford H. C., et al., 1998, in Bely P. Y., Breckinridge J. B., eds, Society of Photo-Optical Instrumentation Engineers (SPIE) Conference Series Vol. 3356, Space Telescopes and Instruments V. pp 234–248, doi:10.1117/12.324464
- Fortney J. J., Lodders K., Marley M. S., Freedman R. S., 2008, A Unified Theory for the Atmospheres of the Hot and Very Hot Jupiters: Two Classes of Irradiated Atmospheres, ApJ, 678, 1419
- Fossati L., Koskinen T., France K., Cubillos P. E., Haswell C. A., Lanza A. F., Pillitteri I., 2018, Suppressed Far-UV Stellar Activity and Low Planetary Mass Loss in the WASP-18

- System, AJ, 155, 113
- Fowler R. H., 1926, On dense matter, MNRAS, 87, 114
- Franzon B., Schramm S., 2017, in Journal of Physics Conference Series. p. 012015 (arXiv:1702.00571), doi:10.1088/1742-6596/861/1/012015
- French J. R., Casewell S. L., Dupuy T. J., Debes J. H., Manjavacas E., Martin E. C., Xu S., 2023, Discovery of a resolved white dwarf-brown dwarf binary with a small projected separation: SDSS J222551.65+001637.7AB, MNRAS, 519, 5008
- Fressin F., et al., 2013, *The False Positive Rate of Kepler and the Occurrence of Planets*, ApJ, 766, 81
- Freudling W., Romaniello M., Bramich D. M., Ballester P., Forchi V., García-Dabló C. E., Moehler S., Neeser M. J., 2013, *Automated data reduction workflows for astronomy. The ESO Reflex environment*, A&A, 559, A96
- Fulton B. J., et al., 2021, California Legacy Survey. II. Occurrence of Giant Planets beyond the Ice Line, ApJS, 255, 14
- Gaia Collaboration et al., 2016, The Gaia mission, A&A, 595, A1
- Gaia Collaboration et al., 2018a, Gaia Data Release 2. Summary of the contents and survey properties, A&A, 616, A1
- Gaia Collaboration et al., 2018b, Gaia Data Release 2. Observational Hertzsprung-Russell diagrams, A&A, 616, A10
- Gaia Collaboration et al., 2022, Gaia Data Release 3: Summary of the content and survey properties, arXiv e-prints, p. arXiv:2208.00211
- Gaia Collaboration et al., 2023, Gaia Data Release 3. The Galaxy in your preferred colours: Synthetic photometry from Gaia low-resolution spectra, A&A, 674, A33
- Gänsicke B. T., Marsh T. R., Southworth J., Rebassa-Mansergas A., 2006, A Gaseous Metal Disk Around a White Dwarf, Science, 314, 1908
- Gänsicke B. T., Schreiber M. R., Toloza O., Gentile Fusillo N. P., Koester D., Manser C. J., 2019, *Accretion of a giant planet onto a white dwarf star*, Nature, 576, 61
- Gänsicke B. T., Rodriguez-Gil P., Gentile Fusillo N. P., Inight K., Schreiber M. R., Pala A. F., Tremblay P.-E., 2020, Single magnetic white dwarfs with Balmer emission lines: A small class with consistent physical characteristics as possible signposts for close-in planetary companions, arXiv e-prints, p. arXiv:2009.11925
- Garcia-Berro E., Iben I., 1994, On the Formation and Evolution of Super–Asymptotic Giant Branch Stars with Cores Processed by Carbon Burning. I. SPICA to Antares, ApJ, 434, 306
- García-Berro E., Oswalt T. D., 2016, *The white dwarf luminosity function*, New Astron. Rev., 72, 1
- Garcia-Berro E., Hernanz M., Mochkovitch R., Isern J., 1988, *Theoretical white-dwarf luminosity functions for two phase diagrams of the carbon-oxygen dense plasma.*, A&A, 193, 141
- García-Berro E., et al., 2012, Double Degenerate Mergers as Progenitors of High-field Magnetic White Dwarfs, ApJ, 749, 25
- Gardner J. P., et al., 2006, The James Webb Space Telescope, Space Sci. Rev., 123, 485
- Ge H., Webbink R. F., Chen X., Han Z., 2020, Adiabatic Mass Loss in Binary Stars. III. From the Base of the Red Giant Branch to the Tip of the Asymptotic Giant Branch, ApJ, 899, 132
- Geier S., Kupfer T., Schaffenroth V., Heber U., 2016, in Bragaglia A., Arnaboldi M., Rejkuba M., Romano D., eds, Vol. 317, The General Assembly of

- Galaxy Halos: Structure, Origin and Evolution. pp 302–303 (arXiv:1510.05989), doi:10.1017/S174392131500681X
- Gentile Fusillo N. P., et al., 2019, A Gaia Data Release 2 catalogue of white dwarfs and a comparison with SDSS, MNRAS, 482, 4570
- Gentile Fusillo N. P., et al., 2021a, White dwarfs with planetary remnants in the era of Gaia I. Six emission line systems, MNRAS, 504, 2707
- Gentile Fusillo N. P., et al., 2021b, *A catalogue of white dwarfs in Gaia EDR3*, MNRAS, 508, 3877
- Gharib-Nezhad E., Marley M. S., Batalha N. E., Visscher C., Freedman R. S., Lupu R. E., 2021, Following the Lithium: Tracing Li-bearing Molecules across Age, Mass, and Gravity in Brown Dwarfs, ApJ, 919, 21
- Giammichele N., Bergeron P., Dufour P., 2012, Know Your Neighborhood: A Detailed Model Atmosphere Analysis of Nearby White Dwarfs, ApJS, 199, 29
- Gianninas A., Bergeron P., Ruiz M. T., 2011, A Spectroscopic Survey and Analysis of Bright, Hydrogen-rich White Dwarfs, ApJ, 743, 138
- Ginzburg S., Fuller J., Kawka A., Caiazzo I., 2022, *Slow convection and fast rotation in crystallization-driven white dwarf dynamos*, MNRAS, 514, 4111
- Girardi L., 2016, Red Clump Stars, ARA&A, 54, 95
- Girardi L., Salaris M., 2001, Population effects on the red giant clump absolute magnitude, and distance determinations to nearby galaxies, MNRAS, 323, 109
- Girven J., Gänsicke B. T., Steeghs D., Koester D., 2011, DA white dwarfs in Sloan Digital Sky Survey Data Release 7 and a search for infrared excess emission, MNRAS, 417, 1210
- Gizis J. E., Monet D. G., Reid I. N., Kirkpatrick J. D., Liebert J., Williams R. J., 2000, New Neighbors from 2MASS: Activity and Kinematics at the Bottom of the Main Sequence, AJ, 120, 1085
- Goldman S. R., et al., 2017, The wind speeds, dust content, and mass-loss rates of evolved AGB and RSG stars at varying metallicity, MNRAS, 465, 403
- Goldreich P., Lynden-Bell D., 1969, Io, a jovian unipolar inductor, ApJ, 156, 59
- Gonzales E. C., Burningham B., Faherty J. K., Cleary C., Visscher C., Marley M. S., Lupu R., Freedman R., 2020, *Retrieval of the d/sdL7+T7.5p Binary SDSS J1416+1348AB*, ApJ, 905, 46
- Gore J., 1891, *The companion of Sirius*, Journal of the British Astronomical Association, 6, 318
- Gosnell N. M., Mathieu R. D., Geller A. M., Sills A., Leigh N., Knigge C., 2014, *Detection of White Dwarf Companions to Blue Stragglers in the Open Cluster NGC 188: Direct Evidence for Recent Mass Transfer*, ApJ, 783, L8
- Green R. F., Schmidt M., Liebert J., 1986, *The Palomar-Green Catalog of Ultraviolet-Excess Stellar Objects*, ApJS, 61, 305
- Green E. M., Dufour P., Fontaine G., Brassard P., 2009, Follow-up Studies of the Pulsating Magnetic White Dwarf SDSS J142625.71+575218.3, ApJ, 702, 1593
- Greenstein J. L., McCarthy J. K., 1985, Emission lines in the magnetic white dwarf GD 356., ApJ, 289, 732
- Greggio L., Renzini A., 1990, Clues on the Hot Star Content and the Ultraviolet Output of Elliptical Galaxies, ApJ, 364, 35
- Greiss S., Gänsicke B. T., Hermes J. J., Steeghs D., Koester D., Ramsay G., Barclay T., Townsley D. M., 2014, KIC 11911480: the second ZZ Ceti in the Kepler field, MNRAS,

- 438, 3086
- Grenfell T. C., 1974, Chemical composition of cool helium and carbon white dwarfs., A&A, 31, 303
- Grether D., Lineweaver C. H., 2006, How Dry is the Brown Dwarf Desert? Quantifying the Relative Number of Planets, Brown Dwarfs, and Stellar Companions around Nearby Sun-like Stars, ApJ, 640, 1051
- Grieves N., et al., 2021, Populating the brown dwarf and stellar boundary: Five stars with transiting companions near the hydrogen-burning mass limit, A&A, 652, A127
- Guidry J. A., et al., 2021, I Spy Transits and Pulsations: Empirical Variability in White Dwarfs Using Gaia and the Zwicky Transient Facility, ApJ, 912, 125
- Guo J., Lin L., Bai C., Liu J., 2016, *The effects of solar Reimers η on the final destinies of Venus, the Earth, and Mars*, Ap&SS, 361, 122
- Habets G. M. H. J., Heintze J. R. W., 1981, Empirical bolometric corrections for the main-sequence., A&AS, 46, 193
- Hale G. E., 1908, On the Probable Existence of a Magnetic Field in Sun-Spots, ApJ, 28, 315
- Hallinan G., et al., 2015, Magnetospherically driven optical and radio aurorae at the end of the stellar main sequence, Nature, 523, 568
- Han Z., 1998, The formation of double degenerates and related objects, MNRAS, 296, 1019
- Han Z., Podsiadlowski P., Eggleton P. P., 1995, *The formation of bipolar planetary nebulae* and close white dwarf binaries, MNRAS, 272, 800
- Han Z., Podsiadlowski P., Maxted P. F. L., Marsh T. R., Ivanova N., 2002, *The origin of subdwarf B stars I. The formation channels*, MNRAS, 336, 449
- Hansen B. M. S., 1999, Cooling Models for Old White Dwarfs, ApJ, 520, 680
- Hansen B., 2004, The astrophysics of cool white dwarfs, Phys. Rep., 399, 1
- Hansen B. M. S., Richer H., Kalirai J., Goldsbury R., Frewen S., Heyl J., 2015, Constraining Neutrino Cooling Using the Hot White Dwarf Luminosity Function in the Globular Cluster 47 Tucanae, ApJ, 809, 141
- Harrington J., Hansen B. M., Luszcz S. H., Seager S., Deming D., Menou K., Cho J. Y. K., Richardson L. J., 2006, *The Phase-Dependent Infrared Brightness of the Extrasolar Planet v Andromedae b*, Science, 314, 623
- Harrison J. H. D., Bonsor A., Madhusudhan N., 2018, *Polluted white dwarfs: constraints on the origin and geology of exoplanetary material*, MNRAS, 479, 3814
- Hatzes A. P., 1998, SPOT activity and the differential rotation on HD 106225 derived from Doppler tomography, A&A, 330, 541
- Hauschildt P. H., Baron E., 1999, *Numerical solution of the expanding stellar atmosphere problem.*, Journal of Computational and Applied Mathematics, 109, 41
- Hawley S., Reid I. N., Gizis J., 2000, in Griffith C. A., Marley M. S., eds, Astronomical Society of the Pacific Conference Series Vol. 212, From Giant Planets to Cool Stars. p. 252
- Heber U., 2009, Hot Subdwarf Stars, ARA&A, 47, 211
- Heintz T. M., Hermes J. J., El-Badry K., Walsh C., van Saders J. L., Fields C. E., Koester D., 2022, Testing White Dwarf Age Estimates Using Wide Double White Dwarf Binaries from Gaia EDR3, ApJ, 934, 148
- Hellier C., 2001, Cataclysmic Variable Stars
- Helling C., Casewell S., 2014, Atmospheres of brown dwarfs, A&ARv, 22, 80

- Hermes J. J., 2018, *Timing by Stellar Pulsations as an Exoplanet Discovery Method*. Springer International Publishing AG, p. 6, doi:10.1007/978-3-319-55333-7_6
- Hermes J. J., Montgomery M. H., Winget D. E., Brown W. R., Kilic M., Kenyon S. J., 2012, SDSS J184037.78+642312.3: The First Pulsating Extremely Low Mass White Dwarf, ApJ, 750, L28
- Hermes J. J., et al., 2013, A new class of pulsating white dwarf of extremely low mass: the fourth and fifth members, MNRAS, 436, 3573
- Hermes J. J., et al., 2015, A Second Case of Outbursts in a Pulsating White Dwarf Observed by Kepler, ApJ, 810, L5
- Hermes J. J., et al., 2017a, White Dwarf Rotation as a Function of Mass and a Dichotomy of Mode Line Widths: Kepler Observations of 27 Pulsating DA White Dwarfs through K2 Campaign 8, ApJS, 232, 23
- Hermes J. J., Gänsicke B. T., Gentile Fusillo N. P., Raddi R., Hollands M. A., Dennihy E., Fuchs J. T., Redfield S., 2017b, *When flux standards go wild: white dwarfs in the age of Kepler*, MNRAS, 468, 1946
- Hernández Santisteban J. V., et al., 2016, *An irradiated brown-dwarf companion to an accreting white dwarf*, Nature, 533, 366
- Herschel W., 1785, Catalogue of Double Stars. By William Herschel, Esq. F. R. S., Philosophical Transactions of the Royal Society of London, 75, 40
- Herwig F., 2005, Evolution of Asymptotic Giant Branch Stars, ARA&A, 43, 435
- Higgins M. E., Bell K. J., 2023, Localizing Sources of Variability in Crowded TESS Photometry, AJ, 165, 141
- Hjellming M. S., Taam R. E., 1991, *The Response of Main-Sequence Stars within a Common Envelope*, ApJ, 370, 709
- Höfner S., Olofsson H., 2018, Mass loss of stars on the asymptotic giant branch. Mechanisms, models and measurements, A&ARv, 26, 1
- Hogg M. A., Cutter R., Wynn G. A., 2021, The effect of a magnetic field on the dynamics of debris discs around white dwarfs, MNRAS, 500, 2986
- Holberg J. B., 2009, *The Discovery of the Existence of White Dwarf Stars: 1862 to 1930*, Journal for the History of Astronomy, 40, 137
- Holberg J. B., Bergeron P., 2006, Calibration of Synthetic Photometry Using DA White Dwarfs, AJ, 132, 1221
- Holberg J. B., Howell S. B., 2011, The Kepler Light Curve of the Unique DA White Dwarf BOKS 53856, AJ, 142, 62
- Holberg J. B., Sion E. M., Oswalt T., McCook G. P., Foran S., Subasavage J. P., 2008, A New Look at the Local White Dwarf Population, AJ, 135, 1225
- Holberg J. B., Oswalt T. D., Sion E. M., McCook G. P., 2016, *The 25 parsec local white dwarf population*, MNRAS, 462, 2295
- Hollands M. A., Koester D., Alekseev V., Herbert E. L., Gänsicke B. T., 2017, *Cool DZ white dwarfs I. Identification and spectral analysis*, MNRAS, 467, 4970
- Hollands M. A., Tremblay P. E., Gänsicke B. T., Gentile-Fusillo N. P., Toonen S., 2018, *The Gaia 20 pc white dwarf sample*, MNRAS, 480, 3942
- Hollands M. A., et al., 2020, An ultra-massive white dwarf with a mixed hydrogen-carbon atmosphere as a likely merger remnant, Nature Astronomy, 4, 663
- Hollands M. A., Tremblay P.-E., Gänsicke B. T., Koester D., Gentile-Fusillo N. P., 2021, Alkali metals in white dwarf atmospheres as tracers of ancient planetary crusts, Nature Astronomy, 5, 451

- Hollands M. A., Tremblay P. E., Gänsicke B. T., Koester D., 2022, Spectral analysis of cool white dwarfs accreting from planetary systems: from the ultraviolet to the optical, MNRAS, 511, 71
- Howell S. B., et al., 2014a, *The K2 Mission: Characterization and Early Results*, PASP, 126, 398
- Howell S. B., et al., 2014b, *The K2 Mission: Characterization and Early Results*, PASP, 126, 398
- Hoyle F., Schwarzschild M., 1955, On the Evolution of Type II Stars., ApJS, 2, 1
- Hsu D. C., Ford E. B., Ragozzine D., Ashby K., 2019, Occurrence Rates of Planets Orbiting FGK Stars: Combining Kepler DR25, Gaia DR2, and Bayesian Inference, AJ, 158, 109
- Hubeny I., Burrows A., Sudarsky D., 2003, A Possible Bifurcation in Atmospheres of Strongly Irradiated Stars and Planets, ApJ, 594, 1011
- Hügelmeyer S. D., Dreizler S., Werner K., Krzesiński J., Nitta A., Kleinman S. J., 2005, Spectral analyses of DO white dwarfs and PG 1159 stars from the Sloan Digital Sky Survey, A&A, 442, 309
- Hurley J. R., Tout C. A., Pols O. R., 2002, Evolution of binary stars and the effect of tides on binary populations, MNRAS, 329, 897
- Hut P., Tremaine S., 1985, Have interstellar clouds disrupted the Oort comet cloud?, AJ, 90, 1548
- Iaconi R., De Marco O., 2019, Speaking with one voice: simulations and observations discuss the common envelope α parameter, MNRAS, 490, 2550
- Iben Icko J., 1967, Stellar Evolution.VI. Evolution from the Main Sequence to the Red-Giant Branch for Stars of Mass 1 M_{sun}, 1.25 M_{sun}, and 1.5 M_{sun}, ApJ, 147, 624
- Iben Icko J., Livio M., 1993, Common Envelopes in Binary Star Evolution, PASP, 105, 1373
- Iben I. J., MacDonald J., 1985, The effects of diffusion due to gravity and due to composition gradients on the rate of hydrogen burning in a cooling degenerate dwarf. I The case of a thick helium buffer layer, ApJ, 296, 540
- Iben I. J., MacDonald J., 1986, The Effects of Diffusion Due to Gravity and Due to Composition Gradients on the Rate of Hydrogen Burning in a Cooling Degenerate Dwarf. II. Dependence on Initial Metallicity and on Buffer Mass, ApJ, 301, 164
- Iben I. J., Renzini A., 1983, Asymptotic giant branch evolution and beyond., ARA&A, 21, 271
- Iben Icko J., Rood R. T., 1970, Metal-Poor Stars. III. on the Evolution of Horizontal-Branch Stars, ApJ, 161, 587
- Iben I. J., Tutukov A. V., 1984a, Supernovae of type I as end products of the evolution of binaries with components of moderate initial mass., ApJS, 54, 335
- Iben I. J., Tutukov A. V., 1984b, Cooling of low-mass carbon-oxygen dwarfs from the planetary nucleus stage through the crystallization stage, ApJ, 282, 615
- Iben Icko J., Tutukov A. V., 1986, On the Number-Mass Distribution of Degenerate Dwarfs Produced by the Interacting Binaries and Evidence for Mergers of Low-Mass Helium Dwarfs, ApJ, 311, 753
- Illarionov A. F., Sunyaev R. A., 1975, Why the Number of Galactic X-ray Stars Is so Small?, A&A, 39, 185
- Isern J., Mochkovitch R., García-Berro E., Hernanz M., 1997, The Physics of Crystallizing

- White Dwarfs, ApJ, 485, 308
- Isern J., García-Berro E., Hernanz M., Chabrier G., 2000, *The Energetics of Crystallizing White Dwarfs Revisited Again*, ApJ, 528, 397
- Isern J., García-Berro E., Külebi B., Lorén-Aguilar P., 2017, A Common Origin of Magnetism from Planets to White Dwarfs, ApJ, 836, L28
- Isern J., Torres S., Rebassa-Mansergas A., 2022, White dwarfs as Physics laboratories: lights and shadows, Frontiers in Astronomy and Space Sciences, 9, 6
- Ivanova N., 2011, Common Envelope: On the Mass and the Fate of the Remnant, ApJ, 730, 76
- Ivanova N., et al., 2013, Common envelope evolution: where we stand and how we can move forward, A&ARv, 21, 59
- Ivezić Ž., et al., 2019, LSST: From Science Drivers to Reference Design and Anticipated Data Products, ApJ, 873, 111
- Janes K. A., Clemens D. P., Hayes-Gehrke M. N., Eastman J. D., Sarcia D. S., Bosh A. S., 2004, in American Astronomical Society Meeting Abstracts #204. p. 10.01
- Jeans J. H., 1924, Cosmogonic problems associated with a secular decrease of mass, MNRAS, 85, 2
- Jenkins J. M., et al., 2016, in Proc. SPIE. p. 99133E, doi:10.1117/12.2233418
- Ji S., et al., 2013, The Post-merger Magnetized Evolution of White Dwarf Binaries: The Double-degenerate Channel of Sub-Chandrasekhar Type Ia Supernovae and the Formation of Magnetized White Dwarfs, ApJ, 773, 136
- Jiang Y.-F., Tremaine S., 2010, The evolution of wide binary stars, MNRAS, 401, 977
- Jimenez R., Gråe JØrgensen U., Verde L., 2020, Giants eating giants: mass loss and giant planets modifying the luminosity of the tip of the giant branch, J. Cosmology Astropart. Phys., 2020, 027
- Jin S., 2021, Relative occurrence rates of terrestrial planets orbiting FGK stars, MNRAS, 502, 5302
- Joergens V., Fernández M., Carpenter J. M., Neuhäuser R., 2003, Rotational Periods of Very Young Brown Dwarfs and Very Low Mass Stars in Chamaeleon I, ApJ, 594, 971
- Johnas C. M. S., Helling C., Dehn M., Woitke P., Hauschildt P. H., 2008, *The influence of dust formation modelling on Na I and K I line profiles in substellar atmospheres*, MNRAS, 385, L120
- Johnstone C. P., 2017, On the fast magnetic rotator regime of stellar winds, A&A, 598, A24
- Jura M., 2003, A Tidally Disrupted Asteroid around the White Dwarf G29-38, ApJ, 584, 1.91
- Jura M., Farihi J., Zuckerman B., 2009, Six White Dwarfs with Circumstellar Silicates, AJ, 137, 3191
- Kafka S., Tappert C., Honeycutt R. K., 2010, Evidence for an accretion steam in the low-accretion-rate polar J2048, MNRAS, 403, 755
- Kantor E. M., Gusakov M. E., 2007, The neutrino emission due to plasmon decay and neutrino luminosity of white dwarfs, MNRAS, 381, 1702
- Kao M. M., Hallinan G., Pineda J. S., Escala I., Burgasser A., Bourke S., Stevenson D., 2016, Auroral Radio Emission from Late L and T Dwarfs: A New Constraint on Dynamo Theory in the Substellar Regime, ApJ, 818, 24
- Kao M. M., Hallinan G., Pineda J. S., Stevenson D., Burgasser A., 2018, The Strongest Magnetic Fields on the Coolest Brown Dwarfs, ApJS, 237, 25

- Karakas A. I., Lattanzio J. C., 2014, *The Dawes Review 2: Nucleosynthesis and Stellar Yields of Low- and Intermediate-Mass Single Stars*, Publ. Astron. Soc. Australia, 31, e030
- Kawaler S. D., 2004, in Maeder A., Eenens P., eds, Vol. 215, Stellar Rotation. p. 561
- Kawaler S., Dahlstrom M., 2000, White Dwarf Stars, American Scientist, 88, 498
- Kawka A., 2020, Clues to the origin and properties of magnetic white dwarfs, arXiv e-prints, p. arXiv:2001.10672
- Kawka A., Vennes S., 2004, in Zverko J., Ziznovsky J., Adelman S. J., Weiss W. W., eds, IAU Symposium Vol. 224, The A-Star Puzzle. pp 879–885, doi:10.1017/S1743921305009920
- Kawka A., Vennes S., Schmidt G. D., Wickramasinghe D. T., Koch R., 2007, *Spectropolarimetric Survey of Hydrogen-rich White Dwarf Stars*, ApJ, 654, 499
- Kawka A., Vennes S., Dupuis J., Chayer P., Lanz T., 2008, *Orbital Parameters and Chemical Composition of Four White Dwarfs in Post-Common-Envelope Binaries*, ApJ, 675, 1518
- Kemp J. C., Swedlund J. B., Landstreet J. D., Angel J. R. P., 1970, *Discovery of Circularly Polarized Light from a White Dwarf*, ApJ, 161, L77
- Kepler S. O., Romero A. D., 2017, in European Physical Journal Web of Conferences. p. 01011 (arXiv:1706.07020), doi:10.1051/epjconf/201715201011
- Kepler S. O., et al., 2013, Magnetic white dwarf stars in the Sloan Digital Sky Survey, MNRAS, 429, 2934
- Kepler S. O., et al., 2015, New white dwarf stars in the Sloan Digital Sky Survey Data Release 10, MNRAS, 446, 4078
- Kepler S. O., et al., 2016, New white dwarf and subdwarf stars in the Sloan Digital Sky Survey Data Release 12, MNRAS, 455, 3413
- Kepler S. O., et al., 2019, White dwarf and subdwarf stars in the Sloan Digital Sky Survey Data Release 14, MNRAS, 486, 2169
- Kepler S. O., Koester D., Pelisoli I., Romero A. D., Ourique G., 2021, White dwarf and subdwarf stars in the Sloan Digital Sky Survey Data Release 16, MNRAS, 507, 4646
- Khodachenko M. L., et al., 2007, Coronal Mass Ejection (CME) Activity of Low Mass M Stars as An Important Factor for The Habitability of Terrestrial Exoplanets. I. CME Impact on Expected Magnetospheres of Earth-Like Exoplanets in Close-In Habitable Zones, Astrobiology, 7, 167
- Kilic M., Redfield S., 2007, A Dusty Disk around WD 1150-153: Explaining the Metals in White Dwarfs by Accretion from the Interstellar Medium versus Debris Disks, ApJ, 660, 641
- Kilic M., von Hippel T., Leggett S. K., Winget D. E., 2006, *Debris Disks around White Dwarfs: The DAZ Connection*, ApJ, 646, 474
- Kilic M., Brown W. R., Allende Prieto C., Agüeros M. A., Heinke C., Kenyon S. J., 2011, *The ELM Survey. II. Twelve Binary White Dwarf Merger Systems*, ApJ, 727, 3
- Kilic M., Brown W. R., Allende Prieto C., Kenyon S. J., Heinke C. O., Agüeros M. A., Kleinman S. J., 2012, The ELM Survey. IV. 24 White Dwarf Merger Systems, ApJ, 751, 141
- Kilic M., Rolland B., Bergeron P., Vand erbosch Z., Benni P., Garlitz J., 2019, *A magnetic white dwarf with five H α components*, MNRAS, 489, 3648
- Kilic M., Bédard A., Bergeron P., Kosakowski A., 2020, Two new double-lined spectroscopic binary white dwarfs, MNRAS, 493, 2805

- Kilic M., Kosakowski A., Moss A. G., Bergeron P., Conly A. A., 2021, *An Isolated White Dwarf with a 70 s Spin Period*, ApJ, 923, L6
- Kilkenny D., Welsh B. Y., Koen C., Gulbis A. A. S., Kotze M. M., 2014, A search for p-mode pulsations in white dwarf stars using the Berkeley Visible Imaging Tube detector, MNRAS, 437, 1836
- Kim S., Prato L., McLean I., 2015, *REDSPEC: NIRSPEC data reduction* (ascl:1507.017) Kiman R., et al., 2021, *Calibration of the Hα Age-Activity Relation for M Dwarfs*, AJ, 161, 277
- Kiminki D. C., Kobulnicky H. A., 2012, An Updated Look at Binary Characteristics of Massive Stars in the Cygnus OB2 Association, ApJ, 751, 4
- Kippenhahn R., Weigert A., Weiss A., 2013, *Stellar Structure and Evolution*, doi:10.1007/978-3-642-30304-3.
- Kiraga M., Stepien K., 2007, Age-Rotation-Activity Relations for M Dwarf Stars, Acta Astron., 57, 149
- Kirkpatrick J. D., Henry T. J., Liebert J., 1993, *The Unique Spectrum of the Brown Dwarf Candidate GD 165B and Comparison to the Spectra of Other Low-Luminosity Objects*, ApJ, 406, 701
- Kirkpatrick J. D., et al., 1999a, Dwarfs Cooler than "M": The Definition of Spectral Type "L" Using Discoveries from the 2 Micron All-Sky Survey (2MASS), ApJ, 519, 802
- Kirkpatrick J. D., Allard F., Bida T., Zuckerman B., Becklin E. E., Chabrier G., Baraffe I., 1999b, *An Improved Optical Spectrum and New Model FITS of the Likely Brown Dwarf GD 165B*, ApJ, 519, 834
- Kissin Y., Thompson C., 2015, Spin and Magnetism of White Dwarfs, ApJ, 809, 108
- Klein B., Jura M., Koester D., Zuckerman B., 2011, Rocky Extrasolar Planetary Compositions Derived from Externally Polluted White Dwarfs, ApJ, 741, 64
- Knutson H. A., et al., 2007, A map of the day-night contrast of the extrasolar planet HD 189733b, Nature, 447, 183
- Kobayashi C., Karakas A. I., Lugaro M., 2020, *The Origin of Elements from Carbon to Uranium*, ApJ, 900, 179
- Kobulnicky H. A., Fryer C. L., 2007, A New Look at the Binary Characteristics of Massive Stars, ApJ, 670, 747
- Kobulnicky H. A., et al., 2012, A Fresh Catch of Massive Binaries in the Cygnus OB2 Association, ApJ, 756, 50
- Kobulnicky H. A., et al., 2014, Toward Complete Statistics of Massive Binary Stars: Penultimate Results from the Cygnus OB2 Radial Velocity Survey, ApJS, 213, 34
- Koester D., 2009, Accretion and diffusion in white dwarfs. New diffusion timescales and applications to GD 362 and G 29-38, A&A, 498, 517
- Koester D., 2010, *White dwarf spectra and atmosphere models*, Mem. Soc. Astron. Italiana, 81, 921
- Koester D., Schoenberner D., 1986, Evolution of white dwarfs., A&A, 154, 125
- Koester D., Wilken D., 2006, The accretion-diffusion scenario for metals in cool white dwarfs, A&A, 453, 1051
- Koester D., Rollenhagen K., Napiwotzki R., Voss B., Christlieb N., Homeier D., Reimers D., 2005, *Metal traces in white dwarfs of the SPY (ESO Supernova Ia Progenitor Survey)* sample, A&A, 432, 1025
- Koester D., Gänsicke B. T., Farihi J., 2014, The frequency of planetary debris around young white dwarfs, A&A, 566, A34

- Koester D., Kepler S. O., Irwin A. W., 2020, New white dwarf envelope models and diffusion. Application to DQ white dwarfs, A&A, 635, A103
- Kollmeier J. A., et al., 2017, SDSS-V: Pioneering Panoptic Spectroscopy, arXiv e-prints, p. arXiv:1711.03234
- Konopacky Q. M., et al., 2012, Rotational Velocities of Individual Components in Very Low Mass Binaries, ApJ, 750, 79
- Kopal Z., 1955, *The classification of close binary systems*, Annales d'Astrophysique, 18, 379
- Korol V., Belokurov V., Toonen S., 2022, A gap in the double white dwarf separation distribution caused by the common-envelope evolution: astrometric evidence from Gaia, MNRAS, 515, 1228
- Kowalski P. M., Saumon D., 2006, Found: The Missing Blue Opacity in Atmosphere Models of Cool Hydrogen White Dwarfs, ApJ, 651, L137
- Kramer M., Schneider F. R. N., Ohlmann S. T., Geier S., Schaffenroth V., Pakmor R., Röpke F. K., 2020, Formation of sdB-stars via common envelope ejection by substellar companions, A&A, 642, A97
- Kruckow M. U., Neunteufel P. G., Di Stefano R., Gao Y., Kobayashi C., 2021, A Catalog of Potential Post-Common Envelope Binaries, ApJ, 920, 86
- Külebi B., Jordan S., Euchner F., Gänsicke B. T., Hirsch H., 2009, *Analysis of hydrogen*rich magnetic white dwarfs detected in the Sloan Digital Sky Survey, A&A, 506, 1341
- Kumar S. S., 1994, Very Low Mass Stars, Black Dwarfs and Planets, Ap&SS, 212, 57
- Kumar V., Rajpurohit A. S., Srivastava M. K., 2023, Exploring the short-term variability of Hα and HHβ emissions in a sample of M Dwarfs, arXiv e-prints, p. arXiv:2302.01643
- Kunimoto M., Matthews J. M., 2020, Searching the Entirety of Kepler Data. II. Occurrence Rate Estimates for FGK Stars, AJ, 159, 248
- Kunitomo M., Ikoma M., Sato B., Katsuta Y., Ida S., 2011, *Planet Engulfment by* ~1.5-3 *M* _{sun} *Red Giants*, ApJ, 737, 66
- Kurtz D. W., Shibahashi H., Dhillon V. S., Marsh T. R., Littlefair S. P., 2008, A search for a new class of pulsating DA white dwarf stars in the DB gap, MNRAS, 389, 1771
- Kurtz D. W., Shibahashi H., Dhillon V. S., Marsh T. R., Littlefair S. P., Copperwheat C. M., Gänsicke B. T., Parsons S. G., 2013, *Hot DAVs: a probable new class of pulsating white dwarf stars*, MNRAS, 432, 1632
- Kwitter K. B., Henry R. B. C., 2022, *Planetary Nebulae: Sources of Enlightenment*, PASP, 134, 022001
- LSST Science Collaboration et al., 2009, *LSST Science Book, Version 2.0*, arXiv e-prints, p. arXiv:0912.0201
- Lagos F., Schreiber M. R., Zorotovic M., Gänsicke B. T., Ronco M. P., Hamers A. S., 2021a, WD 1856 b: a close giant planet around a white dwarf that could have survived a common envelope phase, MNRAS, 501, 676
- Lagos F., Schreiber M. R., Zorotovic M., Gänsicke B. T., Ronco M. P., Hamers A. S., 2021b, WD 1856 b: a close giant planet around a white dwarf that could have survived a common envelope phase, MNRAS, 501, 676
- Lagos F., Schreiber M. R., Parsons S. G., Toloza O., Gänsicke B. T., Hernandez M. S., Schmidtobreick L., Belloni D., 2022, *The white dwarf binary pathways survey VII. Evidence for a bi-modal distribution of post-mass transfer systems?*, MNRAS, 512, 2625
- Laine R. O., Lin D. N. C., 2012, Interaction of Close-in Planets with the Magnetosphere of

- Their Host Stars. II. Super-Earths as Unipolar Inductors and Their Orbital Evolution, ApJ, 745, 2
- Laine R. O., Lin D. N. C., Dong S., 2008, Interaction of Close-in Planets with the Magnetosphere of Their Host Stars. I. Diffusion, Ohmic Dissipation of Time-dependent Field, Planetary Inflation, and Mass Loss, ApJ, 685, 521
- Lamb D. Q., van Horn H. M., 1975, Evolution of crystallizing pure ¹²C white dwarfs., ApJ, 200, 306
- Laming J. M., 2015, *The FIP and Inverse FIP Effects in Solar and Stellar Coronae*, Living Reviews in Solar Physics, 12, 2
- Landolt A. U., 1968, A New Short-Period Blue Variable, ApJ, 153, 151
- Landsman W. B., 1993, in Hanisch R. J., Brissenden R. J. V., Barnes J., eds, Astronomical Society of the Pacific Conference Series Vol. 52, Astronomical Data Analysis Software and Systems II. p. 246
- Landstreet J. D., 1967, Synchrotron Radiation of Neutrinos and Its Astrophysical Significance, Physical Review, 153, 1372
- Landstreet J. D., 1992, Magnetic fields at the surfaces of stars, A&ARv, 4, 35
- Landstreet J. D., 2020, in Wade G., Alecian E., Bohlender D., Sigut A., eds, 0 Vol. 11, Stellar Magnetism: A Workshop in Honour of the Career and Contributions of John D. Landstreet. pp 239–246 (arXiv:2008.01802), doi:10.48550/arXiv.2008.01802
- Landstreet J. D., Bagnulo S., 2019, A new weak-field magnetic DA white dwarf in the local 20 pc volume. The frequency of magnetic fields in DA stars, A&A, 628, A1
- Landstreet J. D., Bagnulo S., Valyavin G. G., Fossati L., Jordan S., Monin D., Wade G. A., 2012, *On the incidence of weak magnetic fields in DA white dwarfs*, A&A, 545, A30
- Landstreet J. D., Bagnulo S., Valyavin G. G., Gadelshin D., Martin A. J., Galazutdinov G., Semenko E., 2015, A novel and sensitive method for measuring very weak magnetic fields of DA white dwarfs. A search for a magnetic field at the 250 G level in 40 Eridani B, A&A, 580, A120
- Landstreet J. D., Bagnulo S., Valyavin G., Valeev A. F., 2017, Monitoring and modelling of white dwarfs with extremely weak magnetic fields. WD 2047+372 and WD 2359-434, A&A, 607, A92
- Lanning H. H., 1982, C1: a white-dwarf-red-dwarf spectroscopic binary., ApJ, 253, 752 Laughlin G., Bodenheimer P., Adams F. C., 1997, The End of the Main Sequence, ApJ, 482, 420
- Lee E. K. H., Casewell S. L., Chubb K. L., Hammond M., Tan X., Tsai S.-M., Pierrehumbert R. T., 2020, Simplified 3D GCM modelling of the irradiated brown dwarf WD 0137-349B, MNRAS, 496, 4674
- Lee E. K. H., Lothringer J. D., Casewell S. L., Kitzmann D., Lew B. W. P., Zhou Y., 2022, Sunbathing under white light 3D modelling of brown dwarf white dwarf atmospheres with strong UV irradiation, arXiv e-prints, p. arXiv:2203.09854
- Leggett S. K., et al., 2018, Distant White Dwarfs in the US Naval Observatory Flagstaff Station Parallax Sample, ApJS, 239, 26
- Leigh N., Knigge C., Sills A., Perets H. B., Sarajedini A., Glebbeek E., 2013, *The origins of blue stragglers and binarity in globular clusters*, MNRAS, 428, 897
- Li J. K., Wu K. W., Wickramasinghe D. T., 1994, Reduced Magnetic Braking in Synchronously Rotating Magnetic Cataclysmic Variables, MNRAS, 268, 61
- Li J., Ferrario L., Wickramasinghe D., 1998, *Planets around White Dwarfs*, ApJ, 503, L151

- Liebert J., 1988, Searches for Magnetic Fields in White Dwarfs Since Babcock, PASP, 100, 1302
- Liebert J., et al., 2005a, Where Are the Magnetic White Dwarfs with Detached, Nondegenerate Companions?, AJ, 129, 2376
- Liebert J., Bergeron P., Holberg J. B., 2005b, *The Formation Rate and Mass and Luminosity Functions of DA White Dwarfs from the Palomar Green Survey*, ApJS, 156, 47
- Liebert J., Ferrario L., Wickramasinghe D. T., Smith P. S., 2015, *Enigmas from the Sloan Digital Sky Survey DR7 Kleinman White Dwarf Catalog*, ApJ, 804, 93
- Lightkurve Collaboration et al., 2018, *Lightkurve: Kepler and TESS time series analysis in Python*, Astrophysics Source Code Library (ascl:1812.013)
- Limoges M. M., Bergeron P., Lépine S., 2015, *Physical Properties of the Current Census of Northern White Dwarfs within 40 pc of the Sun*, ApJS, 219, 19
- Lindegren L., et al., 2018, *Gaia Data Release 2. The astrometric solution*, A&A, 616, A2 Line M. R., et al., 2017, *Uniform Atmospheric Retrieval Analysis of Ultracool Dwarfs. II. Properties of 11 T dwarfs*, ApJ, 848, 83
- Littlefair S. P., Dhillon V. S., Marsh T. R., Gänsicke B. T., Baraffe I., Watson C. A., 2007, SDSS J150722.30+523039.8: a cataclysmic variable formed directly from a detached white dwarf/brown dwarf binary?, MNRAS, 381, 827
- Littlefair S. P., et al., 2014, *The substellar companion in the eclipsing white dwarf binary SDSS J141126.20+200911.1*, MNRAS, 445, 2106
- Livio M., Soker N., 1983, Star-planet systems as progenitors of cataclysmic binaries: tidal effects., A&A, 125, L12
- Lodders K., 1999, Alkali Element Chemistry in Cool Dwarf Atmospheres, ApJ, 519, 793Lodders K., 2002, Titanium and Vanadium Chemistry in Low-Mass Dwarf Stars, ApJ, 577, 974
- Lodders K., 2003, Solar System Abundances and Condensation Temperatures of the Elements, ApJ, 591, 1220
- Lomb N. R., 1976, Least-Squares Frequency Analysis of Unequally Spaced Data, Ap&SS, 39, 447
- Longstaff E. S., Casewell S. L., Wynn G. A., Maxted P. F. L., Helling C., 2017, *Emission lines in the atmosphere of the irradiated brown dwarf WD0137-349B*, MNRAS, 471, 1728
- Longstaff E. S., Casewell S. L., Wynn G. A., Page K. L., Williams P. K. G., Braker I., Maxted P. F. L., 2019, Signs of accretion in the white dwarf + brown dwarf binary NLTT5306, MNRAS, 484, 2566
- Loyd R. O. P., et al., 2023, Flares, Rotation, Activity Cycles, and a Magnetic Star-Planet Interaction Hypothesis for the Far-ultraviolet Emission of GJ 436, AJ, 165, 146
- Luhman K. L., Burgasser A. J., Bochanski J. J., 2011, Discovery of a Candidate for the Coolest Known Brown Dwarf, ApJ, 730, L9
- Luhman K. L., Burgasser A. J., Labbé I., Saumon D., Marley M. S., Bochanski J. J., Monson A. J., Persson S. E., 2012, Confirmation of One of the Coldest Known Brown Dwarfs, ApJ, 744, 135
- Luhman K. L., Morley C. V., Burgasser A. J., Esplin T. L., Bochanski J. J., 2014, Near-infrared Detection of WD 0806-661 B with the Hubble Space Telescope, ApJ, 794, 16
- Ma B., Ge J., 2014, Statistical properties of brown dwarf companions: implications for different formation mechanisms, MNRAS, 439, 2781

- Mace G. N., et al., 2018, Wolf 1130: A Nearby Triple System Containing a Cool, Ultramassive White Dwarf, ApJ, 854, 145
- Madhusudhan N., Apai D., Gandhi S., 2016, Atmospheric Compositions of Three Brown Dwarfs and Implications for their Formation Conditions, arXiv e-prints, p. arXiv:1612.03174
- Maeder A., Meynet G., 1989, *Grids of evolutionary models from 0.85 to 120M : observational tests and the mass limits.*, A&A, 210, 155
- Manser C. J., Gänsicke B. T., Koester D., Marsh T. R., Southworth J., 2016, Another one grinds the dust: variability of the planetary debris disc at the white dwarf SDSS J104341.53+085558.2, MNRAS, 462, 1461
- Manser C. J., et al., 2019, A planetesimal orbiting within the debris disc around a white dwarf star, Science, 364, 66
- Manser C. J., Gänsicke B. T., Gentile Fusillo N. P., Ashley R., Breedt E., Hollands M., Izquierdo P., Pelisoli I., 2020, The frequency of gaseous debris discs around white dwarfs, MNRAS, 493, 2127
- Manser C. J., et al., 2023, DAHe white dwarfs from the DESI Survey, MNRAS, 521, 4976
 Manset N., Donati J.-F., 2003, in Fineschi S., ed., Society of Photo-Optical Instrumentation
 Engineers (SPIE) Conference Series Vol. 4843, Polarimetry in Astronomy. pp 425–436,
 doi:10.1117/12.458230
- Maoz D., Mannucci F., Nelemans G., 2014, Observational Clues to the Progenitors of Type Ia Supernovae, ARA&A, 52, 107
- Marley M. S., Robinson T. D., 2015, On the Cool Side: Modeling the Atmospheres of Brown Dwarfs and Giant Planets, ARA&A, 53, 279
- Marley M. S., Saumon D., Goldblatt C., 2010, A Patchy Cloud Model for the L to T Dwarf Transition, ApJ, 723, L117
- Marley M. S., et al., 2021, The Sonora Brown Dwarf Atmosphere and Evolution Models. I. Model Description and Application to Cloudless Atmospheres in Rainout Chemical Equilibrium, ApJ, 920, 85
- Marsh T. R., 2011, *Double white dwarfs and LISA*, Classical and Quantum Gravity, 28, 094019
- Marsh T. R., Dhillon V. S., Duck S. R., 1995, Low-Mass White Dwarfs Need Friends Five New Double-Degenerate Close Binary Stars, MNRAS, 275, 828
- Martin E. C., et al., 2018, in Evans C. J., Simard L., Takami H., eds, Society of Photo-Optical Instrumentation Engineers (SPIE) Conference Series Vol. 10702, Ground-based and Airborne Instrumentation for Astronomy VII. p. 107020A (arXiv:1808.06024), doi:10.1117/12.2312266
- Mathys G., 1989, *The Observation of Magnetic Fields in Nondegenerate Stars*, Fundamentals Cosmic Phys., 13, 143
- Mauk B. H., et al., 2018, Diverse Electron and Ion Acceleration Characteristics Observed Over Jupiter's Main Aurora, Geophys. Res. Lett., 45, 1277
- Maxted P. F. L., Marsh T. R., 1999, *The fraction of double degenerates among DA white dwarfs*, MNRAS, 307, 122
- Maxted P. F. L., Marsh T. R., Moran C., Dhillon V. S., Hilditch R. W., 1998, *The mass and radius of the M dwarf companion to GD448*, MNRAS, 300, 1225
- Maxted P. F. L., Marsh T. R., Moran C. K. J., 2000, *Radial velocity measurements of white dwarfs*, MNRAS, 319, 305
- Maxted P. F. L., Heber U., Marsh T. R., North R. C., 2001, The binary fraction of extreme

- horizontal branch stars, MNRAS, 326, 1391
- Maxted P. F. L., Napiwotzki R., Dobbie P. D., Burleigh M. R., 2006, Survival of a brown dwarf after engulfment by a red giant star, Nature, 442, 543
- Maxted P. F. L., O'Donoghue D., Morales-Rueda L., Napiwotzki R., Smalley B., 2007, The mass and radius of the M-dwarf in the short-period eclipsing binary RR Caeli, MNRAS, 376, 919
- Maxted P. F. L., et al., 2013, Multi-periodic pulsations of a stripped red-giant star in an eclipsing binary system, Nature, 498, 463
- Mayer A., et al., 2014, Large-scale environments of binary AGB stars probed by Herschel. II. Two companions interacting with the wind of π^1 Gruis, A&A, 570, A113
- McCarthy C., Zuckerman B., 2004, The Brown Dwarf Desert at 75-1200 AU, AJ, 127, 2871
- McCleery J., et al., 2020, Gaia white dwarfs within 40 pc II: the volume-limited Northern hemisphere sample, MNRAS, 499, 1890
- McClure R. D., 1983, The binary nature of the barium stars. II. Velocities, binary frequency, and preliminary orbits., ApJ, 268, 264
- McClure R. D., Fletcher J. M., Nemec J. M., 1980, *The binary nature of the barium stars*., ApJ, 238, L35
- McCook G. P., Sion E. M., 1999, A Catalog of Spectroscopically Identified White Dwarfs, ApJS, 121, 1
- McCrea W. H., 1964, Extended main-sequence of some stellar clusters, MNRAS, 128, 147
- McGraw J. T., Starrfield S. G., Liebert J., Green R., 1979, in van Horn H. M., Weidemann V., Savedoff M. P., eds, IAU Colloq. 53: White Dwarfs and Variable Degenerate Stars. p. 377
- McLean I. S., McGovern M. R., Burgasser A. J., Kirkpatrick J. D., Prato L., Kim S. S., 2003, The NIRSPEC Brown Dwarf Spectroscopic Survey. I. Low-Resolution Near-Infrared Spectra, ApJ, 596, 561
- Meisner A. M., et al., 2020, Spitzer Follow-up of Extremely Cold Brown Dwarfs Discovered by the Backyard Worlds: Planet 9 Citizen Science Project, ApJ, 899, 123
- Melis C., et al., 2012, Gaseous Material Orbiting the Polluted, Dusty White Dwarf HE 1349-2305, ApJ, 751, L4
- Melis C., Klein B., Doyle A. E., Weinberger A., Zuckerman B., Dufour P., 2020, Serendipitous Discovery of Nine White Dwarfs with Gaseous Debris Disks, ApJ, 905, 56
- Mello D. R. C., Daflon S., Pereira C. B., Hubeny I., 2012, *Chemical abundances of hot post-AGB stars*, A&A, 543, A11
- Mengel J. G., Norris J., Gross P. G., 1976, *Binary Hypothesis for the Subdwarf B Stars*, ApJ, 204, 488
- Merle T., Jorissen A., Van Eck S., Masseron T., Van Winckel H., 2016, *To Ba or not to Ba: Enrichment in s-process elements in binary systems with WD companions of various masses*, A&A, 586, A151
- Merlov A., Bear E., Soker N., 2021, A Red Giant Branch Common-envelope Evolution Scenario for the Exoplanet WD 1856 b, ApJ, 915, L34
- Mesquita A. L., Vidotto A. A., 2020, Global trends in winds of M dwarf stars, MNRAS, 494, 1297
- Mestel L., 1952, *On the theory of white dwarf stars. I. The energy sources of white dwarfs*, MNRAS, 112, 583

- Miller Bertolami M. M., 2016, New models for the evolution of post-asymptotic giant branch stars and central stars of planetary nebulae, A&A, 588, A25
- Millholland S., Wang S., Laughlin G., 2017, Kepler Multi-planet Systems Exhibit Unexpected Intra-system Uniformity in Mass and Radius, ApJ, 849, L33
- Miszalski B., Acker A., Moffat A. F. J., Parker Q. A., Udalski A., 2009, *Binary planetary nebulae nuclei towards the Galactic bulge. I. Sample discovery, period distribution, and binary fraction*, A&A, 496, 813
- Mochkovitch R., 1983, Freezing of a carbon-oxygen white dwarf, A&A, 122, 212
- Modigliani A., et al., 2010, in Silva D. R., Peck A. B., Soifer B. T., eds, Society of Photo-Optical Instrumentation Engineers (SPIE) Conference Series Vol. 7737, Observatory Operations: Strategies, Processes, and Systems III. p. 773728, doi:10.1117/12.857211
- Moe M., Di Stefano R., 2017, Mind Your Ps and Qs: The Interrelation between Period (P) and Mass-ratio (Q) Distributions of Binary Stars, ApJS, 230, 15
- Mohamed S., Podsiadlowski P., 2007, in Napiwotzki R., Burleigh M. R., eds, Astronomical Society of the Pacific Conference Series Vol. 372, 15th European Workshop on White Dwarfs. p. 397
- Mohamed S., Podsiadlowski P., 2011, in Kerschbaum F., Lebzelter T., Wing R. F., eds, Astronomical Society of the Pacific Conference Series Vol. 445, Why Galaxies Care about AGB Stars II: Shining Examples and Common Inhabitants. p. 355
- Mohanty S., Basri G., 2003, Rotation and Activity in Mid-M to L Field Dwarfs, ApJ, 583, 451
- Mohanty S., Basri G., Shu F., Allard F., Chabrier G., 2002, *Activity in Very Cool Stars: Magnetic Dissipation in Late M and L Dwarf Atmospheres*, ApJ, 571, 469
- Montegriffo P., et al., 2023, Gaia Data Release 3. External calibration of BP/RP low-resolution spectroscopic data, A&A, 674, A3
- Montgomery M. H., Hermes J. J., Winget D. E., Dunlap B. H., Bell K. J., 2020, *Limits on Mode Coherence in Pulsating DA White Dwarfs Due to a Nonstatic Convection Zone*, ApJ, 890, 11
- Moorwood A., et al., 1999, ISAAC at the VLT., The Messenger, 95, 1
- Morin J., Dormy E., Schrinner M., Donati J. F., 2011, Weak- and strong-field dynamos: from the Earth to the stars, MNRAS, 418, L133
- Moss D., 2001, in Mathys G., Solanki S. K., Wickramasinghe D. T., eds, Astronomical Society of the Pacific Conference Series Vol. 248, Magnetic Fields Across the Hertzsprung-Russell Diagram. p. 305
- Moss A., et al., 2022, Improving White Dwarfs as Chronometers with Gaia Parallaxes and Spectroscopic Metallicities, ApJ, 929, 26
- Moss A., Kilic M., Bergeron P., Firgard M., Brown W., 2023, *Signs of Binary Evolution in 7 Magnetic DA White Dwarfs*, arXiv e-prints, p. arXiv:2306.09254
- Moutou C., Donati J. F., Lin D., Laine R. O., Hatzes A., 2016, *The magnetic properties of the star Kepler-78*, MNRAS, 459, 1993
- Mowlavi N., Eggenberger P., Meynet G., Ekström S., Georgy C., Maeder A., Charbonnel C., Eyer L., 2012, *Stellar mass and age determinations*. *I. Grids of stellar models from* Z = 0.006 to 0.04 and M = 0.5 to 3.5 M_{\odot} , A&A, 541, A41
- Mukadam A. S., Montgomery M. H., Winget D. E., Kepler S. O., Clemens J. C., 2006, Ensemble Characteristics of the ZZ Ceti Stars, ApJ, 640, 956
- Musielak Z. E., Winget D. E., Montgomery M. H., 2005, Atmospheric Oscillations in White Dwarfs: A New Indicator of Chromospheric Activity, ApJ, 630, 506

- Mustill A. J., Villaver E., 2012, Foretellings of Ragnarök: World-engulfing Asymptotic Giants and the Inheritance of White Dwarfs, ApJ, 761, 121
- Napiwotzki R., et al., 2001, Search for progenitors of supernovae type Ia with SPY, Astronomische Nachrichten, 322, 411
- Napiwotzki R., et al., 2003, SPY the ESO Supernovae type Ia Progenitor survey, The Messenger, 112, 25
- Napiwotzki R., Karl C. A., Lisker T., Heber U., Christlieb N., Reimers D., Nelemans G., Homeier D., 2004, *Close binary EHB stars from SPY*, Ap&SS, 291, 321
- Napiwotzki R., et al., 2020, The ESO supernovae type Ia progenitor survey (SPY). The radial velocities of 643 DA white dwarfs, A&A, 638, A131
- Nayak P. K., Ganguly A., Chatterjee S., 2022, *Hunting Down White Dwarf–Main Sequence Binaries Using Multi-Wavelength Observations*, arXiv e-prints, p. arXiv:2212.09800
- Nebot Gómez-Morán A., et al., 2011, Post common envelope binaries from SDSS. XII. The orbital period distribution, A&A, 536, A43
- Nelemans G., Tauris T. M., 1998, Formation of undermassive single white dwarfs and the influence of planets on late stellar evolution, A&A, 335, L85
- Nelemans G., Verbunt F., Yungelson L. R., Portegies Zwart S. F., 2000, Reconstructing the evolution of double helium white dwarfs: envelope loss without spiral-in, A&A, 360, 1011
- Nelson L., Schwab J., Ristic M., Rappaport S., 2018, *Minimum Orbital Period of Precataclysmic Variables*, ApJ, 866, 88
- Neubauer F. M., 1998, The sub-Alfvénic interaction of the Galilean satellites with the Jovian magnetosphere, J. Geophys. Res., 103, 19843
- Newville M., Stensitzki T., Allen D. B., Rawlik M., Ingargiola A., Nelson A., 2016, *Lmfit: Non-Linear Least-Square Minimization and Curve-Fitting for Python* (ascl:1606.014)
- Nielsen E. L., et al., 2019, The Gemini Planet Imager Exoplanet Survey: Giant Planet and Brown Dwarf Demographics from 10 to 100 au, AJ, 158, 13
- Nordhaus J., Blackman E. G., 2006, Low-mass binary-induced outflows from asymptotic giant branch stars, MNRAS, 370, 2004
- Nordhaus J., Spiegel D. S., 2013, On the orbits of low-mass companions to white dwarfs and the fates of the known exoplanets, MNRAS, 432, 500
- Nordhaus J., Spiegel D. S., Ibgui L., Goodman J., Burrows A., 2010, *Tides and tidal engulfment in post-main-sequence binaries: period gaps for planets and brown dwarfs around white dwarfs*, MNRAS, 408, 631
- Nordhaus J., Wellons S., Spiegel D. S., Metzger B. D., Blackman E. G., 2011, Formation of high-field magnetic white dwarfs from common envelopes, Proceedings of the National Academy of Science, 108, 3135
- Nordström B., et al., 2004, The Geneva-Copenhagen survey of the Solar neighbourhood. Ages, metallicities, and kinematic properties of ~14 000 F and G dwarfs, A&A, 418, 989
- O'Brien M. W., et al., 2023, Gaia white dwarfs within 40 pc III. Spectroscopic observations of new candidates in the Southern hemisphere, MNRAS, 518, 3055
- O'Connor C. E., Lai D., 2020, High-eccentricity migration of planetesimals around polluted white dwarfs, MNRAS, 498, 4005
- O'Connor C. E., Liu B., Lai D., 2021, Enhanced Lidov-Kozai migration and the formation of the transiting giant planet WD 1856+534 b, MNRAS, 501, 507
- O'Connor C. E., Bildsten L., Cantiello M., Lai D., 2023, Giant Planet Engulfment by

- Evolved Giant Stars: Light Curves, Asteroseismology, and Survivability, ApJ, 950, 128
- O'Malley E. M., von Hippel T., van Dyk D. A., 2013, A Bayesian Approach to Deriving Ages of Individual Field White Dwarfs, ApJ, 775, 1
- Oomen G.-M., Van Winckel H., Pols O., Nelemans G., 2019, Modelling depletion by re-accretion of gas from a dusty disc in post-AGB stars, A&A, 629, A49
- Oomen G.-M., Pols O., Van Winckel H., Nelemans G., 2020, Disc-binary interactions in depleted post-AGB binaries, A&A, 642, A234
- Oppenheimer B. R., Kulkarni S. R., Matthews K., Nakajima T., 1995, *Infrared Spectrum of the Cool Brown Dwarf Gl 229B*, Science, 270, 1478
- Owen J. E., Alvarez M. A., 2016, UV Driven Evaporation of Close-in Planets: Energy-limited, Recombination-limited, and Photon-limited Flows, ApJ, 816, 34
- Owen J. E., Wu Y., 2016, Atmospheres of Low-mass Planets: The "Boil-off", ApJ, 817, 107
- Pablo H., et al., 2012, Seismic evidence for non-synchronization in two close sdb+dM binaries from Kepler photometry, MNRAS, 422, 1343
- Paczynski B., 1976, in Eggleton P., Mitton S., Whelan J., eds, Vol. 73, Structure and Evolution of Close Binary Systems. p. 75
- Pagano I., Lanza A. F., Leto G., Messina S., Barge P., Baglin A., 2009, *CoRoT-2a Magnetic Activity: Hints for Possible Star-Planet Interaction*, Earth Moon and Planets, 105, 373
- Paquette C., Pelletier C., Fontaine G., Michaud G., 1986, *Diffusion Coefficients for Stellar Plasmas*, ApJS, 61, 177
- Parker Q. A., 2022, *Planetary nebulae and how to find them: A concise review*, Frontiers in Astronomy and Space Sciences, 9, 895287
- Parsons S. G., et al., 2013, Eclipsing post-common envelope binaries from the Catalina surveys, MNRAS, 429, 256
- Parsons S. G., et al., 2017a, *Testing the white dwarf mass-radius relationship with eclipsing binaries*, MNRAS, 470, 4473
- Parsons S. G., et al., 2017b, Two white dwarfs in ultrashort binaries with detached, eclipsing, likely sub-stellar companions detected by K2, MNRAS, 471, 976
- Parsons S. G., et al., 2018, The scatter of the M dwarf mass-radius relationship, MNRAS, 481, 1083
- Parsons S. G., et al., 2020, A pulsating white dwarf in an eclipsing binary, Nature Astronomy, 4, 690
- Parsons S. G., Gänsicke B. T., Schreiber M. R., Marsh T. R., Ashley R. P., Breedt E., Littlefair S. P., Meusinger H., 2021, *Magnetic white dwarfs in post-common-envelope binaries*, MNRAS, 502, 4305
- Passy J.-C., et al., 2012a, Simulating the Common Envelope Phase of a Red Giant Using Smoothed-particle Hydrodynamics and Uniform-grid Codes, ApJ, 744, 52
- Passy J.-C., Mac Low M.-M., De Marco O., 2012b, On the Survival of Brown Dwarfs and Planets Engulfed by Their Giant Host Star, ApJ, 759, L30
- Patten B. M., et al., 2006, Spitzer IRAC Photometry of M, L, and T Dwarfs, ApJ, 651, 502 Pecaut M. J., Mamajek E. E., 2013, Intrinsic Colors, Temperatures, and Bolometric Corrections of Pre-main-sequence Stars, ApJS, 208, 9
- Perets H. B., Kenyon S. J., 2013, Wind-accretion Disks in Wide Binaries, Second-generation Protoplanetary Disks, and Accretion onto White Dwarfs, ApJ, 764, 169
- Petigura E. A., Howard A. W., Marcy G. W., 2013, *Prevalence of Earth-size planets orbiting Sun-like stars*, Proceedings of the National Academy of Science, 110, 19273

- Pfahl E., Rappaport S., Podsiadlowski P., 2003, *The Galactic Population of Low- and Intermediate-Mass X-Ray Binaries*, ApJ, 597, 1036
- Piddington J. H., Drake J. F., 1968, *Electrodynamic Effects of Jupiter's Satellite Io*, Nature, 217, 935
- Pineda J. S., Hallinan G., Kirkpatrick J. D., Cotter G., Kao M. M., Mooley K., 2016, A Survey for Hα Emission from Late L Dwarfs and T Dwarfs, ApJ, 826, 73
- Pineda J. S., Hallinan G., Kao M. M., 2017, A Panchromatic View of Brown Dwarf Aurorae, ApJ, 846, 75
- Politano M., 2004, The Formation of Cataclysmic Variables with Brown Dwarf Secondaries, ApJ, 604, 817
- Politano M., Taam R. E., van der Sluys M., Willems B., 2008, *Common-Envelope Mergers:* A Possible Channel for Forming Single sdB Stars, ApJ, 687, L99
- Potter A. T., Tout C. A., 2010, Magnetic field evolution of white dwarfs in strongly interacting binary star systems, MNRAS, 402, 1072
- Preece H. P., Tout C. A., Jeffery C. S., 2018, *Tidal Interactions of Close Hot Subdwarf Binaries*, MNRAS, 481, 715
- Pribulla T., Rucinski S. M., 2006, Contact Binaries with Additional Components. I. The Extant Data, AJ, 131, 2986
- Pringle J. E., Wade R. A., 1985, Interacting binary stars
- Privitera G., Meynet G., Eggenberger P., Vidotto A. A., Villaver E., Bianda M., 2016, *Star-planet interactions. I. Stellar rotation and planetary orbits*, A&A, 591, A45
- Provencal J. L., Shipman H. L., Høg E., Thejll P., 1998, *Testing the White Dwarf Mass-Radius Relation with HIPPARCOS*, ApJ, 494, 759
- Provencal J. L., Shipman H. L., MacDonald J., 2005, *The Discovery of Oxygen-rich Chromospheres in Two Massive DQ White Dwarfs*, ApJ, 627, 418
- Pshirkov M. S., et al., 2020, Discovery of a hot ultramassive rapidly rotating DBA white dwarf, MNRAS, 499, L21
- Quirion P. O., Fontaine G., Brassard P., 2012, Wind Competing Against Settling: A Coherent Model of the GW Virginis Instability Domain, ApJ, 755, 128
- Raffelt G. G., 1996, Stars as laboratories for fundamental physics: the astrophysics of neutrinos, axions, and other weakly interacting particles
- Rafikov R. R., Garmilla J. A., 2012, *Inner Edges of Compact Debris Disks around Metal-rich White Dwarfs*, ApJ, 760, 123
- Rao S., Meynet G., Eggenberger P., Haemmerlé L., Privitera G., Georgy C., Ekström S., Mordasini C., 2018, Star-planet interactions. V. Dynamical and equilibrium tides in convective zones, A&A, 618, A18
- Rappaport S., et al., 2017, WD 1202-024: the shortest-period pre-cataclysmic variable, MNRAS, 471, 948
- Ray L. C., Su Y. J., Ergun R. E., Delamere P. A., Bagenal F., 2009, *Current-voltage relation of a centrifugally confined plasma*, Journal of Geophysical Research (Space Physics), 114, A04214
- Rayner J. T., Toomey D. W., Onaka P. M., Denault A. J., Stahlberger W. E., Vacca W. D., Cushing M. C., Wang S., 2003, SpeX: A Medium-Resolution 0.8-5.5 Micron Spectrograph and Imager for the NASA Infrared Telescope Facility, PASP, 115, 362
- Rebassa-Mansergas A., Gänsicke B. T., Rodríguez-Gil P., Schreiber M. R., Koester D., 2007, Post-common-envelope binaries from SDSS I. 101 white dwarf main-sequence binaries with multiple Sloan Digital Sky Survey spectroscopy, MNRAS, 382, 1377

- Rebassa-Mansergas A., Nebot Gómez-Morán A., Schreiber M. R., Girven J., Gänsicke B. T., 2011, *Post-common envelope binaries from SDSS-X: the origin of low-mass white dwarfs*, MNRAS, 413, 1121
- Rebassa-Mansergas A., Nebot Gómez-Morán A., Schreiber M. R., Gänsicke B. T., Schwope A., Gallardo J., Koester D., 2012, *Post-common envelope binaries from SDSS XIV. The DR7 white dwarf-main-sequence binary catalogue*, MNRAS, 419, 806
- Rebassa-Mansergas A., Schreiber M. R., Gänsicke B. T., 2013, *M dwarf companions to white dwarfs I. Relating magnetic activity, rotation and age*, MNRAS, 429, 3570
- Rebassa-Mansergas A., Solano E., Xu S., Rodrigo C., Jiménez-Esteban F. M., Torres S., 2019, *Infrared-excess white dwarfs in the Gaia 100 pc sample*, MNRAS, 489, 3990
- Rebassa-Mansergas A., et al., 2021, White dwarf-main-sequence binaries from Gaia EDR3: the unresolved 100 pc volume-limited sample, MNRAS, 506, 5201
- Reding J. S., Hermes J. J., Clemens J. C., 2018, in Proceedings of the 21st European Workshop on White Dwarfs. p. 1, doi:10.26153/tsw/967
- Reding J. S., Hermes J. J., Vanderbosch Z., Dennihy E., Kaiser B. C., Mace C. B., Dunlap B. H., Clemens J. C., 2020, An Isolated White Dwarf with 317 s Rotation and Magnetic Emission, ApJ, 894, 19
- Reding J. S., Hermes J. J., Clemens J. C., Hegedus R. J., Kaiser B. C., 2023, *Two new white dwarfs with variable magnetic Balmer emission lines*, MNRAS, 522, 693
- Reiners A., 2012, Observations of Cool-Star Magnetic Fields, Living Reviews in Solar Physics, 9, 1
- Reiners A., Basri G., 2006, The First High-Resolution Spectra of 1.3 L Subdwarfs, AJ, 131, 1806
- Reiners A., Basri G., 2008, Chromospheric Activity, Rotation, and Rotational Braking in M and L Dwarfs, ApJ, 684, 1390
- Reiners A., Basri G., 2010, A Volume-Limited Sample of 63 M7-M9.5 Dwarfs. II. Activity, Magnetism, and the Fade of the Rotation-Dominated Dynamo, ApJ, 710, 924
- Reiners A., Mohanty S., 2012, Radius-dependent Angular Momentum Evolution in Low-mass Stars. I, ApJ, 746, 43
- Reiners A., Schüssler M., Passegger V. M., 2014, Generalized Investigation of the Rotation-Activity Relation: Favoring Rotation Period instead of Rossby Number, ApJ, 794, 144
- Reiners A., et al., 2022, Magnetism, rotation, and nonthermal emission in cool stars Average magnetic field measurements in 292 M dwarfs, arXiv e-prints, p. arXiv:2204.00342
- Reinhold T., Bell K. J., Kuszlewicz J., Hekker S., Shapiro A. I., 2019, Transition from spot to faculae domination. An alternate explanation for the dearth of intermediate Kepler rotation periods, A&A, 621, A21
- Renedo I., Althaus L. G., Miller Bertolami M. M., Romero A. D., Córsico A. H., Rohrmann R. D., García-Berro E., 2010, New Cooling Sequences for Old White Dwarfs, ApJ, 717, 183
- Reylé C., Jardine K., Fouqué P., Caballero J. A., Smart R. L., Sozzetti A., 2021, *The 10 parsec sample in the Gaia era*, A&A, 650, A201
- Ribeiro T., Baptista R., Kafka S., Dufour P., Gianninas A., Fontaine G., 2013, Accretion and activity on the post-common-envelope binary RR Caeli, A&A, 556, A34
- Ricker G. R., et al., 2015, *Transiting Exoplanet Survey Satellite (TESS)*, Journal of Astronomical Telescopes, Instruments, and Systems, 1, 014003
- Ridgway R. J., et al., 2023, 3D modelling of the impact of stellar activity on tidally locked terrestrial exoplanets: atmospheric composition and habitability, MNRAS, 518, 2472

- Robertson J. A., Eggleton P. P., 1977, *The evolution of W Ursae Majoris systems.*, MNRAS, 179, 359
- Rocchetto M., Farihi J., Gänsicke B. T., Bergfors C., 2015, *The frequency and infrared brightness of circumstellar discs at white dwarfs*, MNRAS, 449, 574
- Rodríguez-Barrera M. I., Helling C., Wood K., 2018, Environmental effects on the ionisation of brown dwarf atmospheres, A&A, 618, A107
- Rodriguez D. R., Zuckerman B., Melis C., Song I., 2011, *The Ultra Cool Brown Dwarf Companion of WD 0806-661B: Age, Mass, and Formation Mechanism*, ApJ, 732, L29
- Rojas-Ayala B., Covey K. R., Muirhead P. S., Lloyd J. P., 2012, Metallicity and Temperature Indicators in M Dwarf K-band Spectra: Testing New and Updated Calibrations with Observations of 133 Solar Neighborhood M Dwarfs, ApJ, 748, 93
- Romero A. D., et al., 2022, Discovery of 74 new bright ZZ Ceti stars in the first three years of TESS, MNRAS, 511, 1574
- Roulston B. R., et al., 2022, New Clues to the Evolution of Dwarf Carbon Stars From Their Variability and X-Ray Emission, ApJ, 926, 210
- Route M., Wolszczan A., 2012, *The Arecibo Detection of the Coolest Radio-flaring Brown Dwarf*, ApJ, 747, L22
- Rueda J. A., et al., 2019, *Electromagnetic emission of white dwarf binary mergers*, J. Cosmology Astropart. Phys., 2019, 044
- Saffer R. A., Wade R. A., Liebert J., Green R. F., Sion E. M., Bechtold J., Foss D., Kidder K., 1993, PG 0308+096 and PG 1026+002: Two New Short Period Binary Stars Resulting From Common-Envelope Evolution, AJ, 105, 1945
- Salaris M., Cassisi S., 2005, Evolution of Stars and Stellar Populations
- Salaris M., Cassisi S., Weiss A., 2002, Red Giant Branch Stars: The Theoretical Framework, PASP, 114, 375
- Sana H., et al., 2012, Binary Interaction Dominates the Evolution of Massive Stars, Science, 337, 444
- Sandage A., 1958, Cepheids in Galactic Clusters. I. CF Cass in NGC 7790., ApJ, 128, 150
- Sandquist E. L., Taam R. E., Chen X., Bodenheimer P., Burkert A., 1998, *Double Core Evolution. X. Through the Envelope Ejection Phase*, ApJ, 500, 909
- Sargent W. L. W., Searle L., 1968, A Quantitative Description of the Spectra of the Brighter Feige Stars, ApJ, 152, 443
- Saumon D., Jacobson S. B., 1999, Pure Hydrogen Model Atmospheres for Very Cool White Dwarfs, ApJ, 511, L107
- Saur J., Grambusch T., Duling S., Neubauer F. M., Simon S., 2013, *Magnetic energy fluxes in sub-Alfvénic planet star and moon planet interactions*, A&A, 552, A119
- Saur J., Willmes C., Fischer C., Wennmacher A., Roth L., Youngblood A., Strobel D. F., Reiners A., 2021, *Brown dwarfs as ideal candidates for detecting UV aurora outside the Solar System: Hubble Space Telescope observations of 2MASS J1237*+6526, A&A, 655, A75
- Scargle J. D., 1982, Studies in astronomical time series analysis. II. Statistical aspects of spectral analysis of unevenly spaced data., ApJ, 263, 835
- Schaffenroth V., et al., 2019, The EREBOS project: Investigating the effect of substellar and low-mass stellar companions on late stellar evolution. Survey, target selection, and atmospheric parameters, A&A, 630, A80
- Schimeczek C., Wunner G., 2014, Atomic Data for the Spectral Analysis of Magnetic DA

- White Dwarfs in the SDSS, ApJS, 212, 26
- Schmidt G. D., Norsworthy J. E., 1991, *Rotation and Magnetism in White Dwarfs*, ApJ, 366, 270
- Schmidt G. D., Weymann R. J., Foltz C. B., 1989, A Moderate-Resolution, High-Throughput CCD Channel for the MMT Spectrograph, PASP, 101, 713
- Schmidt G. D., Szkody P., Smith P. S., Silber A., Tovmassian G., Hoard D. W., Gänsicke B. T., de Martino D., 1996, *AR Ursae Majoris: The First High-Field Magnetic Cataclysmic Variable*, ApJ, 473, 483
- Schmidt G. D., et al., 2005, New Low Accretion Rate Magnetic Binary Systems and their Significance for the Evolution of Cataclysmic Variables, ApJ, 630, 1037
- Schmidt S. J., Cruz K. L., Bongiorno B. J., Liebert J., Reid I. N., 2007a, *Activity and Kinematics of Ultracool Dwarfs, Including an Amazing Flare Observation*, AJ, 133, 2258
- Schmidt G. D., Szkody P., Henden A., Anderson S. F., Lamb D. Q., Margon B., Schneider D. P., 2007b, Two Additions to the New Class of Low Accretion Rate Magnetic Binaries, ApJ, 654, 521
- Schmidt S. J., Hawley S. L., West A. A., Bochanski J. J., Davenport J. R. A., Ge J., Schneider D. P., 2015, *BOSS Ultracool Dwarfs. I. Colors and Magnetic Activity of M and L Dwarfs*, AJ, 149, 158
- Schmidt S. J., et al., 2016, ASASSN-16ae: A Powerful White-light Flare on an Early-L Dwarf, ApJ, 828, L22
- Scholz A., Kostov V., Jayawardhana R., Mužić K., 2015, *Rotation Periods of Young Brown Dwarfs: K2 Survey in Upper Scorpius*, ApJ, 809, L29
- Schreiber M. R., Belloni D., Gänsicke B. T., Parsons S. G., Zorotovic M., 2021a, *The origin and evolution of magnetic white dwarfs in close binary stars*, Nature Astronomy, 5, 648
- Schreiber M. R., Belloni D., Gänsicke B. T., Parsons S. G., 2021b, *Magnetic dynamos in white dwarfs II. Relating magnetism and pollution*, MNRAS, 506, L29
- Schreiber M. R., Belloni D., Zorotovic M., Zapata S., Gänsicke B. T., Parsons S. G., 2022, Magnetic dynamos in white dwarfs III. Explaining the occurrence of strong magnetic fields in close double white dwarfs, MNRAS, 513, 3090
- Schrijver C. J., 2009, On a Transition from Solar-Like Coronae to Rotation-Dominated Jovian-Like Magnetospheres in Ultracool Main-Sequence Stars, ApJ, 699, L148
- Schröder K. P., Smith R. C., 2008, *Distant future of the Sun and Earth revisited*, MNRAS, 386, 155
- Schwab J., 2021, Evolutionary Models for the Remnant of the Merger of Two Carbon-Oxygen Core White Dwarfs, ApJ, 906, 53
- Schwab J., Quataert E., Kasen D., 2016, *The evolution and fate of super-Chandrasekhar mass white dwarf merger remnants*, MNRAS, 463, 3461
- Schwope A. D., Christensen L., 2010, X-Shooting EF Eridani: further evidence for a massive white dwarf and a sub-stellar secondary, A&A, 514, A89
- Schwope A. D., Brunner H., Hambaryan V., Schwarz R., 2002, in Gänsicke B. T., Beuermann K., Reinsch K., eds, Astronomical Society of the Pacific Conference Series Vol. 261, The Physics of Cataclysmic Variables and Related Objects. p. 102
- Schwope A. D., Nebot Gomez-Moran A., Schreiber M. R., Gänsicke B. T., 2009, *Post common envelope binaries from the SDSS. VI. SDSS J120615.73+510047.0: a new low accretion rate magnetic binary*, A&A, 500, 867

- Shagatova N., Skopal A., Shugarov S. Y., Komžík R., Kundra E., Teyssier F., 2021, Wind mass transfer in S-type symbiotic binaries. III. Confirmation of a wind focusing in EG Andromedae from the nebular [O III] λ5007 line, A&A, 646, A116
- Shen K. J., 2015, Every Interacting Double White Dwarf Binary May Merge, ApJ, 805, L6
- Shen K. J., Blouin S., Breivik K., 2023, *The Q Branch Cooling Anomaly Can Be Explained by Mergers of White Dwarfs and Subgiant Stars*, arXiv e-prints, p. arXiv:2308.04559
- Shkolnik E., Walker G. A. H., Bohlender D. A., 2003, Evidence for Planet-induced Chromospheric Activity on HD 179949, ApJ, 597, 1092
- Shkolnik E., Bohlender D. A., Walker G. A. H., Collier Cameron A., 2008, *The On/Off Nature of Star-Planet Interactions*, ApJ, 676, 628
- Siess L., Livio M., 1999, The accretion of brown dwarfs and planets by giant stars I. Asymptotic giant branch stars, MNRAS, 304, 925
- Sion E. M., Greenstein J. L., Landstreet J. D., Liebert J., Shipman H. L., Wegner G. A., 1983, *A proposed new white dwarf spectral classification system.*, ApJ, 269, 253
- Skumanich A., 1972, Time Scales for Ca II Emission Decay, Rotational Braking, and Lithium Depletion, ApJ, 171, 565
- Smith J. C., et al., 2012, Kepler Presearch Data Conditioning II A Bayesian Approach to Systematic Error Correction, PASP, 124, 1000
- Soderblom D. R., 2010, The Ages of Stars, ARA&A, 48, 581
- Soker N., 1998, Can Planets Influence the Horizontal Branch Morphology?, AJ, 116, 1308
- Soker N., 2013, Merger by migration at the final phase of common envelope evolution, New Astron., 18, 18
- Solheim J. E., 2010, AM CVn Stars: Status and Challenges, PASP, 122, 1133
- Stark M. A., 2005, PhD thesis, Pennsylvania State University
- Stassun K. G., et al., 2018, The TESS Input Catalog and Candidate Target List, AJ, 156, 102
- Steckloff J. K., Debes J., Steele A., Johnson B., Adams E. R., Jacobson S. A., Springmann A., 2021, *How Sublimation Delays the Onset of Dusty Debris Disk Formation around White Dwarf Stars*, ApJ, 913, L31
- Steele I. A., Bates S. D., Gibson N., Keenan F., Meaburn J., Mottram C. J., Pollacco D., Todd I., 2008, in Ground-based and Airborne Instrumentation for Astronomy II. p. 70146J (arXiv:0809.3351), doi:10.1117/12.787889
- Steele P. R., Burleigh M. R., Farihi J., Gänsicke B. T., Jameson R. F., Dobbie P. D., Barstow M. A., 2009, *PHL 5038: a spatially resolved white dwarf + brown dwarf binary*, A&A, 500, 1207
- Steele P. R., Burleigh M. R., Dobbie P. D., Jameson R. F., Barstow M. A., Satterthwaite R. P., 2011, White dwarfs in the UKIRT Infrared Deep Sky Survey Large Area Survey: the substellar companion fraction, MNRAS, 416, 2768
- Steele P. R., et al., 2013, *NLTT 5306: the shortest period detached white dwarf+brown dwarf binary*, MNRAS, 429, 3492
- Stello D., Cantiello M., Fuller J., Huber D., García R. A., Bedding T. R., Bildsten L., Silva Aguirre V., 2016, *A prevalence of dynamo-generated magnetic fields in the cores of intermediate-mass stars*, Nature, 529, 364
- Stelzer B., Micela G., Flaccomio E., Neuhäuser R., Jayawardhana R., 2006, X-ray emission of brown dwarfs: towards constraining the dependence on age, luminosity, and

- temperature, A&A, 448, 293
- Stelzer B., et al., 2012, The ultracool dwarf DENIS-P J104814.7-395606. Chromospheres and coronae at the low-mass end of the main-sequence, A&A, 537, A94
- Stelzer B., de Martino D., Casewell S. L., Wynn G. A., Roy M., 2017, X-ray orbital modulation of a white dwarf accreting from an L dwarf. The system SDSS J121209.31+013627.7, A&A, 598, L6
- Stephan A. P., Naoz S., Gaudi B. S., 2021, Giant Planets, Tiny Stars: Producing Short-period Planets around White Dwarfs with the Eccentric Kozai-Lidov Mechanism, ApJ, 922, 4
- Stevenson A. T., Haswell C. A., Barnes J. R., Barstow J. K., 2023, *Combing the brown dwarf desert with Gaia DR3*, MNRAS, 526, 5155
- Stoughton C., et al., 2002, Sloan Digital Sky Survey: Early Data Release, AJ, 123, 485
- Strugarek A., 2021, *Physics of star-planet magnetic interactions*, arXiv e-prints, p. arXiv:2104.05968
- Strugarek A., Brun A. S., Matt S. P., Réville V., 2015, Magnetic Games between a Planet and Its Host Star: The Key Role of Topology, ApJ, 815, 111
- Stumpe M. C., et al., 2012, Kepler Presearch Data Conditioning I—Architecture and Algorithms for Error Correction in Kepler Light Curves, PASP, 124, 985
- Su J., Li Y., 2023, Asteroseismology of the Pulsating Extremely Low-mass White Dwarf SDSS J111215.82 + 111745.0: A Model with p-mode Pulsations Consistent with the Observations, ApJ, 943, 113
- Suárez Mascareño A., Rebolo R., González Hernández J. I., 2016, Magnetic cycles and rotation periods of late-type stars from photometric time series, A&A, 595, A12
- Swan A., Farihi J., Koester D., Hollands M., Parsons S., Cauley P. W., Redfield S., Gänsicke B. T., 2019, *Interpretation and diversity of exoplanetary material orbiting white dwarfs*, MNRAS, 490, 202
- Swan A., Farihi J., Wilson T. G., Parsons S. G., 2020, *The dust never settles: collisional production of gas and dust in evolved planetary systems*, MNRAS, 496, 5233
- Sweigart A. V., 1994, *The Determination of the Core Mass at the Helium Flash in Globular Cluster Stars*, ApJ, 426, 612
- Sweigart A. V., Gross P. G., 1976, *Horizontal-Branch Evolution with Semiconvection II. Theoretical Sequences*, ApJS, 32, 367
- Szkody P., et al., 2010a, Finding the Instability Strip for Accreting Pulsating White Dwarfs From Hubble Space Telescope and Optical Observations, ApJ, 710, 64
- Szkody P., et al., 2010b, Analyzing the Low State of EF Eridani with Hubble Space Telescope Ultraviolet Spectra, ApJ, 716, 1531
- Taam R. E., Ricker P. M., 2010, Common envelope evolution, New Astron. Rev., 54, 65
- Taam R. E., Sandquist E. L., 2000, Common Envelope Evolution of Massive Binary Stars, ARA&A, 38, 113
- Tan X., Showman A. P., 2020, Atmospheric Circulation of Tidally Locked Gas Giants with Increasing Rotation and Implications for White Dwarf-Brown Dwarf Systems, ApJ, 902, 27
- Tannock M. E., et al., 2021, Weather on Other Worlds. V. The Three Most Rapidly Rotating Ultra-cool Dwarfs, AJ, 161, 224
- Tappert C., Gänsicke B. T., Rebassa-Mansergas A., Schmidtobreick L., Schreiber M. R., 2011a, Multiple emission line components in detached post-common-envelope binaries, A&A, 531, A113

- Tappert C., Gänsicke B. T., Schmidtobreick L., Ribeiro T., 2011b, *Accretion in the detached post-common-envelope binary LTT 560*, A&A, 532, A129
- Tielens A. G., 2005, *The physics and chemistry of the interstellar medium*. Cambridge University Press
- Tody D., 1986, in Crawford D. L., ed., Society of Photo-Optical Instrumentation Engineers (SPIE) Conference Series Vol. 627, Proc. SPIE. p. 733, doi:10.1117/12.968154
- Tody D., 1993, in Hanisch R. J., Brissenden R. J. V., Barnes J., eds, Astronomical Society of the Pacific Conference Series Vol. 52, Astronomical Data Analysis Software and Systems II. p. 173
- Tokovinin A., Thomas S., Sterzik M., Udry S., 2006, *Tertiary companions to close spectroscopic binaries*, A&A, 450, 681
- Toonen S., Nelemans G., 2013, The effect of common-envelope evolution on the visible population of post-common-envelope binaries, A&A, 557, A87
- Toonen S., Hollands M., Gänsicke B. T., Boekholt T., 2017, *The binarity of the local white dwarf population*, A&A, 602, A16
- Toriumi S., Airapetian V. S., Hudson H. S., Schrijver C. J., Cheung M. C. M., DeRosa M. L., 2020, Sun-as-a-star Spectral Irradiance Observations of Transiting Active Regions, ApJ, 902, 36
- Tout C. A., Eggleton P. P., 1988, *Tidal enhancement by a binary companion of stellar winds from cool giants.*, MNRAS, 231, 823
- Tout C. A., Wickramasinghe D. T., Ferrario L., 2004, Magnetic fields in white dwarfs and stellar evolution, MNRAS, 355, L13
- Tout C. A., Wickramasinghe D. T., Liebert J., Ferrario L., Pringle J. E., 2008, *Binary star origin of high field magnetic white dwarfs*, MNRAS, 387, 897
- Tremblay P. E., Bergeron P., 2009, Spectroscopic Analysis of DA White Dwarfs: Stark Broadening of Hydrogen Lines Including Nonideal Effects, ApJ, 696, 1755
- Tremblay P. E., Bergeron P., Gianninas A., 2011, *An Improved Spectroscopic Analysis of DA White Dwarfs from the Sloan Digital Sky Survey Data Release* 4, ApJ, 730, 128
- Tremblay P. E., Gianninas A., Kilic M., Ludwig H. G., Steffen M., Freytag B., Hermes J. J., 2015a, 3D Model Atmospheres for Extremely Low-mass White Dwarfs, ApJ, 809, 148
- Tremblay P. E., Fontaine G., Freytag B., Steiner O., Ludwig H. G., Steffen M., Wedemeyer S., Brassard P., 2015b, *On the Evolution of Magnetic White Dwarfs*, ApJ, 812, 19
- Tremblay P.-E., et al., 2019, Core crystallization and pile-up in the cooling sequence of evolving white dwarfs, Nature, 565, 202
- Tremblay P. E., et al., 2020, Gaia white dwarfs within 40 pc I. Spectroscopic observations of new candidates, MNRAS, 497, 130
- Trigilio C., et al., 2023, Star-Planet Interaction at radio wavelengths in YZ Ceti: Inferring planetary magnetic field, arXiv e-prints, p. arXiv:2305.00809
- Tsuboi Y., Maeda Y., Feigelson E. D., Garmire G. P., Chartas G., Mori K., Pravdo S. H., 2003, Coronal X-Ray Emission from an Intermediate-Age Brown Dwarf, ApJ, 587, L51
- Unglaub K., Bues I., 2000, The chemical evolution of hot white dwarfs in the presence of diffusion and mass loss, A&A, 359, 1042
- van der Sluys M. V., Verbunt F., Pols O. R., 2006, *Modelling the formation of double white dwarfs*, A&A, 460, 209
- van Dam M. A., et al., 2006, The W. M. Keck Observatory Laser Guide Star Adaptive Optics System: Performance Characterization, PASP, 118, 310

- van Horn H. M., 1968, Crystallization of White Dwarfs, ApJ, 151, 227
- van Maanen A., 1917, *Two faint stars with large proper motion*, Publications of the Astronomical Society of the Pacific, 29, 258
- van Roestel J., et al., 2021, ZTFJ0038+2030: A Long-period Eclipsing White Dwarf and a Substellar Companion, ApJ, 919, L26
- van Vledder I., van der Vlugt D., Holwerda B. W., Kenworthy M. A., Bouwens R. J., Trenti M., 2016, *The size and shape of the Milky Way disc and halo from M-type brown dwarfs in the BoRG survey*, MNRAS, 458, 425
- van Winckel H., Mathis J. S., Waelkens C., 1992, Evidence from zinc abundances for dust fractiionation in chemically peculiar stars., Nature, 356, 500
- van Winckel H., Waelkens C., Waters L. B. F. M., Molster F. J., Udry S., Bakker E. J., 1998, *The binary RV Tauri star AC HER and evidence for a long-lived dust-disc*, A&A, 336, L17
- von Hippel T., Jefferys W. H., Scott J., Stein N., Winget D. E., De Gennaro S., Dam A., Jeffery E., 2006, *Inverting Color-Magnitude Diagrams to Access Precise Star Cluster Parameters: A Bayesian Approach*, ApJ, 645, 1436
- Vacca W. D., Cushing M. C., Rayner J. T., 2003, A Method of Correcting Near-Infrared Spectra for Telluric Absorption, PASP, 115, 389
- Valyavin G., Bagnulo S., Monin D., Fabrika S., Lee B. C., Galazutdinov G., Wade G. A., Burlakova T., 2005, *Rotation period and magnetic field morphology of the white dwarf WD 0009+501*, A&A, 439, 1099
- Valyavin G., Wade G. A., Bagnulo S., Szeifert T., Landstreet J. D., Han I., Burenkov A., 2008, The Peculiar Magnetic Field Morphology of the White Dwarf WD 1953-011: Evidence for a Large-Scale Magnetic Flux Tube?, ApJ, 683, 466
- Valyavin G., et al., 2014, Suppression of cooling by strong magnetic fields in white dwarf stars, Nature, 515, 88
- VanderPlas J. T., 2018, Understanding the Lomb-Scargle Periodogram, ApJS, 236, 16
- VanderPlas J. T., Ivezić Ž., 2015, *Periodograms for Multiband Astronomical Time Series*, ApJ, 812, 18
- Vanderbosch Z., et al., 2020, A White Dwarf with Transiting Circumstellar Material Far outside the Roche Limit, ApJ, 897, 171
- Vanderburg A., et al., 2015, A disintegrating minor planet transiting a white dwarf, Nature, 526, 546
- Vanderburg A., et al., 2020, A giant planet candidate transiting a white dwarf, Nature, 585, 363
- Vauclair G., Vauclair S., Greenstein J. L., 1979, The chemical evolution of white dwarf atmospheres: diffusion and accretion., A&A, 80, 79
- Venner A., Blouin S., Bédard A., Vanderburg A., 2023, A Crystallizing White Dwarf in a Sirius-Like Quadruple System, arXiv e-prints, p. arXiv:2306.03140
- Veras D., 2016, *Post-main-sequence planetary system evolution*, Royal Society Open Science, 3, 150571
- Veras D., Fuller J., 2019, *Tidal circularization of gaseous planets orbiting white dwarfs*, MNRAS, 489, 2941
- Veras D., Wyatt M. C., Mustill A. J., Bonsor A., Eldridge J. J., 2011, *The great escape: how exoplanets and smaller bodies desert dying stars*, MNRAS, 417, 2104
- Veras D., et al., 2019, Orbital relaxation and excitation of planets tidally interacting with white dwarfs, MNRAS, 486, 3831

- Verbunt F., Zwaan C., 1981, Magnetic braking in low-mass X-ray binaries., A&A, 100, L7
- Vernet J., et al., 2011, X-shooter, the new wide band intermediate resolution spectrograph at the ESO Very Large Telescope, A&A, 536, A105
- Vidotto A. A., 2021, *The evolution of the solar wind*, Living Reviews in Solar Physics, 18, 3
- Vidotto A. A., Bourrier V., 2017, Exoplanets as probes of the winds of host stars: the case of the M dwarf GJ 436, MNRAS, 470, 4026
- Vidotto A. A., Jardine M., Morin J., Donati J. F., Opher M., Gombosi T. I., 2014, *M-dwarf stellar winds: the effects of realistic magnetic geometry on rotational evolution and planets*, MNRAS, 438, 1162
- Villaver E., Livio M., 2007, Can Planets Survive Stellar Evolution?, ApJ, 661, 1192
- Villaver E., Livio M., Mustill A. J., Siess L., 2014, *Hot Jupiters and Cool Stars*, ApJ, 794, 3
- Vincent O., Barstow M. A., Jordan S., Mander C., Bergeron P., Dufour P., 2023, Classification and parameterisation of a large Gaia sample of white dwarfs using XP spectra, arXiv e-prints, p. arXiv:2308.05572
- Vogt S. S., et al., 1994, in Crawford D. L., Craine E. R., eds, Society of Photo-Optical Instrumentation Engineers (SPIE) Conference Series Vol. 2198, Instrumentation in Astronomy VIII. p. 362, doi:10.1117/12.176725
- Vollmann K., Eversberg T., 2006, Remarks on statistical errors in equivalent widths, Astronomische Nachrichten, 327, 862
- Waelkens C., Van Winckel H., Waters L. B. F. M., Bakker E. J., 1996, *Variability and nature of the binary in the Red Rectangle nebula.*, A&A, 314, L17
- Walker G. A. H., et al., 2008, MOST detects variability on τ Bootis A possibly induced by its planetary companion, A&A, 482, 691
- Walters N., et al., 2021, A test of the planet-star unipolar inductor for magnetic white dwarfs, MNRAS, 503, 3743
- Walters N., Farihi J., Marsh T. R., Breedt E., Cauley P. W., von Hippel T., Hermes J. J., 2022, *Two substellar survivor candidates; one found and one missing*, arXiv e-prints, p. arXiv:2207.07022
- Walters N., Farihi J., Dufour P., Pineda J. S., Izzard R. G., 2023, Measurement of stellar and substellar winds using white dwarf hosts, arXiv e-prints, p. arXiv:2306.11806
- Waters L. B. F. M., Trams N. R., Waelkens C., 1992, A scenario for the selective depletion of stellar atmospheres., A&A, 262, L37
- Weaver B. A., 2017, Pydl, doi:10.5281/zenodo.1095151
- Webbink R. F., 1984, Double white dwarfs as progenitors of R Coronae Borealis stars and type I supernovae., ApJ, 277, 355
- Webbink R. F., 2008, in Milone E. F., Leahy D. A., Hobill D. W., eds, Astrophysics and Space Science Library Vol. 352, Astrophysics and Space Science Library. p. 233 (arXiv:0704.0280), doi:10.1007/978-1-4020-6544-6_13
- Webbink R. F., Wickramasinghe D. T., 2002, *Cataclysmic variable evolution: AM Her binaries and the period gap*, MNRAS, 335, 1
- Webbink R. F., Wickramasinghe D. T., 2005, in Hameury J. M., Lasota J. P., eds, Astronomical Society of the Pacific Conference Series Vol. 330, The Astrophysics of Cataclysmic Variables and Related Objects. p. 137
- Wegner G., Yackovich F. H., 1984, Analyses of the visual spectra of white dwarfs contain-

- ing carbon., ApJ, 284, 257
- Weidemann V., Koester D., 1983, The upper mass limit for white dwarf progenitors and the initial-final mass relation for low and intermediate mass stars., A&A, 121, 77
- Weinberg M. D., Shapiro S. L., Wasserman I., 1987, *The Dynamical Fate of Wide Binaries in the Solar Neighborhood*, ApJ, 312, 367
- Weisskopf M. C., Wu K., Trimble V., O'Dell S. L., Elsner R. F., Zavlin V. E., Kouveliotou C., 2007, A Chandra Search for Coronal X-Rays from the Cool White Dwarf GD 356, ApJ, 657, 1026
- Wendell C. E., van Horn H. M., Sargent D., 1987, Magnetic Field Evolution in White Dwarfs, ApJ, 313, 284
- Werner K., Herwig F., 2006, *The Elemental Abundances in Bare Planetary Nebula Central Stars and the Shell Burning in AGB Stars*, PASP, 118, 183
- Werner K., Wolff B., Pakull M. W., Cowley A. P., Schmidtke P. C., Hutchings J. B., Crampton D., 1996, in Greiner J., ed., Vol. 472, Supersoft X-Ray Sources. p. 131, doi:10.1007/BFb0102256
- Wickramasinghe D. T., Ferrario L., 2005, *The origin of the magnetic fields in white dwarfs*, MNRAS, 356, 1576
- Wickramasinghe D. T., Farihi J., Tout C. A., Ferrario L., Stancliffe R. J., 2010, *Does GD356 have a terrestrial planetary companion?*, MNRAS, 404, 1984
- Wickramasinghe D. T., Tout C. A., Ferrario L., 2014a, *The most magnetic stars*, MNRAS, 437, 675
- Wickramasinghe D. T., Tout C. A., Ferrario L., 2014b, *The most magnetic stars*, MNRAS, 437, 675
- Willes A. J., Wu K., 2004, Electron-cyclotron maser emission from white dwarf pairs and white dwarf planetary systems, MNRAS, 348, 285
- Willes A. J., Wu K., 2005, Radio emissions from terrestrial planets around white dwarfs, A&A, 432, 1091
- Williams P. K. G., Cook B. A., Berger E., 2014, Trends in Ultracool Dwarf Magnetism. I. X-Ray Suppression and Radio Enhancement, ApJ, 785, 9
- Williams K. A., Montgomery M. H., Winget D. E., Falcon R. E., Bierwagen M., 2016, Variability in Hot Carbon-dominated Atmosphere (Hot DQ) White Dwarfs: Rapid Rotation?, ApJ, 817, 27
- Willson L. A., 2000, Mass Loss From Cool Stars: Impact on the Evolution of Stars and Stellar Populations, ARA&A, 38, 573
- Wilson P. A., et al., 2016, The SOPHIE search for northern extrasolar planets. IX. Populating the brown dwarf desert, A&A, 588, A144
- Wilson T. G., Farihi J., Gänsicke B. T., Swan A., 2019, The unbiased frequency of planetary signatures around single and binary white dwarfs using Spitzer and Hubble, MNRAS, 487, 133
- Winget D. E., Kepler S. O., 2008, *Pulsating white dwarf stars and precision asteroseis-mology.*, ARA&A, 46, 157
- Winget D. E., Robinson E. L., Nather R. D., Fontaine G., 1982, *Photometric observations of GD 358: OB white dwarfs do pulsate.*, ApJ, 262, L11
- Winget D. E., Hansen C. J., van Horn H. M., 1983, *Do pulsating PG1159-035 stars put constraints on stellar evolution?*, Nature, 303, 781
- Winget D. E., Sullivan D. J., Metcalfe T. S., Kawaler S. D., Montgomery M. H., 2004, A Strong Test of Electroweak Theory Using Pulsating DB White Dwarf Stars as Plasmon

- Neutrino Detectors, ApJ, 602, L109
- Winget D. E., Kepler S. O., Campos F., Montgomery M. H., Girardi L., Bergeron P., Williams K., 2009, The Physics of Crystallization From Globular Cluster White Dwarf Stars in NGC 6397, ApJ, 693, L6
- Wizinowich P. L., et al., 2006, *The W. M. Keck Observatory Laser Guide Star Adaptive Optics System: Overview*, PASP, 118, 297
- Woltjer L., 1964, X-Rays and Type I Supernova Remnants., ApJ, 140, 1309
- Wood B. E., Müller H.-R., Zank G. P., Linsky J. L., 2002, Measured Mass-Loss Rates of Solar-like Stars as a Function of Age and Activity, ApJ, 574, 412
- Wood B. E., Müller H. R., Zank G. P., Linsky J. L., Redfield S., 2005, New Mass-Loss Measurements from Astrospheric Lyα Absorption, ApJ, 628, L143
- Wood B. E., Linsky J. L., Güdel M., 2015, in Lammer H., Khodachenko M., eds, Astrophysics and Space Science Library Vol. 411, Characterizing Stellar and Exoplanetary Environments. p. 19, doi:10.1007/978-3-319-09749-7_2
- Wood B. E., Laming J. M., Warren H. P., Poppenhaeger K., 2018, *A Chandra/LETGS Survey of Main-sequence Stars*, ApJ, 862, 66
- Wood B. E., et al., 2021, New Observational Constraints on the Winds of M dwarf Stars, ApJ, 915, 37
- Woodgate B. E., et al., 1998, *The Space Telescope Imaging Spectrograph Design*, PASP, 110, 1183
- Wright E. L., et al., 2010, The Wide-field Infrared Survey Explorer (WISE): Mission Description and Initial On-orbit Performance, AJ, 140, 1868
- Wright N. J., Drake J. J., Mamajek E. E., Henry G. W., 2011, *The Stellar-activity-Rotation Relationship and the Evolution of Stellar Dynamos*, ApJ, 743, 48
- Wright N. J., Newton E. R., Williams P. K. G., Drake J. J., Yadav R. K., 2018, *The stellar rotation-activity relationship in fully convective M dwarfs*, MNRAS, 479, 2351
- Wu K., 2000, Accretion onto Magnetic White Dwarfs, Space Sci. Rev., 93, 611
- Wu C., Xiong H., Wang X., 2022, Formation of ultra-massive carbon-oxygen white dwarfs from the merger of carbon-oxygen and helium white dwarf pairs, MNRAS, 512, 2972
- Wunner G., Roesner W., Herold H., Ruder H., 1985, Stationary hydrogen lines in white dwarf magnetic fields and the spectrum of the magnetic degenerate GRW +70 8247., A&A, 149, 102
- Wynn G. A., King A. R., Horne K., 1997, A magnetic propeller in the cataclysmic variable AE Aquarii, MNRAS, 286, 436
- Xiong H., Chen X., Podsiadlowski P., Li Y., Han Z., 2017, Subdwarf B stars from the common envelope ejection channel, A&A, 599, A54
- Xu S., Jura M., Pantoja B., Klein B., Zuckerman B., Su K. Y. L., Meng H. Y. A., 2015, A Young White Dwarf with an Infrared Excess, ApJ, 806, L5
- Xu S., Jura M., Dufour P., Zuckerman B., 2016, Evidence for Gas from a Disintegrating Extrasolar Asteroid, ApJ, 816, L22
- Xu S., Lai S., Dennihy E., 2020, Infrared Excesses around Bright White Dwarfs from Gaia and unWISE. I., ApJ, 902, 127
- York D. G., et al., 2000, *The Sloan Digital Sky Survey: Technical Summary*, AJ, 120, 1579 Zapatero Osorio M. R., Martín E. L., Bouy H., Tata R., Deshpande R., Wainscoat R. J., 2006, *Spectroscopic Rotational Velocities of Brown Dwarfs*, ApJ, 647, 1405
- Zarka P., 1998, Auroral radio emissions at the outer planets: Observations and theories, J. Geophys. Res., 103, 20159

- Zhang Z. H., et al., 2017, Primeval very low-mass stars and brown dwarfs I. Six new L subdwarfs, classification and atmospheric properties, MNRAS, 464, 3040
- Zhang Z. H., et al., 2018, Primeval very low-mass stars and brown dwarfs IV. New L subdwarfs, Gaia astrometry, population properties, and a blue brown dwarf binary, MNRAS, 480, 5447
- Zhang Z., et al., 2020, COol Companions ON Ultrawide orbiTS (COCONUTS). I. A High-gravity T4 Benchmark around an Old White Dwarf and a Re-examination of the Surface-gravity Dependence of the L/T Transition, ApJ, 891, 171
- Zhu W., Petrovich C., Wu Y., Dong S., Xie J., 2018, About 30% of Sun-like Stars Have Kepler-like Planetary Systems: A Study of Their Intrinsic Architecture, ApJ, 860, 101
- Zijlstra A. A., Chapman J. M., te Lintel Hekkert P., Likkel L., Comeron F., Norris R. P., Molster F. J., Cohen R. J., 2001, *Bipolar outflows in OH/IR stars*, MNRAS, 322, 280
- Zink J. K., Christiansen J. L., Hansen B. M. S., 2019, Accounting for incompleteness due to transit multiplicity in Kepler planet occurrence rates, MNRAS, 483, 4479
- Zorotovic M., Schreiber M. R., 2022, Close detached white dwarf + brown dwarf binaries: Further evidence for low values of the common envelope efficiency, MNRAS,
- Zorotovic M., Schreiber M. R., Gänsicke B. T., Nebot Gómez-Morán A., 2010, Post-common-envelope binaries from SDSS. IX: Constraining the common-envelope efficiency, A&A, 520, A86
- Zorotovic M., Schreiber M. R., Gänsicke B. T., 2011, Post common envelope binaries from SDSS. XI. The white dwarf mass distributions of CVs and pre-CVs, A&A, 536, A42
- Zuckerman B., 2014, *The Occurrence of Wide-orbit Planets in Binary Star Systems*, ApJ, 791, L27
- Zuckerman B., Reid I. N., 1998, Metals in Cool DA White Dwarfs, ApJ, 505, L143
- Zuckerman B., Koester D., Reid I. N., Hünsch M., 2003, *Metal Lines in DA White Dwarfs*, ApJ, 596, 477
- Zuckerman B., Koester D., Melis C., Hansen B. M., Jura M., 2007, *The Chemical Composition of an Extrasolar Minor Planet*, ApJ, 671, 872
- Zuckerman B., Melis C., Klein B., Koester D., Jura M., 2010, *Ancient Planetary Systems are Orbiting a Large Fraction of White Dwarf Stars*, ApJ, 722, 725